

INHOMOGENEOUS AND DISORDERED QUANTUM SYSTEMS: FROM
DYNAMICS TO TOPOLOGY

Dissertation

zur

Erlangung der naturwissenschaftlichen Doktorwürde
(Dr. sc. nat)

vorgelegt der

Mathematisch-naturwissenschaftlichen Fakultät

der

Universität Zürich

von

Bastien Lapierre

von

Giffers/FR

Promotionskommission

Dr. Luka Trifunovic
Prof. Dr. Titus Neupert
Prof. Dr. Johan Chang

Zürich, 2023

La pensée n'est qu'un éclair au milieu d'une longue nuit. Mais c'est cet éclair qui est tout.

— Henri Poincaré

A B S T R A C T

Translation symmetry is a fundamental concept in condensed matter physics that describes the invariance of the physical properties of a given system under discrete or continuous spatial translations. This symmetry plays a crucial role in the understanding of the behavior of solids, liquids, and other condensed matter systems. For example, the periodic arrangement of atoms in a crystal lattice is a manifestation of translation symmetry, which gives rise to electronic band theory, a cornerstone of our understanding of solid state systems. Moreover, exotic properties of electronic band structures led to the discovery of topological phases of matter. Nevertheless, many real-world systems lack such symmetry due to impurities, defects, and other sources of disorder.

The aim of this thesis is to investigate the physics of condensed matter systems that lack translation symmetry, either through the introduction of impurities and disorder, or through engineered smooth spatial deformations of the Hamiltonian density. Specifically, we focus on topological phases in fully disordered and Anderson localized lattices, for which traditional topological classifications do not apply. Furthermore, we study the non-equilibrium dynamics of spatially inhomogeneous critical models and the emergence of rich spatial structures, in a class of systems that lack full translation symmetry both in space and in time, shedding new light on the peculiar heating properties of driven integrable systems.

The first part of the thesis is concerned with topological phases of matter beyond the paradigmatic periodic classification of topological insulators (TIs) and superconductors (TSCs). We first investigate a generalization to an arbitrary number of electronic bands of the Hopf insulator, a delicate TI whose existence strongly relies on the presence of lattice translation symmetry. We obtain a \mathbb{Z} classification for N -band Hopf insulators, that we relate to the quantized isotropic magnetoelectric coefficient of their bulk. We formulate a general bulk-boundary correspondence for such an N -band Hopf insulator connecting the bulk topology to the quantized Hall conductivity on the boundary, despite the non-uniqueness of the division between bulk and boundary. We then show that on the other hand fully localized, three-dimensional, time-reversal-symmetry-broken disordered insulators do not belong to a single phase of matter but can realize topologically distinct phases that are labeled by integers. The phase transition occurs only when the system becomes conducting at some filling. We find that these novel topological phases are fundamentally distinct from insulators without disorder: they are guaranteed to host delocalized boundary states giving rise to the quantized boundary Hall conductance, whose value is equal to the bulk topological invariant associated to a quantized isotropic magnetoelectric polarizability tensor.

The second part of the thesis is concerned with the dynamics of periodically and quasi-periodically driven inhomogeneous critical quantum systems in $(1+1)$ dimensions, through an effective low energy description comprising inhomogeneous conformal field theories (CFTs). Through conformal maps that encode the time evolution of fields, and lead to the time evolution of energy and entanglement entropy, we establish a correspondence between such driven inhomogeneous CFTs and dynamical systems on the circle. This exact correspondence leads to the emergence of heating and non-heating phase, depending

on the existence or not of fixed points in the one-cycle Floquet map. The heating phase is characterized by emergent Floquet horizons that absorb all energy and entanglement of the driven system. In the limit of large central charge, we show that these horizons act as fast scramblers of quantum information by computing out-of-time-order correlators (OTOCs), and their associated Hawking temperature sets the Lyapunov exponent of the exponential OTOC decay. Furthermore, we corroborate our analytical findings with numerical calculations on driven inhomogeneous free fermion chains, for pure and thermal initial states as well as for closed and dissipative environments.

The last part of the thesis is concerned with the study of Tomonaga-Luttinger liquids (TLLs) thrown out of equilibrium by marginal deformations in the form of interaction modulations. This is modeled by quenching or periodically driving the Luttinger parameter between two different values. Specifically, we obtain exact analytical results for the evolution of the Loschmidt echo and observables such as the particle and energy densities. For generic pure initial states, the quench dynamics are shown to exhibit periodic revivals and temporal orthogonalities. For thermal initial states, we show the equilibration of the TLL to an effective temperature determined by the ratios of the Luttinger parameters. For the periodic drive, we show stability or instability of time-evolved physical quantities dependent on the drive parameters, and prove that the transition between stable and unstable phases is universally described by a critical exponent of one-half. We further study equilibrium properties of marginally deformed TLLs, and compare inequivalent thermal density matrices by non-perturbatively evaluating their Rényi divergence and relative entropy.

PUBLICATIONS

- [1] Bastien Lapierre, Kenny Choo, Clément Tauber, Apoorv Tiwari, Titus Neupert, and Ramasubramanian Chitra. “Emergent black hole dynamics in critical Floquet systems.” In: *Phys. Rev. Res.* 2 (2 2020), p. 023085.
- [2] Bastien Lapierre, Kenny Choo, Apoorv Tiwari, Clément Tauber, Titus Neupert, and R. Chitra. “Fine structure of heating in a quasiperiodically driven critical quantum system.” In: *Phys. Rev. Res.* 2 (3 2020), p. 033461.
- [3] Bastien Lapierre and Per Moosavi. “Geometric approach to inhomogeneous Floquet systems.” In: *Phys. Rev. B* 103 (22 2021), p. 224303.
- [4] Bastien Lapierre, Titus Neupert, and Luka Trifunovic. “ N -band Hopf insulator.” In: *Phys. Rev. Res.* 3 (3 2021), p. 033045.
- [5] Bastien Lapierre, Titus Neupert, and Luka Trifunovic. “Topologically Localized Insulators.” In: *Phys. Rev. Lett.* 129 (25 2022), p. 256401.
- [6] Kenny Choo, Bastien Lapierre, Clemens Kuhlenkamp, Apoorv Tiwari, Titus Neupert, and Ramasubramanian Chitra. “Thermal and dissipative effects on the heating transition in a driven critical system.” In: *SciPost Phys.* 13 (2022), p. 104.
- [7] Shouvik Datta, Bastien Lapierre, Per Moosavi, and Apoorv Tiwari. *Marginal quenches and drives in Tomonaga-Luttinger liquids*. To appear in *SciPost Physics*, arXiv:2206.11287 [cond-mat.stat-mech]. 2022.
- [8] Paolo Molignini, Bastien Lapierre, R. Chitra, and Wei Chen. *Probing Chern number by opacity and topological phase transition by a nonlocal Chern marker*. arXiv:2207.00016 [cond-mat.str-el]. 2022.
- [9] Blagoje Oblak, Bastien Lapierre, Per Moosavi, Jean-Marie Stéphan, and Benoit Estienne. *Anisotropic Quantum Hall Droplets*. arXiv:2301.01726 [cond-mat.mes-hall]. 2023.

A C K N O W L E D G M E N T S

This thesis is the culmination of four years of work, and it would not have been possible without the invaluable support and dedicated guidance of my supervisors and mentors Titus Neupert, Luka Trifunovic, and Ramasubramanian Chitra. They demonstrated with passion how creative and exciting theoretical physics can be, and provided me with the necessary rigor and methods to make progress in my own research. Moreover, they granted me the independence to develop my own research ideas and grow as a young scientist.

I am indebted to all of my collaborators for their contributions to the works presented in this thesis. I would like to extend a special thanks to Apoorv Tiwari, Per Moosavi, and Blagoje Oblak for their long-term collaborations and friendly discussions about physics and beyond. Their positive attitude made our collaborations especially enjoyable and inspiring. I am also grateful to Shinsei Ryu, Piet Brouwer, and Alexander Altland for the fruitful and inspiring exchanges that have led to new ideas and follow-up questions to some of the works presented in this thesis.

I am grateful to my office mates at the University of Zurich for cultivating a pleasant work environment, and for the stimulating brainstorming sessions that have broadened my knowledge of physics, amongst other topics. In particular, I am grateful to Kenny Choo for having taught me better than anyone else how to code, Patrick Lenggenhager for always having been present to help on various physics questions, Nastya Skurativska for her friendly sense of sarcasm, Berni Lüscher for the discussions about music and cinema, and Marti Soldini for her relentless energy, and for being a great friend. I would also like to express my acknowledgments to Michael Denner, Nikita Astrakhantsev, Glenn Wagner, Tarun Tummuru, and Xiaoxiong Liu for fostering a wonderful group dynamic and organizing great events outside of the university.

A PhD thesis is also an invaluable experience of teaching and supervision, and I would like to express my gratitude to the students I had the chance of partially supervising during these four years: Fabian Jaeger, Johannes Christmann, and Valerio Pagni. Overall, I am thankful to all of my students for having made my experience as a teaching assistant so enjoyable and fulfilling.

During the course of my PhD thesis, I had the pleasure of meeting exceptional individuals at conferences and in various settings beyond academia. Although I cannot name them all, I would like to extend my special thanks to Benjamin, Giulia, Aneesh, Euan, Tinbite, Maeva, and Eli.

My long time friends Ladislas, René, Joseph, Etienne, Mahé, Solène, Emilie have been an invaluable source of encouragement throughout this journey. Our numerous excursions over the past four years, from Lausanne to Violès, have been unforgettable breaks from physics.

Lastly, I want to express my heartfelt gratitude to my family, and in particular to my brothers Rémi and Florent, and to Papa and Maman, for their unwavering support throughout these long studies.

C O N T E N T S

I	Introduction	
1	Preface	3
2	Topology and disorder	7
2.1	Anderson localization	7
2.2	Strong topological phases	10
2.3	Beyond tenfold-way topology	15
2.4	Anomalous Floquet-Anderson insulators	16
3	Conformal field theory	19
3.1	Scaling invariance at criticality	19
3.2	Conformal invariance	20
3.3	Torus partition function	24
3.4	Boundary conformal field theory	25
4	Quantum systems out-of-equilibrium	27
4.1	Thermalization of quantum systems	27
4.2	Integrable models	29
4.3	Quantum chaos in thermalizing systems	32
II	From delicate to disordered topological phases	
5	N -band Hopf insulator	39
5.1	Introduction	39
5.2	Hopf Insulator	40
5.3	N -band Hopf insulators	43
5.4	Bulk-boundary correspondence	46
5.5	Orbital magnetization	48
5.6	Examples	50
6	Topologically localized insulators	59
6.1	Introduction	59
6.2	A concrete model of a TLI	59
6.3	Bulk and boundary invariants	61
6.4	Bulk-boundary correspondence	63
6.5	Stability of the TLI phase	64
6.6	Quantized response	67
6.7	Relation to N -band Hopf insulators	68
6.8	Resonant energy model of a TLI	70
III	Non-equilibrium dynamics of inhomogeneous critical systems	
7	Emergent curved spacetime in critical Floquet systems	75
7.1	Introduction	75
7.2	Stroboscopic evolution from Möbius maps	76
7.3	Heating and non-heating phases	80
7.4	Curved light-cones and emergent Floquet horizons	84
7.5	Effective Hamiltonian	90
8	Quasiperiodically driven inhomogeneous critical systems	95
8.1	Introduction	95
8.2	Fibonacci word as quasiperiodic drives	95
8.3	Fine structure of heating	97

8.4	Mapping to quasicrystals	102
8.5	Exceptions to heating	106
8.6	Quasiparticle picture and lattice calculations	108
9	A geometric approach to inhomogeneous Floquet dynamics	113
9.1	Setting and general approach	113
9.2	Floquet dynamics from circles maps	118
9.3	Dynamics of energy and entanglement	120
9.4	Floquet Hamiltonian and critical exponents	126
10	Thermal and dissipative effects on Floquet dynamics	131
10.1	Introduction	131
10.2	Thermal effects on the heating dynamics	133
10.3	Effects of dissipation on the heating transition	138
11	Floquet engineered inhomogeneous quantum chaos	147
11.1	Introduction	147
11.2	Prelude: Quantum chaos at large central charge	147
11.3	OTOCs for inhomogeneous Floquet CFTs	150
11.4	Chaos to non-chaos transitions	154
11.5	OTOC measurements and backward time evolution	156
12	Berry phases from adiabatic drives	161
12.1	Prelude: Berry phases of Virasoro orbits	161
12.2	Adiabatic deformations of critical systems	162
iv	Marginal deformations of Tomonaga-Luttinger liquids	
13	Marginal quenches and drives in Tomonaga-Luttinger liquids	171
13.1	Introduction	171
13.2	Applications	172
13.3	Algebraic framework and Bogoliubov transformations	174
13.4	Quantum quench	181
13.5	Floquet drive	194
13.6	Rényi divergence and relative entropy	208
v	Conclusions and outlook	
14	Outlook	219
14.1	Conclusions on Part ii	219
14.2	Conclusions on Part iii	220
14.3	Conclusions on Part iv	223
vi	Appendix	
A	Two-dimensional N -band Hopf pump	229
A.1	The $N = 2$ Hopf pump	229
A.2	Doubling of the unit cell	230
A.3	The $N = 3$ Hopf pump	231
B	Geometric properties of critical Floquet drives	233
B.1	Proof of properties for periodic points	233
B.2	Practical equations for fixed points	233
B.3	Analytical results for special cases	234
B.4	Computation of entanglement entropy	238
B.5	Computation of mutual information	239
c	Solving the Floquet recursion relation	243
	Bibliography	247

Part I
INTRODUCTION

P R E F A C E

A central theme in modern condensed matter physics is the exploration of quantum phases of matter that evade the Landau paradigm of phase transitions. Topological phases of matter are phases characterized by topology instead of symmetry breaking, and thus provide one of the most prominent counterexamples to the Landau paradigm. The first historical example of a topological quantum phase is the integer quantum Hall effect (IQHE), a two-dimensional electron gas in a strong magnetic field displaying quantized plateaux of the Hall conductivity in units of e^2/h . While quantization of physical observables is a commonplace phenomenon in quantum mechanics, the extremely precise quantization of the Hall conductivity in the IQHE happens in a system that contains a mesoscopic number of electrons, subject to large amounts of impurities and disorder, and its origin is deeply rooted in topology [1]. The quest for understanding the rich IQHE physics led to the discovery of new phases of matter, known as topological insulators (TIs) and topological superconductors (TSCs). These are characterized by perfectly conducting boundary states on the surface of a gapped (insulating or superconducting) bulk. Thanks to this topologically robust boundary property, TIs and TSCs found promising applications in fault-tolerant quantum computation [2], and in the design of more efficient microelectronics [3]. Topological band theory was also used beyond the realm of quantum matter, shedding new light on well-known geophysical phenomena such as equatorial waves [4]. A physically striking property of TIs is their resilience to disorder and impurities, i. e., their boundary states evade the paradigm of Anderson localization [5]. This Anderson “delocalization” [6] allowed for the classification of TIs and TSCs, known as the periodic table of topological insulators and superconductors [7, 8], or simply as “tenfold-way”. This classification predicts the existence of topologically distinct TIs and TSCs depending on the dimension and the symmetries of the system. Not only the boundary of a topological material but also its bulk electronic states have intriguing properties: all topological insulators, in the absence of crystalline and sublattice symmetries, have an obstruction to full localization of their occupied bulk electronic states. This property is best studied in the case of quantum Hall insulators [9], where in the presence of disorder topology guarantees the existence of a single energy per Landau level where delocalized states appear. Similarly, the obstruction to full localization was established for the case of quantum spin Hall [10] and three-dimensional topological insulators [11]. Hence, within the tenfold-way paradigm, a fully localized insulator (i.e., an Anderson insulator at all fillings) is guaranteed to be topologically trivial. In this thesis, our focus is on exploring the possibility of defining new topological phases even in the absence of delocalized bulk states in the entire bulk spectrum. Furthermore, we aim at uncovering the surface signatures intrinsically characterizing such phases.

Another central theme in modern condensed matter physics and statistical physics is the understanding of thermalization and ergodicity in quantum many-body systems. In classical physics, thermalization occurs when energy is exchanged between the system and its environment until the former reaches a state of maximum entropy. However, in a quantum system, the process of

thermalization is much more complex due to the presence of quantum coherence and entanglement. In quantum thermalization, the system exchanges energy with its environment through interactions that cause the system to rapidly lose coherence and become entangled with its surroundings. This results in the system relaxing to a state of thermal equilibrium where its properties, such as temperature and energy, become indistinguishable from those of its environment. A widely accepted definition of quantum thermalization is based on the eigenstate thermalization hypothesis (ETH), that asserts that for a isolated quantum system, all many-body eigenstates of the Hamiltonian are thermal, and thus all subsystems ultimately thermalize [12]. In other words, quantum thermalizing closed systems can serve as their own bath. This is to be contrasted with classical chaotic systems, where time evolution is required in order to fully explore the phase space and eventually reach equilibrium. Nonetheless, there exist various cases where ETH is violated for quantum systems. These include many-body localization [13], quantum scars [14–16], prethermal states [17, 18], and integrable systems. In particular, integrable systems, while being by definition a restricted subset of all many-body systems, provide a particularly fruitful route to the understanding of the general mechanisms that break quantum ergodicity, and naturally emerge in the description of various experiments, such as one-dimensional cold-atomic gases [19, 20]. Integrable systems are expected to equilibrate to a generalized Gibbs ensemble as a consequence of the extensive number of local conserved charges that constrain their dynamics. Perturbing integrable systems with integrability-breaking terms can lead to prethermalization plateaux for exponentially long times, thus proving their extreme resilience to ergodicity. On the other hand, integrable systems driven far-from-equilibrium may accumulate large amounts of energy and entanglement. In this thesis, we address the question *how does an integrable driven systems heats up?* in a large class of exactly solvable driven spatially inhomogenous many-body systems. Our aim will be to understand in what sense the underlying dynamics of heating is intrinsically different from the thermalization to an infinite temperature state of a driven generic quantum system.

This thesis is organized in three distinct parts. Part **ii** is based on [21, 22], and discusses several aspects of topological quantum matter beyond the paradigm of the tenfold-way classification of topological insulators and superconductors. In particular, we introduce a novel phase of topological matter that consists of fully Anderson localized insulators with non-trivial topology. Part **iii** is based on [23–26], and deals with the non-equilibrium dynamics of critical quantum systems whose low energy theory has conformal invariance in (1+1) dimensions. In particular, we focus on non-equilibrium protocol that involve spatially and temporally varying Hamiltonian densities. Part **iv** is based on [27], and is devoted to the non-equilibrium dynamics of Tomonaga-Luttinger liquids whose interaction strength is modulated in time, as well as quantum-information-theoretic aspects of thermal states of Tomonaga-Luttinger liquids.

In the following of this introductory part, we introduce the necessary material to make the thesis self-contained. In Chapter 2, we provide an introduction to topological insulators and their standard classifications, with a strong emphasis on their relation with the paradigm of Anderson localization in disordered quantum systems. In Chapter 3 we provide a short introduction to concepts of conformal field theory (CFT), from the point of view of quantum criticality of lattice models. Finally, Chapter 4 explores general results and paradigms for closed quantum systems undergoing sudden changes in their dynamics, such as

quantum quenches. We delve into the thermalization of many-body systems out-of-equilibrium, with particular emphasis on the absence of thermalization in integrable models. We also examine the quantum chaotic properties of several non-integrable models and the different techniques used to diagnose them.

This chapter focuses on the relationship between disorder and topology in quantum systems. We first introduce the concept of Anderson localization in disordered non-interacting quantum lattice models, and then explore the characterization of strong topological phases and their boundary states, which can avoid Anderson localization as a result of topological terms. Specifically, we examine the cases of the integer quantum Hall effect and Chern insulators, where delocalized states carrying quantized Hall conductivity persist in the presence of large bulk disorder. This discussion serves as motivation for the concept of topologically localized insulators, which we introduce in Chapter 6. Additionally, we briefly touch on aspects of topological insulators beyond the tenfold way classification. In particular, we introduce the delicate two-band Hofstadter insulator, of which we will present an N -band generalization in Chapter 5.

2.1 ANDERSON LOCALIZATION

P. W. Anderson's pioneering work [5] revealed the absence of diffusion in quantum systems subject to disorder, a result later explained by scaling theory [28] and field theory [29, 30]. This discovery has played a central role in the theory of metal-insulator transitions [31], where increasing the amount of impurities in a material of dimension $d \geq 3$ can induce a transition from a metallic to an insulating state, culminating in an Anderson insulator phase where all eigenstates of the Hamiltonian are exponentially localized. Although Anderson localization was originally formulated in the context of non-interacting electronic lattice models, its broad applicability has led to experimental observations of the phenomenon in, e.g., photonics [32, 33] and acoustic waves propagating through random elastic networks [34].

For concreteness, let us define a tight-binding model consisting of electrons hopping in a disordered d -dimensional lattice \mathbb{Z}^d ,

$$H = \sum_{\vec{R}} V_{\vec{R}} |\vec{R}\rangle\langle\vec{R}| + \sum_{\substack{\vec{R}, \vec{R}' \\ \vec{R} \neq \vec{R}'}} \left(t_{\vec{R}\vec{R}'} |\vec{R}\rangle\langle\vec{R}'| + \text{h.c.} \right), \quad (2.1)$$

where the potential $V_{\vec{R}}$ consists of independent and identically distributed random variables over the interval $[-W/2, W/2]$, W is said to be the disorder strength of the model, and we assume hopping amplitudes $t_{\vec{R}\vec{R}'}$ to decay faster than $|\vec{R} - \vec{R}'|^{-3}$. While the hopping terms tend to delocalize electrons over the whole lattice, disorder in the form of a random potential drastically influence their localization property depending on the dimension d of the system and the random ensemble associated to the Hamiltonian (orthogonal, unitary, symplectic). In particular, small impurity density in an otherwise clean system only leads to few scattering events, as predicted by the Drude model, leading to extended plane wave electron wavefunctions. On the other hand, if the density of impurities is extremely large, it leads to localization of electrons around the minima of the associated random potential, and thus produces insulating states that have zero conductance. It can actually be proven that the electronic

eigenstates of (2.1) are localized for arbitrarily weak disorder in one dimension, and in two dimensions in orthogonal and unitary random matrix classes. In one dimension this result can be proven rigorously by using a transfer matrix approach and general results about random matrix theory such as Furstenberg theorem [35]. In $d = 2$, an evidence for localization at any disorder strength was provided by the famous gang of four scaling argument [28], which consists in finding the β function associated to the scaling of the conductance g when going in the thermodynamic limit, i.e., finding the form of

$$\beta(g) = \frac{d \log g}{d \log L}, \quad (2.2)$$

thus assuming it depends on a single parameter. In the strongly localized limit, g scales as $g_* e^{-L/\xi}$, while from classical Drude theory it follows that in the weak disorder limit it scales with the dimensionality as $g \sim L^{d-2}$. The quantum corrections to this scaling explicitly depend on the symmetry class of the disordered Hamiltonian. The resulting scaling flow of the β function is illustrated for $d = 1, 2, 3$ in Fig. 2.1, and leads us to the conclusion that full localization happens in $d = 2$, which is the upper critical dimension of Anderson localization. However, at low conductance g , quantum correction become important and one can prove that this leads in the symplectic class to a finite metal-insulator transition, while the conclusion remain unchanged in $d = 2$ for the unitary and orthogonal classes. Furthermore, in $d > 2$, there is always a critical disorder strength W_c after which all states of the Hamiltonian fully localize.

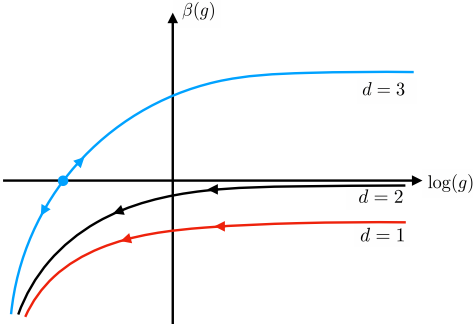


Figure 2.1: Flow of the beta function of the conductance g for dimensions $d = 1, 2, 3$. In the thermodynamic limit, only a localized regime exists in dimensions $d = 1, 2$, while for $d > 2$ there exists a finite metal-insulator transition.

Another fruitful perspective on Anderson localization comes from the underlying low energy theory that classifies Anderson localized phases. Such effective field theories are described by non-linear sigma models (NLSMs) [6], and enable to compute single particle Green's function. As a warm-up example, let us consider the NLSM description of the classical magnet in d dimensions. In the long wavelength limit, the Heisenberg ferromagnet is described by an $O(3)$ NLSM of the form

$$S[\vec{n}] = \frac{1}{t} \int d^d r \partial_\mu \vec{n} \cdot \partial_\mu \vec{n}, \quad (2.3)$$

for a coupling constant t that incorporates the different scales of the microscopic problem, such as exchange interaction, spin magnitude, temperature, and \vec{n} being a 3-dimensional unit vector. The path integral of the action (2.3) is taken over the target space $S^2 = O(3)/O(2)$ in which the order parameter lives after spontaneous symmetry breaking $O(3) \rightarrow O(2)$. We now apply these ideas to the Anderson localization-delocalization transition. The Goldstone bosons associated to Anderson localization are diffusive modes called “diffusons”, described by the NLSM action

$$S[X] = \frac{1}{t} \int d^d r g_{ab}[X] \partial_\mu X^a \partial_\mu X^b, \quad (2.4)$$

where the order parameter field X^a lives in the target space manifold G/H , and g_{ab} is the metric on the target space. One should think of the coupling t of the NLSM to be inversely proportional to the conductivity. The metallic and insulating phases of the Anderson transition correspond to the unbroken and broken symmetry phases, respectively. The single parameter scaling hypothesis discussed above implies that the NLSM is described solely by the parameter t , which leads to a simple classification of the possible target spaces manifolds of the NLSM, called symmetric spaces, coming in ten different classes as shown on Table 2.1. The Anderson transition from a field-theoretic point of view thus solely depends on the dimension, the choice of symmetric space and the conductivity. The single parameter scaling theory implies that at large enough disorder, the coupling constant will always flow to a zero-conductivity state $t \rightarrow \infty$, leading to Anderson localization, in the same way that a paramagnetic phase is realized in the infinite temperature limit of a Heisenberg magnet. However, we will see in the next section that non-trivial topology of symmetric spaces gives rise to extra terms in the NLSM action that may circumvent such a flow to zero conductivity.

AZ classes	NLSM target space
A	$\frac{U(n+m)}{U(n) \times U(m)}$
AIII	$U(n)$
AI	$\frac{\mathrm{Sp}(n+m)}{\mathrm{Sp}(n) \times \mathrm{Sp}(m)}$
BDI	$U(2n)$
D	$\frac{\mathrm{Sp}(n)}{U(n)}$
DIII	$O(n)$
AII	$\frac{O(n+m)}{O(n) \times O(m)}$
CII	$\frac{U(n)}{O(n)}$
C	$\frac{\mathrm{Sp}(2n)}{U(n)}$
CI	$\mathrm{Sp}(n)$

Table 2.1: Target spaces of the NLSM for the ten Altland-Zirnbauer classes, also called tenfold-way symmetry classes.

In order to diagnose the localization properties of a given disordered Hamiltonian, one can use tools from random matrix theory. In particular, the spectral statistics of such a Hamiltonian, when averaged over a large number of

different disorder realizations, can predict the localization properties of the eigenstates. In practice, one studies the distribution $P(s_n)$ of the level spacings $s_n = E_{n+1} - E_n \leq 0$. In the presence of delocalized states, level repulsion occurs between neighboring energies as $s_n \rightarrow 0$ leading to a drop to zero of the distribution $P(s_n)$. This is described by Gaussian ensembles, that depend on the symmetry of the disorder, defining the Gaussian orthogonal, unitary and symplectic ensembles. On the other hand, in a fully localized regime level repulsion is avoided, leading to a Poisson ensemble for $P(s_n)$. Practically, one defines the level spacing ratio

$$r_n = \frac{\max\{s_n, s_{n+1}\}}{\min\{s_n, s_{n+1}\}}, \quad (2.5)$$

such that $r = \langle \langle r \rangle_n \rangle_W \approx 0.386294$ for Poisson ensembles and $r \approx 0.535898$ for Gaussian orthogonal ensembles, where $\langle \dots \rangle_n$ denotes spectral average and $\langle \dots \rangle_W$ denotes average over random realizations [36].

2.2 STRONG TOPOLOGICAL PHASES

In this section we introduce topological insulators (TIs) and topological superconductors (TSCs), which are characterized by perfectly conducting boundary states on the surface of a gapped (insulating or superconducting) bulk. As the following of the thesis will discuss aspects of topological matter in the presence of disorder [see Chapter 6], we take the perspective in the following of the section to define topological phases by their obstruction to Anderson localization under the presence of arbitrary boundary disorder. Furthermore, we discuss the obstruction to complete localization of the bulk states under bulk disorder for specific examples of TIs, such as the integer quantum Hall effect (IQHE), Chern insulators, and quantum spin Hall insulators.

The obstruction to Anderson localization at the boundary of TIs and TSCs for arbitrary boundary disorder can be referred as “Anderson delocalization” [6], and is connected to the absence of an atomic limit for topological insulators and superconductors. It can be understood from the underlying low energy NLSM description of the problem, introduced in Sec. 2.1. As the NLSM of the Anderson localization/delocalization transition admits a single coupling t , the classification of the target manifolds of the NLSM is provided by the topological classification of symmetric spaces. As discussed in Sec. 2.1, symmetric spaces come in ten distinct classes, which can have a non-trivial topology. This leads to an extra topological term in the NLSM action

$$S \mapsto S[X] + iS_{\text{topo}}[X] \quad (2.6)$$

where the topological part only depends on global configurations of fields, and can lead to new renormalization group flows by interferences of such field configurations. Topological terms include for instance theta terms, famously leading to the Haldane gap when applied to quantum magnets of integer spin [37]. In the case of the anomalous boundary of a TI or TSC, the relevant topological terms are Wess-Zumino-Witten (WZW) terms and \mathbb{Z}_2 topological terms, which cannot be tuned continuously by smooth deformations of the microscopic model. These topological terms turn the system at the critical point of the Anderson localization transition, where the system is effectively metallic because of the divergence of localization length. By understanding the topology of symmetric spaces in a given dimension and symmetry class, one can

infer the existence of topological terms. More specifically, WZW terms appear when the $(d+1)$ -th homotopy group is $\pi_{d+1}(G/H) = \mathbb{Z}$, and \mathbb{Z}_2 topological terms when $\pi_d(G/H) = \mathbb{Z}_2$. We thus conclude that Anderson delocalization happens at the boundary of TI and TSCs depending on the dimension and symmetry class of the problem, leading to fully metallic boundaries, immune to arbitrary *boundary* disorder. This general principle classifies strong topological phases, giving rise to the periodic classification of TIs and TSCs, see Table 2.2, and provides a physical meaning to topological phases as hosting anomalous metallic boundaries.

AZ	\mathcal{T}	\mathcal{P}	\mathcal{C}	1	2	3	4	5	6	7	8
A	0	0	0	0	\mathbb{Z}	0	\mathbb{Z}	0	\mathbb{Z}	0	\mathbb{Z}
AIII	0	0	1	\mathbb{Z}	0	\mathbb{Z}	0	\mathbb{Z}	0	\mathbb{Z}	0
AI	1	0	0	0	0	0	\mathbb{Z}	0	\mathbb{Z}_2	\mathbb{Z}_2	\mathbb{Z}
BDI	1	1	1	\mathbb{Z}	0	0	0	\mathbb{Z}	0	\mathbb{Z}_2	\mathbb{Z}_2
D	0	1	0	\mathbb{Z}_2	\mathbb{Z}	0	0	0	\mathbb{Z}	0	\mathbb{Z}_2
DIII	-1	1	1	\mathbb{Z}_2	\mathbb{Z}_2	\mathbb{Z}	0	0	0	\mathbb{Z}	0
AII	-1	0	0	0	\mathbb{Z}_2	\mathbb{Z}_2	\mathbb{Z}	0	0	0	\mathbb{Z}
CII	-1	-1	1	\mathbb{Z}	0	\mathbb{Z}_2	\mathbb{Z}_2	\mathbb{Z}	0	0	0
C	0	-1	0	0	\mathbb{Z}	0	\mathbb{Z}_2	\mathbb{Z}_2	\mathbb{Z}	0	0
CI	1	-1	1	0	0	\mathbb{Z}	0	\mathbb{Z}_2	\mathbb{Z}_2	\mathbb{Z}	0

Table 2.2: Tenfold-way classification of TIs and TSCs for non-interacting fermionic models, for the ten Altland-Zirnbauer (AZ) symmetry classes, corresponding to the ten distinct symmetric spaces (see Table 2.1) and the first 8 spatial dimensions. The classification in higher dimensions follows from Bott periodicity.

As discussed in the language of Anderson localization, the Cartan classification of the symmetric spaces of NLSM lead to ten distinct classes. These classes coincide with the ten symmetry classes obtained by combining three symmetries of the microscopic Hamiltonian:

1. Time-reversal symmetry, a antiunitary operator implemented by the operator \mathcal{T} such that

$$\mathcal{T}H\mathcal{T}^{-1} = H, \quad (2.7)$$

2. Particle-hole symmetry, a antiunitary operator implemented by the operator \mathcal{P} such that

$$\mathcal{P}H\mathcal{P}^{-1} = -H, \quad (2.8)$$

3. Chiral symmetry, a unitary operator implemented by $\mathcal{C} = \mathcal{T}\mathcal{P}$, such that

$$\mathcal{C}H\mathcal{C}^{-1} = -H. \quad (2.9)$$

Enumerating all combinations of the three symmetries, taking into account the signs of \mathcal{T}^2 and \mathcal{P}^2 lead ten distinct classes, comprising two complex without

any antiunitary symmetry and eight real classes with at least one antiunitary symmetry.

In order to make an explicit connection between the symmetric spaces of the NLSM and the ten symmetry classes of microscopic fermionic Hamiltonians, we consider a spectrally flattened (or flat band) translationally invariant model described by the Bloch Hamiltonian

$$Q(\vec{k}) = U_{\vec{k}} \begin{pmatrix} \mathbb{I}_m & 0 \\ 0 & -\mathbb{I}_n \end{pmatrix} U_{\vec{k}}^\dagger, \quad (2.10)$$

that assigns energies 1 for the m states above the gap, and -1 for the n states below. The flat band Hamiltonian $Q(\vec{k})$ has a gauge freedom $U(n) \times U(m)$ inherited by the degeneracy of each subspace. Thus, $Q(\vec{k})$ defines a map

$$Q(\vec{k}) : \text{BZ} \rightarrow \frac{U(n+m)}{U(n) \times U(m)}, \quad \vec{k} \mapsto Q(\vec{k}), \quad (2.11)$$

which is an element of the complex symmetric space in class A. In particular, $\pi_d(U(n+m)/(U(n) \times U(m)))$ classifies the number of topologically distinct flat band Hamiltonians, and gives the IQHE universality in $d = 2$, comprising Chern insulators. The topological invariant for topologically non-trivial Hamiltonians in class A and even space dimensions $d = 2p$ is the p -th Chern number, defined as

$$\text{Ch}^{(p)} = \frac{2}{p!} \left(\frac{i}{2\pi} \right)^p \int_{\text{BZ}} \text{Tr}(F^p), \quad (2.12)$$

where F is the Berry curvature form, and $F^p = F \wedge F \dots \wedge F$.

We now consider chiral symmetric Hamiltonians belonging to the second complex class AIII. In this case, chiral symmetry implies that $H(\vec{k})$ has an even number of bands $N = 2n$, such that in the eigenbasis of the chiral symmetry operator \mathcal{C} the flat band Hamiltonian reads

$$Q(\vec{k}) = \begin{pmatrix} 0 & q(\vec{k}) \\ q^\dagger(\vec{k}) & 0 \end{pmatrix}, \quad (2.13)$$

for $q(\vec{k}) \in U(n)$, such that

$$q(\vec{k}) : \text{BZ} \rightarrow U(n), \quad \vec{k} \mapsto q(\vec{k}), \quad (2.14)$$

which as expected is an element of the symmetric space in class AIII, giving a non-trivial topological phase in, e.g., $d = 3$. The topological invariant that classifies topological phases with integer classification in the presence of chiral symmetry is the winding number of q . Indeed, as the two flat bands are related by chiral symmetry, they carry an equal Chern number, implying that the Chern number has to be zero for each band in order for it to sum to zero. Nevertheless, a non-trivial topological invariant can be defined in a similar fashion in odd dimensions of space d as

$$\begin{aligned} W[q] &= \frac{(-1)^{(d-1)/2}((d-1)/2)!}{d!} \left(\frac{i}{2\pi} \right)^{(d+1)/2} \epsilon_{i_1 \dots i_d} \\ &\times \int_{\text{BZ}} d^d k \text{Tr}[q(\vec{k}) \partial_{i_1} q(\vec{k}) \dots \partial_{i_d} q(\vec{k})]. \end{aligned} \quad (2.15)$$

The above classification of topological phases, as well as the associated topological invariants, was done purely from the perspective of the translational-invariant bulk. However, we have seen that TIs and TSCs have metallic boundaries that evade localization for arbitrary *boundary* disorder. In order to connect the topology of a d -dimensional bulk to a quantized response on the $(d - 1)$ -dimensional boundary, it is fruitful to consider adiabatic pumps. Adiabatic pumps are families of gapped Hamiltonians $H(\vec{k}, t)$ defined in $(d - 1)$ dimensions that depend parametrically on time t , such that $H(\vec{k}, t + T) = H(\vec{k}, t)$. The time evolution is assumed to be adiabatic in the sense that the ground state stays gapped at any time $t \in [0, T]$. While the topological classification of adiabatic pumps parallels the classification of TIs and TSCs, given by Table 2.2, we will for simplicity focus on class A in two dimensions. The resulting $(1 + 1)$ -dimensional pump was first proposed by D. J. Thouless [38], and will thus be referred as Thouless pump. Thouless pumps $H(k, t)$ are classified by the Chern number defined on $\text{BZ} \times S^1$,

$$\text{Ch}^{(1)} = \frac{i}{2\pi} \int_{\text{BZ} \times S^1} \text{Tr}(F(k, t)) dk dt, \quad (2.16)$$

where S^1 parametrizes the periodic time evolution of the topological pump, and $F(k, t)$ is the Berry curvature defined over the (k, t) 2-torus. A concrete tight-binding model for the Thouless pump is

$$H(k, t) = \vec{h}_{k,t} \cdot \vec{\sigma}, \quad \vec{h}_{k,t} = (t \sin k, \sin t, (3/2 - \cos k - \cos t)), \quad T = 2\pi, \quad (2.17)$$

which pumps a non-trivial charge after one cycle as $\text{Ch}^{(1)} = 1$. The associated physical signature is the *spectral flow* of boundary modes: while the one-dimensional system does not hold any protected boundary modes, the system pumps a quantized number of boundary modes during the adiabatic evolution, such that the boundary modes connect the conduction and valence bands as a function of time t , as illustrated on Fig. 2.2. If the boundary modes move from the conduction (valence) to the valence (conduction) band, a quantized boundary mode is pumped to (away from) the boundary after one period, $t = T$. While à priori the spectral flow after one cycle of the adiabatic pump

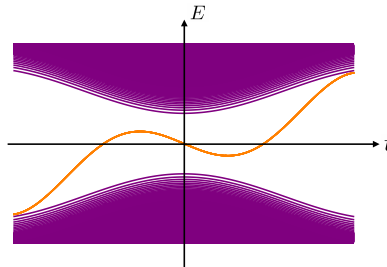


Figure 2.2: Sketch of the spectral flow of a Thouless pump, leading to chiral Dirac modes adiabatically crossing from occupied to unoccupied bands as a function of t .

is not directly related to the Chern number, the index theorem states their equality. This gives the first elementary example of the so-called bulk-boundary

correspondence, which provides a bridge between topological invariant in the bulk of TIs and TSCs to quantized and robust boundary effects, such as a quantized Hall conductivity in the IQHE class.

We now discuss the effect of bulk disorder in particular examples of strong topological phases. While it was long-believed that an arbitrary disordered potential would prevent any delocalized state to survive in the thermodynamic limit in dimension $d \leq 2$, the discovery of the IQHE provided a notable counterexample to complete localization of bulk spectrum. In the IQHE, bulk delocalized states carrying quantized Hall conductivity remain in each broadened Landau level even in the presence of strong disorder [39], playing a crucial role for the appearance of quantized plateaux in Hall conductivity for extended range of applied external magnetic fields. The persistence of a mobility edge in each band is in contradiction with the expectation of full Anderson localization of two dimensional systems, and is a consequence of the non-trivial bulk topology of the IQHE. In fact, the persistence of bulk delocalized states in the IQHE can be understood by a theta term in the bulk NLSM action, called Pruisken term. Alternatively, the finite-sized Hilbert space version of the IQHE is the Chern insulator, for which the total Chern number sums up to zero, as opposed to the IQHE. In the presence of sufficiently weak disorder, all bulk states localize apart from topologically protected delocalized states at a single energy per band, as illustrated on Fig. 2.3(a), that survive even in the thermodynamic limit, and that carry a quantized Chern number in each band [10, 11]. Increasing disorder strength further, such delocalized states first levitate from each other, and eventually pair annihilate (see Fig. 2.3(b)), such that the mobility gap of the Chern insulator closes and the system is driven to a trivial Anderson insulator, with a fully localized bulk. The particular form of such a phase

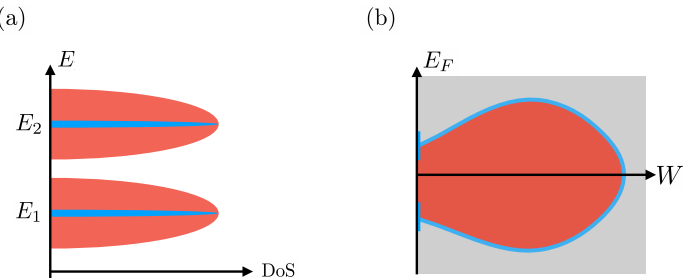


Figure 2.3: (a) Two-band Chern insulator at a finite disorder W that does not close its mobility gap. The system in the thermodynamic limit hosts bulk delocalized states at a single energy per bulk band, E_1 and E_2 . (b) Phase diagram (W, E_F) for the disordered two-band Chern insulator. The non-trivial Chern insulating phase (red region) survives a wide range of disorder strength W , before the closure of the mobility gap that leads to a fully localized Anderson insulator (grey region). The two topologically distinct phases are separated by a metallic phase boundary with bulk delocalized states (blue line).

diagram directly implies that increasing disorder can drive a transition from a clean trivial insulator to a TI, called “topological Anderson insulator” [40], and can again be traced back from NLSM approach [41]. We finally note that the persistence of delocalized states in the presence of bulk disorder also happens in

other symmetry classes. For instance, quantum spin Hall insulators, described by a \mathbb{Z}_2 topological term in class AII in two dimensions, host delocalized states in the presence of bulk disorder for an extended range of energies. This leads to the existence of a metallic phase separating the topologically trivial and non-trivial phases [42], in contrast to Chern insulators where both phases are separated by a metallic phase boundary (see Fig. 2.3(b)).

2.3 BEYOND TENFOLD-WAY TOPOLOGY

While the quest for new topological materials is still an ongoing effort, some more recent theoretical efforts are concerned with the following question: in which way does a modification of the tenfold-way classification rules alter the established classification results? Such “beyond tenfold-way” classification schemes include delicate and fragile (i.e., unstable) topological classifications. Recently, many fragile topological insulators [43, 44] were discovered while comparing the classification results of “Topological quantum chemistry” [45] and that of “Symmetry-based indicators” [46]. “Fragile” topological equivalence allows for the addition of trivial conduction bands while the number of valence bands is fixed. In other words, the fragile classification rules are halfway between that of tenfold-way (i.e., stable) and delicate topological classification that does not allow for the additional bands in either conduction or valence sectors. Yet another possibility of going beyond the tenfold-way is to introduce additional constraints on the band structure. For example, the boundary-obstructed classification [47] requires that the so-called Wannier gap is maintained. We note that so far, the efforts were mainly focused on obtaining such modified classifications. Despite efforts [48, 49] to formulate a bulk-boundary correspondence, it is still unclear if any (possibly subtle) quantized boundary effect can be used to uniquely identify any of the “beyond tenfold-way” phases.

For delicate topological insulators, both the number of conduction and valence bands is fixed. The most well studied representative of delicate topological insulator is two-band Hopf insulator [44, 50]. The Hopf insulator is a three dimensional insulator in class A, in which case there is no strong topological phase predicted by the tenfold-way classification. It is defined as a two band Bloch Hamiltonian [50]

$$H(\vec{k}) = \vec{h}_{\vec{k}} \cdot \vec{\sigma}, \quad (2.18)$$

where $h_{\vec{k}}$ defines a map from the three-torus BZ \mathbb{T}^3 to the two-sphere S^2 . A non-trivial topology of the Hopf insulator is associated to a non-trivial homotopy group of the set of such maps $h_{\vec{k}}$, as was first classified by Pointryagyn. An example of such a non-trivial map is

$$h_{\vec{k}} = \vec{v} \cdot \vec{\sigma}, \quad (2.19)$$

with $v_i = \vec{z}^\dagger \sigma_i \vec{z}$, where $\vec{z} = (z_1, z_2)^T$, with $z_1 = \sin(k_x) + i\sin(k_y)$ and $z_2 = \sin(k_z) + i[\cos(k_x) + \cos(k_y) + \cos(k_z) - \frac{3}{2}]$. The above model has a quantized third winding number, defining the Hopf invariant

$$W_3[U_{\vec{k}}] = \int_{\text{BZ}} \frac{d^3 k}{8\pi^2} \text{Tr} \left(U_{\vec{k}}^\dagger \partial_{k_x} U_{\vec{k}} [U_{\vec{k}}^\dagger \partial_{k_y} U_{\vec{k}}, U_{\vec{k}}^\dagger \partial_{k_z} U_{\vec{k}}] \right), \quad (2.20)$$

where $U_{\vec{k}}$ is the unitary that flattens the Bloch Hamiltonian (2.18) to $\text{diag}(-1, 1)$. For strong TIs, there is an obstruction in localizing all Wannier functions (WFs)

exponentially, because of the impossibility to choose a $U(n)$ smooth gauge for Bloch wavefunctions as a consequence of the non-vanishing topological indices. On the other hand, the WFs of the Hopf insulator can be made exponentially localized, although not localizable down to the trivial atomic limit, a property called multicellularity [51].

As we will demonstrate in Chapter 5, the constraint of the Hopf insulator to possess only two bands can be relaxed to a more general constraint of an arbitrary number of bands, each separated by a band gap. As we will see, in this case a Hopf invariant can still be defined for the bulk, associated to a quantized isotropic bulk magnetoelectric polarizability tensor. Furthermore, the boundary carries anomalous Hall conductivity equal to the bulk Hopf invariant, even in the absence of a unique division between bulk and boundary.

2.4 ANOMALOUS FLOQUET-ANDERSON INSULATORS

Another example of a topological phase that goes beyond the tenfold-way classification of topological insulators is the anomalous Floquet-Anderson insulator (AFAI) [52]. This class of TIs generalize arguments from the Thouless adiabatic pump to non-adiabatic regimes, and features chiral edge modes coexisting with a fully localized bulk, which cannot be the case for static strong TIs (see Sec. 2.2). To describe such class of insulators, we consider families of Hamiltonians that depend parametrically on time, $H(t)$, such that $H(t+T) = H(t)$, defining a Floquet system. Floquet theory, a time analogue of Bloch theory, introduces a set of eigenstates Ψ of the Floquet (or stroboscopic) unitary operator

$$U_F = \mathcal{T} e^{-i \int_0^T dt' H(t')} = e^{-i H_F T}, \quad (2.21)$$

such that $U_F \Psi = e^{-i \epsilon T} \Psi$. Alternatively, eigenvalues of the Floquet Hamiltonian H_F are the quasienergies ϵ . A first and natural step to uncover topology in Floquet systems is to consider a translation invariant Floquet Hamiltonian $H_F(\vec{k})$ and study its topological properties, such as bands carrying non-zero Chern number. This provides a general approach to uncover driven topological phases that possess a static counterpart, as is the case for topological Anderson insulators and their periodically driven cousin [53].

On the other hand, AFAIs exhibit localized bulk bands together with chiral edge states at all quasienergies, thus having no static counterpart in the tenfold-way classification in class A. The simplest construction in (2+1)-dimensions of AFAIs consists of a piecewise-constant Floquet drive made of five static steps on a square lattice with A and B sublattices, as illustrated on Fig. 2.4. At each of the four first steps, the hopping amplitudes are turned-off to zero apart from those connecting each site in sublattice A to the site in sublattice B below, to the right, above, or to the left of it. The fifth step consists only of an on-site potential introducing a potential difference between sublattices A and B of π/T . Additionally, one introduces a disordered potential at the fifth step, of strength $\delta V < \pi/(2T)$ such that the spectral gap between the two bands corresponding to the two sublattices stays open. When excluding the disordered potential of the fifth step of the drive that introduces on-site disorder, one can find exactly the Floquet eigenstates and quasienergies of $H(t)$ for such a model [54]. The bulk spectrum consists of flat bands, while linearly dispersing chiral edge modes in the bulk quasienergy gaps appear upon termination of the system. Adding disorder during the fifth step of the drive, the bulk flat bands

of the clean system broaden by an amount δV . When terminating the system on a cylinder, a mode starting at time $t = 0$ on the upper boundary at $(x, 0)$ is shown to move two sites to the right after one Floquet period, and to acquire a phase $e^{-i(\pi/2+T/5V(x+2,0))}$. This leads to edge states delocalized over the whole edge, realizing the anomalous boundary of the AFAI phase.

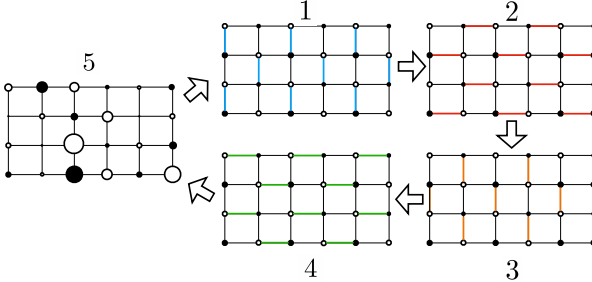


Figure 2.4: Illustration of the five piecewise constant Hamiltonians applied for times $T/5$ constituting the periodically driven AFAI Hamiltonian $H(t)$ over a full period T [52]. The hollow and full circles correspond to the A and B sublattices, and the colored legs between them indicate which hopping amplitudes are not turned-off to zero at a given stage of the evolution. While the Hamiltonian has translation invariance in the four first steps, the last step introduces on-site disorder in order to localize bulk states.

While all the bulk states are fully localized with localization length ξ , they still lead to a non-trivial topological invariant, given by the third winding number [see (2.15)]. In fact, threading through the bulk some time-independent fluxes $\Phi = (\varphi_x, \varphi_y)$, one defines a deformed unitary evolution operator

$$U_\epsilon(\Phi, t) = U(t) e^{iH_{F,\epsilon}t}, \quad (2.22)$$

where $U(t)$ is the time evolution after a time t with $H(\Phi, t)$, and $H_{F,\epsilon}$ the Floquet Hamiltonian for a period T , such that $U_\epsilon(\Phi, T) = \mathbb{I}$. The dependence of the Floquet Hamiltonian on a precise quasienergy ϵ originates from the choice of the branch cut of the logarithm on the complex plane. Then, we define the third winding number of $U_\epsilon(\Phi, t)$ as an integral over the 3-torus consisting of the two-dimensional flux space and the periodic Floquet evolution,

$$W_\epsilon = \int_0^T dt \int \frac{d^2\Phi}{8\pi^2} \text{Tr} \left[U_\epsilon^\dagger \partial_t U_\epsilon [U_\epsilon^\dagger \partial_{\varphi_x} U_\epsilon, U_\epsilon^\dagger \partial_{\varphi_y} U_\epsilon] \right]. \quad (2.23)$$

As long as the quasienergy ϵ is taken to be in a spectral gap of the Floquet unitary, $W \equiv W_\epsilon$ is quantized and independent of ϵ .

On the other hand, in the clean limit the chiral edge states lying in bulk quasienergy gaps carry a non-zero winding number [54]. Adding disorder broadens the bulk bands, but as bulk states are localized, chiral edge states will persist even in a bulk band. This can be understood by threading a flux φ_x through the cylinder, which leads to a non-trivial spectral flow of the edge states while the bulk states are insensitive because of their localization. This implies the existence of delocalized edge states that carry the spectral flow. The edge topological invariant can be defined by deforming the Hamiltonian

$H(\varphi_x, t)$ in such a way that it stays the same in the regions at a distance $l_0 \gg \xi$ from the edges, while we deform it in the bulk in such a way that the localized bulk states take the quasienergy $\epsilon = 0$. This implies that the deformed evolution operator takes the block diagonal form

$$\tilde{U}_\epsilon(\varphi_x, T) = \text{diag}(\tilde{U}_{\epsilon,1}(\varphi_x, T), \mathbb{I}_{\text{bulk}}, \tilde{U}_{\epsilon,2}(\varphi_x, T)), \quad (2.24)$$

where $\tilde{U}_{\epsilon,i}(\varphi_x, T)$ are defined up to a distance l_0 to the upper and lower edges. The edge winding number of the upper edge of the cylinder is then defined as

$$n = \int_0^{2\pi} \frac{d\varphi_x}{2\pi} \text{Tr}[\tilde{U}_{\epsilon,1}^\dagger(\varphi_x, T) \partial_{\varphi_x} \tilde{U}_{\epsilon,1}(\varphi_x, T)]. \quad (2.25)$$

In particular, the winding number of the total deformed system is zero, leading to the constraint that the upper and lower edge winding numbers have opposite signs, implying opposite propagation direction of the edge modes.

A non-zero edge invariant n directly implies that existence of delocalized states along the edges of the cylinder. The physical response associated to such delocalized states can be anticipated from the Thouless pump arguments [see Sec. 2.2] as a quantized non-adiabatic charge pump. To see this, we thread a flux φ_x through the cylinder and consider an initial state $|\Psi(t=0)\rangle$ in which all sites are fully filled from one edge of the cylinder up to a distance l from that edge, such that $l \gg \xi$. The charge pumped after N Floquet cycles is

$$\langle Q \rangle_{NT} = \int_0^{NT} dt \langle \Psi(t) | \frac{\partial H(\varphi_x, t)}{\partial \varphi_x} | \Psi(t) \rangle. \quad (2.26)$$

It can be shown that in the long time limit, $N \rightarrow \infty$, the averaged pumped charge $\langle Q \rangle_{NT}/N$ converges to the edge invariant n , up to exponentially small corrections in l . Additionally, the quantized pumped charge can be shown to be equal to the bulk winding number W , leading to the bulk-edge correspondence of the AFAI.

As we will demonstrate in Chapter 6, there exist static $(3+0)$ -dimensional topological phases in class A that possess a fully localized bulk while supporting on their surface anomalous delocalized states carrying quantized Hall conductivity. While these topologically localized phases will appear to form a static cousin to the AFAI phase, they will be shown to display completely distinct bulk and boundary topological signatures.

CONFORMAL FIELD THEORY

In this chapter, we present a concise introduction to key concepts in conformal field theory (CFT) that are relevant to the thesis, with a particular focus on their importance in describing quantum critical systems in $(1+1)$ D. The material covered will serve as a basis for Parts **iii** and **iv**, which delve into non-equilibrium dynamics of CFTs and their application to critical lattice systems. For a more in-depth treatment of the subject matter, readers are encouraged to consult literature reviews and lectures, such as e.g., [55, 56].

3.1 SCALING INVARIANCE AT CRITICALITY

Conformal invariance provides a powerful framework to find the critical exponents and correlation functions of statistical mechanics models at a second order phase transition, as well as quantum system at their quantum critical point. The canonical example is the two dimensional Ising model, with classical spins $\sigma_i = \pm 1$ on a square lattice, which displays a second order phase transition between an ordered ferromagnetic phase $\langle \sigma \rangle \neq 0$ at low temperature and a disordered phase $\langle \sigma \rangle = 0$ at high temperature. The spin configurations at the phase transitions fluctuate over all length scales, leading to a scale invariant coarse-grained field theory. Scale invariance of statistical or quantum mechanical lattice models generally implies conformal invariance. While conformal invariance does not contain more information than ordinary scale invariance in $d > 2$, in two dimensions it implies the existence of an infinite number of local conserved charges forming the infinite dimensional conformal algebra. This provides a way to classify two-dimensional second order phase transitions through a finite number of data that characterize the coarse-grained conformally invariant field theory, such as the central charge c , related to the conformal anomaly upon quantization of the theory. For instance, the Ising universality class is described by a $c = 1/2$ CFT. From a renormalization group perspective, all quantum field theories at the ultra-violet (UV) fixed point are conformal, thus all well-defined quantum field theories are CFTs or points that go between two CFTs under the renormalization group flow. This allows for CFTs to ultimately describe the criticality of statistical models. We want to emphasize that the utility of CFTs for determining critical exponents is not restricted to two-dimensional systems. In fact, the recent advancement on the conformal Bootstrap technique strive to solve CFTs in a non-perturbative manner, thereby enabling highly precise predictions of critical exponents for systems of any dimension. This has resulted in state-of-the-art estimates for the critical exponents of the three-dimensional Ising model [57]. Returning to condensed matter physics, for one-dimensional lattice models at quantum criticality conformal invariance constrains the scaling of, e.g., the entanglement entropy S_A , such that it satisfies a logarithmically violated area law, $S_A \sim c/3 \log(l)$, where $l = |A|$. This provides a powerful tool to identify the universality class of a given critical lattice model, as entanglement entropy can be efficiently computed from density matrix renormalization group (DMRG) methods.

3.2 CONFORMAL INVARIANCE

A CFT is defined as a field theory in $D = d+1$ dimensions that is invariant under conformal transformations. In practice, the group of conformal transformations is defined as the set of transformations that leave the metric $g_{\mu\nu}$ invariant up to a local scale factor,

$$g_{\mu\nu}(x) \mapsto g'_{\mu\nu}(x') = \Omega(x)g_{\mu\nu}(x). \quad (3.1)$$

In other words, conformal transformations locally preserve angles, as the scalar product is defined through the metric tensor. The elements of the conformal group are combinations of

1. dilations $x' = \lambda x$,
2. translations, $x' = x + a$
3. Lorenz transformations, $x' = \Lambda x$, $\Lambda \in \text{SO}(1, d)$,
4. special conformal transformations, defined as the composition of an inversion, a translation and a second inversion,

$$x' = \frac{x + bx^2}{1 + 2bx + b^2x^2}. \quad (3.2)$$

While the conformal group is finite dimensional, leading to only a finite number of constraints on the field content of the theory in general spacetime dimensions D , in two dimensions an infinite number of local constraints arise as a consequence of the special role of conformal invariance in the complex plane. More precisely, is due to the fact that the generators of the conformal group in $D = 2$ must satisfy the Cauchy-Riemann equation, leading to the conclusion that conformal transformations coincide with analytic function of the complex plane. It is then natural to consider complex coordinates, z and \bar{z} , such that conformal transformations are denoted by $f(z)$ and $\bar{f}(\bar{z})$. Infinitesimal conformal transformations, at the level of the classical field theory, span an infinite dimensional algebra,

$$l_n = -z^{n+1}\partial_z, \quad \bar{l}_n = -\bar{z}^{n+1}\partial_{\bar{z}}, \quad n \in \mathbb{Z}. \quad (3.3)$$

Each copy of the conformal algebra commute, $[l_n, \bar{l}_m] = 0$, and satisfy individually a Witt algebra

$$[l_n, l_m] = (m - n)l_{m+n}. \quad (3.4)$$

In particular, the set of generators $\{l_0, l_1, l_{-1}\}$ forms the algebra of global conformal transformations, and the associated conformal maps on the complex plane are Möbius transformations, of the form

$$f(z) = \frac{az + b}{cz + d}, \quad \bar{f}(\bar{z}) = \frac{\bar{a}\bar{z} + \bar{b}}{\bar{c}\bar{z} + \bar{d}}, \quad (3.5)$$

where $ad - bc = \bar{a}\bar{d} - \bar{b}\bar{c} = 1$. In particular, rotations, translations, dilations, special conformal transformations are all represented on the complex plane as Möbius transformations (for instance, dilations are obtained with $a = d^{-1} = \lambda$ and $b = c = 0$). The fact that the local conformal algebra is infinite dimensional

leads to strong constraints on the operator content of the theory, as well as on the form of correlation functions of fields, which may be evaluated non-perturbatively thanks to these underlying symmetries. A particularly relevant set of fields are called quasi-primary fields, and satisfy the following transformation rule under an arbitrary conformal transformation $f(z)$

$$\Phi(z, \bar{z}) \mapsto \left(\frac{\partial f(z)}{\partial z} \right)^h \left(\frac{\partial \bar{f}(\bar{z})}{\partial \bar{z}} \right)^{\bar{h}} \Phi(f(z), \bar{f}(\bar{z})), \quad (3.6)$$

where the tuple (h, \bar{h}) is called conformal dimension of the field $\Phi(z)$. In particular, N -point correlation functions of primary fields transform similarly under conformal transformations. Using this fact and the invariance under rotations and translations that have a unit jacobian, two-point functions of quasi-primary fields are shown to satisfy

$$\langle 0 | \Phi(z_1, \bar{z}_1) \Phi(z_2, \bar{z}_2) | 0 \rangle = \frac{1}{|z_1 - z_2|^{2h}} \frac{1}{|\bar{z}_1 - \bar{z}_2|^{2\bar{h}}}. \quad (3.7)$$

From the symmetries imposed by the conformal algebra, the form of three-point functions is also fully constrained, and the form of four-point function is shown to only depend on a universal function $\mathcal{F}(\eta)$, where η is the cross ratio defined as

$$\eta = \frac{z_{12}z_{34}}{z_{13}z_{24}}, \quad (3.8)$$

with $z_{ij} = z_i - z_j$. Determining the precise form of such a function requires the knowledge of the full operator content of the theory at hand. However, as we will shortly see, there is a subset of CFTs for which such field content can be determined exhaustively.

The quantization of the two-dimensional CFT goes under the name of radial quantization. It consists of a map from the Euclidean spacetime, that has the topology of a cylinder with a compactified space direction, to the complex plane. Coordinates on the cylinder are denoted by $\omega = \tau + ix$, and the map to the complex plane is done using the exponential map,

$$\omega \mapsto z = e^{\frac{2\pi}{L}\omega}, \quad (3.9)$$

which maps time-slices on the cylinder to concentric circles on the complex plane. Infinitely negative Euclidean times are thus mapped to the origin of the complex plane, and infinitely positive times are mapped to the point at infinity. It is thus clear that time evolution on the complex plane is radial, in the sense that it maps one concentric circle to another of a larger radius; thus time-ordering translates to a radial ordering of operators on the complex plane. In other words, the Hamiltonian is the generator of dilation on the complex plane. Local conformal transformation on the complex plane are generated by the holomorphic and antiholomorphic components of the stress-energy tensor, $T(z)$ and $\bar{T}(\bar{z})$. The radially ordered operator product expansions (OPE) of these fields with themselves lead to

$$T(z_1)T(z_2) = \frac{c/2}{(z_1 - z_2)^4} + \frac{2}{(z_1 - z_2)^2} T(z_1) + \frac{1}{z_1 - z_2} \partial T(z_1), \quad (3.10)$$

where the constant c plays the role of the conformal anomaly of the CFT after radial quantization, and distinguishes different universality classes of CFTs. Free

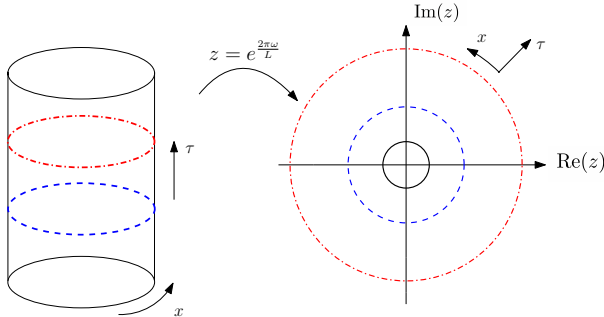


Figure 3.1: Exponential mapping from the Euclidean spacetime cylinder on a system to the complex plane. Each time slide is mapped to a circle on the complex plane, such that time evolution corresponds to scaling transformations, and time ordering corresponds to radial ordering.

boson universality class, that contains the Luttinger liquid theory, corresponds to $c = 1$, while the transverse field Ising model belongs to $c = \frac{1}{2}$. An important class of exactly solvable CFTs, called minimal models, are constrained by $c < 1$. In particular, from the OPE of T and \bar{T} , we deduce that these fields are quasi-primary that satisfy

$$T(z) \mapsto (\partial f)^2 T(f(z)) + \frac{c}{12} \{f(z), z\}, \quad (3.11)$$

where $\{f(z), z\}$ is the Schwarzian derivative of f , defined as $\{f(z), z\} = (f' f''') - (f'')^2)/f'^2$. The central charge also appears as the central extension of the Witt algebra after quantization, extending it to the so-called Virasoro algebra, that is satisfied by the Laurent modes of T and \bar{T} ,

$$T(z) = \sum_{n \in \mathbb{Z}} z^{-n-2} T_n, \quad \bar{T}(\bar{z}) = \sum_{n \in \mathbb{Z}} \bar{z}^{-n-2} \bar{T}_n. \quad (3.12)$$

In fact, the Virasoro generators L_n satisfy

$$[L_m, L_n] = \underbrace{(m-n)L_{m+n}}_{\text{classical part}} + \underbrace{\frac{c}{12}(m^3 - m)\delta_{m,-n}}_{\text{central extension}}. \quad (3.13)$$

We note that the global conformal algebra, that generates the Möbius transformations on the complex plane, form an $\mathfrak{sl}(2)$ subalgebra

$$\begin{cases} [L_0, L_{-1}] = L_{-1}, \\ [L_0, L_1] = -L_1, \\ [L_1, L_{-1}] = 2L_0, \end{cases}$$

that does not have any central extension. In fact, this is the part of the algebra that survives in arbitrary dimensions. In particular, the Hamiltonian, seen as generator of dilations on the complex plane, is defined as

$$H = \frac{2\pi}{L}(L_0 + \bar{L}_0), \quad (3.14)$$

while the momentum operator corresponds to the difference of L_0 and \bar{L}_0 . The Hilbert space of the CFT is constructed from the eigenstates of (3.14). By using the OPE between an arbitrary primary field $\Phi(z, \bar{z})$ of weight $(h + \bar{h})$ and $T(z)$, we conclude that any primary field gives rise to a state in the CFT Hilbert space of energy $\frac{2\pi}{L}(h + \bar{h})$, called primary or highest-weight state,

$$|h\rangle = \lim_{z \rightarrow 0} \Phi(z)|0\rangle, \quad (3.15)$$

where $|0\rangle$ is the $SL(2, \mathbb{C})$ vacuum of the theory, defined as $L_0|0\rangle = L_{\pm 1}|0\rangle = 0$. We note that although $L_0|0\rangle = 0$, because of the exponential map from the cylinder to the plane the stress tensors $T(z)$ and $\bar{T}(\bar{z})$ pick up a Schwarzian derivative term from (3.11) that leads to a Casimir shift of the spectrum proportional to the central charge c of the theory. More precisely, ones finds ¹

$$\langle 0 | H | 0 \rangle = -\frac{\pi c}{12L}. \quad (3.16)$$

The correspondence between fields and states is actually a bijection, as a consequence of radial quantization that maps all infinitely negative times to a single point: all states can be seen as created by a unique field inserted at the origin of the complex plane, and all fields inserted at the origin of the complex plane give rise to a unique state. Each primary state leads to a infinitely large tower of descendant states, called Verma module, generated by the action of L_{-n} ,

$$L_{-n_1} \dots L_{-n_k} |h\rangle, \quad n_1 < \dots < n_k. \quad (3.17)$$

For instance, the lowest energy excitations are $L_{-1}|h\rangle$, of level $h+1$, $L_{-2}|h\rangle$ and $L_{-1}^2|h\rangle$ of level $h+2$ and so forth, with a degeneracy at level N given by its partition $P(N)$.

As an application of the above formalism, we consider the free boson CFT, $c = 1$, that when compactified on a circle provides through Luttinger liquid theory the effective low energy description of a variety of critical models, such as the XXZ model, the Lieb-Liniger model, and quasi-one dimensional condensates of ultra-cold atoms. The action describing the (non-compactified) free boson on the complex plane is

$$S = \frac{1}{4\pi} \int dz d\bar{z} \partial_z \partial_{\bar{z}} \varphi(z, \bar{z}). \quad (3.18)$$

The classical equation of motion of such an action is

$$\partial \bar{\partial} \varphi(z, \bar{z}) = 0, \quad (3.19)$$

which naturally leads to conserved $U(1)$ currents forming purely chiral and antichiral primary fields

$$J(z) = i\partial \varphi(z, \bar{z}), \quad \bar{J}(\bar{z}) = i\bar{\partial} \varphi(z, \bar{z}), \quad (3.20)$$

of conformal weights $(1, 0)$ and $(0, 1)$ respectively. The Laurent modes of these fields form two copies of a current (or Kac-Moody) algebra,

$$[J_m, J_n] = Kn\delta_{n+m,0}. \quad (3.21)$$

¹ The Casimir shift of the CFT spectrum provides a first route to numerically identify the central charge of a given CFT from a given critical lattice model. However, the scaling of entanglement entropy is a more efficient approach to determined c .

As the two-point correlator of the bosonic field φ is logarithmic, it is thus clear that these are not primary fields. However, we can introduce the set of vertex operators, which together with the chiral and antichiral currents, provide the set of all primary fields of the theory. Specifically, they are defined as

$$V_\alpha(z, \bar{z}) = :e^{i\alpha\varphi(z, \bar{z})}: , \quad (3.22)$$

where $:...:$ denotes normal (Wick) ordering. It can readily be deduced that their scaling dimension is $(\alpha^2/2, \alpha^2/2)$. Importantly, interpreting vertex operators in the plane as electric charges of charge α , the n -point correlator of vertex operators is non-zero if and only if the collection of charges is electrically neutral, i.e., $\sum_{i=1}^n \alpha_i = 0$. In this case, using Wick's theorem, one finds

$$\langle V_{\alpha_1}(z_1, \bar{z}_1) \dots V_{\alpha_n}(z_n, \bar{z}_n) \rangle = \prod_{i < j} |z_i - z_j|^{2\alpha_i \alpha_j}. \quad (3.23)$$

3.3 TORUS PARTITION FUNCTION

We have so far discussed conformal field theory on a cylinder, which describes either a finite system at zero temperature, or an infinite system at finite temperature, as both are related by S-transformation. As the cylinder can be conformally mapped to the complex plane, we could use the power of complex analysis to deduce results on correlation functions of fields on the plane. However, considering both finite system size and finite temperature compactifies both space and time directions, resulting in a torus-shaped spacetime. To go from the plane to the torus, one has a freedom in the way to identify the points on the plane, such that $\omega \sim \omega + m\alpha_1 + n\alpha_2$, for $m, n \in \mathbb{Z}$, and (α_1, α_2) a pair of complex numbers, that span a two dimensional lattice, whose unit cell forms the fundamental domain of the torus. The shape of the torus is parametrized by the modular parameter $\tau = \frac{\alpha_1}{\alpha_2} = \tau_1 + i\tau_2$. Different choices of lattices are related by modular transformations $SL(2, \mathbb{Z})/\mathbb{Z}_2$, which implies that the modular parameter leaves the torus invariant under

$$\tau \mapsto \frac{a\tau + b}{c\tau + d}, \quad \begin{pmatrix} a & b \\ c & d \end{pmatrix} \in SL(2, \mathbb{Z})/\mathbb{Z}_2. \quad (3.24)$$

This modular invariance of the torus motivates the definition of the partition function of a CFT as

$$Z(\tau_1, \tau_2) = \text{Tr}(e^{-2\pi\tau_2 H} e^{-2\pi\tau_1 P}), \quad (3.25)$$

where the trace is taken over all states of the Hilbert space, and H and P are the generators of time and space translations, which can thus be rewritten as

$$Z(\tau) = \text{Tr}(q^{L_0 - \frac{c}{24}} \bar{q}^{\bar{L}_0 - \frac{c}{24}}), \quad q = e^{2\pi i\tau}. \quad (3.26)$$

In particular, because of the invariance of the torus under modular transformations, the partition function Z has to be invariant under modular transformations (3.24). In the following, we provide expressions for the partition function of the compactified free boson theory, also known as Luttinger liquid, which will be an important building block to construct the Rényi divergence of two different Luttinger liquid at thermal equilibrium in Chapter 13. In this case,

the bosonic field $\varphi(z, \bar{z})$ is defined on a circle, $\varphi(z, \bar{z}) \sim \varphi(z, \bar{z}) + 2\pi Rn$. Then, the partition function is

$$Z(\beta) = \frac{1}{|\eta(i\beta/L)|^2} \sum_{m,w \in \mathbb{Z}} \exp \left[-\pi \frac{\beta}{L} \left(\frac{m^2}{R} + R w^2 \right) \right], \quad (3.27)$$

where η is the Dedekind eta function

$$\eta(\tau) = q^{1/24} \prod_{n=1}^{\infty} (1 - q^n), \quad (3.28)$$

that has the correct modular invariance properties ensuring that the free boson torus partition function (3.27) is modular invariant. Furthermore, the partition function of the compactified free boson on a circle of radius R is equal to the one of a boson compactified on a circle of radius $2/R$. This is a manifestation of T-duality. In particular, the fixed point of this duality is the radius $R = \sqrt{2}$, which is self-dual. In the language of Tomonaga-Luttinger liquid theory [see Part iv], the self-dual point corresponds to a Luttinger parameter $K = 1$, i.e., the non-interacting point of the Tomonaga-Luttinger liquid.

3.4 BOUNDARY CONFORMAL FIELD THEORY

Although the preceding sections focused exclusively on CFTs defined on a Euclidean cylinder with a fixed length L , there are situations where it may be advantageous to define the CFT on a Euclidean spacetime strip instead, such as to describe lattice models with open boundaries. In such cases, it is important to impose boundary conditions that preserve conformal invariance. These boundary conditions themselves lead to constraint, called conformal boundary conditions, that need to be taken into account in the construction of the theory. In particular, holomorphic and anti-holomorphic components of fields are no longer decoupled, and are related by the boundary conditions. The correlation functions of fields are no longer evaluated on the full complex plane, but to the upper-half plane (UHP), which can be mapped to from the Euclidean strip by the exponential map

$$e^{\pi\omega/L}, \quad (3.29)$$

such that the boundaries of the strip are mapped to the real axis. Different boundary conditions at the two sides of the strip lead to different boundary conditions on the positive and negative real axis. In order to account for such a change of boundary conditions, one typically inserts a boundary condition changing (BCC) operator at $z = 0$. In particular, we note that the Floquet dynamics of CFTs periodically driven by a BCC operator was studied in [58]. It can be derived that on the UHP, $T_{xy}(x, 0) = 0$, which implies the absence of energy flow across the boundary, and ensures that a given boundary condition preserves conformal invariance. Writing this condition in complex coordinates leads to

$$T(z) = \bar{T}(\bar{z}), \quad \text{for } z = \bar{z}, \quad (3.30)$$

which introduces a coupling between the two copies of the CFT. Equivalently, we can write the condition. In particular, correlation functions can be evaluated

$$\langle \mathcal{B} | q^{L_0 + \bar{L}_0 - \frac{c}{12}} | \mathcal{B} \rangle \quad \text{Tr}_{\mathcal{H}_B} \left[q^{L_0 + \bar{L}_0 - \frac{c}{12}} \right]$$

Figure 3.2: Duality between the closed CFT tree level amplitude of a boundary state $|\mathcal{B}\rangle$ and the boundary CFT partition function, where the trace is taken over the BCFT Hilbert space \mathcal{H}_B (for simplicity in the case of identical boundary conditions on both ends of the system).

on the upper-half plane by using analogies with electrostatics and introducing mirror charges on the lower-half plane, and evaluate the doubled correlation function on the full complex plane. The position of the image charge should be adjusted in such a way that the correlation function verifies the boundary condition on the real axis.

The partition function, defined in the periodic case on a torus, can be defined in the presence of boundaries on a cylinder, and is characterized by a single modular parameter t . In particular, the cylinder partition function on a BCFT can be seen, by replacing space by time and vice-versa, as a tree-level amplitude $\langle \mathcal{B} | e^{-\tau H t} | \mathcal{B} \rangle$, for a specific state $|\mathcal{B}\rangle$: this correspondence is illustrated on Fig. 3.2. The state in the periodic CFT whose time evolution is dual to the BCFT partition function is called a boundary states, or Cardy state, and can be explicitly constructed for particular examples of CFTs. In the case of the free boson CFT, only Neumann and Dirichlet boundary conditions are allowed, and the resulting boundary state is

$$|\mathcal{B}_N\rangle = \exp \left(- \sum_{k=1}^{\infty} \frac{1}{k} J_{-k} \bar{J}_{-k} \right) |0\rangle \quad \text{for Neumann boundary condition,} \quad (3.31)$$

$$|\mathcal{B}_D\rangle = \exp \left(+ \sum_{k=1}^{\infty} \frac{1}{k} J_{-k} \bar{J}_{-k} \right) |0\rangle \quad \text{for Dirichlet boundary condition.} \quad (3.32)$$

Boundary states play a fundamental role in the study of the massive quench dynamics of CFTs, as is briefly discussed in Sec. 4.2, where the correspondence between the partition function of the open CFT and the return amplitude $\langle \mathcal{B} | e^{-iHt} | \mathcal{B} \rangle$ can be used to compute the Loschmidt echo after a quantum quench starting from a massive initial state modeled by a smeared boundary state.

This chapter provides an overview of non-equilibrium dynamics in many-body systems. We begin in Sec. 4.1 by discussing the thermalization of interacting quantum systems, including the eigenstate thermalization hypothesis. In Sec. 4.2, we focus on integrable models, a special class of systems that can evade thermalization due to the presence of a large number of local conserved charges. In particular we examine non-equilibrium phenomena in integrable models, such as quantum quenches. Finally, in Sec. 4.3, we briefly touch on the chaotic properties of non-integrable systems and the methods for diagnosing them.

4.1 THERMALIZATION OF QUANTUM SYSTEMS

For a generic many-body quantum system brought out-of-equilibrium, one expects ergodicity to take over the dynamics of the system in the long time limit, such that the steady state it reaches is only characterized by a single conserved charge, the energy, whose Lagrange multiplier defines the inverse temperature at which the system thermalizes. More specifically, let us consider a generic non-integrable quantum many-body system without global symmetries. In this case we generally decompose the time-evolved average of any local observable ϑ_A defined over a finite region A as

$$\langle \vartheta^A(t) \rangle = \langle \Psi(t) | \vartheta^A | \Psi(t) \rangle = \sum_n |c_n|^2 \vartheta_{nn}^A + \sum_{n \neq m} c_n c_m^* e^{-i(E_n - E_m)t} \vartheta_{nm}^A, \quad (4.1)$$

where we used the decomposition of a generic state $|\psi(t)\rangle$ in the eigenbasis $\{|n\rangle\}$ of the Hamiltonian. The system equilibrates whenever the expectation value tends to a steady state value

$$\lim_{t \rightarrow \infty} \langle \vartheta^A(t) \rangle = \vartheta_{\text{eq}}^A. \quad (4.2)$$

In the particular case where the steady state of the system is well-described by a thermal Gibbs ensemble, i.e.,

$$\lim_{t \rightarrow \infty} \lim_{N \rightarrow \infty} \langle \vartheta_A(t) \rangle = \text{Tr} \left(\vartheta_A e^{-\beta_{\text{eff}} H} / Z \right), \quad (4.3)$$

the system is said to thermalize at an effective temperature β_{eff}^{-1} given by the micro-canonical energy E , i.e., $E = \text{Tr} (H e^{-\beta_{\text{eff}} H} / Z)$. Alternatively, thermalization properties can be seen from reduced density matrices over the subsystem A ,

$$\rho_A(t) = \text{Tr}_{\bar{A}} |\Psi(t)\rangle \langle \Psi(t)|, \quad (4.4)$$

where $\text{Tr}_{\bar{A}}$ denotes the partial trace with respect to the complement of A . In fact, for a thermalizing system, one expects the reduced density matrix of any subsystem A to converge to a thermal state

$$\lim_{t \rightarrow \infty} \lim_{N \rightarrow \infty} \rho_A = \text{Tr}_{\bar{A}} \frac{e^{-\beta H}}{Z}, \quad (4.5)$$

i.e., any subregion of the system equilibrates to a thermal ensemble even though the system is closed and its evolution is unitary. This *local* loss of memory of the initial conditions can be understood by the fact that spreading of quantum correlations is intrinsically non-local because of quantum entanglement.

A fundamental issue is to then find a minimal set of requirements for a quantum system to thermalize. Such requirements can be formulated into an ansatz known as the eigenstate thermalization hypothesis (ETH). More precisely, ETH is an ansatz for the matrix elements ϑ_{mn} of certain local observables ϑ in the eigenbasis of the Hamiltonian H , in eigenstates that lie in the middle of the spectrum. These matrix elements are predicted to take the form

$$\vartheta_{mn} = O(\bar{E})\delta_{mn} + e^{-S(\bar{E})/2}f_\vartheta(\bar{E}, \omega)R_{mn}, \quad (4.6)$$

where $\bar{E} = (E_n + E_m)/2$ is the averaged energy of the two states and $\omega = E_n - E_m$ is their level spacing. The diagonal matrix elements are given by $O(\bar{E})$ which is the microcanonical expectation value at the averaged energy, while off-diagonal matrix elements are randomly distributed according to the random numbers R_{mn} that have zero mean and unit variance, and $f_\vartheta(\bar{E}, \omega)$ is a smooth function. In particular, zooming on small energy windows, ETH leads to consistent results with random matrix theory, that predicts Gaussian distribution of the off-diagonal elements ϑ_{mn} for thermalizing Hamiltonians. To prove that the ETH ansatz implies thermalization of local observables, one starts from the definition of $\bar{\vartheta}^A$ in the diagonal ensemble,

$$\langle \bar{\vartheta}^A \rangle \equiv \lim_{T \rightarrow \infty} \int_0^T dt \langle \vartheta^A(t) \rangle = \text{Tr} \left(\rho_{\text{DE}} \vartheta^A \right), \quad (4.7)$$

with $\rho_{\text{DE}} = \sum_n |c_n|^2 |n\rangle \langle n|$, and one then inserts the ETH ansatz (4.6). By using the equivalence of the statistical ensembles, one relates Gibbs expectation values to microcanonical ones, and concludes in the thermodynamic limit from saddle-point arguments that

$$\bar{\vartheta} \sim \langle \vartheta \rangle_\beta \sim \langle E | \vartheta | E \rangle. \quad (4.8)$$

The function $f_\vartheta(\bar{E}, \omega)$ also enables to recover the fluctuation-dissipation theorem (FDT) [59]. In fact, defining the response function and the noise function as

$$\begin{aligned} \chi_\vartheta(t_1, t_2) &= -i\vartheta(t_1 - t_2) \langle [\vartheta(t_1), \vartheta(t_2)] \rangle, \\ S_\vartheta(t_1, t_2) &= \langle \{\vartheta(t_1), \vartheta(t_2)\} \rangle - 2\langle \vartheta(t_1) \rangle \langle \vartheta(t_2) \rangle, \end{aligned} \quad (4.9)$$

their Fourier transform can be approximated by the ETH ansatz, leading to the relations

$$\begin{aligned} \chi''_\vartheta(E, \omega) &\approx 2\pi \sinh(\beta\omega/2) |f_\vartheta(E, \omega)|^2, \\ S_\vartheta(E, \omega) &\approx 4\pi \cosh(\beta\omega/2) |f_\vartheta(E, \omega)|^2. \end{aligned} \quad (4.10)$$

These expressions for the fluctuation and dissipation correlators lead to the usual form of the FDT

$$\chi''_\vartheta(E, \omega) = \frac{1}{2} \tanh(\beta\omega/2) S_\vartheta(E, \omega). \quad (4.11)$$

Thus, we conclude that ETH implies thermalization of local observables, making pure energy states indistinguishable from thermal states, both from the matrix

elements of local observables and two-point correlation functions through the FDT.

There are several characterizations of quantum thermalization, from entanglement entropy to level spacing statistics. The von Neumann entanglement entropy S_A is defined for any reduced density matrix ρ_A of a subsystem A as

$$S_A = -\text{Tr}\rho_A \log \rho_A. \quad (4.12)$$

In the case of the ground state of local gapped Hamiltonians, the scaling of entanglement entropy follows an area law, $S_A \sim L^{d-1}$ in d dimensions: this is explained by the fact that all entanglement is shared between correlations at the boundary of the subsystem A . However, for high-energy states of a generic many-body system, ETH leads to thermal correlations of local observables, and the entanglement entropy S_A is given by the thermal entropy of the reduced density matrix ρ_A , giving an extensive contribution, or volume law, $S_A \sim L^d$. On the other hand, thermalizing quantum systems share similarities with quantum chaotic systems (see Sec. 4.3), which are described by random matrix theory. On general grounds, it is expected for non-integrable quantum many-body systems that level repulsion will arise in the spectrum, which can be characterized by the emergence of Gaussian ensembles in the level spacing statistics $P(s_n)$ (see Sec. 2.1 for definitions of the different statistical ensembles and of level spacing statistics). The absence of level repulsion, characterized by the emergence of a Poisson ensemble, is observed in any ergodicity-breaking quantum system, such as integrable systems (see Sec. 4.2) or many-body localized phases [13].

Finally, let us mention other mechanisms that lead to weak breaking of ergodicity, such as quantum scars [14–16], Hilbert space fragmentation [60] or prethermalization [17, 18]. For instance, prethermalized regimes may happen in many-body systems that consist of an integrable Hamiltonian perturbed by an integrability-breaking term controlled by an energy scale $\Delta \gg 1$. The system may first relax to an athermal state as a consequence of the integrability of the original Hamiltonian, and finally thermalize to a Gibbs ensemble after time scales larger than Δ^{-1} , leading to a two-step thermalization with a parametrically long prethermalization plateau. On the other hand, quantum scars appear as a set of extensive athermal eigenstates of a non-integrable Hamiltonian, characterized by a low (typically area law) entanglement entropy compared to the usual thermal states.

4.2 INTEGRABLE MODELS

An important class of counterexamples to thermalization for closed many-body systems out-of-equilibrium are integrable systems. Besides the theoretical relevance of integrable systems to gain analytical insights on general features of many-body systems out-of-equilibrium, such systems naturally arise in certain cold-atomic experiments. A seminal example of this is the Lieb-Liniger model that provides a precise description of cold-atomic gases constrained to one-dimensional tubes [19, 20]. Furthermore, integrable systems fundamentally affect the non-equilibrium physics of interacting systems, as was observed in the quantum Newton cradle experiment, in which clouds of Rubidium atoms were shown to collide without thermalizing [61]. Integrable quantum systems are characterized by an extensive number of local conservation laws that strongly constrain their dynamics, avoiding thermalization and ergodicity, i.e., they avoid maximal loss of information of the initial state. It is believed

that the steady state of an integrable system brought far from equilibrium is a generalized Gibbs ensemble (GGE) [62] characterized by an extensive number of local charges $\{Q_n\}_{n \in \mathbb{N}}$, taking the form

$$\frac{e^{\sum_{i=1}^{\infty} e^{-\mu_i Q_i}}}{\text{Tr}(e^{\sum_{i=1}^{\infty} e^{-\mu_i Q_i}})}, \quad (4.13)$$

described by an extensive number of Lagrange multipliers μ_i . The validity of the GGE has been demonstrated in a multitude of integrable lattice systems, such as the transverse field Ising model [63] and hard-core bosons [64].

A particularly powerful method to study the non-equilibrium properties of integrable quantum many-body systems is generalized hydrodynamics (GHD) [65, 66]. This formalism applies to quantum systems with a macroscopic number of conservation laws that are solvable by the thermodynamic Bethe ansatz. More specifically, GHD applies at the emergent hydrodynamics scales, which are large enough to contain a thermodynamic number of particles but small enough to admit slow variations in spacetime. In other words, such state satisfies local entropy maximisation, i.e., $\langle \mathcal{O}(x, t) \rangle = \langle \mathcal{O}(0, 0) \rangle_{\beta(x, t)}$, for a local observable \mathcal{O} . Such a state describes any local observable at (x, t) in the same way, parametrized by $\beta(x, t)$. This principle of local entropy maximisation applied to integrable systems described by GGE leads to the fundamental GHD equations

$$\partial_t q_i(x, t) + \partial_x j_i(x, t) = 0 \quad (4.14)$$

for the i -th local conserved charge $Q_i = \int dx q_i(x, t)$. This (infinite) set of conservation equations enable to access exact currents in non-equilibrium steady states, e.g., to solve the dynamics of the Riemann problem of hydrodynamics, or more generally, quantum partitioning protocols, where one brings into contact two halves that are initially thermalized in different equilibrium quantum states, for generic integrable non-conformal models [65, 66].

Another simple yet insightful approach to integrable quantum systems away from equilibrium are quantum quenches. Such protocols consist in brutally changing some parameters of a quantum system initially at equilibrium, and study the response of such a system at later times. In particular, important results were found for the quench dynamics of critical one-dimensional systems described by conformal field theories (CFTs) [67–69]. In such systems, scale invariance opens a pathway to analytically compute different quantities after the quench, such as entanglement entropy $S_A(t)$ [67], light-cone spreading of correlations [70], revivals in finite systems [71]. More specifically, we consider the time evolution of a (1+1)D CFT, starting from a massive initial state $|\psi_0\rangle$, e.g., the ground state of a gapped Hamiltonian H_0 initialized at negative times. Then, we let such initial state unitarily evolve with a uniform CFT Hamiltonian H . Such class of protocols, often referred as massive quenches, describes the low-energy physics of, for instance, an abrupt change of the anisotropy parameter of the XXZ model, driving the system from a gapped ferromagnetic phase to a paramagnetic phase. In particular, using conformal invariance of the system, one can compute general correlation functions

$$C(x, t) = \langle \psi_0 | e^{iHt} \Phi_1(x_1) \dots \Phi_n(x_n) e^{-iHt} | \psi_0 \rangle, \quad (4.15)$$

for arbitrary primary fields Φ_i . The general strategy to compute such a correlation function is to rotate to a Euclidean spacetime, $t \mapsto i\tau$, and notice that this

is the correlation function of a boundary conformal field theory, whose boundary conditions are encoded by the short-ranged state $|\mathcal{B}\rangle$, that is understood as a boundary (or Cardy) state, such that $|\psi_0\rangle = e^{-\tau_0 H} |\mathcal{B}\rangle$, in order for the initial state to be regularized. These correlation functions can be mapped onto the upper-half plane and evaluated from boundary CFT techniques, leading to the exact time evolution of equal-time correlations after the quench. Applying this computation to two-point function of twist fields operators $\mathcal{T}(x)$, the entanglement entropy after the quantum quench can be computed by making use of the replica trick [72]. The von Neumann entanglement entropy S_A of a subsystem A is obtained from the n -th Rényi entropy as

$$S_A(t) = \lim_{n \rightarrow 1} \frac{1}{1-n} \log \text{Tr}(\rho_A^n(t)), \quad (4.16)$$

where $\rho_A^n(t)$ is the n -th power of the reduced density matrix ρ_A . The replica trick of the CFT enables to write $\text{Tr}(\rho_A^n(t))$ as a two-point correlator of twist fields of conformal dimension $c/12(n - 1/n)$ on an n -sheeted Riemann surface. For a subsystem A consisting of a single interval of length l , the entanglement entropy $S_A(t)$ grows as

$$S_A(t) \approx \frac{c}{3} \log \tau_0 + \frac{\pi c t}{6\tau_0}, \quad t < l/2, \quad S_A(t) \approx \frac{c}{3} \log \tau_0 + \frac{\pi l c}{12\tau_0}, \quad t > l/2, \quad (4.17)$$

i.e., the (single interval) entanglement entropy linearly increases until it reaches its steady state value after a time $t = l/2$, that solely depends on the central charge c of the given critical theory and on the subsystem size l . This particularly simple temporal evolution of entanglement can be attributed to a generic property of integrable models: the existence of stable long-lived quasiparticles. In fact, such a linear growth and steady state value of $S_A(t)$ can be obtained after a quench for any integrable model (conformal or non-conformal) from a simple quasiparticle picture, by assuming that all the entanglement is carried by different species of quasiparticles that propagate ballistically at a given velocity. At the initial time $t = 0$, such pairs of quasiparticles are produced at each point of spacetime, and entanglement between the two disjoint subsystems A and B linearly grows as long as pairs of quasiparticles are such that one member of the pair is in A and the other in B . By ballistic propagation of the excitation, it is clear that the saturation time has to depend on linearly on the subsystem size l , and additionally that the entanglement entropy has to increase linearly and then saturate to a steady state value that also depends linearly on the subsystem size l . In the particular case of CFTs, only one species of quasiparticles exists: massless quasiparticles with a linear dispersion, that come in pairs of left and right moving quasiparticles, that propagate at the Fermi velocity. The existence of such long-lived quasiparticles directly implies that information after the quantum quench has to propagate along light-cones, as was observed experimentally in cold-atomic gases [70]. Furthermore, for CFTs defined on a system of finite size L , it implies that at times $t_* = kL/2$, $k \in \mathbb{N}$ for periodic boundary conditions, and $t_* = kL$ for open boundary conditions, all quasiparticles emitted at $t = 0$ arrive again at their initial positions, such that the Loschmidt echo goes back to one, $F(t) = |\langle \psi(0) | \psi(t_*) \rangle|^2 = 1$ [71]. In

order to show this result explicitly, we note that the Loschmidt amplitude is defined as

$$\langle \psi_0 | e^{-iHt} | \psi_0 \rangle = \frac{\langle \mathcal{B} | e^{-\beta H/4} e^{-iHt} e^{-\beta H/4} | \mathcal{B} \rangle}{\langle \mathcal{B} | e^{-\beta H/4} e^{-\beta H/4} | \mathcal{B} \rangle}. \quad (4.18)$$

We now use the BCFT to closed CFT duality to express the return amplitude as a partition function of the associated BCFT [see Sec. 3.4],

$$\frac{\langle \mathcal{B} | e^{-\beta H/4} e^{-iHt} e^{-\beta H/4} | \mathcal{B} \rangle}{\langle \mathcal{B} | e^{-\beta H/4} e^{-\beta H/4} | \mathcal{B} \rangle} = \frac{Z(\beta/2 + it, L)}{Z(\beta/2, L)}. \quad (4.19)$$

We can then use the fact that the partition function of a BCFT has linear decomposition in the Virasoro characters,

$$Z = \sum_{\Delta} |B_{\Delta}|^2 \chi_{\Delta}(q) = \sum_{\tilde{\Delta}} n_{BB}^{\tilde{\Delta}} \chi_{\tilde{\Delta}}(\tilde{q}), \quad (4.20)$$

where B_{Δ} are the coefficients of the decomposition of the boundary state in terms of Ishibashi states, n_{BB} are the fusion rules coefficients. Using modular transformations on the characters, one can thus compute the partition function in different limits, and observe a characteristic revival at integer multiples of L . These revivals have been numerically and analytically observed in a multitude of quenched critical systems which realize different universality classes of CFTs, such as the Luttinger model [73] and the transverse field XY model [74]. This property directly implies the non-ergodicity of critical quantum system after a quantum quench: the quantum fidelity (or Loschmidt echo) permanently oscillates between one and a finite non-zero value for infinite times, precluding any ergodic effects because of the emergence of an infinite number of local conserved charges. However, the asymptotic state reached after the massive quench of a CFT that we discussed is not described by a GGE, as it can be shown that the reduced density matrix of an arbitrary interval converges exponentially to the one of a thermal ensemble, which does not display all the infinite number of local conserved charges of the theory. This is due to the fact that the initial massive state $|\psi_0\rangle$ should in general include all possible irrelevant deformations $\tilde{\Phi}_i$ of the CFT, and generically takes the form [75]

$$|\psi_0\rangle \sim e^{-2\tau_0 H} \prod_i e^{-\mu_i \int \tilde{\Phi}_i dx} |\mathcal{B}\rangle. \quad (4.21)$$

By using a path integral formulation of the reduced density matrix, one can show that the steady state value of the reduced density matrix for any interval is indeed of the form of a GGE (4.13). This provides a general proof that massive quenches of rational models of CFTs generally equilibrate to a GGE, with an infinite number of conserved charges inherited from the infinite dimension of the conformal algebra in two dimensions.

4.3 QUANTUM CHAOS IN THERMALIZING SYSTEMS

Classical chaos is traditionally defined from the exponential sensitivity of the phase space trajectories to initial conditions. This phenomenon has been observed in numerous classical systems, such as weather, motion of planets in the

solar system, and behavior of fluids. In classical physics, a notable counterexample to chaotic systems are integrable systems, that are characterized by a large number of integrals of motions that confine all trajectories in phase space to invariant tori. In particular, weak integrability-breaking terms in classical mechanics only slightly deform the phase space and do not affect the stability of the system for long times, a result known as Kolmogorov–Arnold–Moser (KAM) theorem. On the other hand, defining chaos for quantum systems turns out to be subtle as the notion of trajectories in phase space does not apply. The most commonly accepted route to define quantum chaos is through random matrix theory and the ETH [see Sec. 4.1]. The relevant spectral properties of chaotic systems are usually diagnosed through level spacing: level repulsion is expected in the level spacings of chaotic systems, leading to Gaussian distributions, contrary to integrable systems that display a Poisson distribution. A natural question that arises is whether there exists a quantum analog to the KAM theorem for weak integrability-breaking of integrable quantum systems. It has been shown that certain perturbations lead to prethermalization [76] described by an effective GGE, with quasi-conserved charges.

Another approach to quantum chaos is based on the notion of scrambling in operator space, referred to as operator scrambling. In order to probe non-local spreading of operators during the unitary time evolution, one introduces the squared commutator

$$C(t) = -\langle [W(t), V]^2 \rangle, \quad (4.22)$$

for two initially commuting observables W and V . $C(t)$ can be rewritten as a single four-point correlator of the form $\langle VW(t)VW(t) \rangle$, named out-of-time-order correlators (OTOC) [77]. The growth of the OTOC indicates a growth of the non-commutativity of two initially commuting observables, thus defining a notion of operator scrambling through the system over time. In fact, the initial operator $W(0)$ will evolve to a complicated operator $W(t) = e^{iHt}W(0)e^{-iHt}$, which admits the expansion

$$W(t) = W(0) + it[H, W] - \frac{t^2}{2!}[H, [H, W]] - \frac{it^3}{3!}[H, [H, [H, W]]] + \dots, \quad (4.23)$$

which, at order n , leads to n local operators acting non-trivially on a large part of the system. This implies that the commutator $[W(t), V]$ generally has a large weight [78], thus motivating the OTOC definition. We note that these objects have a peculiar acausal structure that makes their experimental measurement complicated. In fact, in order to measure OTOCs one first needs to evolve the system at a time t , apply the operator W , go backward in time to the initial $t = 0$, and insert the operator V . Alternatively, one needs to prepare a second quantum state by first acting with V , evolving for time t , applying W , and going backward to initial time. Such a backward time evolution may be complicated to realize in experimental setups, and cannot be measured in, e.g., angle-resolved photo-emission spectroscopy and neutron scattering from linear response theory, contrary to usual time-ordered correlation functions. It has nonetheless been measured in different platforms, such as nuclear magnetic resonance quantum simulator, where the backward time evolution is engineered through a sign change of the magnetic field [79].

The classical limit of the squared commutator provides a fruitful connection to classical chaos: it is related to the square of derivatives of the classical trajectory in phase space for given initial conditions. Therefore, classical chaos

readily implies exponential growth of the OTOC in the quantum regime. The Lyapunov exponent that characterizes such an exponential growth of the OTOC is claimed to be bounded by

$$\lambda_L \leq \frac{2\pi}{\beta}. \quad (4.24)$$

The saturation of the bound on quantum chaos is reached in the large N limit of the Sachdev-Ye-Kitaev model (SYK), as well as for holographic CFTs. A common feature of these strongly interacting models is their lack of a stable quasiparticle description, as well as their classical holographic dual. We stress that not all non-integrable models display an exponential growth of the OTOC described by a Lyapunov exponent. In particular, non-integrable lattice models do not exhibit an exponential growth [80]. Another diagnose of quantum chaos is based on the spectral properties of the Hamiltonian. While the level spacing reveals chaotic properties of quantum systems, it does not probe energy levels that are far apart. This property can be incorporated by studying the spectral form factor (SFF), defined for holographic CFTs as $|Z(\beta + it)|$, where Z is the torus partition function [see Sec. 3.3]. At late time the SFF tends to a plateau and only probes nearest neighbor levels. On the other hand, at earlier times the SFF is a powerful probe of the spectral rigidity, namely the tendency for the system to show level repulsion between energy levels that are far apart, leading to a ramp evolution of the SFF before saturating to its plateau value. Finally, short times lead to a non-universal dip structure in the SFF; thus for chaotic systems, a typical dip-ramp-plateau is expected, as observed in the SYK model [81]. We note that both the OTOC and the SFF can be obtained as different types of analytic continuations of the torus partition function for chaotic CFTs [82]; thus, for such systems the central probe of quantum chaos is the partition function, as expected from the information it contains on the spectral statistics of the problem.

Another definition of scrambling of quantum information through the system is captured by the notion of entanglement scrambling. It is usually identified from the negativity of the tripartite mutual information, defined for a system divided in four regions A , B , C and D as

$$I_3(A, B, C) = I(A, B) + I(A, C) - I(A, BC), \quad (4.25)$$

where the mutual information is defined as $I(A, B) = S_A + S_B - S_{AB}$, and $AB = A \cup B$. The tripartite mutual information (4.25) measures the amount by which one cannot reconstruct A by local measurements of B and C separately. In particular, negativity of $I_3(A, B, C)$ captures the information that can be recovered by measuring the union of B and C but not by measuring them individually, leading to information scrambling through the system. The notion of operator scrambling and exponential growth of OTOC is in general distinct from the notion of entanglement scrambling, as the former probes scrambling in the space of observables, and the latter probes scrambling of wavefunctions. However, in the context of unitary quantum channels, it has been shown that the OTOC butterfly effect implied entanglement scrambling in the system. The precise relation between both notions of scrambling relies on a relation between the averaged OTOC over a complete set of operators and the second Rényi entropy [83].

To wrap up this section, we briefly highlight another recent advance in the field of quantum chaos, from the perspective of random matrix theory. We focus

our attention on translational-invariant many-body quantum systems, and in particular on Floquet unitary circuits, such as the kicked Ising model and brick wall models [84]. Translational-invariant quantum circuits are associated by a spacetime duality to non-Hermitian dual transfer matrices, that possess a complex spectrum [85]. While the characterization of the late-time quantum chaos via spectral statistics of the Hamiltonian is characterized by level repulsion and Gaussian ensembles, the spectrum of the dual non-Hermitian transfer matrix that encodes “evolution” in space has been shown to be characterized by a non-Hermitian Ginibre ensemble¹ [87]. In order to characterize the emergence of quantum chaos from this dual perspective, we define the spectral form factor in the case of dual unitary circuits as

$$K(t, L) = \langle |\text{Tr}_{\mathcal{H}}(\prod_{t'=1}^t U(t', L))|^2 \rangle = \langle |\text{Tr}_{\tilde{\mathcal{H}}}(\prod_{j=1}^L T(t, j))|^2 \rangle, \quad (4.26)$$

where U is the single-step time evolution operator in the unitary circuit, and T the dual spatial evolution operator, performing the evolution on the dual Hilbert space $\tilde{\mathcal{H}}$. One can then establish for a given dual unitary circuit model a regime diagram in terms of (t, L) . By increasing L and keeping t fixed, one finds a crossover from a linear ramp regime $K(t, L) \sim tL$ to an exponential regime in L . The linear ramp regime is the dual indicator of many-body chaos, and necessarily requires a description of the dual spatial evolution operator with the Ginibre ensemble [87]. We stress that the emergence of the Ginibre ensemble is unique to many-body systems as it requires a non-trivial spatial structure, as opposed to the Gaussian ensemble that does not require strong correlations to emerge.

¹ We recall that the Ginibre ensemble is defined as the ensemble of $n \times n$ random matrices whose entries are complex numbers with real and imaginary parts sampled from a normal distribution with zero mean and variance $1/2n$. In the limit of large n , almost all eigenvalues follow the circular law: they are uniformly distributed in the unit disk [86].

Part II

FROM DELICATE TO DISORDERED TOPOLOGICAL PHASES

This part of the thesis deals with the exploration of topological phases of matter that lie beyond the paradigm of the tenfold-way classification. Chapter 5 generalizes the concept of Hopf insulator, a delicate two-band topological insulator whose topology is related to the Hopf invariant, to an arbitrary number of bands separated by band gaps. The obtained \mathbb{Z} classification of such a N -band Hopf insulator is related to the quantized isotropic magnetoelectric coefficient of its bulk. The boundary of a N -band Hopf insulator can be fully gapped, and we find that there is no unique way of dividing a finite system into bulk and boundary. Despite this non-uniqueness, we find that the magnetoelectric coefficient of the bulk and the anomalous Hall conductivity of the boundary are quantized to the same integer value. We propose an experiment where the quantized boundary effect can be measured in a non-equilibrium state. Chapter 6 introduces topologically localized insulators (TLIs), a novel class of insulators whose bulk is insulating at *arbitrary* filling, with all bulk states fully localized, while its anomalous boundary carries quantized Hall conductivity. We construct an explicit model for such a novel phase, and show the robust quantization of its bulk and boundary topological invariants.

The content of this part of the thesis is based on [21, 22].

N - B A N D H O P F I N S U L A T O R

5.1 INTRODUCTION

In this chapter we focus our attention on fragile topological phases, as introduced in Sec. 2.3. In such systems, the constraint that the number of bands needs to be fixed hinders direct application to crystalline materials. For example, the Hopf insulator has exactly one conduction and one valence band, whereas crystals have typically many bands. Although the Hopf insulator can be turned into a stable topological phase through additional symmetry constraints [88], here we take a different route and relax the requirements of the delicate topological classification to allow for a trivial band to be added if separated by the gaps from all the other bands, see Fig. 5.1(d). The idea of multi-gap classification is not a new one. The stable multi-gap classification was used to classify Floquet insulators [89], whereas the delicate multi-gap classification, with exception of the one-dimensional systems described by real Hamiltonians [90–92], has been largely unexplored.

Specifically, we consider three-dimensional systems with no additional symmetry constraints, and find that delicate multi-gap topological classification is the same as the classification of the Hopf insulator. The obtained phases are dubbed N -band Hopf insulators. Unlike the tenfold-way topological insulators, the boundary of the N -band Hopf insulator can be fully gapped and there is no unique way of defining the boundary subsystem, see Sec. 5.4. Remarkably, despite this non-uniqueness, we are able to formulate the bulk-boundary correspondence for the N -band Hopf insulator: a finite sample of the N -band Hopf insulator can be seen as the bulk, with the isotropic orbital magnetoelectric polarizability coefficient (of all the bulk bands)¹ taking an integer value, wrapped in a Chern insulator sheet with the total Chern number of all the boundary bands equal to minus the same integer, see Fig. 5.2. A bulk-boundary correspondence for $N = 2$ Hopf insulator was formulated in [49], albeit for a subset of boundary conditions that leave the boundary gapped. In this chapter we show that such bulk-boundary correspondence is a physical one: the quantized boundary effect can be measured in certain non-equilibrium states. Specifically, a finite sample fully filled with electrons does not exhibit any quantized effect, the quantized response is obtained only by driving the system into a non-equilibrium state where the region close to the boundary (bulk) is fully filled with electrons while the bulk (boundary) is unoccupied.

The results of topological classifications apply equally well to periodically and adiabatically driven crystals. In fact, there is a well known one-to-one correspondence between a two-dimensional Quantum Hall system and a one-dimensional Thouless pump [38]. The quantized Hall conductance translates into quantized charge pumped during one period of the adiabatic drive. Analogously, there is one-to-one correspondence between a three-dimensional N -band topological insulator and certain two-dimensional adiabatic pumps: the quantized magnetoelectric polarizability coefficient of the three-dimensional bulk translates

¹ The magnetoelectric polarizability tensor is isotropic if the contributions from all the bands are considered, see [93].

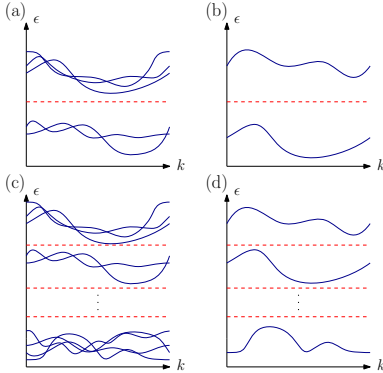


Figure 5.1: The band structure of a band insulator, where the existence of a single band gap is guaranteed (a). The same as in the panel (a) for the case of two bands (b). The band insulator can have $N - 1$ band gaps that divide the bands into N disjoint sets (c). The same as in the panel (c) for the case when each of N sets contains exactly one band (d).

into the quantized orbital magnetization of the two-dimensional bulk of the pump, while the surface Chern number translates into the edge Thouless pump. We explicitly construct one such two-dimensional N -band Hopf pump which happens to also represent an anomalous Floquet insulator (AFI) [54]. Unlike Floquet insulators, where the condition of the gap in the quasienergy spectrum is difficult to verify experimentally, the requirements of N -band Hopf insulators are experimentally accessible.

The remaining of the chapter is organized as follows. In Sec. 5.2 we review the definition and the classification of Hopf insulators. Sec. 5.3 considers N -band Hopf insulators and derives their classification and topological invariant. The bulk-boundary correspondence for N -band Hopf insulators is formulated in Sec. 5.4. In Sec. 5.5, we consider a two-dimensional N -band Hopf pump and discuss its orbital magnetization. Examples of both three-dimensional Hopf insulator and two-dimensional N -band Hopf pump with $N = 2$ and $N = 3$ can be found in Sec. 5.6.

5.2 HOPF INSULATOR

Consider a three-dimensional, gapped 2-band Bloch Hamiltonian $h_{\vec{k}}$. Assuming that the two bands are “flattened” such that the Bloch eigenvalues become ± 1 , we write

$$h_{\vec{k}} = U_{\vec{k}} \sigma_3 U_{\vec{k}}^\dagger, \quad (5.1)$$

where σ_3 is Pauli matrix and $U_{\vec{k}} \in SU(2)$. At each \vec{k} -point in the Brillouin zone (BZ), $h_{\vec{k}}$ can be seen as an element of the quotient group $SU(2)/U(1)$, where $U(1) \in SU(2)$ describes gauge transformation that changes the relative phase between the two Bloch eigenvectors. The group $SU(2)/U(1)$ is isomorphic to 2-sphere S^2 , hence $h_{\vec{k}}$ is seen as a map from BZ (3-torus T^3) to S^2 : $h_{\vec{k}} : T^3 \rightarrow S^2$. This map is defined by the representation of the Bloch state $|u_{\vec{k}1}\rangle$ on the Bloch

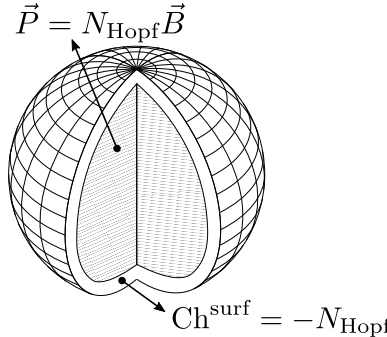


Figure 5.2: A finite N -band Hopf insulator has the bulk with the total (all the bulk bands combined) isotropic magnetoelectric polarizability coefficient equal to N_{Hopf} (where $e = h = 1$) with the gapped boundary that has Hall conductivity equal to $-N_{\text{Hopf}}$. The division between the bulk and the boundary is achieved by representing the bulk by set of exponentially localized Wannier functions.

sphere. It follows that the classification of three-dimensional 2-band Bloch Hamiltonians is given by homotopy classification of the maps $h_{\vec{k}} : T^3 \rightarrow S^2$. The complete classification of such maps was first obtained by Pointryagin [94]. There are three weak topological invariants² classifying the maps from $T^2 \rightarrow S^2$ with $T^2 \subset T^3$ —these invariants are Chern numbers in (k_x, k_y) -, (k_y, k_z) - and (k_x, k_z) -manifolds. If any of the weak invariants is non-zero, the homotopy classification of $h_{\vec{k}}$ does not have a group structure. In this article we assume that the weak invariants vanish, in which case the \mathbb{Z} classification is obtained, given by the Hopf invariant $N_{\text{Hopf}} = 2P_3^1$, with P_3^1 Abelian the third Chern-Simons form (Abelian axion coupling)

$$P_3^n = \int_{\text{BZ}} \frac{d^3k}{8\pi^2} \vec{A}_n \cdot \vec{\nabla} \times \vec{A}_n, \quad (5.2)$$

with $\vec{A}_n = i\langle u_{\vec{k}n} | \vec{\nabla}_{\vec{k}} | u_{\vec{k}n} \rangle$.

We now proceed with an alternative derivation of the above results. Vanishing of the weak invariants implies the homotopy classification of maps $T^3 \rightarrow S^2$ is given by the homotopy group $\pi_3(S^2)$ that classifies maps $S^3 \rightarrow S^2$. Instead of calculating $\pi_3(SU(2)/U(1)) = \pi_3(S^2)$, we calculate the relative homotopy group $\pi_3(SU(2), U(1))$ which is isomorphic to $\pi_3(SU(2)/U(1))$. The relative homotopy group $\pi_3(SU(2), U(1))$ classifies the maps from the 3-disc D^3 to the group $SU(2)$ with the constraint that the disc's boundary is mapped to the subgroup $U(1)$, $\partial D^3 \rightarrow U(1)$. The topological invariants for the group

² For the tenfold-way classification, the distinction between strong and weak topological invariants is related to the effects of disorder; The value of a strong topological invariant cannot change due to inclusion of translation-symmetry-breaking perturbations. On the other hand, delicate topological phases depend crucially on the presence of translational symmetry. Hence, in this chapter we use a more general definition, where the strong topological invariants are those invariants that can be defined on a d -dimensional sphere instead of BZ.

$\pi_3(SU(2), U(1))$ can be obtained from the knowledge of homotopy groups for $SU(2)$ and $U(1)$ with help of the following exact sequence [95–97]

$$\begin{aligned} \pi_3(U(1)) &\xrightarrow{i_3} \pi_3(SU(2)) \xrightarrow{i} \pi_3(SU(2), U(1)) \\ &\xrightarrow{\partial} \pi_2(U(1)) \xrightarrow{i_2} \pi_2(SU(2)). \end{aligned} \quad (5.3)$$

The exactness of the above sequence means that the image of each homomorphism is equal to the kernel of the subsequent homomorphism. The homomorphisms i_3 and i_2 are induced by the inclusion $U(1) \rightarrow SU(2)$, the homomorphism i identifies the maps from $S^3 \rightarrow SU(2)$ as maps $D^3 \rightarrow SU(2)$ where the boundary ∂D^3 is mapped to the identity element of the group $SU(2)$. Lastly, the boundary homomorphism ∂ restricts the map $D^3 \rightarrow SU(2)$ to its boundary map $\partial D^3 = S^2 \rightarrow U(1)$ which is classified by the group $\pi_2(U(1))$. In this particular case the groups $\pi_3(U(1))$ and $\pi_2(U(1))$ are trivial, hence the exactness of the sequence (5.3) implies

$$\pi_3(SU(2), U(1)) = \pi_3(SU(2)) = \mathbb{Z}. \quad (5.4)$$

The topological invariant for the homotopy group $\pi_3(SU(2))$ is the third winding number $W_3[U_{\vec{k}}]$, $U_{\vec{k}} \in SU(2)$

$$W_3[U_{\vec{k}}] = \int_{\text{BZ}} \frac{d^3 k}{8\pi^2} \text{Tr} \left(U_{\vec{k}}^\dagger \partial_{k_x} U_{\vec{k}} [U_{\vec{k}}^\dagger \partial_{k_y} U_{\vec{k}}, U_{\vec{k}}^\dagger \partial_{k_z} U_{\vec{k}}] \right), \quad (5.5)$$

where $[A, B]$ denotes the commutator. Finally, the isomorphism between the groups $\pi_3(SU(2), U(1))$ and $\pi_3(SU(2)/U(1))$ implies that there is a relation between the winding number (5.5) and the Hopf invariant (5.2). Indeed, the following relation holds

$$N_{\text{Hopf}} = W_3[U_{\vec{k}}] = P_3^1 + P_3^2 = 2P_3^1 = N_{\text{Hopf}}, \quad (5.6)$$

where $|u_{\vec{k}1}\rangle$ and $|u_{\vec{k}2}\rangle$ are two Bloch eigenvectors that define $P_3^{1,2}$ via Eq. (5.2), and $U_{\vec{k}} : T^3 \rightarrow SU(2)$ is defined in Eq. (5.1). We now derive the relation (5.6) following closely the derivation presented in [98]. We denote the set of orbitals in the unit cell by $\{|1\rangle, |2\rangle\}$, and the unitary matrix transforming this basis to the Bloch eigenvectors $\{|u_{\vec{k}1}\rangle, |u_{\vec{k},2}\rangle\}$ by $U_{\vec{k}}$, i.e., $|u_{\vec{k}a}\rangle = U_{\vec{k}}|a\rangle$, with $a = 1, 2$. The winding number (5.5) of the unitary matrix $U_{\vec{k}}$ can be written in the following form

$$W_3[U_{\vec{k}}] = \int_{\text{BZ}} \frac{d^3 k}{24\pi^2} \epsilon^{ijk} \sum_{a,b,c,d} U_{ab}^\dagger \partial_i U_{bc} \partial_j U_{cd}^\dagger \partial_k U_{da}, \quad (5.7)$$

where indices i and j run over k_x, k_y, k_z , whereas a, b, c, d run over the two band indices, and the summation over repeated indices is assumed. The matrix elements of the unitary $U_{\vec{k}}$ are defined as $U_{ab}(\vec{k}) = \langle a|U_{\vec{k}}|b\rangle$.

$$W_3[U_{\vec{k}}] = \int_{\text{BZ}} \frac{d^3 k}{24\pi^2} \epsilon^{ijk} \sum_{a,b,c,d} \langle u_{\vec{k}a}|b\rangle \partial_i \langle b|u_{\vec{k}c}\rangle \partial_j \langle u_{\vec{k}c}|d\rangle \partial_k \langle d|u_{\vec{k}a}\rangle. \quad (5.8)$$

We note that the derivatives act only on the Bloch eigenstates, which leads to

$$W_3[U_{\vec{k}}] = \int_{\text{BZ}} \frac{d^3 k}{24\pi^2} \epsilon^{ijk} \sum_{a,c} \langle u_{\vec{k}a}|\partial_i u_{\vec{k}c}\rangle \langle \partial_j u_{\vec{k}c}|\partial_k u_{\vec{k}a}\rangle. \quad (5.9)$$

Taking the summation over the two bands, we obtain four terms

$$W_3[U_{\vec{k}}] = \int_{BZ} \frac{d^3k}{24\pi^2} \epsilon^{ijk} [W_1 + W_2 + W_3 + W_4], \quad (5.10)$$

where

$$\begin{cases} W_1 = u_{\vec{k}1}^\dagger \partial_i u_{\vec{k}1} \partial_j u_{\vec{k}1}^\dagger \partial_k u_{\vec{k}1}, \\ W_2 = u_{\vec{k}1}^\dagger \partial_i u_{\vec{k}2} \partial_j u_{\vec{k}2}^\dagger \partial_k u_{\vec{k}1}, \\ W_3 = u_{\vec{k}2}^\dagger \partial_i u_{\vec{k}1} \partial_j u_{\vec{k}1}^\dagger \partial_k u_{\vec{k}2}, \\ W_4 = u_{\vec{k}2}^\dagger \partial_i u_{\vec{k}2} \partial_j u_{\vec{k}2}^\dagger \partial_k u_{\vec{k}2}. \end{cases} \quad (5.11)$$

By following the procedure outlined in [98], the first and fourth terms give an equal contribution, $W_1 = W_4$, while the second and third term give also an equal contribution, $W_2 = W_3 = 2W_1$. Therefore we conclude that

$$W_3[U_{\vec{k}}] = 2 \int_{BZ} \frac{d^3k}{8\pi^2} \epsilon^{ijk} u_{\vec{k}1}^\dagger \partial_i u_{\vec{k}1} \partial_j u_{\vec{k}1}^\dagger \partial_k u_{\vec{k}1} \quad (5.12)$$

using the definition of the Berry connection, $(\vec{A}_n)_j = i\langle u_{\vec{k}n} | \partial_j u_{\vec{k}n} \rangle$, we note that $\epsilon^{ijk} (\vec{A}_n)_i \partial_j (\vec{A}_n)_k = \vec{A}_n \cdot \vec{\nabla} \times \vec{A}_n$. We finally recover the expression for Abelian third Chern-Simons form, hence we conclude that $W_3[U_{\vec{k}}] = P_3^1 + P_3^2 = 2P_3^1$ holds.

5.3 N-BAND HOPF INSULATORS

The gap of a band insulator divides the Hilbert space into two mutually orthogonal subspaces, with the projector $\mathcal{P}_{\vec{k}}$ ($\mathcal{Q}_{\vec{k}} \equiv 1 - \mathcal{P}_{\vec{k}}$) defined by occupied (empty) Bloch eigenvectors; see Fig. 5.1(a). The topological classification of band insulators is obtained by classifying the subspace $\mathcal{P}_{\vec{k}}$, or equivalently $\mathcal{Q}_{\vec{k}}$. Within the K -theory classification, the ranks of these two projectors, $\mathcal{P}_{\vec{k}}$ and $\mathcal{Q}_{\vec{k}}$, can be varied by an addition of topologically trivial bands. On the other hand, the fragile topological classification [43] allows the ranks of $\mathcal{Q}_{\vec{k}}$ to be varied while the rank of the projector $\mathcal{P}_{\vec{k}}$ is fixed. If the ranks of both $\mathcal{P}_{\vec{k}}$ and $\mathcal{Q}_{\vec{k}}$ are required to take some fixed values, as is the case for the $N = 2$ band Hopf insulator in Fig. 5.1(b), one then talks about delicate topological classification.

In this chapter we modify the classification rules by requiring not one but $N - 1$ band gaps are to be maintained, see Fig. 5.1. Such a band structure defines N projectors $\mathcal{P}_{\vec{k}n}$, $n = 1, \dots, N$, which are projectors onto the subspaces spanned by the Bloch eigenvectors with the eigenvalues laying between two neighbouring band gaps.

As in the case of a single band-gap classification, for the $(N - 1)$ band-gap classification one can apply various classification rules. The K -theoretic version of the classification, see Fig. 5.1(c), allows the rank of all projectors $\mathcal{P}_{\vec{k}n}$ to be varied by the addition of trivial bands—such classification is directly related to a single band-gap classification, see [89]. On the other hand,³ if the rank of all

³ There are more possibilities herein [99], one can define fragile classifications by allowing only certain ranks $\mathcal{P}_{\vec{k}n}^n$ to be varied, although the physical relevance of such classification schemes is unclear.

the projectors $\mathcal{P}_{\vec{k}n}$ is fixed, we refer to this classification as delicate multi-gap classification. In contrast to K -theoretic classification, the delicate multi-gap classification is not always related to delicate single-gap classification [91, 100].

Below we show that the delicate $(N - 1)$ -gap classification of the three-dimensional Bloch Hamiltonians (with vanishing Chern numbers) is \mathbb{Z} for $N \geq 2$ if $\text{rank } \mathcal{P}_{\vec{k}n} = 1$ for $n = 1, \dots, N$. Since the non-trivial topological insulators for $N = 2$ are called Hopf insulators [50], we call the non-trivial insulators for $N > 2$ N -band Hopf insulators.

The complete classification of N -band Hopf insulators goes along the lines of $N = 2$ classification of Sec. 5.2. Given N -band Bloch Hamiltonian $h_{\vec{k}}$ is flattened such that its eigenvalues are distinct integers $[1, N]$, the diagonalized Hamiltonian is written as

$$h_{\vec{k}} = U_{\vec{k}} \text{diag}(1, \dots, N) U_{\vec{k}}^\dagger, \quad (5.13)$$

where $U_{\vec{k}} \in SU(N)$ is continuous on the BZ. At each \vec{k} -point in the BZ, $h_{\vec{k}}$ is seen as an element of the group $SU(N)/U(1)^{N-1}$, where the subgroup $U(1)^{N-1} \subset SU(N)$ is generated by $U(1)$ gauge transformations of individual bands. Under the assumption of vanishing weak topological invariants, that are defined for each $\mathcal{P}_{\vec{k}n}$, the BZ can be regarded as 3-sphere S^3 . In other words, the strong classification of N -band Hopf insulators is given by the homotopy group $\pi_3(SU(N)/U(1)^{N-1})$. We proceed with help of the following isomorphism⁴

$$\pi_3(SU(N)/U(1)^{N-1}) = \pi_3(SU(N), U(1)^{N-1}), \quad (5.14)$$

where $\pi_3(X, A)$ for $A \subseteq X$ denotes the relative homotopy group introduced in the previous Section. The exact sequence, analogous to the one in Eq. (5.3), reads

$$\begin{aligned} \pi_3(U(1)^{N-1}) &\xrightarrow{i_3} \pi_3(SU(N)) \xrightarrow{i} \pi_3(SU(N), U(1)^{N-1}) \\ &\xrightarrow{\partial} \pi_2(U(1)^{N-1}) \xrightarrow{i_2} \pi_2(SU(N)), \end{aligned} \quad (5.15)$$

implying that $\pi_3(SU(N), U(1)^{N-1}) = \pi_3(SU(N))$ because the homotopy groups $\pi_3(U(1)^{N-1})$ and $\pi_2(U(1)^{N-1})$ are trivial. The topological invariant, a member of the group $\pi_3(SU(N)) = \mathbb{Z}$, is the third winding number, which provides the complete classification of N -band Hopf insulators. The advantage of our classification approach is that it gives the complete set of topological invariants that were previously not known.

The above considerations give the topological invariant of the N -band Hopf insulator

$$N_{\text{Hopf}} = W_3[U_{\vec{k}}], \quad (5.16)$$

i.e., N_{Hopf} is the third winding number of the unitary $N \times N$ matrix $U_{\vec{k}} \in SU(N)$ in Eq. (5.13). Although $U_{\vec{k}}$ explicitly depends on the choice of $U(1)$ gauge for each Bloch eigenvector, such gauge transformations cannot change the third

⁴ The group $\pi_i(X, A)$ is not isomorphic to $\pi_i(X/A)$ in general. For example, when $X = D^2$ and $A = S^1$, the group $\pi_i(D^2, S^1)$ is trivial for $i > 2$ as seen by exact sequence similar to Eq. (5.3), whereas the $\pi_i(D^2/S^1 = S^2)$ is non-trivial for infinitely many values of i . The isomorphism (5.14) follows directly from the long exact sequence for the fibration $U(1)^N \rightarrow U(N) \rightarrow U(N)/U(1)^N$.

winding number of $U_{\vec{k}}$. (This follows directly from the exact sequence (5.15), since $\text{img } i_3$ is trivial.) The following relation holds

$$N_{\text{Hopf}} = P_3 \in \mathbb{Z}, \quad (5.17)$$

where P_3 is non-Abelian third Chern-Simons form

$$P_3 = \int_{\text{BZ}} \frac{d^3 k}{8\pi^2} \text{tr} \left(\vec{\tilde{A}}_{\vec{k}} \cdot \vec{\nabla} \times \vec{\tilde{A}}_{\vec{k}} + \frac{2i}{3} \vec{\tilde{A}}_{\vec{k}} \cdot \vec{\tilde{A}}_{\vec{k}} \times \vec{\tilde{A}}_{\vec{k}} \right), \quad (5.18)$$

with $(\vec{\tilde{A}}_{\vec{k}})_{nm} = i \langle u_{\vec{k}n} | \nabla_{\vec{k}} | u_{\vec{k}m} \rangle$. To prove the relation (5.17), we note that under a gauge transformation $U_{\vec{k}}$, the non-Abelian third Chern-Simons form transforms in the following way [8]

$$P_3 \mapsto \tilde{P}_3 + W_3[U_{\vec{k}}]. \quad (5.19)$$

In the basis of orbitals of the unit cell $\{|1\rangle, \dots, |N\rangle\}$, the non-Abelian third Chern-Simons form vanishes, $\tilde{P}_3 = 0$. If we apply a gauge transformation $U_{\vec{k}}$, the new basis corresponds to the Bloch eigenvectors $\{|u_{\vec{k}1}\rangle, \dots, |u_{\vec{k}N}\rangle\}$. In this new basis, by the gauge transformation law (5.19), we have that the non-Abelian third Chern-Simons form satisfies $P_3 = W_3[U_{\vec{k}}]$, proving the relation (5.17) using Eq. (5.16).

The above topological invariant differs from the tenfold-way topological invariants, which vanish when summed over all the bands. Furthermore, for tenfold-way classification, the non-Abelian third Chern-Simons form (5.18) has an integer ambiguity which is removed by requiring N band gaps to stay open, or equivalently, requiring $|u_{\vec{k}n}\rangle$ to be continuous over the BZ for all n .

The obtained topological invariant (5.17) has a physical meaning of the isotropic magnetoelectric polarizability coefficient α of all the bulk bands combined [93, 101]. The magnetoelectric polarizability coefficient is a tensor quantity, which has two contributions: [93] a topological (isotropic) contribution is given by non-Abelian Chern-Simons form (5.18) which is equal to N_{Hopf} by virtue of Eq. (5.17), and a non-topological contribution which vanishes in the absence of unoccupied bands. Unlike the tenfold-way topological invariants which can be assigned to each band (or group of bands) separately, the above topological invariant can only be assigned to the whole band structure. Indeed, we can express the isotropic magnetoelectric polarizability coefficient α as

$$N_{\text{Hopf}} = \alpha = \sum_{n=1}^N \alpha_n, \quad (5.20)$$

where α_n is the isotropic component of the magnetoelectric polarizability tensor for the n th band. There are two contributions [93] to the magnetoelectric polarizability coefficient $\alpha_n = \alpha_n^{\text{top}} + \alpha_n^{\text{nontop}}$, where the topological piece α_n^{top} is expressed via the Abelian third Chern-Simons form (5.2) that involves only Bloch eigenvector of the n th band

$$\alpha_n^{\text{top}} = P_3^n, \quad (5.21)$$

while for the non-topological piece α_n^{nontop} , the knowledge of the whole band structure is required [93]. We note that, generally, a non-quantized value of $\sum_{n=1}^N \alpha_n^{\text{top}} (\sum_{n=1}^N \alpha_n^{\text{nontop}})$ cannot change upon a deformation of the Hamiltonian that maintains all $N - 1$ gaps.

5.4 BULK-BOUNDARY CORRESPONDENCE

To formulate bulk-boundary correspondence for N -band Hopf insulator, we consider slab geometry with arbitrary termination along y -direction described by the $NN_y \times NN_y$ slab Hamiltonian $h_{k_x k_z}$. We assume that all weak topological invariants (Chern numbers) vanish, hence, there exist continuous bulk Bloch eigenfunctions $|\psi_{\vec{k}n}\rangle$, $n = 1, \dots, N$, of the Hamiltonian $h_{k_x k_z}$. In other words, each bulk band can be separately ‘‘Wannierized’’: the many-body wavefunction of the fully occupied n th band can be obtained by occupying exponentially localized single-electron bulk Wannier functions (WFs) $|w_{\vec{R}n}\rangle$. The bulk WFs are obtained from continuous Bloch eigenfunctions

$$|w_{\vec{R}n}\rangle = \frac{1}{\sqrt{N_x N_y N_z}} \sum_{\vec{k}} e^{i\vec{k} \cdot \vec{R}} |\psi_{\vec{k}n}\rangle. \quad (5.22)$$

For a slab terminated in y -direction, we use hybrid bulk WFs

$$|w_{k_x R_y k_z n}\rangle = \frac{1}{\sqrt{N_x N_z}} \sum_{R_x, R_z} e^{-i(k_x R_x + k_z R_z)} |w_{\vec{R}n}\rangle. \quad (5.23)$$

The goal is to divide the slab into the three subsystems: the two surfaces and the bulk, the latter being defined by the choice of the bulk WFs, see Fig. 5.3. Using the above WFs we perform a Wannier cut [102] on all the bands⁵ to obtain the projector $\mathcal{P}_{k_x k_z}^L$ onto the two surfaces by removing the hybrid bulk WFs from the middle of the slab

$$\mathcal{P}_{k_x k_z}^L(\vec{x}', \vec{x}) = \delta_{\vec{x}' \vec{x}} - \sum_{\substack{n=1 \\ R_y=-L}}^{n=N} w_{k_x R_y k_z n}(\vec{x}')^* w_{k_x R_y k_z n}(\vec{x}), \quad (5.24)$$

which, for large enough integers N_y , L with $N_y \gg (N_y - 2L)$ and $2L < N_y$, defines the projector onto the upper surface

$$\mathcal{P}_{k_x k_z}^{\text{surf}}(\vec{x}', \vec{x}) \equiv \mathcal{P}_{k_x k_z}^L(\vec{x}', \vec{x}) \theta(y) \theta(y'), \quad (5.25)$$

where $\vec{x} = (x, y, z)$ indexes the orbitals of the slab supercell, $\theta(y)$ is the Heaviside theta function, and we assume that the $y = 0$ plane passes through the middle of the slab. The integer L should be chosen as large as possible while requiring that in the region where the bulk WFs $|w_{k_x L k_z n}\rangle$ have support, the Hamiltonian $h_{k_x k_z}$ is bulk-like. For the slab’s width much larger than the WFs’ size, the operator $\mathcal{P}_{k_x k_z}^{\text{surf}}$ is a projector. In fact, thanks to exponential localization of the bulk WFs, $(\mathcal{P}_{k_x k_z}^{\text{surf}})^2 - \mathcal{P}_{k_x k_z}^{\text{surf}}$ converges exponentially to 0 as the slab’s width is increased. Hence, the first Chern number of $\mathcal{P}_{k_x k_z}^{\text{surf}}$, denoted by Ch^{surf} , reads

$$\text{Ch}^{\text{surf}} = i \int_{\text{BZ}} \frac{dk_x dk_z}{2\pi} \text{Tr} \left(\mathcal{P}_{k_x k_z}^{\text{surf}} [\partial_{k_x} \mathcal{P}_{k_x k_z}^{\text{surf}}, \partial_{k_z} \mathcal{P}_{k_x k_z}^{\text{surf}}] \right). \quad (5.26)$$

The bulk-boundary correspondence states

$$\text{Ch}^{\text{surf}} = -N_{\text{Hopf}}. \quad (5.27)$$

⁵ Since the Wannier cut is performed on all the bands, unlike in [102], no condition on the crystal’s termination needs to be imposed, i.e., a metallic termination is allowed.

The above correspondence can be proved by noticing that Ch^{surf} cannot be changed by surface decorations since their first Chern number summed over all the bands vanishes. In the previous section we proved that N_{Hopf} is the unique bulk topological invariant of the N -band Hopf insulator, it follows that Ch^{surf} can be expressed in terms of N_{Hopf} . Hence, to prove the relation (5.27) it is sufficient to show that it holds for the generators of the N -band Hopf insulator, see Sec. 5.6. We note that compared to tenfold-way classification, where the topological classification group structure is given by the direct sum of two Hamiltonians, the group structure of the classification of the N -band Hopf insulator is obtained by concatenation of the BZs of the two band structures. Hence, whereas for tenfold-way topological phases there is a single generator for the classification group \mathbb{Z} , for the N -band Hopf insulator there is one generator for each N . Alternatively, the relation (5.27) follows from Eq. (5.17) and “Surface theorem for axion coupling” of [103]. The correspondence (5.27), for $N = 2$, is a generalization of recently discussed bulk-boundary correspondence for the Hopf insulator [49, 104].

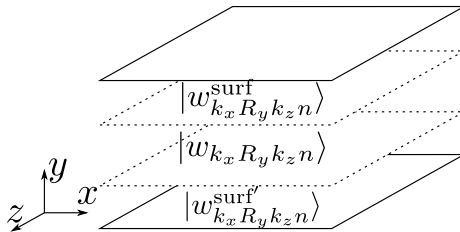


Figure 5.3: The Hilbert space, spanned by the orbitals of the slab’s supercell, is divided at each (k_x, k_z) -point into the three mutually orthogonal subspaces corresponding to the bulk and the two surfaces. The bulk hybrid WFs $|w_{k_x R_y k_z n}\rangle$ are continuous in the (k_x, k_z) -space. On the other hand, for a non-trivial N -band Hopf insulator, there is an obstruction in finding continuous surface WFs $|w_{k_x R_y k_z n}^{\text{surf}}\rangle$.

The above procedure divides a finite sample of the N -band Hopf insulator into bulk and surface subsystems. It is important to note that such division is not unique. Choosing different bulk WFs or different assignment of the bulk WFs to their home unit cell yields different bulk and surface subsystems.⁶ Despite this non-uniqueness, a finite sample of the N -band Hopf insulator can be seen to consist of the bulk, with isotropic magnetoelectric polarizability coefficient [93] being quantized to $\alpha = N_{\text{Hopf}}$, “wrapped” into a sheet of a Chern insulator with the total Chern number being equal to $-N_{\text{Hopf}}$, see Fig. 5.2. (To define the Chern number one considers torus geometry of the boundary.) Clearly, such a “wrapping paper” cannot exist as a standalone object since the total Chern number (of all the bands) of a two-dimensional system needs to vanish.

Recently [51], the concept of multicellularity for band insulators was discussed. A band insulator is said to be multicellular if it can be Wannierized and if it is not possible to deform the band structure such that all the bulk WFs are localized within a single unit cell. The examples of multicellular band

⁶ A direct consequence of this non-uniqueness is inability to uniquely define edge polarization and quadrupole moment of two-dimensional insulators [102, 105]

structures include the $N = 2$ Hopf insulator and certain insulators constrained by crystalline symmetries. The bulk-boundary correspondence (5.27) implies that the N -band Hopf insulator is a multicellular phase: if all the bulk WFs are to be localized within a single unit cell, the resulting projector onto the upper surface (5.25) would be (k_x, k_z) -independent and the surface Chern number (5.26) would vanish.

If a finite N -band Hopf insulator, fully filled with electrons, is placed into an external magnetic field, the bulk gets polarized due to the isotropic magnetoelectric effect, $\vec{P} = \alpha \vec{B} = N_{\text{Hopf}} \vec{B}$. This polarization does not result in an excess charge density at the boundary, because the excess charge is compensated by the surface Chern insulator, which is a direct consequence of the Streda formula [106] when applied to the surface subsystem. Hence, we see that the two quantized effects, one in the bulk and the other on the boundary, mutually cancel. It is easy to understand this cancellation by noticing that the many-body wavefunction of a fully occupied slab is independent of the Hamiltonian. Therefore, the fully occupied slab exhibits no magnetoelectric effect, implying that the bulk and the boundary magnetoelectric effects mutually cancel. In order to measure a quantized effect, one needs to drive the system into a non-equilibrium state where either the boundary or the bulk subsystem are fully filled with electrons, but not both.

5.5 ORBITAL MAGNETIZATION

Every three-dimensional Bloch Hamiltonian $h_{\vec{k}}$ of a band insulator defines a periodic adiabatic pump of a two-dimensional band structure, and vice versa. The substitution $k_z \rightarrow 2\pi t/T$ gives the Hamiltonian of the two-dimensional adiabatic pump $h_{k_x k_y t}$ corresponding to the three-dimensional Hamiltonian $h_{\vec{k}}$. As we discuss below, this viewpoint sheds light on the link between the N -band Hopf insulators, introduced in this chapter, and the recently studied anomalous Floquet insulator [54].

We start by applying the bulk-boundary correspondence (5.27) to the N -band Hopf pump $h_{k_x k_y t}$. Consider a ribbon $h_{k_x t}^{\text{ribb}}$ consisting of N_y unit cells in y -direction. Similar to Eq. (5.25), we divide the ribbon-supercell Hilbert space into the two edge and the bulk subspaces

$$\mathbb{I}_{NN_y \times NN_y} = \mathcal{P}_{k_x t}^{\text{edge}} + \mathcal{P}_{k_x t}^{\text{bulk}} + \mathcal{P}_{k_x t}^{\text{edge}'}, \quad (5.28)$$

where the right-hand side is the sum of three mutually orthogonal projectors. Importantly, the $\mathcal{P}_{k_x t}^{\text{bulk}}$ projects onto the space spanned by the bulk hybrid WFs $|w_{k_x R_y tn}\rangle$ with $R_y \in [-L, L]$, and the spaces onto which $\mathcal{P}_{k_x t}^{\text{edge}}$ and $\mathcal{P}_{k_x t}^{\text{edge}'}$ project do not contain the orbitals from the middle of the ribbon. This way, at each (k_x, t) -point the ribbon is divided into the bulk and the two edge subsystems, see Fig. 5.4. The WFs in the bulk subsystem can be chosen to be periodic,

$$|w_{k_x R_y Tn}\rangle = |w_{k_x R_y 0n}\rangle, \quad (5.29)$$

i.e., the bulk WFs return to their initial state after one period. On the other hand, from the bulk-boundary correspondence (5.27), it follows that the upper edge $\mathcal{P}_{k_x t}^{\text{edge}}$ has non-zero Chern number equal to N_{Hopf} . As a consequence, the

edge WF $|w_{k_x R_y 0m}^{\text{edge}}\rangle$ is shifted to $|w_{k_x R_y + N_{\text{Hopf}}; Tm}^{\text{edge}}\rangle$ for some $m \in [1, N]$.⁷ The edge subsystem acts as a Thouless pump even after considering all the bands—such a situation cannot occur for a standalone one-dimensional system.

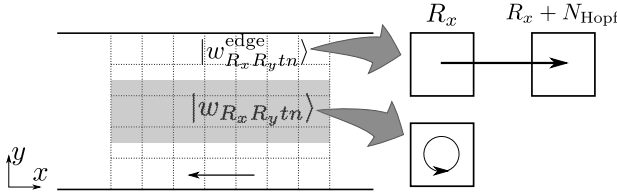


Figure 5.4: The adiabatic process of a ribbon corresponding to N -band Hopf pump. The ribbon's supercell is divided into the three regions, where the middle (gray) region is spanned by the bulk WFs. Whereas the bulk WFs perform periodic motion, some WFs of the edge subsystems get shifted to the left or right.

Let us consider a fully occupied ribbon. From the relation (5.17) and the results of [107], we have that the bulk subsystem has (geometric) orbital magnetization equal to eN_{Hopf}/T . To see this, we consider all contributions to orbital magnetization [107, 108]

$$\mathfrak{m} = \mathfrak{m}_{\text{pers}} + \mathfrak{m}^{\text{top}} + \mathfrak{m}^{\text{non-top}}, \quad (5.30)$$

where the last two terms are the topological and non-topological contribution to the geometric orbital magnetization, and the first term represents the contribution from persistent currents that may exist in the absence of adiabatic drive. Using the relation $\mathfrak{m}^{\text{top}}T = P_3$, we conclude that the topological contribution to orbital magnetization is quantized and equal to N_{Hopf}/T , see Eq. (5.17). On the other hand, $\mathfrak{m}^{\text{non-top}} = 0$ when all the bands are occupied. Finally, the contribution from persistent currents has to vanish for a fully filled system: such contribution is given by the change of the total energy E_{tot} of the system induced by external magnetic field B perpendicular to the system, $\mathfrak{m}_{\text{pers}} = -\frac{\partial E_{\text{tot}}}{\partial B}$. It follows that $\mathfrak{m}_{\text{pers}}$ vanishes because $E_{\text{tot}} = \text{Tr}(H_B) = \text{Tr}(H_{B=0})$, since the external magnetic field only enters in non-diagonal components (in the position basis) of the Hamiltonian. Therefore, we conclude that the orbital magnetization is quantized and given by the Hopf invariant. The orbital magnetization gives rise to an edge current that exactly cancels the current pumped by the edge subsystem. Hence, the bulk and the boundary anomalies mutually cancel similar to the three-dimensional case discussed at the end of the previous Section.

In order to observe the quantized orbital magnetization, we need to prepare the ribbon at time $t = 0$ such that only the regions close to the edges are fully filled with electrons. To achieve such an initial state, we start from the fully filled band structure illustrated Fig. 5.5(a), and apply a gate voltage, such that in equilibrium, the states in the middle of the ribbon are emptied, as illustrated in Fig. 5.5(b). After the gate voltage is switched-off, the desired initial non-equilibrium state is obtained, as shown on Fig. 5.5(c). Such an initial

⁷ The more precise statement is that the total shift from all the edge bands is N_{Hopf} , i.e., the shift does not need to be carried by a single band.

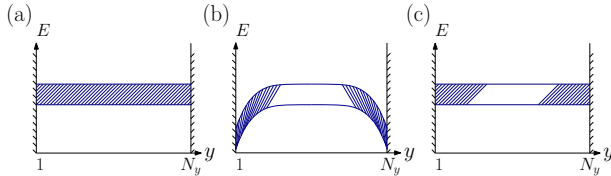


Figure 5.5: (a) Energy bands of a ribbon, finite in y -direction, as a function of y -coordinate, where all the states are fully filled with electrons. (b) After applying a gate voltage an equilibrium state is reached where the electrons from the middle of the ribbon are empty (i.e., they move to the drain gate). (c) After switching-off the gate voltage, a non-equilibrium state is obtained with the states close to the edges filled.

state will generally diffuse under the time evolution and eventually electrons leak into the bulk, in which case, as discussed above, no quantization of the orbital magnetization is expected.⁸ Hence, the quantized (geometric) orbital magnetization can be measured in the transient state where the filled regions are separated by an empty bulk. The flat band limit, see Sec. 5.6, is a special case where the diffusion coefficient is fine-tuned to zero.

The above conclusions parallel the discussion of the so-called anomalous Floquet insulator (AFI) [54]. This is not a coincidence, since in Sec. 5.6, we show that the N -band Hopf pump can, at the same time, be an AFI, although not every AFI is a N -band Hopf insulator nor vice-versa. One important difference between Floquet insulator and N -band Hopf pump is that the latter is not stable against translation-symmetry-breaking perturbations. Indeed, as we discuss in Appendix a.2, doubling of the unit cell violates the condition of having a single band between the two neighbouring band gaps.

5.6 EXAMPLES

Below, we first consider the three-dimensional Moore-Ran-Wen model [50] ($N = 2$ band Hopf insulator), that we use to illustrate the bulk-boundary correspondence of Sec. 5.4, which generalizes the approach of [49]. Furthermore, two two-dimensional examples corresponding to periodic adiabatic processes are considered, which clarify the relation between the N -band Hopf insulator and the AFI.

MOORE-RAN-WEN MODEL OF HOPF INSULATOR Here we present an example of a 2-band three-dimensional Hopf insulator, the Moore-Ran-Wen model. The Bloch Hamiltonian is defined as [50]

$$h_{k_x k_y k_z} = \vec{v} \cdot \vec{\sigma}, \quad (5.31)$$

with $v_i = \vec{z}^\dagger \sigma_i \vec{z}$, where $\vec{z} = (z_1, z_2)^T$, with $z_1 = \sin(k_x) + i \sin(k_y)$ and $z_2 = \sin(k_z) + i[\cos(k_x) + \cos(k_y) + \cos(k_z) - \frac{3}{2}]$. The above model (5.31) has $N_{\text{Hopf}} = 1$. In the following we apply the procedure described in Sec. 5.4 to obtain the surface Chern number (5.26) for a three-dimensional lattice

⁸ Such ‘leakage’ occurs also for time-independent band insulators”” [105]

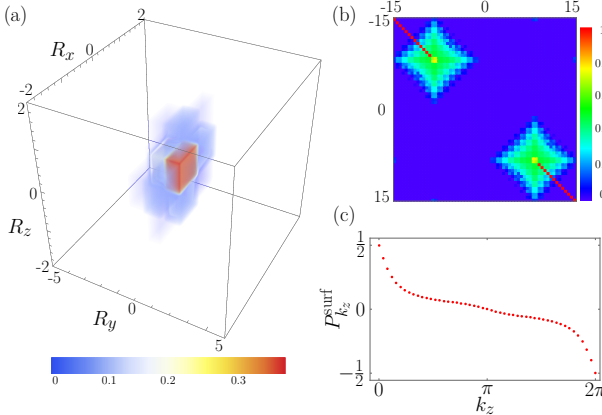


Figure 5.6: (a) The charge density $|w_{(0,0,0)}|^2$ of the Wannier function $|w_{(0,0,0)}\rangle$ localized at the center of the lattice, for $N_y = 11$, $N_x = N_z = 5$. (b) The absolute value of the matrix elements of the projector in Eq. (5.24), $|\mathcal{P}_{k_x k_z}^L(\vec{x}, \vec{x}')|$, for $N_y = 31$ with cutoff $L = 8$. (c) The surface polarization along x -direction $P_{k_z}^{\text{surf}}$ for k_z between 0 and 2π for $N_y = 31$ with cutoff $L = 8$.

with $N_x \times N_y \times N_z$ unit cells. The two normalized eigenvectors of the Bloch Hamiltonian (5.31) are

$$\begin{aligned} |u_{\vec{k}1}\rangle &= |\vec{z}|^{-1}(z_1, z_2)^T, \\ |u_{\vec{k}2}\rangle &= |\vec{z}|^{-1}(z_2^*, -z_1^*)^T, \end{aligned} \quad (5.32)$$

which are continuous functions of \vec{k} . We extend these two Bloch eigenvectors to the whole lattice by defining $\psi_{\vec{k}n}(\vec{x}) = e^{-i\vec{k} \cdot \vec{x}} u_{\vec{k}n}(\vec{x})$.

The WFs $|w_{(0,0,0)n}\rangle$, $n = 1, 2$, with the home unit cell at $\vec{R} = (0, 0, 0)$ are given by Eq. (5.22) and shown in Fig. 5.6(a). For arbitrary $\vec{R} = (x, y, z)^T$, the WFs are obtained from the components $w_{(0,0,0)}(\vec{x})$ of $|w_{(0,0,0)}\rangle$

$$w_{\vec{R}n}(\vec{x}) = w_{(0,0,0)n}(\vec{x} - \vec{R}). \quad (5.33)$$

We use the above choice of the bulk WFs to define the bulk subsystem. To this end, we perform the Fourier transform in x - and y -directions to obtain the hybrid bulk WFs $|w_{k_x R_y k_z n}\rangle$. Considering only the components $w_{k_x R_y k_z n}(\vec{x})$ of the hybrid bulk WFs with \vec{x} in a supercell, we obtain the $2N_y \times 2N_y$ projector $|w_{k_x R_y k_z n}\rangle \langle w_{k_x R_y k_z n}|$. From Eq. (5.24) we compute the projector $\mathcal{P}_{k_x k_z}^L$ onto the two surfaces. As shown in Fig. 5.6(b), after removing the hybrid bulk WFs assigned to the units cells at $R_y \in [-8, 8]$, the two surfaces do not overlap and $\mathcal{P}_{k_x k_z}^L$ is obtained from the upper-left block of the matrix $\mathcal{P}_{k_x k_z}^L$. The surface Chern number can be obtained from the k_z -dependent surface polarization of all the bands

$$P_{k_z}^{\text{surf}} = -\frac{i}{2\pi} \ln \det' \prod_{k_x} \mathcal{P}_{k_x k_z}^{\text{surf}}, \quad (5.34)$$

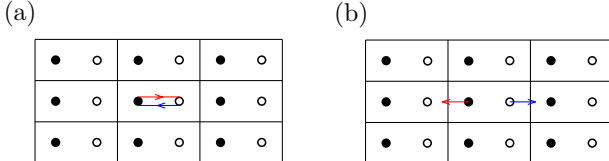


Figure 5.7: Two different adiabatic processes. The full and empty dots denote $|\vec{R}1\rangle$ and $|\vec{R}2\rangle$ orbitals. If the orbital $|\vec{R}1\rangle$ is occupied, the electron is adiabatically transferred (red arrow) to the orbital $|\vec{R}2\rangle$, see Eq. (5.35). At the end of such process the orbital $|\vec{R}1\rangle$ is empty while the orbital $|\vec{R}2\rangle$ is occupied. The very same adiabatic process (a) transfers the electron from the orbital $|\vec{R}2\rangle$ to the orbital $|\vec{R}1\rangle$ as indicated by blue arrow. The second adiabatic process corresponds to an incomplete transfer between the two orbitals (b). In that case the final occupied states is superposition orbitals $|\vec{R}1\rangle$ and $|\vec{R}2\rangle$.

where $\det'(X)$ denotes the product of the non-zero eigenvalues of the matrix X . The surface Chern number Ch^{surf} implies that the surface polarization $P_{k_z}^{\text{surf}}$ is not continuous as functions of k_z but jumps by Ch^{surf} . The winding of $P_{k_z}^{\text{surf}}$ is shown in Fig. 5.6(c), where the surface polarization winds once, implying that $\text{Ch}^{\text{surf}} = -1$.

TWO-DIMENSIONAL HOPF PUMPS Here we present examples of $N = 2$ and $N = 3$ Hopf pumps. The adiabatic evolution $h_{k_x k_y t}$ is piecewise defined, where each time-segment describes an adiabatic transfer of an electron between two selected orbitals of the two-dimensional square lattice.

The models considered in this subsection are most easily specified pictorially. In Fig. 5.7 we consider adiabatic process in a system with 2-sites per unit cell. At $t = 0$, the orbitals $|\vec{R}1\rangle$ (black dots) have negative energy whereas the orbitals $|\vec{R}2\rangle$ (empty dots) have positive energy (see Fig. 5.7). We consider the following “building-block” adiabatic process

$$h_t = Be^{-i\sigma_2 \pi t/T} \sigma_3 e^{i\sigma_2 \pi t/T}, \quad (5.35)$$

where the Pauli matrices act in the space spanned by the two orbitals. For the initial state $|\vec{R}1\rangle$, the adiabatic process is depicted in Fig. 5.7(a) by the red arrow. The evolution of the excited state $|\vec{R}2\rangle$ is shown in Fig. 5.7(a) with the blue arrow. Lastly, one can stop the above adiabatic process at times $t < T$, in which case the charge transfer between the sites $|\vec{R}1\rangle$ and $|\vec{R}2\rangle$ is incomplete. The final state is then a superposition of $|\vec{R}1\rangle$ and $|\vec{R}2\rangle$, as shown in Fig. 5.7(b). The pictorial representation of the adiabatic process consists of oriented line segments. The start (end) point of a line segment corresponds to the initial (final) state. Below we consider the adiabatic processes where the end points of the line segments lie either on the lattice sites or on the line segment connecting the two neighbouring lattice sites. In the latter case, the initial (final) state is the superposition of the two orbitals located at these two neighbouring sites. In the following, the number of arrows enumerates the time-segments, for example, “ \rightarrow ” describes the first segment, “ $\rightarrow\rightarrow$ ” the second etc. The two examples that follow consider translationally invariant systems,

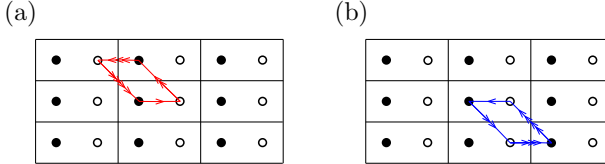


Figure 5.8: Two level periodic drive made of 4 steps of equal duration. Panel (a) shows adiabatic evolution for the initial states $|1\rangle$. The same as the panel (a) for the initial state $|2\rangle$ (b).

hence the adiabatic process (5.35) is extended in a translationally-symmetric manner to the whole two-dimensional lattice.

$N = 2$ BAND HOPF PUMP Here, we consider a periodically driven system with two states per unit cell, labeled by $\{|\vec{R}1\rangle, |\vec{R}2\rangle\}$, where the vector \vec{R} belongs to the square two-dimensional lattice. The driving protocol is of period T and is made of 4 steps of equal duration $\frac{T}{4}$, see Fig. 5.8. At each of those steps, the Hamiltonian reads

$$h_{k_x k_y t} = \mathcal{U}_{k_x k_y t}^\dagger e^{-2\pi i \sigma_2 t/T} B \sigma_3 e^{2\pi i \sigma_2 t/T} \mathcal{U}_{k_x k_y t}, \quad (5.36)$$

with

$$\mathcal{U}_{k_x k_y t} = \begin{cases} \sigma_0 & t \in [0, \frac{T}{4}), \\ \text{diag}(1, e^{-ik_y}) & t \in [\frac{T}{4}, \frac{T}{2}), \\ \text{diag}(e^{ik_x}, 1) & t \in [\frac{T}{2}, \frac{3T}{4}), \\ \text{diag}(1, e^{-i(k_x - k_y)}) & t \in [\frac{3T}{4}, T), \end{cases} \quad (5.37)$$

where the Pauli matrices σ_i act on the space spanned by the two orbitals in the unit cell. This two-band Hamiltonian can equivalently be written as the Hamiltonian of a spin in a time- and momentum-dependent magnetic field, $h_{k_x k_y t} = \vec{B}_{k_x k_y t} \cdot \vec{\sigma}$. Therefore, the unitary transformation in Eq. (5.1) is given by

$$U_{k_x k_y t} = e^{-2\pi i \vec{n}_{k_x k_y t} \cdot \vec{\sigma} t/T}, \quad (5.38)$$

where $\hat{n}_{k_x k_y t}$ is the unit vector along the $\vec{B}_{k_x k_y t} \times \hat{e}_z$ vector. The straightforward calculation gives

$$N_{\text{Hopf}} = W_3[e^{-2\pi i \vec{n}_{k_x k_y t} \cdot \vec{\sigma} t/T}] = 1. \quad (5.39)$$

In other words, the adiabatic process (5.36) is non-trivial $N = 2$ Hopf pump. Using the Bloch eigenvectors

$$|u_{k_x k_y tn}\rangle = U_{k_x k_y t}|n\rangle, \quad (5.40)$$

with $n = 1, 2$, we find that the Berry connection $A_{kt}^n = A_t^n$ depends only on time and the Chern-Simons 3-form is given by the area enclosed by the electron

$$P_3^n = \frac{1}{2} \int_0^T dt \vec{A}_t^n \times \partial_t \vec{A}_t^n = \frac{1}{2}. \quad (5.41)$$

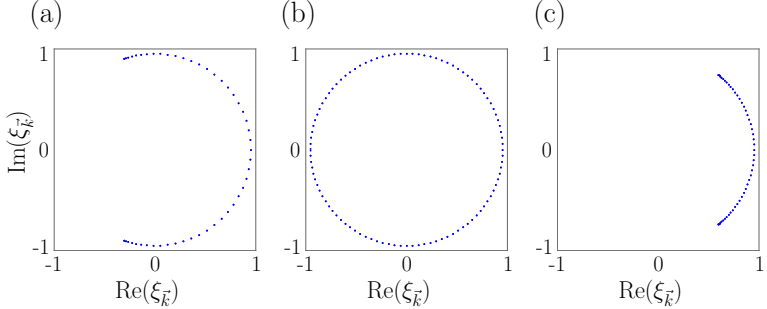


Figure 5.9: The spectrum $\xi_{\vec{k}}$ of the 1-cycle unitary operator $U_{k_x k_y T}^F$ defined in Eq. (5.42) for different values of BT . (a) $BT = 3$. (b) $BT = 5$, around which the quasienergy gap closes. (c) $BT = 9$, after reopening of the quasienergy gap.

Therefore the two Chern-Simons 3-forms sum up to 1, confirming the validity of the relation (5.6).

We now show that the time-dependent Hamiltonian (5.36) is at the same time an AFI. The time-evolution unitary $U_{k_x k_y t}^F$ during each of the four segments is readily obtained as

$$U_{k_x k_y t}^F = e^{-2\pi i \hat{n}_{k_x k_y t} \cdot \vec{\sigma}(t-t_0)/T} e^{-i(BT\sigma_3 - 2\pi \hat{n}_{k_x k_y t} \cdot \vec{\sigma})(t-t_0)/T}. \quad (5.42)$$

In the adiabatic limit, $BT \gg 1$, the solution simplifies to

$$U_{k_x k_y t}^F = e^{-2\pi i \hat{n}_{k_x k_y t} \cdot \vec{\sigma}(t-t_0)/T} e^{-iB\sigma_3(t-t_0)}. \quad (5.43)$$

As expected [109], the unitary $U_{k_x k_y t}^F$ differs from the one in Eq. (5.38) only by a dynamical phase. Since in the adiabatic limit, $U_{k_x k_y T}^F = e^{-iBT\sigma_3}$, we conclude that the model (5.36) corresponds to Floquet insulator, which remains to hold as long as $BT \sim 5$, see Fig. 5.9. Choosing BT to be integer multiple of 2π , the relation $U_{k_x k_y T}^F = \sigma_0$ holds, and we find that

$$W_3[U_{k_x k_y t}^F] = N_{\text{Hopf}} = 1, \quad (5.44)$$

i.e., the time-dependent Hamiltonian (5.36) describes anomalous Floquet insulator when $BT \sim 5$. See Appendix a.1 for details on the computation of $W_3[U_{k_x k_y t}^F]$.

Lastly, we want to verify the bulk-boundary correspondence (5.27), by computing explicitly the edge Chern number (5.26). We impose open boundary conditions in the y -direction, and for concreteness take 4 layers in this direction, which defines the ribbon supercell of 8 orbitals $|n\rangle$, $n = 1, \dots, 8$; see Fig. 5.10. We note that we can consider such a narrow ribbon because in this model the

WFs are highly localized. The WFs $|w_{R_x R_y tn}\rangle$ take the following form in the bulk

$$|w_{R_x R_y t1}\rangle = \begin{cases} \cos(t_0)|\vec{R}1\rangle - \sin(t_0)|\vec{R}2\rangle, \\ -\cos(t_{\frac{1}{4}})|\vec{R}2\rangle - \sin(t_{\frac{1}{4}})|\vec{R} + \vec{a}_y 1\rangle, \\ -\cos(t_{\frac{1}{2}})|\vec{R} + \vec{a}_y 1\rangle + \sin(t_{\frac{1}{2}})|\vec{R} + \vec{a}_y - \vec{a}_x 2\rangle, \\ \cos(t_{\frac{3}{4}})|\vec{R}\vec{a}_y - \vec{a}_x 2\rangle + \sin(t_{\frac{3}{4}})|\vec{R}1\rangle, \end{cases} \quad (5.45)$$

$$|w_{R_x R_y t2}\rangle = \begin{cases} \cos(t_0)|\vec{R}2\rangle + \sin(t_0)|\vec{R}1\rangle, \\ \cos(t_{\frac{1}{4}})|\vec{R}1\rangle - \sin(t_{\frac{1}{4}})|\vec{R} - \vec{a}_y 2\rangle, \\ -\cos(t_{\frac{1}{2}})|\vec{R} - \vec{a}_y 2\rangle - \sin(t_{\frac{1}{2}})|\vec{R} - \vec{a}_y + \vec{a}_x 1\rangle, \\ -\cos(t_{\frac{3}{4}})|\vec{R} - \vec{a}_y + \vec{a}_x 1\rangle + \sin(t_{\frac{3}{4}})|\vec{R}2\rangle, \end{cases} \quad (5.46)$$

where we used the notation $t_n = \frac{2\pi}{T}(t - nT)$ and the four expressions for the bulk WFs correspond to the four time-segments as in Eq. (5.37). The Fourier transform along the x -direction gives the hybrid bulk WFs $|w_{k_x R_y tn}\rangle$, that are used to compute the edge projector $\mathcal{P}_{k_x t}^{\text{edge}}$ given in Eq. (5.25). We perform a Wannier cut by removing four bulk WFs from the middle of the ribbon, followed by projecting onto the upper half of the ribbon supercell. The only nonzero contributions to the edge Chern number come from the time-segments $t \in [\frac{T}{2}, T]$. For $t \in [\frac{T}{2}, \frac{3T}{4})$, $\mathcal{P}_{k_x t}^{\text{edge}} = \text{diag}(A, A)$, with

$$A = \begin{pmatrix} \sin(t_{\frac{1}{2}})^2 & e^{-ik_x} \cos(t_{\frac{1}{2}}) \sin(t_{\frac{1}{2}}) \\ e^{ik_x} \cos(t_{\frac{1}{2}}) \sin(t_{\frac{1}{2}}) & \cos(t_{\frac{1}{2}})^2 \end{pmatrix}, \quad (5.47)$$

where the basis $\{|1\rangle, |2\rangle, |3\rangle, |4\rangle\}$ has been used to write $\mathcal{P}_{k_x t}^{\text{edge}}$. In this case, we obtain that

$$\text{Tr} \left(\mathcal{P}_{k_x t}^{\text{edge}} [\partial_{k_x} \mathcal{P}_{k_x t}^{\text{edge}}, \partial_t \mathcal{P}_{k_x t}^{\text{edge}}] \right) = \frac{4\pi i}{T} \sin \left(\frac{4\pi t}{T} \right). \quad (5.48)$$

Similarly, for $t \in [\frac{3T}{4}, T)$,

$$\mathcal{P}_{k_x t}^{\text{edge}} = \begin{pmatrix} 1 & 0 & 0 & 0 \\ 0 & \sin(t_{\frac{3}{4}})^2 & -e^{ik_x} \cos(t_{\frac{3}{4}}) \sin(\frac{3}{4}) & 0 \\ 0 & -e^{-ik_x} \cos(t_{\frac{3}{4}}) \sin(t_{\frac{3}{4}}) & \cos(t_{\frac{3}{4}})^2 & 0 \\ 0 & 0 & 0 & 0 \end{pmatrix}, \quad (5.49)$$

we obtain that $\text{Tr} \left(\mathcal{P}_{k_x t}^{\text{edge}} [\partial_{k_x} \mathcal{P}_{k_x t}^{\text{edge}}, \partial_t \mathcal{P}_{k_x t}^{\text{edge}}] \right) = \frac{2\pi i}{T} \sin \left(\frac{4\pi t}{T} \right)$. Therefore $\text{Ch}^{\text{edge}} = -1$, confirming the bulk-boundary correspondence (5.27).

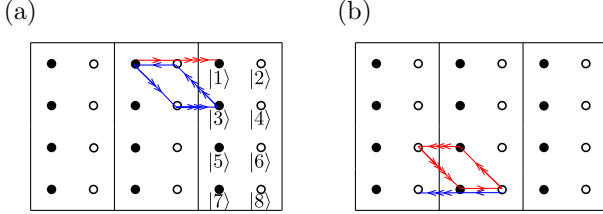


Figure 5.10: (a) Adiabatic time evolution of the upper edge subsystem $\mathcal{P}_{k_x t}^{\text{edge}}$. (b) The same as panel (a) for the lower edge subsystem $\mathcal{P}_{k_x t}^{\text{edge}}$, (b). The orbital of the ribbon supercell are labeled by $|n\rangle$, $n = 1, \dots, 8$ as shown in panel (a).

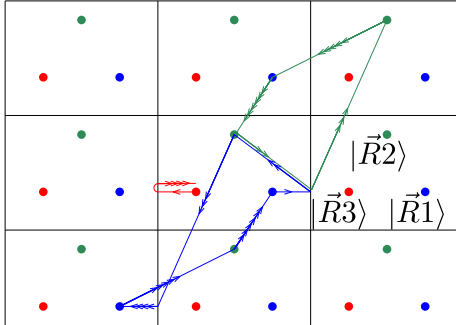


Figure 5.11: Three level periodic drive made of 6 steps of equal duration. At the first and fourth stages, we consider an incomplete rotation between the orbitals $|\vec{R}1\rangle$ and $|\vec{R} + \vec{a}_x\rangle$, such that the area enclosed by the trajectory of the third orbital is zero. This is controlled by the parameter $\delta \in [0, 1)$.

$N = 3$ BAND HOPF PUMP In this example, we consider a $N = 3$ band model that is obtained from the $N = 2$ band model, introduced in the previous subsection, after adding an additional orbital in the unit cell. Furthermore, we introduce a parameter δ in the model, such that $\delta = 0$ corresponds to the previously discussed $N = 2$ Hopf insulator with the additional orbital not being involved in the adiabatic process. This way, for $\delta = 0$ we have $P_3^1 = P_3^2 = \frac{1}{2}$, while $P_3^3 = 0$. For $\delta \neq 0$ the model is chosen to have the property $P_3^1 \neq P_3^2$ (and $P_3^3 = 0$), as we discuss below.

We consider a driven model with three sites per unit cell, labeled by $\{|\vec{R}1\rangle, |\vec{R}2\rangle, |\vec{R}3\rangle\}$. The driving protocol has the period T and is made of 6 time segments of equal duration $\frac{T}{6}$, which are illustrated in Fig. 5.11.

The eigenvalues of the Hamiltonian $h_{k_x k_y t}$ are chosen to be time-independent and take the values 1, 2, 3

$$h_{k_x k_y t} = \sum_{n=1}^3 n |u_{k_x k_y tn}\rangle \langle u_{k_x k_y tn}|, \quad (5.50)$$

where the Bloch eigenvectors $|u_{k_x k_y t n}\rangle$ can be read off from Fig. 5.11 and are explicitly given in Appendix a.3. At each of the six time segments, the adiabatic process involves only two orbitals. For example, during the first segment, see Fig. 5.11, the orbitals involved are $|\vec{R}1\rangle$ and $|(\vec{R} + \vec{a}_x)3\rangle$, where the final state is a δ -dependent superposition of these two states. Explicit calculation gives

$$\begin{cases} P_3^1 = \frac{1}{2} (1 - \sin^2 (\frac{\pi}{2} \delta)) \leq \frac{1}{2}, \\ P_3^2 = \frac{1}{2} (1 + \sin^2 (\frac{\pi}{2} \delta)) \geq \frac{1}{2}, \\ P_3^3 = 0. \end{cases} \quad (5.51)$$

The contributions P_3^1 and P_3^2 are not anymore quantized and equal if $\delta \neq 0$. However the sum turns out to be quantized and equal to 1, just like in the previous example. The winding number can be computed along the same lines as in the previous section, and is given by $N_{\text{Hopf}} = W [U_{\vec{k}t}] = 1$. Since $N_{\text{Hopf}} = \sum_{n=1}^N P_3^n$ holds, we conclude that the non-topological orbital magnetization [107] $\sum_{n=1}^N m_n^{\text{nontop}}$ vanishes for this example.

6

TOPOLOGICALLY LOCALIZED INSULATORS

6.1 INTRODUCTION

In this chapter, we introduce a new notion of topology that applies to fully localized insulators, i.e., Anderson insulator at *all* fillings, in contrast to tenfold-way topological phases which are required to be insulating only at one particular filling. In particular, we consider three-dimensional systems without time-reversal symmetry and find topologically distinct fully localized insulators that can be labelled by integers. The phase transition can occur only if the system becomes conducting at some filling, i.e., a delocalized state appears in the bulk spectrum. We refer to these topologically non-trivial phases as *topologically localized insulators* (TLIs). We show that, although all the bulk states of a TLI are exponentially localized, there is an obstruction to localizing them all the way down to an atomic limit. Importantly, electronic states with support close to the boundary carry quantized Hall conductance which can be measured in the Corbino geometry via flux insertion. Note that, for the slab geometry in Fig. 6.1(a), the boundary consists of two disjoint planes with normals $\pm\hat{e}_z$, and the Hall conductances of these two planes are quantized to the opposite value due to their opposite orientation. Furthermore, at each of these planes, topologically protected delocalized states [39] emerge and remain so under an arbitrarily strong disorder at the boundary, see Fig. 6.1(b)–(c). We conclude that the boundary of a TLI is anomalous since it cannot be realized as a two-dimensional system: a disordered two-dimensional Chern insulator can host delocalized bulk states only up to disorder strengths that do not close its mobility gap [42].

6.2 A CONCRETE MODEL OF A TLI

We construct a TLI by stacking two-dimensional layers in z -direction. We divide the Hilbert space spanned by electronic orbitals of a single layer into the blue and the orange subspaces, see Fig. 6.2(a). We require that for the blue (orange) subspace filled with electrons, the layer has Hall conductance $\sigma_{xy} = e^2/h$ ($\sigma_{xy} = -e^2/h$). Hence, not all blue (orange) orbitals in Fig. 6.2(a) can be exponentially localized. On the other hand, if we couple the blue orbitals from the layer z to the orange orbitals from the layer $z+1$, the hybridized orbitals can be all exponentially localized, as in the case of eigenstates of the following tight-binding model of a TLI

$$H = \sum_{\vec{R}\alpha, \vec{R}'\alpha'} t_{\vec{R}\alpha}^{\vec{R}'\alpha'} |\vec{R}\alpha\rangle\langle\vec{R}'\alpha'|, \quad (6.1)$$

with the hopping amplitudes and onsite potentials (for $\vec{R} = \vec{R}'$) expressed as

$$t_{\vec{R}\alpha}^{\vec{R}'\alpha'} = \sum_{\vec{R}''\alpha''} W_{\vec{R}''\alpha''} C_{\vec{R}\alpha}^{\vec{R}''\alpha''} (C_{\vec{R}'\alpha'}^{\vec{R}''\alpha''})^*. \quad (6.2)$$

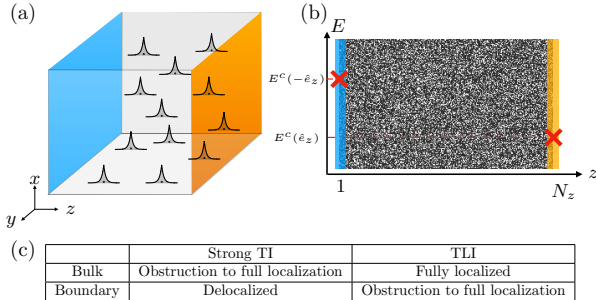


Figure 6.1: (a) TLI with $N_{\text{TLI}} = 1$ for open boundary conditions along z -direction only: all the bulk states are localized by disorder, while the two boundary surfaces (orange and blue) host delocalized states and have opposite quantized Hall conductance. (b) The energies $E^c(\pm \hat{e}_z)$ of delocalized states are not constrained by the bulk. (c) Comparison between TLIs and strong TIs. (A TI is called strong if its existence does not rely on translational symmetry.)

The atomic orbitals of the above stack of layers are denoted by $|\vec{R}\alpha\rangle$, with $\alpha \in \{1, 2\}$ an orbital degree of freedom and \vec{R} a three-dimensional cubic lattice vector. $W_{\vec{R}\alpha}$ are independent, uniformly distributed in $[-W, W]$, random real numbers. The coefficients $C_{\vec{R}'\alpha'}^{\vec{R}\alpha}$ are defined through the lattice vector basis expansion of the wavefunctions

$$|w_{\vec{R}\alpha}\rangle \equiv \mathcal{P}_z^- |\vec{R}\alpha\rangle + \mathcal{P}_{z+1}^+ |(\vec{R} + \hat{e}_z)\alpha\rangle, \quad (6.3)$$

i.e., $|w_{\vec{R}\alpha}\rangle = \sum_{\vec{R}'\alpha'} C_{\vec{R}'\alpha'}^{\vec{R}\alpha} |\vec{R}'\alpha'\rangle$, where \mathcal{P}_z^+ (\mathcal{P}_z^-) is the projector onto the blue (orange) subspace of the layer z . Such \mathcal{P}_z^+ and \mathcal{P}_z^- can be obtained as the projectors on the occupied and empty bands of a two-band (disorder-free) Chern insulator defined on layer z . It is crucial to note that $|w_{\vec{R}\alpha}\rangle$ are exponentially localized, and orthonormal $\langle w_{\vec{R}'\alpha'} | w_{\vec{R}\alpha} \rangle = \delta_{\vec{R}\vec{R}'} \delta_{\alpha\alpha'}$, leading to exponentially decaying matrix elements $t_{\vec{R}\alpha}^{\vec{R}'\alpha'}$, see Fig. 6.2(b). The exponential localization of $|w_{\vec{R}\alpha}\rangle$ follows from that of $\mathcal{P}_z^\pm |\vec{R}\alpha\rangle$ [110], whereas orthonormality can be satisfied only for the Hilbert space onto which $(\mathcal{P}_z^- + \mathcal{P}_{z+1}^+)$ projects. The states $|w_{\vec{R}\alpha}\rangle$ form a complete set of localized eigenstates of H under periodic boundary conditions (PBC).

From the above construction it is evident that for a z -terminated crystal, there are unpaired blue (orange) orbitals on the layer $z = 1$ ($z = N_z$) which, when filled with electrons, give quantized Hall conductance $\sigma_{xy} = e^2/h$ ($\sigma_{xy} = -e^2/h$), see Fig. 6.1. Additionally, if a magnetic flux quantum $\Phi_0 = h/e$ is threaded through the layers, the blue subspace of each layer expands to accommodate one more electron while the orange subspace shrinks by the same amount — this statement is known as Streda's theorem [106]. Hence, if the bulk is fully filled with electrons, the applied flux Φ_0 transfers one electron from layer z to layer $z + 1$ resulting in the bulk polarization $P_z \sim 1$. Accordingly, the corresponding component of the bulk magnetoelectric polarizability tensor is quantized, $(\alpha_{\text{ME}})_{zz} = 1$.

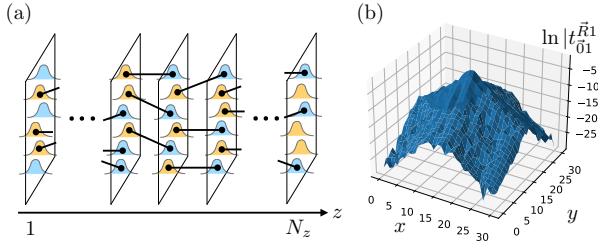


Figure 6.2: (a) TLI construction from stack of two-dimensional layers in z -direction. The Hilbert space of each layer is divided into two subspaces spanned by blue and orange orbitals: occupying only blue (orange) orbitals with electrons results in quantized Hall conductance of the layer $\sigma_{12} = e^2/h$ ($\sigma_{12} = -e^2/h$). The blue (orange) orbitals cannot all have exponential localization; Exponential localization is obtained by hybridizing differently colored orbitals from neighbouring layers. (b) Distance dependence of the hopping elements $\ln |t_{01}^{\vec{R}1}|$ of the TLI with $\vec{R} = (x, y, 0)$ for the system size $N_x = N_y = 31$, where $t_{01}^{\vec{R}1}$ is defined below Eq. (6.1). We observe an exponential decay of the hopping elements $t_{01}^{\vec{R}1}$ in all directions.

The construction presented above resembles pictorially the construction of both one-dimensional dimerized Su-Schrieffer-Heeger model [111] and Kitaev chain; Despite this similarity, we find the obtained phase to be truly three-dimensional: the quantized surface Hall conductance takes the same value for every orientation of the boundary as we demonstrate numerically further below. Furthermore, the bulk magnetoelectric polarizability tensor is found to be isotropic $\alpha_{\text{ME}} \equiv (\alpha_{\text{ME}})_{ii} = 1$. This statement is further corroborated by the existence of a truly three-dimensional bulk topological invariant.

6.3 BULK AND BOUNDARY INVARIANTS

We now define the topological invariants associated to the TLI phase for the bulk and the surface. For a bulk Hamiltonian H , with all eigenstates exponentially localized, the unitary U that diagonalizes H can be chosen such that its matrix elements are exponentially localized in the basis $|\vec{R}\alpha\rangle$

$$\langle \vec{R}'\alpha' | U | \vec{R}\alpha \rangle \sim e^{-\gamma |\vec{R}-\vec{R}'|}, \quad (6.4)$$

for some positive constant γ . More concretely, we define U as mapping localized eigenstates $|\psi_n\rangle$ of H onto atomic orbitals $|\vec{R}\alpha\rangle$, i.e., $U|\vec{R}\alpha\rangle = |\psi_{n(\vec{R},\alpha)}\rangle$, such that condition (6.4) is satisfied. The assignment defined by $n(\vec{R}, \alpha)$ is not unique¹. The bulk integer invariant can be expressed as the third winding number of the unitary U ². We recall that for translationally invariant unitaries $U = \bigoplus_{\vec{k}} U_{\vec{k}}$, in the thermodynamic limit, the third winding number is defined

$$\nu[U_{\vec{k}}] = \int_{\text{BZ}} \frac{d^3k}{8\pi^2} \text{Tr} \left(U_{\vec{k}}^\dagger \partial_{k_x} U_{\vec{k}} \left[U_{\vec{k}}^\dagger \partial_{k_y} U_{\vec{k}}, U_{\vec{k}}^\dagger \partial_{k_z} U_{\vec{k}} \right] \right), \quad (6.5)$$

¹ $U(1)$ gauge freedom and non-uniqueness of $n(\vec{R}, \alpha)$ do not affect the value of the bulk invariant.

² We note that similar invariant appears in the anomalous Floquet-Anderson insulator [52] and its multi-drive generalization [112].

while for finite systems, the integral is replaced by a sum over discrete momenta \vec{k} . For unitaries that lack translational symmetry but satisfy condition (4), the third winding number can be defined [113]

$$\nu[U] = \frac{i\pi}{3} \frac{1}{N_x N_y N_z} \epsilon^{ijk} \text{Tr} \left(U^{-1} [\hat{X}_i, U] U^{-1} [\hat{X}_j, U] U^{-1} [\hat{X}_k, U] \right), \quad (6.6)$$

where $\hat{X}_i = \sum_{\vec{R}\alpha} R_i |\vec{R}\alpha\rangle\langle\vec{R}\alpha|$ is the position operator in direction $i = 1, 2, 3$, $\vec{R} = (x, y, z)$, and summation over repeated indices is assumed. The above expression takes non-zero integer values only in the thermodynamic limit. In order to apply it to finite systems, we approximate the commutators $[X_i, U]$ by $\lfloor X_i, U \rfloor$, i.e., linear combination of unitaries with integer number of flux quanta inserted

$$\lfloor \hat{X}_i, U \rfloor = \sum_{m=1}^{N_i-1} c_m e^{2\pi im\hat{X}_i/N_i} U e^{-2\pi im\hat{X}_i/N_i}. \quad (6.7)$$

The choice of coefficients c_m , giving the correct thermodynamic-limit value of $\lfloor X_i, U \rfloor$, is not unique [42, 113]. In general, these are the coefficients of the discrete Fourier transform of a function $f(x)$ defined on the circle $[-\lfloor \frac{N_i}{2} \rfloor, \lfloor \frac{N_i}{2} \rfloor]$ that is periodic and equal to $f(x) = x$ for $x < \alpha \lesssim \lfloor \frac{N_i}{2} \rfloor$. In this chapter, we take c_m to be the Fourier coefficients of the function $\tilde{f}(x) = x$,

$$c_m = \frac{e^{2\pi im(\lfloor \frac{N_i}{2} \rfloor + 1)/N_i}}{1 - e^{2\pi im/N_i}}. \quad (6.8)$$

We stress that (6.6) is guaranteed to take integer values as long as (6.4) is satisfied [113]. This implies that the winding number is necessarily quantized for TLIs, by the exponential localization of bulk states.

In order to define the surface invariant of the TLI phase, we consider a slab geometry with the width much larger than the localization length of bulk states. Let us denote the eigenstates of H that are localized on one of the two surfaces by $\{|\psi_n^{\text{surf}}\rangle\}$, irrespective of their energy. Since all the bulk states are localized, some of these states can be safely included in the set $\{|\psi_n^{\text{surf}}\rangle\}$ without affecting the resulting surface Chern number. The Hall conductance of the system when the states $\{|\psi_n^{\text{surf}}\rangle\}$ are filled with electrons is given by the Chern number [42] $\sigma_{12}^\partial = \frac{e^2}{h} \text{Ch}[\mathcal{P}^{\text{surf}}]$, where $\mathcal{P}^{\text{surf}} = \sum_n |\psi_n^{\text{surf}}\rangle\langle\psi_n^{\text{surf}}|$. We recall that for a translationally invariant projector $\mathcal{P} = \bigoplus_{k_x k_y} \mathcal{P}_{k_x k_y}$, in the thermodynamic limit, the Chern number of the Hilbert space, onto which this projector projects, is defined [8]

$$\text{Ch}[\mathcal{P}_{k_x k_y}] = i \int_{\text{BZ}} \frac{dk_x dk_y}{2\pi} \text{Tr} \left(\mathcal{P}_{k_x k_y} [\partial_{k_x} \mathcal{P}_{k_x k_y}, \partial_{k_y} \mathcal{P}_{k_x k_y}] \right), \quad (6.9)$$

for finite systems, the above integral is replaced by a sum over discrete momenta (k_x, k_y) . When the projector \mathcal{P} lacks translational symmetry, but satisfied the condition

$$\langle \vec{R}' \alpha' | \mathcal{P} | \vec{R} \alpha \rangle \sim e^{-\gamma |\vec{R} - \vec{R}'|}, \quad (6.10)$$

for some positive γ , the Chern number in xy plane in the therodynamic limit can be defined [42]

$$\text{Ch}[\mathcal{P}] = \frac{2\pi i}{N_x N_y} \text{Tr} \left(\mathcal{P} \left[[\hat{X}_1, \mathcal{P}], [\hat{X}_2, \mathcal{P}] \right] \right). \quad (6.11)$$

For finite systems, the commutator $[\hat{X}_1, \mathcal{P}]$ is approximated by $[\hat{X}_i, P]$, see Eq. (6.7). When the matrix elements of $\mathcal{P}^{\text{surf}}$ are exponentially localized, analogous to condition (6.4) with $\mathcal{P}^{\text{surf}}$ in place of U , $\text{Ch}[\mathcal{P}^{\text{surf}}]$ is guaranteed to take integer values [42].

6.4 BULK-BOUNDARY CORRESPONDENCE

In this section we show that the third winding number for the model (1) is quantized to a non-zero value given by the Chern number of the blue subspace of a single layer. Although the model (6.1) lacks translational symmetry, its eigenstates $|w_{\vec{R}\alpha}\rangle$ are related to each other by translational symmetry. Below, we first prove the following relation for the unitary $U = \bigoplus_{\vec{k}} U_{\vec{k}}$ that diagonalizes the model (6.1)

$$U_{\vec{k}} = \mathcal{U}_{k_x k_y} \mathcal{D} \mathcal{U}_{k_x k_y}^\dagger, \quad (6.12)$$

where $\mathcal{U}_{k_x k_y}$ is a unitary that diagonalizes the Bloch Hamiltonian of the two-dimensional, two-band Chern insulator whose positive (negative) energy states define the blue (orange) subspace in Fig. 6.2(a); The matrix $\mathcal{D} = \text{diag}(e^{ik_z}, 1)$ translates the Bloch eigenstate with the positive energy by one unit cell in z -direction. The Bloch states with negative energy at layer z , and positive energy at layer $z+1$ are

$$\begin{cases} |u_{z k_x k_y}^-\rangle = a_{k_x k_y}|z1\rangle + b_{k_x k_y}|z2\rangle, \\ |u_{(z+1) k_x k_y}^+\rangle = b_{k_x k_y}^*|(z+1)1\rangle - a_{k_x k_y}^*|(z+1)2\rangle, \end{cases} \quad (6.13)$$

where we used the notation $\mathcal{U}_{k_x k_y} = \begin{pmatrix} a_{k_x k_y} & b_{k_x k_y}^* \\ b_{k_x k_y} & -a_{k_x k_y}^* \end{pmatrix}$. The two states above are discontinuous over the BZ. We consider linear combination of the two states that is continuous

$$\begin{cases} |\tilde{u}_{k_x k_y}^-\rangle = a_{k_x k_y}^*|u_{z k_x k_y}^-\rangle + b_{k_x k_y}|u_{(z+1) k_x k_y}^+\rangle, \\ |\tilde{u}_{k_x k_y}^+\rangle = b_{k_x k_y}^*|u_{z k_x k_y}^-\rangle - a_{k_x k_y}|u_{(z+1) k_x k_y}^+\rangle. \end{cases} \quad (6.14)$$

After performing the Fourier transform in the z -direction, we conclude that the continuous unitary is of the form (6.12). In order to compute the third winding of the above unitary, we use Eq. (6.5) which gives eight different terms. We can group four of them as

$$\begin{aligned} & 2i\text{Tr} \left(\text{diag}(1, 0) \left[\mathcal{U}_{k_x k_y}^\dagger (\partial_{k_x} \mathcal{U}_{k_x k_y}), \mathcal{U}_{k_x k_y}^\dagger (\partial_{k_y} \mathcal{U}_{k_x k_y}) \right] \right) \\ &= 2i \left[\mathcal{U}_{k_x k_y}^\dagger (\partial_{k_x} \mathcal{U}_{k_x k_y}), \mathcal{U}_{k_x k_y}^\dagger (\partial_{k_y} \mathcal{U}_{k_x k_y}) \right]_{00}, \end{aligned} \quad (6.15)$$

additional two terms as

$$\begin{aligned} & ie^{-ik_z} \left((\partial_{k_x} \mathcal{U}_{k_x k_y}^\dagger) \mathcal{U}_{k_x k_y} \mathcal{D} \mathcal{U}_{k_x k_y}^\dagger (\partial_{k_y} \mathcal{U}_{k_x k_y}) \right)_{00} \\ & -ie^{-ik_z} \left(\mathcal{U}_{k_x k_y}^\dagger (\partial_{k_y} \mathcal{U}_{k_x k_y}) \mathcal{D} (\partial_{k_x} \mathcal{U}_{k_x k_y}^\dagger) \mathcal{U}_{k_x k_y} \right)_{00}, \end{aligned} \quad (6.16)$$

and the two last terms are

$$\begin{aligned} & ie^{ik_z} \left((\partial_{k_x} \mathcal{U}_{k_x k_y}^\dagger) \mathcal{U}_{k_x k_y} \mathcal{D}^* \mathcal{U}_{k_x k_y}^\dagger (\partial_{k_y} \mathcal{U}_{k_x k_y}) \right)_{00} \\ & -ie^{ik_z} \left(\mathcal{U}_{k_x k_y}^\dagger (\partial_{k_y} \mathcal{U}_{k_x k_y}) \mathcal{D}^* (\partial_{k_x} \mathcal{U}_{k_x k_y}^\dagger) \mathcal{U}_{k_x k_y} \right)_{00}. \end{aligned} \quad (6.17)$$

The terms (6.15)-(6.16) cancel out after integrating over k_z from 0 to 2π . Hence, we consider only the terms in Eq. (6.15). Using the fact that the Chern number for the lower band reads

$$\text{Ch} = \int_{\text{BZ}} \frac{d^2 k}{2\pi i} \left(\langle \partial_{k_x} u_{k_x, k_y}^- | \partial_{k_y} | u_{k_x, k_y}^- \rangle - \langle \partial_{k_y} u_{k_x, k_y}^- | \partial_{k_x} | u_{k_x, k_y}^- \rangle \right) \quad (6.18)$$

together with $\mathcal{U}_{k_x k_y} |0\rangle = |u_{k_x k_y}^-\rangle$, and

$$\mathcal{U}_{k_x k_y}^\dagger (\partial_{k_x} \mathcal{U}_{k_x, k_y}) \mathcal{U}_{k_x k_y}^\dagger (\partial_{k_y} \mathcal{U}_{k_x, k_y}) = -(\partial_{k_x} \mathcal{U}_{k_x k_y}^\dagger) (\partial_{k_y} \mathcal{U}_{k_x k_y}), \quad (6.19)$$

we obtain

$$\nu[U_{\vec{k}}] = \text{Ch}. \quad (6.20)$$

We note that in the case where $\mathcal{D} = \text{diag}(e^{ik_z}, 1)$ with $l \in \mathbb{Z}$, the obtained relation becomes $\nu[U_{\vec{k}}] = l\text{Ch}$. We demonstrated that

$$\sigma_{12}^\partial = N_{\text{TLI}} \frac{e^2}{h}. \quad (6.21)$$

holds for the model above Eq. (6.1), for the z -terminated crystal. Below we demonstrate numerically that it also holds for the x - and y -terminated crystals (hard-wall boundary), as well as for a perturbed version of the model (6.1). The general proof of relation (6.21) for an arbitrary model of a TLI in the same phase as (6.1) directly follows, as the surface Hall conductance can change only if delocalized states move to the surface, which is forbidden for TLIs in the same phase as all the states in the bulk are localized.

6.5 STABILITY OF THE TLI PHASE

As discussed in Sec. 2.1, there is a finite metal to insulator transition in three dimensions, i.e., there exists a finite value of disorder strength W_c above which the mobility gap closes and all states become fully localized. In order for the TLI to be a topological phase of matter, it has to be stable under perturbations of the Hamiltonian that do not create a mobility edge in the bulk. We thus perturb the model in Eq. (6.1) by including nearest-neighbor hopping that eventually push the TLI into a metallic phase. We define $H(\lambda) = H + \lambda H'$ with

$$H' = \sum_{\langle \vec{R} \vec{R}' \rangle \alpha} \left(t_1 |\vec{R}' \alpha\rangle \langle \vec{R} \alpha| + t_2 |\vec{R}' \alpha\rangle \langle \vec{R} \bar{\alpha}| \right) + \text{h.c.}, \quad (6.22)$$

where $\bar{1} = 2$, $\bar{2} = 1$, and $\langle \vec{R}, \vec{R}' \rangle$ denotes summation over all nearest-neighbor pairs of lattice vectors. Below, we set $t_1 = 10t_2 = 1$, $W = 1$, and consider one-parameter family of the Hamiltonians $H(\lambda)$, $0 \leq \lambda \leq 1$.

As a first step, we study the metal to TLI transition by using spectral statistics. To this end, we compute the average level spacing ratio [114, 115]

$$r = \langle \langle r_n \rangle_n \rangle_W, \quad r_n = \min\{s_n, s_{n+1}\} / \max\{s_n, s_{n+1}\} \quad (6.23)$$

around the middle of the spectrum, with $s_n = E_{n+1} - E_n \geq 0$ being the level spacing and E_n , $n = 1, \dots, 2V$, the ordered eigenvalues of $H(\lambda)$. For $\lambda < \lambda_c$, r decreases with increasing system size, approaching the value $r_{\text{PE}} \approx 0.38$ of the Poisson Ensemble (PE). All eigenstates are localized in this regime. For $\lambda > \lambda_c$, r increases with increasing system size, approaching the value $r_{\text{GUE}} \approx 0.60$ of the Gaussian Unitary Ensemble (GUE). The system is in a metallic phase at half-filling (a mobility edge appears). From this one-parameter scaling, we find the metal-insulator transition at half-filling occurs at $\lambda_c \approx 0.088 \pm 0.002$, see Fig. 6.4(a).

Having established the Anderson transition at a finite value of the hopping λ_c , we now provide numerical evidence for the quantization of the bulk and surface topological invariants for any $\lambda < \lambda_c$ in the thermodynamic limit. As long as $H(\lambda)$ is in the localized phase, the condition (6.4) of exponential localization of the unitary U is satisfied and N_{TLI} and σ_{12}^∂ are guaranteed to take integer values for large enough system size [42, 113]. For the numerical calculations in this chapter, the projectors \mathcal{P}_z^\pm used for the model (1) are obtained as the projectors onto one of the two bands of the following model for Chern insulator

$$H_{2D} = \sin(k_x)\sigma_x + \sin(k_y)\sigma_y + (1 - \cos(k_x) - \cos(k_y))\sigma_z. \quad (6.24)$$

The eigenstates of the Hamiltonian (6.1), are

$$|w_{\vec{R}\alpha}\rangle = (\mathcal{P}_z^- + \mathcal{P}_{z+1}^+) (|\vec{R}\alpha\rangle + |\vec{R} + \hat{e}_z\alpha\rangle), \quad (6.25)$$

with eigenenergy $W_{\vec{R}\alpha}$. Hence,

$$H = \sum_{\vec{R}\alpha} W_{\vec{R},\alpha} |w_{\vec{R}\alpha}\rangle \langle w_{\vec{R}\alpha}| \quad (6.26)$$

In other words, the above Hamiltonian $H = U H_W U^\dagger$ is unitarily related to Hamiltonian H_W of a trivial localized insulator, with the unitary U satisfying the localization condition (4). To show the orthonormality relation $\langle w_{\vec{R}\alpha'} | w_{\vec{R}\alpha} \rangle = \delta_{\vec{R}\vec{R}'} \delta_{\alpha\alpha'}$, we denote $\vec{R} = (\vec{r}, z)$, with \vec{r} two-dimensional lattice vector, and consider the scalar product

$$\begin{aligned} \langle w_{\vec{r}'z\alpha'} | w_{\vec{r}z\alpha} \rangle &= (\langle \vec{r}'z\alpha' | + \langle \vec{r}'(z+1)\alpha' |) (\mathcal{P}_z^+ + \mathcal{P}_{z+1}^-) (\langle \vec{r}z\alpha | + \langle \vec{r}(z+1)\alpha |) \\ &= \langle \vec{r}'z\alpha' | \mathcal{P}_z^+ | \vec{r}z\alpha \rangle + \langle \vec{r}'z\alpha' | \mathcal{P}_z^- | \vec{r}z\alpha \rangle = \delta_{\vec{r}\vec{r}'} \delta_{\alpha\alpha'}, \end{aligned} \quad (6.27)$$

where we used that $\mathcal{P}_z^+ + \mathcal{P}_z^- = \mathbb{I}$ on the subspace of the Hilbert space corresponding to the layer z . For $z \neq z'$, it is sufficient to consider $z' = z + 1$,

$$\begin{aligned} \langle w_{\vec{r}(z+1)\alpha} | w_{\vec{r}z\alpha} \rangle &= (\langle \vec{r}(z+1)\alpha | + \langle \vec{r}(z+2)\alpha |) (\mathcal{P}_{z+1}^+ + \mathcal{P}_{z+2}^-) \\ &\quad \times (\mathcal{P}_z^+ + \mathcal{P}_{z+1}^-) (\langle \vec{r}z\alpha | + \langle \vec{r}(z+1)\alpha |) \\ &= \langle \vec{r}(z+1)\alpha | \mathcal{P}_{z+1}^+ \mathcal{P}_{z+2}^- | \vec{r}(z+1)\alpha \rangle = 0. \end{aligned} \quad (6.28)$$

In the above derivation, we used that $\mathcal{P}_{z+1}^+ \mathcal{P}_{z+1}^- = 0$.

Below, we explain how the unitary U_W of the perturbed model $H(\lambda)$ given by (6.22) is constructed, where we set $t_1 = 10t_2 = 1$. All $2V$ eigenstates $\{|\psi_n\rangle\}$ of $H(\lambda)$ are localized for $\lambda < \lambda_c$ in the thermodynamic limit. The unitary U_W is constructed from these localized eigenstates, after sorting them such that U_W maps $|\vec{R}\alpha\rangle$ to the two eigenstates $|\psi_{n(\vec{R},\alpha)}\rangle$, localized closest to the orbitals at $|\vec{R}\alpha\rangle$. To this end, we compute $\arg(\langle\psi_n|e^{2\pi i \hat{X}_j/N_j}|\psi_n\rangle)$, where the operators $e^{2\pi i \hat{X}_j/N_j}$ are compatible with PBC. This way, we obtain the following coordinate vectors on the 3-torus (\mathbb{T}^3)

$$\vec{v}(|\psi_n\rangle) = \left(\frac{N_x}{2\pi} \arg(\theta_{n,x}), \frac{N_y}{2\pi} \arg(\theta_{n,y}), \frac{N_z}{2\pi} \arg(\theta_{n,z}) \right)^T, \quad (6.29)$$

with

$$\theta_{n,x} = \langle\psi_n|e^{2\pi i \hat{X}/N_x}|\psi_n\rangle, \quad (6.30)$$

$$\theta_{n,y} = \langle\psi_n|e^{2\pi i \hat{Y}/N_y}|\psi_n\rangle, \quad (6.31)$$

$$\theta_{n,z} = \langle\psi_n|e^{2\pi i \hat{Z}/N_z}|\psi_n\rangle, \quad (6.32)$$

where we choose the branch cut of $\arg(\xi)$ to be $[0, \infty)$, such that $0 \leq \arg(\xi) < 2\pi$. The sorting procedure is the following: we first minimize the distance between $\vec{v}(|\psi_n\rangle)$ and $\vec{v}(|\vec{R}\alpha\rangle)$ by computing

$$\|\vec{v}(|\vec{R}\alpha\rangle) - \vec{v}(|\psi_n\rangle)\|_{\mathbb{T}^3} = \sqrt{\sum_{i=1}^3 d(R_i, (\vec{v}(|\psi_n\rangle)_i))^2} \quad (6.33)$$

where $d(x, y)$ is the following metric on the circle of radius $\frac{N_i}{2\pi}$,

$$d(x, y) = \min\{|x - y|, N_i - |x - y|\}. \quad (6.34)$$

To each orbital $|\vec{R}\alpha\rangle$, we associate eigenvector $|\psi_n\rangle$ closest to it according to the metric (6.33), unless this eigenvector is already assigned to a different lattice vector, in which case next-closest unassigned eigenvector is used. This defines a unitary U_W , $U_W|\vec{R}\alpha\rangle = |\psi_{n(\vec{R},\alpha)}\rangle$, satisfying the localization condition (4). As the metallic phase is approached, the eigenstates $|\psi_n\rangle$ become plane-wave-like, implying that $|\langle\psi_n|e^{2\pi i \hat{X}_j/N_j}|\psi_n\rangle| \rightarrow 0$. Since $\arg(\xi)$ is not well-defined at $\xi = 0$, the above procedure is not well-defined in a metallic phase. For finite systems, we compute $\langle\|\vec{v}(|\psi_n\rangle)\|_{\mathbb{T}^3}\rangle_n$, in order to define the region in parameter space in which the winding number is still well-defined. Such region exists for certain values of λ which are smaller than λ_c , see Fig. 6.3(a).

We now define the projector $\mathcal{P}_W^{\text{surf}}$ onto the surface perpendicular to z -axis. This is achieved by removing localized eigenstates $|\psi_n\rangle$ within the bulk of the system, such that the obtained projector projects onto two decoupled surfaces. We first define the set of localized eigenstates in the bulk of the slab as

$$\text{bulk}(W) = \left\{ |\psi_n\rangle, 1 - \sum_{\substack{x,y,\alpha, \\ z=[N_z/2]-L}}^{z=[N_z/2]+L} |\langle\vec{R}\alpha|\psi_n\rangle|^2 < \epsilon \right\}, \quad (6.35)$$

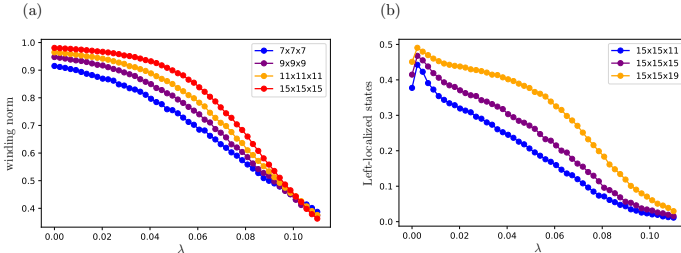


Figure 6.3: (a) The average $\langle \|\vec{v}(|\psi_n\rangle)\|_{\mathbb{T}^3} \rangle_n$ over all eigenstates as function of parameter λ , see Eq. (6.22). This quantity goes from 1, deep in the localized phase, to 0 in the metallic phase. (b) Portion of eigenstates that are localized in the left-half of the system, i.e. for $z \in \{1, \dots, \lfloor N_z/2 \rfloor\}$. This fraction goes from approximately one-half, at $\lambda = 0$, to 0, for $\lambda > \lambda_c$.

where L is some bulk cut-off that needs to be large enough such that the upper and lower boundaries are fully decoupled, and ϵ is taken to be 10^{-1} . The eigenstates that do not belong to $\text{bulk}(W)$ are assigned to one of the two boundary surfaces which defines the projector $\mathcal{P}_W^{\text{surf}}$

$$\mathcal{P}_W^{\text{surf}}(\vec{x}, \vec{x}') = \left[\delta_{\vec{x}, \vec{x}'} - \sum_{|\psi_n\rangle \in \text{bulk}(W)} \psi_n(\vec{x}')^* \psi_n(\vec{x}) \right] \times \theta(z - \lfloor N_z/2 \rfloor) \theta(z' - \lfloor N_z/2 \rfloor), \quad (6.36)$$

where $\theta(z)$ is the Heaviside theta function, and we assumed that the plane $z = \lfloor N_z/2 \rfloor$ passes through the middle of the slab. As the system approaches metallic phase, portion of surface-localized states decreases to zero, see Fig. 6.3(b).

In practice, for the system sizes we consider in Fig. 6.4, we find that the quantization of N_{TLI} and $\sigma_{12}^0 h/e^2$ breaks before the value of λ_c is reached. In Fig. 6.4, we show that the range of λ for which N_{TLI} and $\sigma_{12}^0 h/e^2$ are quantized extends as the system size is increased, showing the tendency towards the value λ_c . We note that although the tight-binding model (6.1) has exponentially decaying hopping amplitudes (Fig. 6.2), the system remains in the same phase for a finite-range hopping version of this model. We have checked this explicitly by truncating the exponential tail of the wavefunctions $|w_{\vec{R}\alpha}\rangle$, i.e., setting $C_{\vec{R}'\alpha'}^{\vec{R}\alpha} = 0$ for $|\vec{R} - \vec{R}'| > N_t$. The results for $N_t = 4$ are given by dashed curves in Fig. 6.4(c-d), from where one can conclude that the phase is stable under such truncation, although the truncation increases the localization length as indicated by less good quantization.

6.6 QUANTIZED RESPONSE

The chiral hinge states that appear in TLIs are an extrinsic signature, i.e., these can be removed by gluing Chern insulators on the corresponding faces. Without the chiral states, a non-zero quantized Hall conductance can be measured in genus-one (Corbino) geometry. Below we propose a setup, inspired by the setup of [116], that shows unique quantized signature of the bulk topology of TLIs.

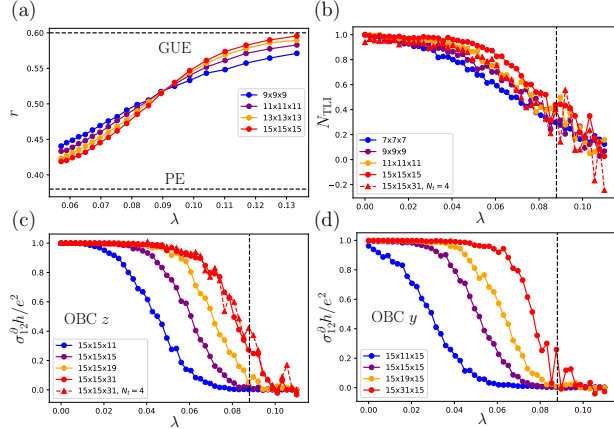


Figure 6.4: (a) Estimate of λ_c from mean level spacing ratio r as function of λ . r is computed over 500 eigenstates in the middle of the spectrum, considering 10^3 disorder realizations. (b) The winding number N_{TLI} is computed for different system sizes with increasing hopping strength λ , where the quantized plateau increases with system size for $\lambda < \lambda_c$. (c) Surface Chern number for the hard-wall termination in z -direction as function of λ . (d) Same as (c), for the termination in y -direction. No disorder averaging was performed for the winding and Chern numbers, apart from the blue curves where average was performed over 5 disorder realizations as well as the red curves in (b) and (c) for $\lambda < \lambda_c$. The dashed curves in panels c-d are for the finite-range hopping version of the model (6.1) with $N_t = 4$.

We consider the geometry of a thick Corbino disc, as shown in Fig. 6.5(a), and assume that the boundary is doped with electrons, such that *all* boundary states are occupied. In this setup, an extrinsic second-order TI [117], which consists of a trivial fully-localized bulk with a Chern insulator covering (fully or partially) its boundary, does not react to (adiabatic) time-dependent magnetic flux insertion $\Phi(t) = \Phi_0 t/T$. On the other hand, according to Laughlin argument, the boundary of TLIs pumps n_{TLI} electrons during the period T around its cross-section, see Fig. 6.5(b). In order to measure this charge pumping, a source-drain voltage, much larger than the bulk mobility gap, is applied. In the presence of such voltage, the charge is removed from the bottom surface. Hence, we expect that in the steady state the top surface remains fully occupied, while the bottom one is empty, see Fig. 6.5(b). (We neglect the effects of the charging energy.) Although such a non-uniform E_F^∂ gives rise to chiral states, these states do not connect source to drain: the quantized transfer of n_{TLI} electrons during one period T occurs via pumping of the boundary states from source to drain via the top surface. Alternatively, by optically exciting [118] the boundary of the system, one could possibly tell TLIs and extrinsic TIs apart.

6.7 RELATION TO N -BAND HOPF INSULATORS

The models of TLIs, introduced in Eq. (6.1), as well as its N -band generalization discussed in 6.4, become translationally invariant if we change $W_{\vec{R}\alpha}$ from

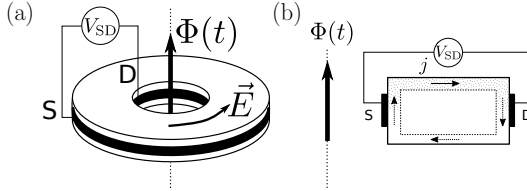


Figure 6.5: (a) A non-trivial TLI in Corbino geometry is threaded by magnetic flux $\Phi(t) = \Phi_0 t / T$, with a large source-drain voltage V_{SD} applied. (b) The cross section of the Corbino setup. As the magnetic flux is varied, the charge en_{TLI} is being pumped via the top surface (Laughlin pump). The dotted region (top surface) is filled with electrons in the steady-state, while the bulk is assumed to be empty.

being random numbers to $W_{\vec{R}\alpha} = \alpha$, with $\alpha = 1, \dots, N$. Such deformation of the model does not change the unitary (6.12); The resulting, translationally invariant model, corresponds to topologically non-trivial N -band Hopf insulator discussed in Chapter 5. Nevertheless, TLIs and N -band Hopf insulators belong to different phases of matter: the constraint of fully-localized bulk implies that TLIs are insulating at an arbitrary filling, whereas N -band Hopf insulators are insulating only at integer fillings. This distinction is important, since it implies that the boundary Fermi energy E_F^∂ of N -band Hopf cannot be varied independently of that of the bulk. As a consequence, its quantized boundary response can be measured only in a transient state.

Topology of N -band Hopf insulator crucially depends on the presence of translational symmetry. For example, inclusion of perturbations that reduce the translational symmetry down to one of its subgroups can trivialize N -band Hopf insulators. Nevertheless, we show that every N -band Hopf insulator can be deformed to a TLI phase with the same bulk topological invariant. We illustrate this point using $N = 2$ Moore-Ran-Wen model [50]. As discussed in Chapter 5, the two-band Bloch Hamiltonian is defined as

$$h_{k_x k_y k_z} = \vec{v} \cdot \vec{\sigma}, \quad (6.37)$$

with $v_i = \vec{z}^\dagger \sigma_i \vec{z}$, where $\vec{z} = (z_1, z_2)^T$, with $z_1 = \sin(k_x) + i \sin(k_y)$ and $z_2 = \sin(k_z) + i[\cos(k_x) + \cos(k_y) + \cos(k_z) - \frac{3}{2}]$. The unitary $U_{\vec{k}}$, that diagonalizes above Bloch Hamiltonian, has a non-zero third winding number $\nu[U_{\vec{k}}] = 1$. The two normalized eigenvectors of the Bloch Hamiltonian (6.37) are

$$\begin{aligned} |u_{\vec{k}1}\rangle &= |\vec{z}|^{-1} (z_1, z_2)^T, \\ |u_{\vec{k}2}\rangle &= |\vec{z}|^{-1} (z_2^*, -z_1^*)^T, \end{aligned} \quad (6.38)$$

which are continuous functions of \vec{k} . We extend these two Bloch eigenvectors to the whole lattice by defining $\psi_{\vec{k}\alpha}(\vec{x}) = e^{-i\vec{k} \cdot \vec{x}} u_{\vec{k}\alpha}(\vec{x})$. Using these two Bloch eigenvector, we define Wannier functions $|w_{(0,0,0)\alpha}\rangle$, $\alpha = 1, 2$,

$$|w_{\vec{R}\alpha}\rangle = \frac{1}{\sqrt{N_x N_y N_z}} \sum_{\vec{k}} e^{i\vec{k} \cdot \vec{R}} |\psi_{\vec{k}\alpha}\rangle. \quad (6.39)$$

We use the above Wannier functions to define the following disordered Hamiltonian

$$H_1 = \sum_{\tilde{R}\alpha} W_{\tilde{R}\alpha} |w_{\tilde{R}\alpha}\rangle \langle w_{\tilde{R}\alpha}|. \quad (6.40)$$

As the bulk Wannier functions of the Hopf insulator are exponentially localized, the unitary $U|\tilde{R}\alpha\rangle = |w_{\tilde{R}\alpha}\rangle$ satisfies localization condition (6.4) and the winding number can be computed using (6.6), $\nu[U] = \nu[U_{\tilde{k}}] = 1$. By virtue of the bulk-boundary correspondence of the Hopf insulator discussed in Chapter 5, imposing open boundary conditions in any of the three spatial directions results in surface Chern number equal to $\nu[U] = 1$.

6.8 RESONANT ENERGY MODEL OF A TLI

In the model defined in Eq. (6.1) disorder is introduced in a highly non-trivial way that is not natural to occur in experimental systems. Here we suggest an alternative model realization of a TLI can be obtained by stacking two-dimensional Chern insulators with generic disorder. We assume that each Chern insulator has two bands and a band gap Δ or 2Δ (depending on the layer) that is much larger than the band width. Disorder will broaden the “bands” to a band with Δ_b , but should be weak enough to maintain $\Delta_b \ll \Delta$. There is a single energy per band [42] where delocalized states appear. We mark these energies in blue or orange in Fig. 6.6, depending on the sign of their quantized Hall conductance. The parameters of the layers repeat with the period three, and the system is tuned such that differently colored delocalized states from neighbouring layers are on-resonance. When only resonant interlayer coupling is considered, the model is dimerized, with each dimer being a fully localized phase since it belongs to a two-dimensional unitary class and has zero Hall conductance. Hence, the delocalized states from neighbouring layers “pair annihilate”, leaving only unpaired delocalized states on the boundary of the resulting three-dimensional system. We anticipate the localization length (in the xy -plane) of each dimer to be rather large in this model due to exponential sensitivity of the localization length in two-dimensional unitary class [119]. The off-resonant interlayer coupling tends to delocalize some bulk states, but we expect for strong enough disorder and for large enough flatness ratio Δ/Δ_b (see Fig. 6.6) that the system is in the same phase as the above-mentioned dimerized limit.

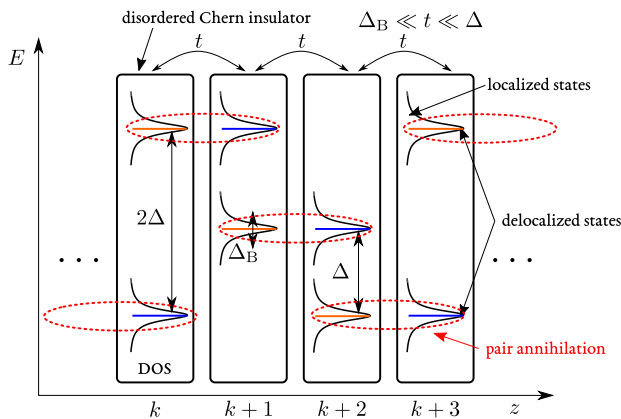


Figure 6.6: Sketch of the layer construction for the three-dimensional TLI. A stack along z -direction of two-band disordered Chern insulators, with the bandwidth Δ_B and the gap Δ or 2Δ , becomes fully localized due to interlayer coupling t such that $\Delta_B \ll t \ll \Delta$. For each layer, density of states (DOS) is shown, and the delocalized states depicted in orange (blue) carry a positive (negative) quantized Hall conductance.

Part III

NON-EQUILIBRIUM DYNAMICS OF INHOMOGENEOUS CRITICAL SYSTEMS

This part of this thesis is devoted to the study of the far from equilibrium dynamics of quantum critical systems in (1+1) dimensions. We harness the conformal symmetry of such critical systems to analytically study the non-equilibrium dynamics of their low energy theory, namely two-dimensional conformal field theories (CFTs). CFTs describe a wide range of physical systems, from integrable models, such as the Tomonaga-Luttinger liquid, to chaotic models in the limit of large central charge. In particular, we consider CFTs with spatially dependent energy densities, referred as inhomogeneous CFTs. The various non-equilibrium protocols considered in the following chapters consist in temporally varying such spatial deformations, in a periodic or quasi-periodic fashion. We find that under such driving protocols, the time evolution of (quasi-)primary fields that encode the dynamics of physical observables such as energy, entanglement entropy, can be encoded in conformal transformations. This elegant link between dynamics of conformal fields under Floquet drives and dynamical systems leads us to universal predictions on the growth of entanglement and energy after (quasi-)periodic drives, that apply to arbitrary CFTs, and only depend on their respective central charge. These thus constitute classes of non-equilibrium many-body dynamics that are non-trivial, universal, and exactly solvable.

The content of this part of the thesis is based on [23–26].

EMERGENT CURVED SPACETIME IN CRITICAL FLOQUET SYSTEMS

7.1 INTRODUCTION

In this chapter, and for the rest of the part of this thesis, we consider a (1+1)D CFT of system size L , described by coordinates (x, t) . Instead of assuming time evolution to be given by the usual Hamiltonian $H_0 = \int_0^L T_{00}(x)dx$, we consider a Hamiltonian that is generally described by

$$H = \int_0^L v(x)T_{00}(x)dx, \quad (7.1)$$

where the velocity profile $v(x)$ is a smooth function of space. This *inhomogeneous CFT* can provide the effective low energy description of various inhomogeneous models in one dimension, such as critical spin chains with smoothly varying couplings [120]. These systems have been shown to display a rich phenomenology, such as the emergence of curved light cones [121], that have recently been observed in quantum simulators [122]. Furthermore, spatially dependent couplings naturally arise in cold-atomic experiments, motivating the study of critical systems in the absence of perfect translation invariance. We aim to study the non-equilibrium dynamics of such inhomogeneous CFTs, through Floquet and quasi-periodic drives. In other words, we will consider deformations $v(x, t)$ that depend both on space and on time. For Floquet drives, we impose the additional restriction that $v(x, t + T) = v(x, t)$, in order to preserve a discrete subgroup of translation symmetry in time. In the case of quasi-periodic drive, we will consider system that have neither time or space translation symmetries, but that can be solved analytically thanks to the constraints imposed by conformal invariance. The physics of driven inhomogeneous critical system has received a lot of attention recently. The Floquet dynamics of inhomogeneous CFTs was studied in details through different approaches in [23, 25, 123–130]. In addition, the extension to quasiperiodic drives was studied in [24, 131], and the extension to fully random drives was studied in [132].

The aim of this chapter is to address the question of *how does an inhomogeneous system heat up?*, when periodically driven with such time-dependent deformations. To answer this question, we consider a two-step drive between a homogeneous Hamiltonian and a so-called $\mathfrak{sl}(2)$ Hamiltonian (see Fig. 7.1(a-b)), that both belong to a finite subalgebra of the full Virasoro algebra. This simple structure will help us to get an analytic handle on the stroboscopic time evolution of entanglement entropy, Loschmidt echo and energy density. We will analytically prove the emergence of a heating and a non-heating phase, and study the evolution of physical observables in both of these regimes. While one generically expects the heating phase of a generic driven many-body system to lead to infinite temperature state and wash away any non-trivial structure in the problem, we find a “integrable heating” in our problem, where energies increases exponentially only at a finite number of points in the system, which share growing entanglement. These points, interpreted from the curved light-cone interpretation of inhomogeneous critical systems of [121], are effective black

hole horizon that absorb all the quasiparticles emitted by the periodic drive. In particular, their associated Hawking temperature plays the role of the effective temperature of the heating problem, and determines the timescale at which quasiparticles get absorbed by the emergent Floquet horizons.

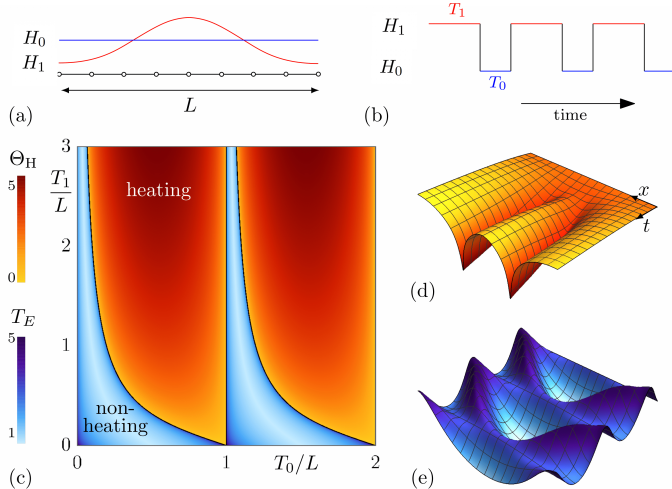


Figure 7.1: (a) Uniform and sine-square deformed Hamiltonian, here denoted by H_1 . (b) Floquet drive alternating between the uniform Hamiltonian H_0 and H_1 . (c) Phase diagram (colorbars in log scale). The heating phase is characterized by a heating rate Θ_H , a signature of emergent black holes in the effective dynamics, whose spacetime is illustrated in (d). The non-heating phase is characterized by a pseudo-periodicity T_E , with effective spacetime illustrated in (e). The phase diagram is $\frac{T_0}{L}$ periodic.

The rest of the chapter is organized as follows. We define the basic protocol, as well as the analytical methods to find the stroboscopic evolution of primary fields in 7.2. We then describe the emergence of heating and non-heating phases through evolution of various physical observables in Sec. 7.3. We interpret the heating phase as leading to emergent Floquet horizons in Sec. 7.4. We finally analyze the Floquet problem from the perspective of the effective Floquet Hamiltonian in Sec. 7.5.

7.2 STROBOSCOPIC EVOLUTION FROM MÖBIUS MAPS

In this chapter we consider two-step Floquet drives between a homogeneous CFT H_0 , for which $v = 1$, and a class of inhomogeneous Hamiltonians H_1 with deformation profile that involve a single Fourier mode,

$$v_1(x) = \sigma_0 + \sigma_+ \cos\left(\frac{2\pi x}{L}\right) + \sigma_- \sin\left(\frac{2\pi x}{L}\right). \quad (7.2)$$

These classes of deformations span a finite-dimensional algebra that is isomorphic to $\mathfrak{sl}(2)$, and will thus be dubbed $\mathfrak{sl}(2)$ deformed Hamiltonians throughout

the following chapters. A particular example of $\mathfrak{sl}(2)$ deformed Hamiltonian that has been thoroughly studied in the literature is the so-called sine-square deformed (SSD) Hamiltonian [133–138], defined with $\sigma_0 = 1$, $\sigma_+ = -1$, $\sigma_- = 0$, i.e., $v_1(x) = 2 \sin^2(\frac{\pi x}{L})$, see Fig. 7.1(a). In order to understand this algebraic structure, we use the decomposition of the chiral and antichiral parts of the stress tensor $T_{00}(x)$ in terms of Laurent modes,

$$T(z) = \sum_{n \in \mathbb{Z}} z^{-n-2} L_n, \quad \bar{T}(\bar{z}) = \sum_{n \in \mathbb{Z}} \bar{z}^{-n-2} \bar{L}_n. \quad (7.3)$$

The Laurent modes of the stress tensors, called Virasoro generators, generate the conformal algebra in two dimensions, and form the infinite dimensional Virasoro algebra (3.13). In particular, the global conformal group is generated by the subset of Virasoro generators $\{L_0, L_1, L_{-1}\}$, that form an $\mathfrak{sl}(2)$ algebra. Thus, the different Fourier modes of the deformation $v(x)$ correspond to different Virasoro modes of the stress tensor, such that

$$\begin{aligned} H &= \int_0^L v(x) T_{00}(x) dx \\ &= \frac{2\pi}{L} \left(\sigma_0 L_0 + \sum_{n=1}^{\infty} \sigma_{+,n} \frac{(L_n + L_{-n})}{2} + \sum_{n=1}^{\infty} \sigma_{-,n} \frac{(L_n - L_{-n})}{2i} \right). \end{aligned} \quad (7.4)$$

In particular, it is clear that the deformation $v_1(x)$ given by (7.2) corresponds to the Hamiltonian

$$H_1 = \frac{2\pi}{L} \left(\sigma_0 L_0 + \sigma_+ \frac{(L_1 + L_{-1})}{2} + \sigma_- \frac{(L_1 - L_{-1})}{2i} \right). \quad (7.5)$$

In order to understand the dynamics of (quasi-)primary fields under a time-evolution given by H_1 in imaginary time $\tau = it$, we express it as a contour integral on the complex plane using radial quantization, $z = e^{2\pi i(x+i\tau)/L}$,

$$H_1^{(z)} = \frac{2\pi}{L} \oint \frac{dz}{2\pi i} \left(\sigma_0 z + \frac{1}{2} (\sigma_+ - i\sigma_-) z^2 + \frac{1}{2} (\sigma_+ + i\sigma_-) \right) T(z), \quad (7.6)$$

where we omitted for simplicity the anti-chiral part. We can now perform a global conformal transformation, represented on the complex plane by a Möbius transformation $z'(z)$,

$$z' = \frac{\alpha z + \beta}{\gamma z + \delta}, \quad (7.7)$$

with [130]

$$\begin{cases} \alpha = -\frac{i}{2}, \\ \beta = \frac{\sigma_+ + i\sigma_-}{\sqrt{c^{(2)}}}, \\ \gamma = \frac{-\sqrt{c^{(2)}} + i\sigma_0}{2(\sigma_+ + i\sigma_-)}, \\ \delta = \frac{-\sigma_0 + i\sqrt{c^{(2)}}}{\sqrt{c^{(2)}}}, \end{cases}$$

where we have introduced the quadratic Casimir of $\mathfrak{sl}(2)$, $c^{(2)} = -\sigma_0^2 + \sigma_+^2 + \sigma_-^2$. Using the fact that $T(z)$ is a quasi-primary field with conformal weight 2, we find that the Hamiltonian in the coordinates $z'(z)$ is

$$H_1^{(z')} = -\frac{2\pi i \sqrt{c^{(2)}}}{L} \oint \frac{dz}{2\pi i} z' T(z'). \quad (7.8)$$

This change of variable essentially flattened the inhomogeneous Hamiltonian H_1 , and brought it to the form of the uniform Hamiltonian H_0 in new coordinates $z'(z)$. Thus, the imaginary time evolution of an arbitrary primary field $\Phi(z', \bar{z}')$ of conformal weight (h, \bar{h}) in these coordinates is given by

$$e^{H_1^{(z')} \tau} \Phi(z', \bar{z}') e^{-H_1^{(z')} \tau} = e^{-2\pi i \tau h \sqrt{c^{(2)}} / L} \Phi(e^{-2\pi i \tau h \sqrt{c^{(2)}} / L} z', \bar{z}'), \quad (7.9)$$

i.e., it is simply a dilation in the z' -coordinate, as expected for a uniform time evolution that is solely generated by L_0 . In order to go back to the original z -coordinates, we perform a conformal transformation given by (7.7), and use the transformation law of primary fields under conformal transformations, to conclude that

$$e^{iH_1 t} \Phi(z, \bar{z}) e^{-iH_1 t} = \left(\frac{\partial \tilde{z}}{\partial z} \right)^h \left(\frac{\partial \bar{\tilde{z}}}{\partial \bar{z}} \right)^{\bar{h}} \Phi(\tilde{z}, \bar{\tilde{z}}), \quad (7.10)$$

with $\tilde{z}(z)$ the total Möbius transformation that combines the transformation from z to z' -coordinates, the dilation in z' -coordinates and the transformation back to the original z -coordinates and finally the analytic continuation $\tau \rightarrow i\tau$, given by $\tilde{z} = \frac{az+b}{b^*z+a^*}$, with [130]

$$a = \cosh \left(\frac{\pi \sqrt{c^{(2)}}}{L} t \right) + i \frac{\sigma_0}{\sqrt{c^{(2)}}} \sinh \left(\frac{\pi \sqrt{c^{(2)}}}{L} t \right), \quad (7.11)$$

$$b = i \frac{\sigma_+ + i\sigma_-}{\sqrt{c^{(2)}}} \sinh \left(\frac{\pi \sqrt{c^{(2)}}}{L} t \right), \quad (7.12)$$

Thus, the dynamics of primary fields is encoded in a Möbius transformation. Such transformations are classified in three distinct classes depending on the sign of

$$\text{Tr}^2 \begin{pmatrix} a & b \\ c & d \end{pmatrix} - 4. \quad (7.13)$$

Such classes are called elliptic, parabolic and hyperbolic classes. Equivalently, the sign of the quadratic Casimir $c^{(2)}$ delineates the different classes.

We now turn to the Floquet dynamics of primary fields: instead of considering a time evolution with a single Hamiltonian H_1 , we consider a two-step drive between H_0 and H_1 , such that the Floquet unitary reads

$$U_F = e^{-iH_0 T_0} e^{-iH_1 T_1}, \quad (7.14)$$

for driving parameters T_0 and T_1 , such that the periodicity of the Floquet drive is $T = T_0 + T_1$. The time evolution with the uniform Hamiltonian amounts to a dilation of the primary field. On the other hand, the time evolution with H_1

also amounts to a Möbius transformation, $\tilde{z}_1(z)$. Thus, the time evolution after a single Floquet period simply amounts to a change of coordinates of the form $\tilde{z}_0 \circ \tilde{z}_1(z)$. By virtue of the group properties of the Möbius transformation, such a one-cycle transformation is again a Möbius transformation. In particular, when H_1 is the SSD Hamiltonian, the one-cycle transformation takes the simple form

$$\tilde{z}_1 = \frac{(1 + \frac{\pi i T_1}{L}) e^{\frac{2\pi i T_0}{L}} z - \frac{\pi i T_1}{L}}{\frac{\pi i T_1}{L} e^{\frac{2\pi i T_0}{L}} z + (1 - \frac{\pi i T_1}{L})}. \quad (7.15)$$

The classification of the different one-cycle transformations for this particular example leads to the phase boundary (corresponding to the parabolic class)

$$\Delta = \left[1 - \left(\frac{\pi T_1}{L} \right)^2 \right] \sin^2 \left(\frac{\pi T_0}{L} \right) + \frac{\pi T_1}{L} \sin \left(\frac{2\pi T_0}{L} \right), \quad (7.16)$$

corresponding to parabolic Möbius transformations, which gives the phase diagram Fig. 7.1(c). We now use the fact that the full stroboscopic time evolution U_F^n , for any $n > 0$ reduces to a conformal map $\tilde{z}_n(z)$, such that

$$\tilde{z}_n(z) = \underbrace{(\tilde{z}_1 \circ \dots \circ \tilde{z}_1)}_{n \text{ times}}(z). \quad (7.17)$$

This n -th iteration of the one-cycle map can be explicitly evaluated by introducing the fixed points of the one-cycle map, γ_1 and γ_2 , as well as the multiplier ξ ,

$$\begin{cases} \gamma_1 = \frac{a-d-\sqrt{(a-d)^2+4bc}}{2c}, \\ \gamma_2 = \frac{a-d+\sqrt{(a-d)^2+4bc}}{2c}, \\ \xi = \frac{(a+d)+\sqrt{(a-d)^2+4bc}}{a+d-\sqrt{(a-d)^2+4bc}}. \end{cases} \quad (7.18)$$

Using these, the n -cycle Möbius map reads

$$\tilde{z}_n = \frac{a_n z + b_n}{c_n z + d_n} = \frac{(\gamma_1 - \xi^n \gamma_2)z + (\xi^n - 1)\gamma_1 \gamma_2}{(1 - \xi^n)z + \gamma_1 \xi^n - \gamma_2}, \quad (7.19)$$

In particular, the dynamics of the primary fields will strongly depend on which class the one-cycle map belongs to. In fact, in the elliptic class there is no fixed points, i.e., $\gamma_{1,2}$ do not belong to the unit circle, and $|\xi| = 1$. In this case, the stroboscopic position of the primary fields will just oscillates pseudo-periodically. On the other hand, in the hyperbolic class γ_1 is a stable fixed point and γ_2 an unstable fixed point, and the multiplier ξ belongs to the real positive axis, such that $\lim_{n \rightarrow \infty} \tilde{z}_n(z) = \gamma_1$ for any value of the initial position of the field $z = e^{2\pi i x/L}$ at time $t = 0$. These two distinct behaviours of primary fields under the flow of the Floquet map (7.19) are illustrated on Fig. 7.2, and only depend on the choice of the driving parameters $(\frac{T_0}{L}, \frac{T_1}{L})$. We stress that although we have shown the stroboscopic evolution of primary fields to be encoded in compositions of the one-cycle Möbius map for specific two-step drives, this reasoning applies to any periodic drive $v(x, t)$ as long as the deformation belongs to the $\mathfrak{sl}(2)$ subalgebra at all times t . We will

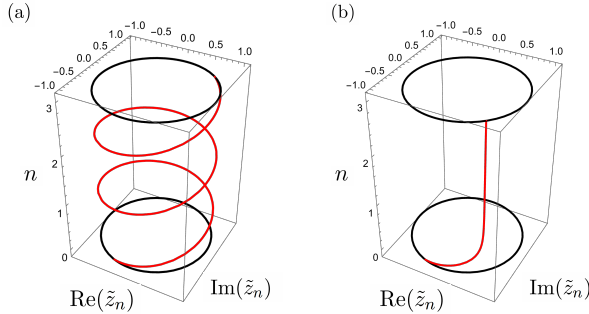


Figure 7.2: (a) Flow of the n -cycle Möbius transformation in the elliptic class, or non-heating phase. Here, the flow of primary fields oscillate as a function of the stroboscopic time $n(T_0 + T_1)$. (b) Flow of the n -cycle Möbius transformation in the hyperbolic class, or heating phase. Here, the flow of primary fields converges to the stable fixed point γ_1 as n goes to infinity (apart in the particular case where the field is inserted at time $t = 0$ at the position of the unstable fixed point γ_2). These two distinct behaviours emerge as a function of the driving parameters $(T_0/L, T_1/L)$.

show in Chapter 9 that a similar strategy holds when generalizing to arbitrary deformation, involving the full Virasoro algebra, enlarging the one-cycle map from being a Möbius transformation to any diffeomorphism of the circle. We further note that our approach based on conformal maps applies to any initial state at time $t = 0$, and arbitrary choice of conformally invariant boundary conditions, being either periodic or open.

7.3 HEATING AND NON-HEATING PHASES

We now compute different physical quantities by exploiting the stroboscopic time evolution of (quasi-)primary fields. We will focus in this chapter on two different examples that are relevant diagnosis of the heating and non-heating dynamics. The first physical quantity of interest is the energy density evolution $E(x, t)$, defined as

$$E(x, t) = \langle \psi_0 | (U_F^n)^\dagger T(z) U_F^n | \psi_0 \rangle + \langle \psi_0 | (U_F^n)^\dagger \bar{T}(\bar{z}) U_F^n | \psi_0 \rangle, \quad (7.20)$$

with $z = e^{2\pi i x/L}$. In order to evaluate the stroboscopic time evolution of the chiral and antichiral components of the energy-momentum tensor in Heisenberg picture, we can use the fact that both of these components are quasi-primary fields, such that their time evolution can be encoded in a Möbius transformation according to (7.19). In particular, we find that the chiral part $T(z)$ transforms as

$$(U_F^n)^\dagger T(z) U_F^n = \left(\frac{2\pi}{L} \right)^2 \left(\frac{\partial \tilde{z}_n}{\partial z} \right)^2 T(\tilde{z}_n) + \frac{c}{12} \{ \tilde{z}_n, z \}. \quad (7.21)$$

where $\{ \tilde{z}_n, z \}$ stands for the Schwarzian derivative associated to the Möbius map (7.7). However, using the fact that Schwarzian derivatives are zero for any Möbius transformation, this term vanishes. Following similar lines the

stroboscopic transformation for the antichiral part $\bar{T}(\bar{z})$ can be computed. The last step is to evaluate the equilibrium one-point functions $\langle T(\bar{z}_n) \rangle$ and $\langle \bar{T}(\bar{z}_n) \rangle$ for a specific choice of initial state $|\psi_0\rangle$. In particular, such a one-point function is zero if the initial state is the ground state of the homogenous Hamiltonian H_0 . One can thus consider the initial state to be a primary state, and use conformal Ward identities to evaluate the one-point function of the stress tensor, or consider the ground state $|G\rangle$ of H_0 with open boundary conditions. In the latter case, the one-point function can be evaluated by mapping the complex plane with a branch cut on the real positive axis to the upper-half plane, using the map $z \mapsto \sqrt{z}$, and similarly for the anti-holomorphic coordinates. On the upper-half plane, scale invariance constrains the one-point functions of the stress tensor to be zero, $\langle T \rangle = \langle \bar{T} \rangle = 0$, and thus the only non-zero contribution comes from the Schwarzian derivative term picked up by the square root transformation, i.e.,

$$\langle G|T(z)|G \rangle = \{z, \sqrt{z}\} = \frac{c}{32z^2}. \quad (7.22)$$

We can finally combine (7.21) and (7.22) to find the stroboscopic evolution of the energy density,

$$E(x, t) = \left(\frac{2\pi}{L}\right)^2 \frac{c}{32} \left[\frac{z^2}{(a_n z + b_n)^2 (c_n z + d_n)^2} + \frac{\bar{z}^2}{(a_n \bar{z} + b_n)^2 (c_n \bar{z} + d_n)^2} \right]. \quad (7.23)$$

Depending on the classification of the one-cycle Floquet map, the energy density

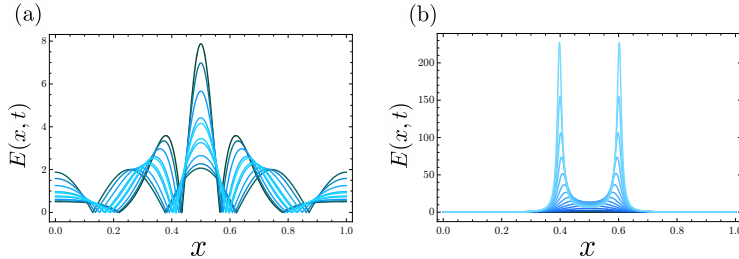


Figure 7.3: Time evolution of the energy density $E(x, t)$ for different stroboscopic times (from dark to light blue) in (a) the non-heating phase, where energy density oscillates through the system and in (b) the heating phase, where energy accumulates at two spatial positions x_* and $L - x_*$.

behaves in distinct ways. In the elliptic class, that defines the non-heating phase, energy density oscillates throughout the system in a periodic fashion, see Fig. 7.3(a). On the other hand, in the hyperbolic class, which defines the heating phase, energy density decays exponentially at every point in space apart from two points, $x_* = L/(2\pi)\arg(\gamma_2)$ and $L - x_*$, as illustrated on Fig. 7.3(b). The formation of these two hotspots in energy will be interpreted in Sec. 7.4 as emergent Floquet horizons that absorb chiral and antichiral quasiparticles, respectively. We note that the position x_* is an emergent property of the drive, and solely depends on the deformation profiles constituting the Floquet

drive, as well as the driving parameters $(T_0/L, T_1/L)$ through (7.18). This can be understood from the flow of the one-cycle Floquet map (see Fig. 7.2(b)), as the n -th iteration of the Floquet map tends to the stable fixed point γ_1 , $\lim_{n \rightarrow \infty} \tilde{z}_n = \gamma_1$, leading the energy density to accumulate around the unstable fixed point γ_2 from (7.23). We finally note that at the phase transition, the stable and unstable fixed point merge into a single fixed point through a saddle-node bifurcation, leading to a single emergent fixed point at which energy grows only quadratically, as expected for the parabolic class of Möbius transformations.

We can further distinguish the heating and non-heating phases by integrating the energy density (7.23) using the residue theorem, and obtain the total energy $E(t)$. One thus finds

$$E(t) = \int_0^L E(x, t) dx = \frac{2\pi}{L} \frac{c}{16} (a_n d_n + b_n c_n). \quad (7.24)$$

Although this result holds for a particular choice of initial state, i.e., the ground state of the uniform Hamiltonian with open boundaries, we stress that the same time evolution would follow for arbitrary pure or thermal initial state, irrespective of the choice of boundary conditions. The interested reader is advised to consult Sec. 10.2 from Chapter 10 for a derivation of the energy growth starting from a thermal initial state at temperature β^{-1} . Depending on the different phases classified by the one-cycle Möbius transformation, the total energy displays radically different behaviours. In the non-heating phase, the total energy is found to oscillate at an emergent periodicity given by

$$T = 2\pi \frac{(T_0 + T_1)}{|\log \xi|}. \quad (7.25)$$

On the other hand, the absorbed energy grows exponentially in time in the heating phase, $E(t) \sim E_0 e^{\Theta_H t}$, with a heating rate Θ_H given by

$$\Theta_H = \frac{|\log \xi|}{2\pi(T_0 + T_1)}. \quad (7.26)$$

The order parameter for the phase transition is the periodicity T in the non-heating phase and the heating rate Θ_H in the heating phase. In fact, we can show that the periodicity diverges as $1/|T - T_*|^{1/2}$ when going from the non-heating to the heating phase, such that the phase transition is characterized by a critical exponent of $\frac{1}{2}$. The same conclusion holds by studying the divergence of the inverse heating rate when going from the heating to the non-heating phase. We stress that this critical exponent is found to be universal, and generalizes to any inhomogeneous Floquet drive. A general proof of this universal property, for arbitrary choice of smooth deformations and arbitrary choice of periodic driving sequence, is provided in Chapter 9. The two distinct time evolution of the total energy, as well as the evolution at the phase transition are illustrated on Fig. 7.4(a).

We now study the stroboscopic time evolution of the Loschmidt echo (or fidelity) $F(t)$ during the periodic drive,

$$F(t) = |\langle \psi_0 | \psi(t) \rangle|^2. \quad (7.27)$$

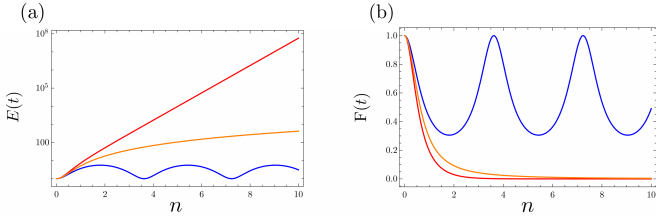


Figure 7.4: (a) Stroboscopic time evolution of total energy $E(t = n(T_0 + T_1))$. In the heating phase (red), energy grows exponentially at a rate given by (7.26), while in the non-heating phase (blue) it oscillates in time at a period given by (7.25). At the phase transition, the energy grows quadratically (orange). (b) Stroboscopic time evolution of the Loschmidt echo $F(t)$ for the same driving parameters.

As a warm-up, let us first compute the Loschmidt echo for a single quench with the SSD Hamiltonian at $t = 0$, starting from a highest-weight excited state $|\Phi\rangle$ of H . The Loschmidt echo is then

$$F(t) = |\langle\Phi|e^{-iHt}|\Phi\rangle|^2 \quad (7.28)$$

Any highest-weight state $|\Phi\rangle$ can be written as an in-state generated by a primary field $\phi(z, \bar{z})$ of conformal weights (h, \bar{h}) acting on the $SL(2, \mathbb{C})$ invariant vacuum $|0\rangle$ at $\tau \rightarrow -\infty$, which corresponds to inserting the field at the origin of the complex plane after applying the exponential mapping in the z coordinates,

$$|\Phi\rangle = \lim_{z, \bar{z} \rightarrow 0} \phi(z, \bar{z}) |0\rangle. \quad (7.29)$$

The computation then reduces to

$$\langle\Phi|e^{-H\tau}|\Phi\rangle = \lim_{z_1, \bar{z}_1 \rightarrow 0} \lim_{z_2, \bar{z}_2 \rightarrow 0} z_2^{-2h} \bar{z}_2^{-2\bar{h}} \langle 0 | \phi(z_2^{-1}, \bar{z}_2^{-1}) e^{-H\tau} \phi(z_1, \bar{z}_1) | 0 \rangle.$$

We now insert the identity $\mathbb{I} = e^{H\tau} e^{-H\tau}$, and use the fact that $|0\rangle$ is an eigenstate of H , as $L_0|0\rangle = L_{\pm 1}|0\rangle = 0$, therefore $e^{-H\tau}$ acting on $|0\rangle$ gives a phase irrelevant for the Loschmidt echo. By going to the $\tilde{z}_0(z)$ coordinates, explicitly given by (8.4), we obtain

$$\begin{aligned} \langle\Phi|e^{-H\tau}|\Phi\rangle &= \lim_{z_1, \bar{z}_1 \rightarrow 0} \lim_{z_2, \bar{z}_2 \rightarrow 0} \left(\frac{\partial \tilde{z}_0}{\partial z} \Big|_{z_1} \right)^h \left(\frac{\partial \bar{z}_0}{\partial \bar{z}} \Big|_{\bar{z}_1} \right)^{\bar{h}} \times z_2^{-2h} \bar{z}_2^{-2\bar{h}} \\ &\quad \times \langle 0 | \phi(z_2^{-1}, \bar{z}_2^{-1}) \phi(\tilde{z}_0(z_1), \tilde{z}_0(\bar{z}_1)) | 0 \rangle. \end{aligned} \quad (7.30)$$

Finally, $\langle 0 | \phi(z_2^{-1}, \bar{z}_2^{-1}) \phi(\tilde{z}_0(z_1), \tilde{\bar{z}}_0(\bar{z}_1)) | 0 \rangle$ is a simple two point function in the \tilde{z} coordinates, leading to

$$\begin{aligned} \langle \Phi | e^{-H\tau} | \Phi \rangle &= \lim_{z_1, \tilde{z}_1 \rightarrow 0} \lim_{z_2, \tilde{z}_2 \rightarrow 0} \left(\frac{\partial \tilde{z}_0}{\partial z} \Big|_{z_1} \right)^h \left(\frac{\partial \tilde{\bar{z}}_0}{\partial \bar{z}} \Big|_{\bar{z}_1} \right)^{\bar{h}} \\ &\times \frac{z_2^{-2h}}{|z_2^{-1} - \tilde{z}_0(z_1)|^{2h}} \frac{\bar{z}_2^{-2\bar{h}}}{|\bar{z}_2^{-1} - \tilde{\bar{z}}_0(\bar{z}_1)|^{2\bar{h}}}. \end{aligned} \quad (7.31)$$

The limits can then be taken, giving the same result independently of their order,

$$\lim_{z_1, z_2 \rightarrow 0} \frac{z_2^{-2h}}{|z_2^{-1} - \tilde{z}_0(z_1)|^{2h}} = \lim_{z_2 \rightarrow 0} \frac{z_2^{-2h}}{|z_2^{-1} - \alpha|^{2h}} = 1. \quad (7.32)$$

Therefore only the derivative terms contribute, whose limit give, after analytic continuation to real time $\tau \mapsto it$,

$$F(t) = \frac{1}{\left(1 + \frac{\pi^2 t^2}{L^2}\right)^{2(h+\bar{h})}}. \quad (7.33)$$

We thus find a quadratic decay of the Loschmidt echo after the SSD quench. In order to generalize the above derivation to the case of an $\mathfrak{sl}(2)$ periodic drive, we simply needs to replace $\tilde{z}_1(z)$ by $\tilde{z}_n(z)$. The result now reads

$$F(t) = \langle \Phi | U_F^n | \Phi \rangle = |d_n|^{-4(h+\bar{h})}, \quad (7.34)$$

at stroboscopic times $t = n(T_0 + T_1)$. By exploiting the properties of the Möbius transformation in the different phases, we thus conclude that the Loschmidt echo oscillates between one and a finite value in the non-heating phase with periodicity T given by (7.25), signalling periodic revival of the initial state of period T given by (7.25), while it decays exponentially in the heating phase with the heating rate Θ_H given by (7.26). These two distinct time evolution of the Loschmidt echo, as well as the quadratic decay of the echo at the phase transition, are illustrated on Fig. 7.4(b). This exponential loss of information on the initial state may signal that the system effectively enters an ergodic phase. We will however show that the integrable structure of CFTs prevent such an ergodicity to take place, even in the heating phase.

7.4 CURVED LIGHT-CONES AND EMERGENT FLOQUET HORIZONS

Conformal field theories being gapless theories in the limit of infinite system size $L \rightarrow \infty$, they support gapless quasiparticles that propagate through the system at the Fermi velocity v . In particular, quenching the system by starting from a massive state, such as a boundary state, and letting such state evolve with a uniform Hamiltonian $H_0 = \int_{-\infty}^{\infty} T_{00}(x)dx$ from $t = 0$ leads to a linear growth of entanglement entropy $S_A(t)$ in time, and then a saturation to a steady state value determined by the size of A , as discussed in Sec. 4.2. An

intuitive way to understand this picture is to assume that the perturbation at time $t = 0$ produces pairs of entangled quasiparticles, with a chiral and an antichiral quasiparticle propagating at v in opposite direction, such that the linear growth of $S_A(t)$ is contributed by pairs of quasiparticles emitted in A , such that one quasiparticle leaves A before its entangled partner. The steady state value of entanglement entropy after the quantum quench is reached when all emitted pairs of quasiparticles are in the complement B , see Sec. 4.2. However, this quasiparticle picture holds assuming that the Fermi velocity is uniform and does not vary over the whole system, which will typically not be true for disordered systems. Describing these disordered effects on a critical system is a difficult task, as it can move the theory away from its critical point, for instance with a spatially dependent Luttinger parameter $K(x)$ in a free boson theory. In this chapter we consider a simplified approach to take into account such effects by considering an inhomogeneous quantum quench with a post-quench Hamiltonian of the form $H = \int_{-\infty}^{\infty} v(x) T_{00}(x) dx$. In this case, the Fermi velocity becomes position dependent, $v = v(x)$, and quasiparticles can be shown to propagate along the lightlike geodesics of the Lorentzian spacetime metric

$$ds^2 = dx^2 - v(x)^2 dt^2. \quad (7.35)$$

In other words, by using the fact that in a $(1+1)$ -dimensional spacetime all null curves $ds^2 = 0$ are lightlike geodesics, the trajectory of chiral and antichiral quasiparticles emitted at time t_0 follow

$$t - t_0 = \pm \int_{x_0}^x \frac{1}{v(x')} dx', \quad (7.36)$$

where $+$ ($-$) stands of chiral (antichiral) quasiparticles. As a first example

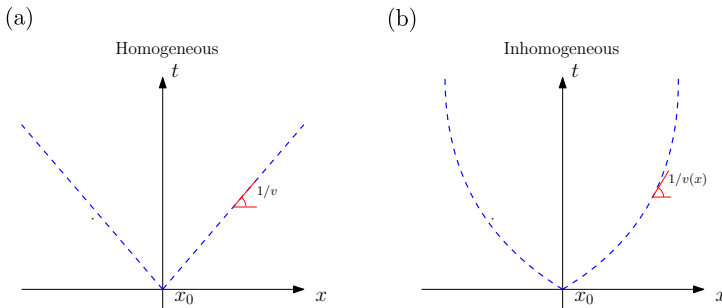


Figure 7.5: spacetime propagation of the chiral and antichiral quasiparticles in (a) an homogeneous critical system with Fermi velocity v , and (b) an inhomogeneous system with a spatially dependent Fermi velocity $v(x)$. We note the emergence of curved light-cone propagation of quasiparticles following the geodesics (7.36).

of the emergence of curved light-cones, we consider a quantum quench at time $t = 0$ with an $\mathfrak{sl}(2)$ deformed Hamiltonian with velocity $v(x) = 1 -$

$\frac{1}{2} \tanh(2\theta) \cos(2\pi x/L)$. In this case the geodesics can be explicitly computed, leading to

$$\begin{aligned} t &= \pm \int_{x_0}^x dx' \frac{1}{1 - \tanh 2\theta \cos \frac{2\pi x}{L}} \\ &= \pm \frac{L \cosh 2\theta}{\pi} \left(\tan^{-1} \left(e^{2\theta} \tan \frac{\pi x}{L} \right) - \tan^{-1} \left(e^{2\theta} \tan \frac{\pi x_0}{L} \right) \right) \end{aligned} \quad (7.37)$$

The resulting curved-light cones can be probed by computing dynamical two-point functions of any primary field $\phi(z, \bar{z})$ of conformal weight (h, \bar{h}) ,

$$G(x_0, x; t) = \langle 0 | \phi(x_0, 0) \phi(x, t) | 0 \rangle. \quad (7.38)$$

This two-point function can be computed explicitly by using the general approach outlined in Sec. 7.2, and encoding the time evolution of primary fields through change of Möbius conformal maps \tilde{z} . This leads to the result. It is straightforward to show that the poles of (7.38) are given by

$$x_{\pm}(t) = \frac{L}{\pi} \tan^{-1} \left(e^{-2\theta} \tan \left(\pm \frac{\pi t}{L \cosh(2\theta)} + \tan^{-1} \left(e^{2\theta} \tan \frac{\pi x_0}{L} \right) \right) \right), \quad (7.39)$$

which coincide with the light-like geodesics of the curved spacetime (7.37). The agreement is further illustrated on Fig. 7.6 for a particular value of θ . We stress that the curved spacetime (7.35) is not merely a wrong choice of

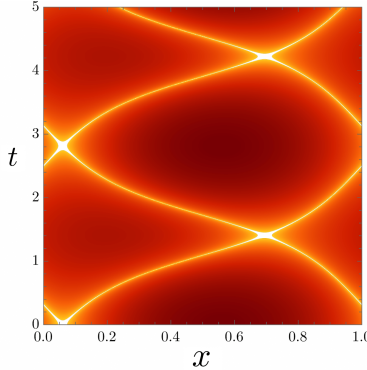


Figure 7.6: Dynamical two-point function $G(x_0, x; t)$ for the $\mathfrak{sl}(2)$ deformation $v(x) = 1 - \frac{1}{2} \tanh(2\theta) \cos(2\pi x/L)$, with $\theta = 0.6$, $L = 1$, and periodic boundary conditions. The red dashed curves are the geodesics of the associated spacetime metric, explicitly given by (7.39). We observe recurrences in the time evolution of a period of $L/c^{(2)}$, inherited from the level spacing of the deformed Hamiltonian.

coordinates to describe the problem. In fact, while all metrics in $(1+1)$ -dimensional spacetimes are related to the flat Minkowski metric via a conformal transformation, $\tilde{g} = e^{-2\sigma(x,t)} g$, the Ricci scalar encoding the curvature is not invariant under such transformations:

$$\tilde{R} = e^{-2\sigma(x,t)} \left[R + 2 \left(\frac{\partial^2 \sigma}{\partial t^2} + \frac{\partial^2 \sigma}{\partial x^2} \right) \right]. \quad (7.40)$$

In particular, in our concrete example the Ricci scalar is $R = \frac{8\pi^2}{L^2} \frac{\cos \frac{2\pi x}{L}}{\cos \frac{2\pi x}{L} - \coth 2\theta}$, which diverges at $x = 0$ in the SSD limit $\theta \rightarrow \infty$, reflecting the fact that the velocity goes to zero at this point, leading to an infinite time for information to propagate through it.

We will now derive the stroboscopic spacetime metric for the Floquet drive defined at stroboscopic times. We are interested in finding some coordinates \tilde{z}_n in which the effective metric describing the n -cycle Floquet drive is conformally flat, and then going back to the original coordinates (x, τ) to get the expression of the metric. Such coordinates are called isothermal coordinates and always exist in $(1+1)$ -dimensional spacetimes. For the Floquet drive, they are given by the effective Möbius transformation (7.19), so that the metric reads

$$ds^2 = e^{-2\sigma(x, \tau)} d\tilde{z}_n d\bar{\tilde{z}}_n. \quad (7.41)$$

Introducing the real and imaginary parts of \tilde{z}_n

$$\begin{cases} \tilde{u}_n(x, \tau) = \text{Re}(\tilde{z}_n) = \frac{a_n c_n + b_n d_n + (a_n d_n + b_n c_n) \cos(\frac{2\pi x}{L})}{c_n^2 + d_n^2 + 2c_n d_n \cos(\frac{2\pi x}{L})}, \\ \tilde{v}_n(x, \tau) = \text{Im}(\tilde{z}_n) = \frac{(a_n d_n - b_n c_n) \sin(\frac{2\pi x}{L})}{c_n^2 + d_n^2 + 2c_n d_n \cos(\frac{2\pi x}{L})}. \end{cases}$$

The effective metric reads $e^{2\sigma(x, \tau)} ds^2 = d\tilde{u}_n^2 + d\tilde{v}_n^2$. It is now straightforward to apply the change to (x, τ) coordinates. After some computations, the metric takes the familiar form, after analytic continuation:

$$d\tilde{z}_n d\bar{\tilde{z}}_n = e^{2\sigma(x, \tau)} (dx^2 - g(x)dt^2 + 2h(x)dxdt). \quad (7.42)$$

The value we find for $g(x)$ and $h(x)$ are then given by (7.43) and (7.44)

$$g(x) = \zeta^2 \prod_{i=1}^2 \left[1 + \gamma_i^2 - 2\gamma_i \cos\left(\frac{2\pi x}{L}\right) \right], \quad (7.43)$$

$$h(x) = i\zeta(\gamma_1\gamma_2 - 1) \sin\left(\frac{2\pi x}{L}\right), \quad (7.44)$$

where $\zeta = -\frac{L}{2\pi i} \frac{1}{(T_0+T_1)} \frac{\log(\xi)}{(\gamma_1 - \gamma_2)}$, and as before ξ is the multiplier of the Möbius transformation, which is a complex exponential in the non-heating phase and a real exponential in the heating phase, and γ_1, γ_2 are the two fixed-points of the 1-cycle Möbius transformation. After analytic continuation, both $g(x)$ and $h(x)$ are real-valued functions. The Weyl prefactor $e^{2\sigma(x, \tau)}$ is a positive number before analytic continuation,

$$e^{2\sigma(x, \tau)} = \left(\frac{2\pi}{L}\right)^2 \frac{\partial \tilde{z}_n}{\partial z} \Big|_{z_1} \frac{\partial \bar{\tilde{z}}_n}{\partial \bar{z}} \Big|_{\bar{z}_1}. \quad (7.45)$$

Inverting the Weyl transformation, the metric in the original coordinates (x, t) is thus

$$ds^2 = dx^2 - g(x)dt^2 + 2h(x)dxdt. \quad (7.46)$$

In particular we note the following fact concerning isothermal coordinates: the correlation functions in curved spacetime coordinates (x, τ) are related to

correlation functions in conformally flat spacetime in the isothermal coordinates $(\tilde{u}_n, \tilde{v}_n)$ by the formula [124, 139]:

$$\langle \phi(x, \tau) \phi(x_0, 0) \rangle = e^{2h\sigma(x_0, 0)} e^{2h\sigma(x, \tau)} \langle \phi(\tilde{z}_n, \bar{\tilde{z}}_n) \phi(\tilde{z}_0, \bar{\tilde{z}}_0) \rangle_{\text{flat}}. \quad (7.47)$$

The correlation function $\langle \phi(\tilde{z}_n, \bar{\tilde{z}}_n) \phi(\tilde{z}_0, \bar{\tilde{z}}_0) \rangle_{\text{flat}}$ is just a correlation function evaluated in usual flat spacetime. In the case of periodic boundary conditions, this is simply the usual two-point correlator of primary fields,

$$\langle \phi(\tilde{z}_n, \bar{\tilde{z}}_n) \phi(\tilde{z}_0, \bar{\tilde{z}}_0) \rangle_{\text{flat}} = \frac{1}{(z_0 - \tilde{z}_n)^{2h}} \frac{1}{(\bar{z}_0 - \bar{\tilde{z}}_n)^{2h}}. \quad (7.48)$$

Putting this equation together with (7.45) in (7.47), we obtain the dynamical two-point function evolution,

$$\langle 0 | \phi(x, t) \phi(x_0, 0) | 0 \rangle = \left(\frac{2\pi}{L} \right)^{4h} \left[\frac{\partial \tilde{z}_n}{\partial z} \Big|_{z_1} \frac{\partial \bar{\tilde{z}}_n}{\partial \bar{z}} \Big|_{\bar{z}_1} \right]^h \frac{1}{(z_0 - \tilde{z}_n)^{2h}} \frac{1}{(\bar{z}_0 - \bar{\tilde{z}}_n)^{2h}}, \quad (7.49)$$

from our curved spacetime approach. The dynamical two-point correlator is shown on Fig. 7.7 for both the heating and the non-heating phases. The null

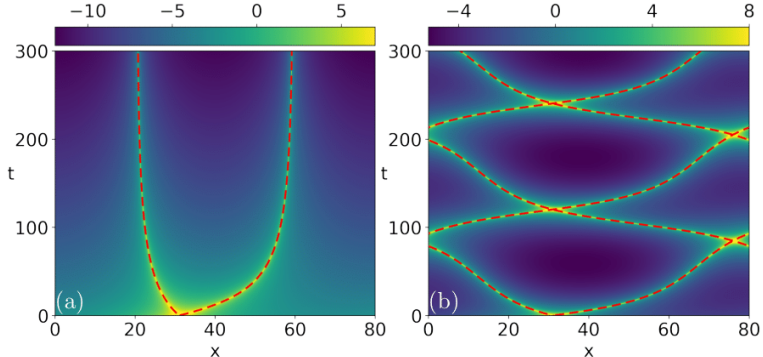


Figure 7.7: CFT two-point function $|\langle \phi(x, t) \phi(x_0, 0) \rangle|$ for the Floquet drive ($L = 80$, $x_0 = 31$, colorbars in log scale). (a) Heating phase ($T_0 = T_1 = 34$). The excitations are attracted by two black hole horizons at x^* and $L - x^*$. (b) Non-heating phase ($T_0 = T_1 = 25$). The dynamics is pseudo-periodic. In both cases, the dashed curves are the null-geodesics of the curved stationary metric, explicitly given by (7.50).

geodesics of this $(1+1)$ -dimensional spacetime are uniquely determined by the condition $ds^2 = 0$. Thus they are the solutions of the equation $2h(x(t))\dot{x}(t) + \dot{x}^2(t) - g(x(t)) = 0$:

$$\pm t(x) = \int_{x_0}^x dx' \frac{1}{\sqrt{h(x')^2 + g(x')} \mp h(x')}. \quad (7.50)$$

Then the local group velocity of the excitations is $v(x) = h(x) \mp \sqrt{h(x)^2 + g(x)}$, where the sign corresponds to chiral and anti-chiral excitations. The expression (7.46) is not time-reversal invariant because of the $dx dt$ term. Only if

$\gamma_1\gamma_2 = 1$, $h(x) = 0$ and the system is time-reversal invariant. This can be fulfilled by starting the drive in a symmetric way. For concreteness, we shift the origin of time by $\frac{T_0}{2}$

$$H(t) = \begin{cases} H_0 & 0 < t < \frac{T_0}{2}, \\ H_1 & \frac{T_0}{2} < t < \frac{T_0}{2} + T_1, \\ H_0 & \frac{T_0}{2} + T_1 < t < \frac{3T_0}{2} + T_1, \\ \text{etc.} & \end{cases} \quad (7.51)$$

The associated 1-cycle Möbius transformation is therefore given by the equation

$$\tilde{z}_1 = \frac{\left(1 + \frac{\pi\tau_1}{L}\right) e^{\frac{\pi\tau_0}{L}} z - \frac{\pi\tau_1}{L}}{\frac{\pi\tau_1}{L} z + \left(1 - \frac{\pi\tau_1}{L}\right) e^{-\frac{\pi\tau_0}{L}}}. \quad (7.52)$$

It is interesting to compare (7.52) and (7.15). The coefficients a and d are the same as in the non symmetric case, but not b and c . Furthermore bc is unchanged. Thus, looking at the definitions of the fixed points and the multiplier, this only redefines the denominators of γ_1 and γ_2 , and keeps the multiplier ξ invariant. It can then be shown that $\gamma_1\gamma_2 = 1$. Furthermore in the heating phase $|\gamma_1| = |\gamma_2| = 1$, therefore in the time-reversal symmetric situation $\gamma_1 = \gamma_2^*$, whereas in the non-heating phase, γ_1 and γ_2 are both real and inverse of each other. In this case, the metric is simplified to $ds^2 = dx^2 - g(x)dt^2$. Applying the time-reversal condition, one finds that

$$v(x) = [g(x)]^{1/2} = \frac{1}{2\pi i} \frac{L \log(\xi)}{(T_0 + T_1)} \frac{\left(1 + \gamma_1^2 - 2\gamma_1 \cos \frac{2\pi x}{L}\right)}{\gamma_1^2 - 1}. \quad (7.53)$$

This is the effective velocity of the excitations. In the heating phase their local group velocity goes to 0 at two points, which are found to be $x_* = \frac{L}{2\pi} \arccos\left(\frac{1+\gamma_1^2}{2\gamma_1}\right)$ and $L - x_*$. After analytic continuation, it can be shown that $x_* = \frac{L}{2\pi} \arccos(\cos \frac{\pi T_0}{L} + \frac{L}{\pi T_1} \sin \frac{\pi T_0}{L})$. Thus $x_* \in [0, \frac{L}{2}]$ in the heating phase, and x_* is a complex number in the non-heating phase, therefore the velocity never goes to 0. Thus the heating phase at these two points, the velocity of the excitations vanishes, meaning that their worldlines, following null geodesics of the metric, will tend to one of these two points. We rewrite the metric in the heating phase in terms of the horizon x_* . We first notice that as $\cos\left(\frac{2\pi x_*}{L}\right) = \frac{1}{2} \frac{\gamma_1^2 + 1}{\gamma_1}$, then the effective deformation is rewritten directly in terms of the horizon

$$v(x) = A \left(1 - \frac{\cos\left(\frac{2\pi x}{L}\right)}{\cos\left(\frac{2\pi x_*}{L}\right)} \right), \quad (7.54)$$

with $A = \frac{1+\gamma_1^2}{\gamma_1^2 - 1} \frac{1}{2\pi i(T_0 + T_1)} L \log(\xi)$. Using trigonometric formulae, this leads to the desired form of the velocity

$$v(x) = 2A \frac{\sin\left[\frac{\pi}{L}(x - x_*)\right] \sin\left[\frac{\pi}{L}(x + x_*)\right]}{\cos\left(\frac{2\pi x_*}{L}\right)}, \quad (7.55)$$

The effective metric can now be easily expressed in terms of the horizon x_*

$$ds^2 = -4A^2 \frac{\sin^2\left[\frac{\pi}{L}(x - x_*)\right] \sin^2\left[\frac{\pi}{L}(x + x_*)\right]}{\cos^2\left(\frac{2\pi x_*}{L}\right)} dt^2 + dx^2. \quad (7.56)$$

This form is still hard to interpret in terms of black hole metric. However, by doing an expansion around one of the two horizons, i.e., around x_* or $L - x_*$, and keeping only the lowest order contribution, only the contribution from one of the horizons should matter and the metric should be simpler. Therefore we expand the expression (7.56) around x_* . At leading order in $x - x_*$, we may simplify

$$\sin^2\left[\frac{\pi}{L}(x - x_*)\right] \sin^2\left[\frac{\pi}{L}(x + x_*)\right] \approx \frac{\pi^2}{L^2} (x - x_*)^2 \sin^2\left(\frac{2\pi x_*}{L}\right). \quad (7.57)$$

The metric finally simplifies to

$$ds^2 = -4A^2 \tan^2\left(\frac{2\pi x_*}{L}\right) \frac{\pi^2}{L^2} (x - x_*)^2 dt^2 + dx^2. \quad (7.58)$$

This metric is known as the Rindler metric, which describes an accelerated frame transformation of the flat Minkowski metric. Writing $C^2 = 4A^2 \tan^2\left(\frac{2\pi x_*}{L}\right) \frac{\pi^2}{L^2}$, the metric reads $ds^2 = -C^2(x - x_*)^2 dt^2 + dx^2$. One can now introduce the following coordinate change: $\frac{C}{2}(x - x_*)^2 = (y - x_*)$. In the new coordinates, the metric reads

$$ds^2 = -2C(y - x_*) dt^2 + \frac{1}{2C} \frac{1}{(y - x_*)} dy^2. \quad (7.59)$$

This is a particular form of a black-hole metric in $(1+1)$ dimensions [140–142]. Thus expanding our spacetime effective metric around one of the two horizons gives (at leading order) a metric containing an emergent Floquet horizon at $x = x_*$. One can perform a similar calculation for the second Floquet horizon by expanding the metric around $L - x_*$, to get similar results: $ds^2 = -2C[y - (L - x_*)] dt^2 + \frac{1}{2C} \frac{1}{[y - (L - x_*)]} dy^2$. The emergence of such black hole horizon in the stroboscopic trajectories of quasiparticles from the dynamical two point correlator is shown on Fig. 7.7(a). In particular, the Hawking temperature associated to such horizons is readily found to be given by the heating rate Θ_H given by (7.26).

7.5 EFFECTIVE HAMILTONIAN

While in general driven systems fully break time translation symmetry, periodically driven system only break it down to a discrete subgroup. Because of this, the full stroboscopic time evolution of a Floquet systems can be seen as a quantum quench with an effective Hamiltonian, called Floquet Hamiltonian, H_F , and defined as [see also (2.21)]

$$U_F = \mathcal{T} e^{-i \int_0^T dt' H(t')} = e^{-i H_F T}, \quad (7.60)$$

for any generic Floquet drive of period T . While the knowledge of the Floquet Hamiltonian can greatly help to classify a given Floquet problem, finding the

Floquet Hamiltonian in general is a difficult task. In the case of $\mathfrak{sl}(2)$ drives, the Floquet Hamiltonian could be obtained by capitalizing on the $\mathfrak{su}(1, 1)$ symmetry of the problem. By construction H_F takes the general form

$$H_F = \int_0^L [v_{\text{eff}}^-(x)T(x) + v_{\text{eff}}^+(x)\bar{T}(x)]dx, \quad (7.61)$$

where the effective Floquet velocities for the chiral and antichiral parts can in general be different. The derivation of the emergent stroboscopic spacetime metric of the previous section provides us with the effective Floquet velocities. For a generic drive, they are given by

$$v_{\text{eff}}^\pm(x) = 2L\Theta_H \frac{\sin[\frac{\pi}{L}(x \mp x_{*,1})]\sin[\frac{\pi}{L}(x \mp x_{*,2})]}{\sin[\frac{\pi}{L}(x_{*,1} - x_{*,2})]}, \quad (7.62)$$

where $x_{*,1}$ is the stable and $x_{*,2}$ the unstable fixed point of the one-cycle Floquet map, i.e., $x_{*,i} = \frac{L}{2\pi i} \log \gamma_i$. The emergence of the horizons thus becomes transparent in the effective Hamiltonian in the heating phase. We note that the effective Hamiltonian H_F bears similarities with the entanglement Hamiltonian of CFTs [143]. Alternatively, we decompose these effective velocities in Fourier space to write the Floquet Hamiltonian as

$$H_F = \sigma_0 L_0 + \sigma_+ L_+ + \sigma_- L_-, \quad (7.63)$$

with the coefficients given by

$$\begin{aligned} \sigma_0 &= \frac{i}{T_0 + T_1} \frac{\log \xi}{(\gamma_1 + \gamma_2)\gamma_1 - \gamma_2}, \\ \sigma_+ &= -\frac{i}{T_0 + T_1} \frac{\log \xi}{(\gamma_1 + \gamma_2)\gamma_1 - \gamma_2} (\gamma_1\gamma_2 + 1), \\ \sigma_- &= -\frac{i}{T_0 + T_1} \frac{\log \xi}{(\gamma_1 + \gamma_2)\gamma_1 - \gamma_2} (\gamma_1\gamma_2 - 1), \end{aligned} \quad (7.64)$$

and $\bar{\sigma}_0 = \sigma_0$, $\bar{\sigma}_+ = \sigma_+$, $\bar{\sigma}_- = -\sigma_-$. The algebraic classification of the Floquet problem thus becomes transparent in this formalism: the sign of the quadratic Casimir $c^{(2)}$ associated to H_F provides the stability of the phase. The different classes of Floquet Hamiltonians are thus given by the co-adjoint orbits of the $SL(2, \mathbb{R})$ group, as illustrated on Fig. 7.8. The non-heating phase corresponds to a Floquet Hamiltonian with invariant in the elliptic class, the heating phase to an invariant in the hyperbolic class, and the phase transition in the parabolic class. In particular, the Möbius map encoding the continuous time evolution of primary fields after a quantum quench with H_F is given by

$$\tilde{z}_i(t) = \frac{\alpha z_i + \beta}{\beta^* z_i + \alpha^*}, \quad \bar{\tilde{z}}_i(t) = \frac{\alpha \bar{z}_i + \beta}{\beta^* \bar{z}_i + \alpha^*}, \quad (7.65)$$

with α, β given by

$$\begin{aligned} \alpha &= \cosh[\pi\Theta_H t] + \text{sgn}(\log \xi) \frac{\gamma_1 + \gamma_2}{\gamma_1 - \gamma_2} \sinh[\pi\Theta_H t], \\ \beta &= -\text{sgn}(\log \xi) \frac{2\gamma_1\gamma_2}{\gamma_1 - \gamma_2} \sinh[\pi\Theta_H t]. \end{aligned} \quad (7.66)$$

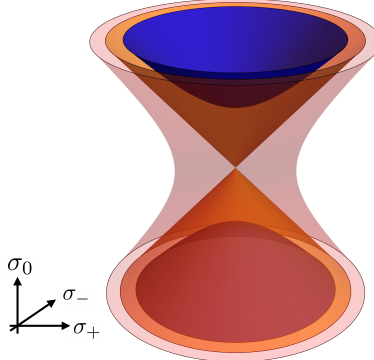


Figure 7.8: The three different types of co-adjoint orbits of the group $SL(2, \mathbb{R})$: The blue manifold corresponds to negative quadratic Casimir invariant, $c^{(2)} < 0$, and belongs to the elliptic class. The orange “light-cone” manifold corresponds to $c^{(2)} = 0$, and is the parabolic class. The red manifold is belongs to the hyperbolic class, $c^{(2)} > 0$. A point on a given manifold can be brought to any other point of the same manifold via actions of the $SL(2, \mathbb{R})$ group.

We note that in the time-reversal symmetric situation, the effective velocities of both the chiral and antichiral sectors coincide,

$$v_{\text{eff}}(x) = v_{\text{eff}}^+(x) = v_{\text{eff}}^-(x) = 2L\Theta_H \frac{\sin[\frac{\pi}{L}(x - x_*)] \sin[\frac{\pi}{L}(x + x_*)]}{\sin[\frac{2\pi x_*}{L}]} \quad (7.67)$$

Despite the apparent difference between the symmetric and non-symmetric cases, we now present a simple quasiparticle picture that unifies both protocols from a Floquet Hamiltonian standpoint, as illustrated on Fig. 7.9. In the non-symmetric case, two distinct fixed points emerge for each sector: a stable and an unstable fixed points. At the unstable fixed point, quasiparticles are getting repelled as the sign of the deformation changes (quasiparticles of the same chirality but at different positions x_1 and x_2 , such that $v_+(x_1) < 0 < v_+(x_2)$, propagate in opposite directions), while they get attracted at the stable fixed point, leading to a chiral emergent horizon. The same mechanism leads to an anti-chiral horizon at a symmetric position, see Fig. 7.9(a). In the time-reversal symmetric case, the unstable fixed point of the chiral sector merges with the stable fixed point of the anti-chiral sector and vice-versa as shown on Fig. 7.9(b), which again leads to two emergent Floquet horizons. An important difference between these two effective description of the Floquet drive is that the Floquet Hamiltonian in the non-symmetric case carries a non-zero momentum, i.e., $T - \bar{T} \neq 0$, leading to asymmetric quasiparticle propagation. In this case the effective velocity profiles can have a different sign between the two chiralities, leading to a propagation of chiral and anti-chiral quasiparticles in the same direction, despite the boundaries being periodic and the two sectors thus being uncoupled. This emergent phenomena of the Floquet drive is however forbidden for time-reversal symmetric drives, and is a direct consequence of the zero net momentum carried by the Floquet Hamiltonian in this case.

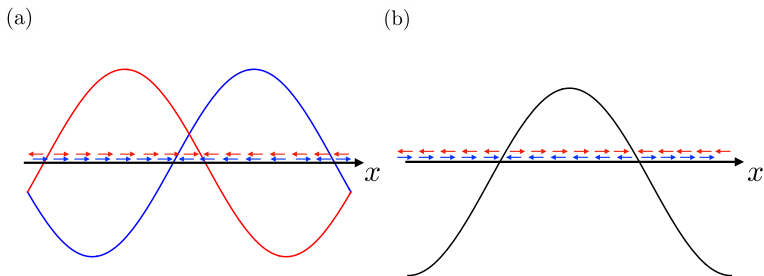


Figure 7.9: Quasiparticle picture for a quench with the $\mathfrak{sl}(2)$ Floquet Hamiltonian. (a) The Floquet Hamiltonian H_F for a non-time-reversal symmetric drive leads to different components $v_{\text{eff}}^-(x)$ and $v_{\text{eff}}^+(x)$ for chiral and anti-chiral sectors, see (7.61), as illustrated with the blue and red curves. In this case the Floquet velocities for both sectors are distinct, leading to two distinct fixed points for each chirality: one acts as a quasiparticle source and one as a sink. This leads to the emergence of two Floquet horizons at symmetric positions. (b) The Floquet Hamiltonian H_F for a time-reversal symmetric drive. In this case both Floquet velocities coincide, and are given by (7.67), such that the unstable fixed point of the chiral sector is the stable fixed point of the antichiral sector and vice-versa.

QUASIPERIODICALLY DRIVEN INHOMOGENEOUS CRITICAL SYSTEMS

8.1 INTRODUCTION

In this chapter, we study heating in a system with broken time and space translation symmetry. We uncover (i) a fractal phase diagram with lines of vanishing heating surrounded by regions of very slow heating and (ii) heating phases with a particular structure of hot-spots where the energy density increase nucleates. The latter finding demonstrates that even a heating regime can support non-trivial *emergent* structures as a system is driven towards the infinite-temperature fixed point. Our system breaks translation symmetry in space via a smooth deformation of hopping parameters, rather than short-range correlated disorder, and in time due to a quasiperiodic drive, which has also been in the focus of several other recent works that study (the absence of) heating [144–148]. Our quasiperiodic drive sequence is generated by a deterministic recursion relation that does not contain any periodic pattern. Such a protocol is inspired from quasi-crystals with a quasi-periodicity in space which have been intensively studied in the past [149, 150]. More precisely, here we study a protocol that alternates between homogeneous CFT and SSD according to the celebrated Fibonacci sequence. This results in an exactly solvable quasi-periodically driven interacting model.

Focusing on the evolution of the total energy and the Loschmidt echo, as in Chapter 7, we show that the energy (almost) always increases exponentially at large times while the Loschmidt echo decays exponentially. Both quantities are controlled by the same rate, called the Lyapunov exponent λ_L . Thus, the system generically and unsurprisingly heats up. However, we find that this happens with a remarkably broad range of heating rates, depending on the parameters of the drive. We observe fast heating areas analogous to the Floquet setup, as well as regions where the heating rate is very slow, with λ_L close to zero. Moreover, there exists a region of the parameter space where λ_L is exactly zero, so that the system escapes heating even at infinite times, but this region has a Cantor set fractal structure of zero measure. Forming a measure zero subspace, these regions are not directly accessible in the SSD case. However, they are evidenced by very slow heating neighborhoods in parameter space which remain non-heating for all experimentally and physically relevant time scales. We further show that quasiperiodic sequences with Hamiltonian deformations belonging to the elliptic class of the $\mathfrak{sl}(2)$ subalgebra of the Virasoro algebra lead to a direct access to such non-heating regions.

8.2 FIBONACCI WORD AS QUASIPERIODIC DRIVES

In this chapter we consider a specific type of quasiperiodic driving sequence inspired from the one-dimensional Fibonacci quasicrystals (see Sec. 8.4). More specifically, as in the previous chapter, we consider a spatial deformation of a

generic homogeneous $(1+1)$ -dimensional CFT with central charge c and of spatial extent L , defined by the Hamiltonian,

$$H[f] = \int_0^L dx v(x) T_{00}(x), \quad (8.1)$$

where $T_{00}(x)$ is the energy density of the CFT. As in the previous chapter, we will restrict to the $\mathfrak{sl}(2)$ subalgebra of the full Virasoro algebra. In the periodic

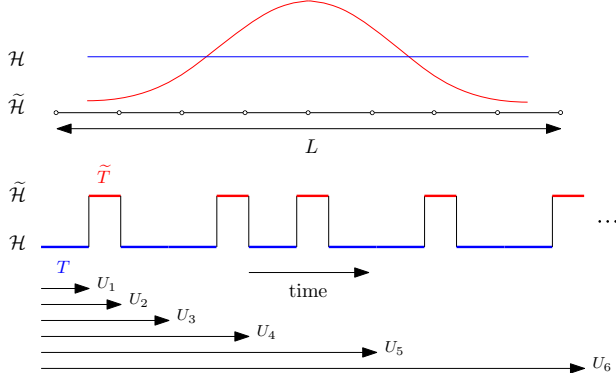


Figure 8.1: Top: Uniform Hamiltonian H and the SSD Hamiltonian \tilde{H} . Bottom: Fibonacci quasiperiodic drive. The time evolution follows the relation (8.2). At every Fibonacci step n , the time evolution involves F_{n+1} unitary operators comprising F_{n-1} times U_0 and F_n times U_1 .

case studied in Chapter 7, we have seen that the classification of Möbius transformations which encode the time evolution of primary fields over one period gives rise to a phase diagram comprising both heating and non-heating phases. On the other hand, in the limit of a purely random drive, the system was shown to lead to always heat up [132]. A natural question is what happens in the intermediate case, where the driving protocol is neither periodic nor completely random - i.e., the case of *quasiperiodic driving* where the drive is determined by a recursion relation, but for which one cannot extract any periodic pattern. We will address this question in the present chapter, for a particular choice of a quasiperiodic driving sequence, although the argument can be repeated to other examples of such a sequence [131]. In particular, a canonical choice for such a sequence is the Fibonacci driving, where the relevant recursion relation which determines the driving sequence is the Fibonacci word, defined in the context of quasicrystals as [144, 145]

$$U_{n+2} = U_n U_{n+1}. \quad (8.2)$$

As the Fibonacci word defines a binary sequence, we will pick two driving Hamiltonians defining the building blocks of the quasiperiodic drive: the uniform Hamiltonian H , and the SSD Hamiltonian \tilde{H} , both defined in Chapter 7. Furthermore, we will pick the initial conditions $U_0 = e^{-i\tilde{T}\tilde{H}}$ and $U_1 = e^{-iT\tilde{H}}$, where T and \tilde{T} are the periods of the stroboscopic steps with respectively H and \tilde{H} . Denoting the pulse associated to H as A and the pulse associated to \tilde{H}

as B , the first few terms in the driving sequence are $ABAABABAABABAAB\dots$, as illustrated on Fig. 8.1. Such a drive is fully characterized by only three parameters: (T, \tilde{T}, L) . In particular, the number of unitary operators at the step n is given by F_{n-1} for U_0 and F_n for U_1 , where F_n is the n -th Fibonacci number, giving F_{n+1} unitary operators at the step n . Therefore, the number of operators at the step n grows exponentially with n ; for large n , F_n scales as $\frac{\Phi^n}{\sqrt{5}}$, where $\Phi = \frac{1+\sqrt{5}}{2}$ is the Golden ratio. For practical purposes, we also introduce a “stroboscopic” time which counts the unitary operators one by one, that we denote by N . One way to count the evolution operators one by one is to introduce $\nu(N) \in \{0, 1\}$, with $\nu(N) = \lfloor (N+1)\Phi \rfloor - \lfloor N\Phi \rfloor - 1$. If $\nu(N) = 0$, the unitary operator which appears at step N is U_0 , and if $\nu(N) = 1$ the unitary operator at step N is U_1 . The main question is to understand whether a non-heating region can still survive in the quasiperiodic drive, or if only heating will exist as in the random case. An apparent difficulty in determining the existence of a non-heating regime for the quasiperiodic drive is the dynamics is not only encoded in a stroboscopic Hamiltonian as time-translation symmetry is fully broken and not discrete time-translation symmetry survives.

8.3 FINE STRUCTURE OF HEATING

The time evolution under the quasiperiodic drive is obtained in a similar way as for the periodic case: we first note that in the Heisenberg picture, the time evolution of any primary field $\Phi(x, \tilde{T}) = e^{i\tilde{H}\tilde{T}}\Phi(x, 0)e^{-i\tilde{H}\tilde{T}}$ amounts to a simple conformal mapping. This can be seen by: (i) rotating to imaginary time $t \rightarrow \tau$ and (ii) mapping the spacetime manifold to the complex plane with the exponential mapping $z = e^{\frac{2\pi(\tau+ix)}{L}}$ and finally, (iii) using the fact that the time evolution is encoded in a particular conformal transformation of the complex plane, denoted $\tilde{z}_0(z)$. Following this procedure, the full time evolution of the primary field Φ of conformal weight $h = \bar{h}$ is given by

$$\Phi(x, \tilde{\tau}) = \left(\frac{2\pi}{L} \right)^{2h} \left(\frac{\partial \tilde{z}_0}{\partial z} \right)^{2h} \left(\frac{\partial \bar{\tilde{z}}_0}{\partial \bar{z}} \right)^{2h} \Phi(\tilde{z}_0, \bar{\tilde{z}}_0), \quad (8.3)$$

with $\tilde{z}_0(z)$ given by a simple Möbius transformation

$$\tilde{z}_0(z) = \frac{(1 + \frac{\pi\tilde{\tau}}{L})z - \frac{\pi\tilde{\tau}}{L}}{\frac{\pi\tilde{\tau}}{L}z + (1 - \frac{\pi\tilde{\tau}}{L})}. \quad (8.4)$$

Similarly, the time evolution, with respect to H is a simple dilation in the complex plane, such that in (8.3), $\tilde{z}_0 \rightarrow \tilde{z}_1 = e^{\frac{2\pi\tau}{L}}z$. Consequently, the *Fibonacci time evolution* with the Fibonacci quasiperiodic drive amounts to composing the conformal mappings $\tilde{z}_1(z)$ and $\tilde{z}_0(z)$ following the recursion relation (8.2)

$$\tilde{z}_{n+2}(z) = \tilde{z}_n \circ \tilde{z}_{n+1}(z). \quad (8.5)$$

Equivalently, time evolution with the *stroboscopic time* N can also be obtained via the recursion relation

$$\tilde{z}_N(z) = \tilde{z}_{\nu(N)} \circ \tilde{z}_{N-1}(z). \quad (8.6)$$

The group properties of the invertible Möbius transformations directly imply that \tilde{z}_N is also a Möbius transformation for any step N . We can then introduce the matrices M_N with unit determinants associated to the conformal

transformations \tilde{z}_N , such that the stroboscopic time evolution amounts to a sequential multiplication of $SL(2, \mathbb{C})$ matrices with the recursion relation $M_N = M_{\nu(N)} M_{N-1}$, and for the Fibonacci times n such that $N = F_{n+1}$, the relation is $M_{n+2} = M_n M_{n+1}$ where

$$M_0 = \begin{pmatrix} 1 + \frac{i\pi\tilde{T}}{L} & -\frac{i\pi\tilde{T}}{L} \\ \frac{i\pi\tilde{T}}{L} & 1 - \frac{i\pi\tilde{T}}{L} \end{pmatrix}, \quad M_1 = \begin{pmatrix} e^{i\pi T/L} & 0 \\ 0 & e^{-i\pi T/L} \end{pmatrix},$$

and the general matrix after N steps is denoted by

$$M_N = \begin{pmatrix} \alpha_N & \beta_N \\ \gamma_N & \delta_N \end{pmatrix}. \quad (8.7)$$

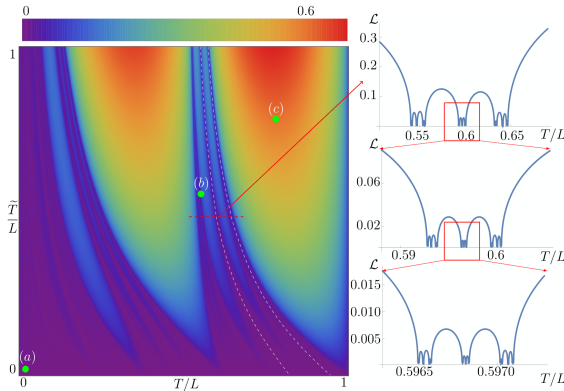


Figure 8.2: Phase diagram obtained from the Lyapunov exponent (Eq. (8.10)) for the Fibonacci drive. The high frequency regime around point (a) corresponds to non-heating phases whereas the bright regions, for instance around point (c), correspond to heating phases. For clarity, only two Cantor lines where the Lyapunov exponent is strictly zero are shown in this phase diagram. To elucidate the fractal structure of the phase diagram, we zoom successively across a representative horizontal cut indicated by the red dashed lines. As we approach the Cantor points embedded in this cut, the system starts to manifest slow heating concomitant with an increasing stroboscopic delocalization of the quasiparticle excitations. The three marked points marked (a),(b) and (c) represent these three regimes and will be extensively discussed in the rest of the chapter.

To diagnose heating in this quasiperiodic problem, we compute the time dependent energy density, $\mathcal{E}(x, t) = \langle \psi(t) | T_{00}(x) | \psi(t) \rangle$, where $|\psi(t)\rangle$ is the time evolved ground state $|G\rangle$ under the quasiperiodic drive. We choose our initial state $|G\rangle$ to be the ground state of the uniform CFT H with open boundary conditions. Such a state is in general not an eigenstate of \tilde{H} , and therefore the time evolution under the drive is non-trivial. For the sake of clarity, we now consider the case $T = \tilde{T}$. Using boundary CFT techniques, as outlined in Chapter 7, the total energy $E(t) = \int_0^L dx \mathcal{E}(x, t)$ computed at *stroboscopic times*

$t = NT$, depends solely on the matrix M_N and takes the following explicit form,

$$E(t = NT) = \frac{\pi c}{8L} \frac{\alpha_N \delta_N + \beta_N \gamma_N}{\alpha_N \delta_N - \beta_N \gamma_N}, \quad (8.8)$$

where c is the central charge of the CFT.

Another quantity of interest is the Loschmidt echo $F(t)$, as a measure of revival/coherent evolution in the system. It is determined by the overlap between the initial ground state $|\psi(0)\rangle = |G\rangle$, and its time evolved counterpart $|\psi(t)\rangle$, $F(t) = |\langle\psi(0)|\psi(t)\rangle|^2$ and can be easily accessed in the context of boundary-driven CFTs [58]. For any $|G\rangle = \lim_{z, \bar{z} \rightarrow 0} \Phi(z, \bar{z})|0\rangle$, where $\Phi(z, \bar{z})$ is a primary field of the boundary theory with conformal weights $(\Delta, \bar{\Delta})$, and $|0\rangle$ being the $SL(2, \mathbb{C})$ invariant vacuum, one obtains (see Chapter 7):

$$F(t = NT) = |\delta_N|^{-4(\Delta + \bar{\Delta})} \quad (8.9)$$

As we will show later, $E(t)$ and $F(t)$ are formally related and this will help a clear characterization of the physics induced by quasiperiodic driving. We note that the conformal weights $(\Delta, \bar{\Delta})$ of the primary field generating the ground state with open boundary conditions does not appear in the expression of the energy (8.8). This is a consequence of the fact that $\langle G|T(z)|G\rangle_{\mathbb{H}}$ evaluated on the upper-half plane \mathbb{H} , or equivalently on the unit disk vanishes because of rotational symmetry[72].

As in dynamical systems [151], the growth of stroboscopic total energy or the decay of the Loschmidt echo for a quasiperiodic drive can be characterized by a Lyapunov exponent λ_L defined by (see [152] for a review on Lyapunov exponents)

$$\lambda_L = \lim_{N \rightarrow \infty} \frac{1}{N} \log \text{Tr}(M_N)^2. \quad (8.10)$$

Equivalently, the corresponding exponent for the Fibonacci time reads $\lambda_L = \lim_{n \rightarrow \infty} \frac{1}{F_{n+1}} \log \text{Tr}(M_n)^2$. As we will show, if the Lyapunov exponent $\lambda_L > 0$, then the system will heat, and the heating rate is precisely given by λ_L . Since the structure of the matrix M is known, the Lyapunov exponent can be numerically computed for all T, \bar{T} , for a sufficient large number of iterations N . For the Fibonacci quasiperiodic drive, the Lyapunov exponent traces the phase diagram shown in Fig. 8.2. Different regions emerge, some of them correspond to a strong heating with high Lyapunov exponent, whereas other regions display a fractal structure and rather small values of the Lyapunov exponent. This raises the following questions: are these two regions heating and if yes, are they heating the same way? To answer these, we explicitly compute the stroboscopic evolution of the total energy $E(t)$ and the Loschmidt echo $F(t)$ using Eqs. (8.8) and (8.9).

First, note that in Eq. (8.7), $\alpha_N = \delta_N^*$ as $M_N \in SL(2, \mathbb{C})$ and because of the form of M_0 and M_1 . Parametrising $\alpha_N = R_N e^{i\phi_N}$, we obtain $\text{Tr}^2(M_N) = 4R_N^2 \cos^2(\phi_N)$ and the constraint that M_N has a unit determinant implies, $\alpha_N \delta_N - \beta_N \gamma_N = 1$, and $\alpha_N \delta_N + \beta_N \gamma_N = 2|\alpha_N|^2 - 1 = 2R_N^2 - 1$. Using these relations, the stroboscopic energy $E(t = NT)$ defined in Eq. (8.8) satisfies,

$$\text{Tr}(M_N)^2 = \left[\frac{16L}{\pi c} E(NT) + 2 \right] \cos^2(\phi_N). \quad (8.11)$$

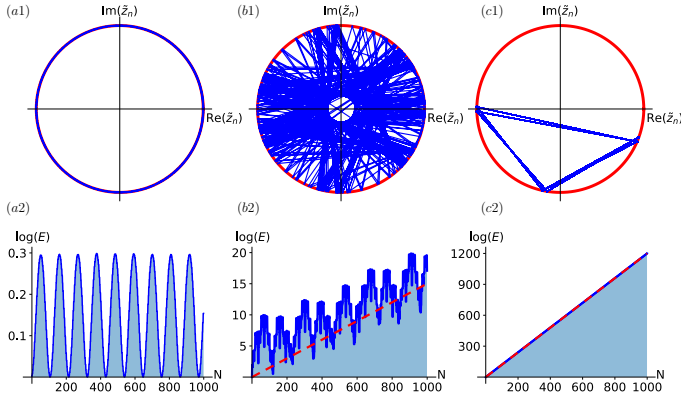


Figure 8.3: Top: Flow of the conformal mapping \tilde{z}_N when driven by the Fibonacci sequence with $T = \tilde{T}$ for upto $N = 1000$ and $L = 100$. With reference to the phase diagram: (a1) $T = 1$, in the high-frequency regime the system escapes heating and such a flow is dense on the unit circle. (b1) $T = 55.101$, in the slow heating regime, the excitation alternate between a large number of recurring regions. (c1) $T = 78$, as the system strongly heats up, the excitations localize in the system and \tilde{z}_N only has a few recurring points. Bottom: Stroboscopic time evolution of the logarithm of the total energy $E(t = NT)$, as a function of the number of iterations N . (a2) in the non-heating high-frequency regime the energy only oscillates, (b2) in the fractal regime the energy fluctuates and increases very slowly and (c2) in the heating regime the energy grows exponentially fast with minimal fluctuations. The red dashed lines correspond to the heating rates of the exponentially growing energy at long time, and is given by the Lyapunov exponent (8.10).

Similarly, the Loschmidt echo Eq. (8.9) can also be simplified and we obtain

$$F(t) = \left| \frac{\alpha_N \delta_N - \beta_N \gamma_N}{\delta_N^2} \right|^{2(\Delta+\bar{\Delta})} = \left(\frac{2}{\frac{8L}{\pi c} E(t) + 1} \right)^{2(\Delta+\bar{\Delta})}. \quad (8.12)$$

We now establish that the Lyapunov exponent λ_L is indeed the heating rate in the long time limit. From Eqs. (8.10) and (8.11), we see that the Lyapunov exponent

$$\lambda_L = \lim_{N \rightarrow \infty} \frac{1}{N} \log \left(\left[\frac{16L}{\pi c} E(t) + 2 \right] \cos^2(\phi_N) \right). \quad (8.13)$$

Since the oscillatory term $\lim_{N \rightarrow \infty} \frac{1}{N} \log(\cos^2(\phi_N))$ becomes negligible at long times, we infer that for an exponential growth of total energy, the Lyapunov exponent indeed determines the heating rate at long times:

$$\begin{cases} E(t) \underset{t \rightarrow \infty}{\sim} e^{\lambda_L t / T}, \\ F(t) \underset{t \rightarrow \infty}{\sim} e^{-2(\Delta+\bar{\Delta})\lambda_L t / T}. \end{cases} \quad (8.14)$$

This gives a physical meaning for the Lyapunov exponent, which sets the timescale after which the system will lose its coherence as the Loschmidt echo decays exponentially to 0.

In the case of a periodic drive, the stroboscopic evolution of E and F show one of three distinct behaviours: (i) E grows exponentially and F decays exponentially with time in the heating phase, (ii) E and F oscillate with time in the non-heating phase and (iii) E grows quadratically and F decays as a power law with time at the transition between the heating and non-heating regimes. The results for the quasiperiodic drive are summarised in Fig. 8.3 where we show three representative scenarios indicated by the dots (a, b, c) in Fig. 8.2. In the high frequency regime, $T, \tilde{T} \ll L$ in Fig. 8.3(a2), λ_L is very small and the total energy and the Loschmidt echo oscillate in time akin to the periodic case, illustrating that the system avoids heating for a very large number of drive cycles. In Fig. 8.3(c2), λ_L is large and we see standard heating i.e., exponential growth of energy concomitant with an exponential decay of the echo, modulo some oscillations that were not present in the periodic drive case. However, for the case of T, \tilde{T} corresponding to Fig. 8.3(b2) where λ_L changes sharply (see point (b) in Fig. 8.2) new behaviour emerges. We see that the energy mostly fluctuates and shows very slow growth, while the Loschmidt echo decays slowly and displays strong revivals. A fundamental question is then to understand if there exist regions in the phase diagram which can always avoid this exponential growth of energy even at arbitrary long times. We note that at the transition lines $T = kL$, for any $k \in \mathbb{N}$ and any \tilde{T} , $\lim_{N \rightarrow \infty} \tilde{z}_N = 1$, and the oscillatory term $\cos(\phi_N)^2 \sim \frac{1}{N^2}$ as N goes to infinity. Therefore this term is not negligible anymore and the energy will grow quadratically even though $\text{Tr}(M_N)^2$ is bounded, thus the Lyapunov exponent is zero. The Loschmidt echo is then decaying quadratically to 0 as a consequence of Eq. (8.12). Therefore the asymptotic formula (8.14) is not valid on the transition lines $T = kL$. We note that this quadratic growth of the total energy was already observed in periodic drive at $T = kL$ [23], together with a logarithmic growth of entanglement entropy. This dynamics effectively corresponds to a single quantum quench

with \tilde{H} . This can be understood from the quasiparticle picture: if $T = kL$, after the time evolution with H , the quasiparticles will go back to their initial positions. Therefore effectively the system only evolves with \tilde{H} , implying that all the energy of the system accumulate at the edges of the system, and grow quadratically.

The behaviour of the energy and the echo are dictated by the stroboscopic evolution of the Möbius transformations \tilde{z}_N given by Eq. (8.6). For periodic driving, the non-heating phase is characterized by a \tilde{z}_N which oscillates with N and an periodically oscillating energy [23]. In the heating phase, \tilde{z}_N converges to a stable fixed point, $\lim_{n \rightarrow \infty} \tilde{z}_N = \gamma_1$, where $\gamma_{1,2}$ are respectively the stable and unstable fixed points of the 1-cycle Möbius transformation. This in turn leads to the creation of two stroboscopic horizons at spatial points x_c and $L - x_c$ determined by the unstable fixed point of the Möbius transformation, $\gamma_2 = e^{2\pi i x_c/L}$ and $\gamma_2^* = e^{2\pi i (L-x_c)/L}$ at which the energy accumulates at large times. For quasiperiodic driving the situation is more subtle. In the high frequency regime, \tilde{z}_N traces the unit circle with increasing N . The total energy oscillates periodically in this parameter regime [see Fig. 8.3(a1)]. In regimes where the Lyapunov exponent is large, \tilde{z}_N almost converges to a fixed point like scenario but alternates between a small set of points , cf. Fig. 8.3(c1) resulting in small fluctuations of the energy. The extreme case of this subset comprising only one point, corresponds to the heating regime of the periodic drive discussed earlier. As the value of the Lyapunov exponent decreases and approaches parameter zones where the fractal nature of λ_L becomes apparent, the flow of \tilde{z}_N becomes more and more dense on the unit circle as seen in Fig. 8.3(b1), leading to strong fluctuations concomitant with a very slow growth of the total energy. It is in these regimes that interesting slow dynamics manifests.

8.4 MAPPING TO QUASICRYSTALS

The fractal structure of λ_L in Fig. 8.2 as a function of T, \tilde{T} is reminiscent of the spectra of a one dimensional Fibonacci quasiperiodic crystal [153, 154]. In this section, we will demonstrate that the fractality of λ_L in our Fibonacci quasiperiodic drive of the CFT can indeed be related to the spectral properties of the Fibonacci chain. In fact, the quasiperiodicity introduced by the Fibonacci sequence has been widely studied in the context of one dimensional quasicrystal literature [153, 155, 156]. The problem of finding the spectrum of a quasiperiodic Schrödinger operator for this type of one-dimensionnal quasicrystal can be solved using the Fibonacci trace map approach. The tight-binding Hamiltonian matrix describing the quasiperiodic Fibonacci chain is [157]

$$H_{mn} = \delta_{m,n+1} + \delta_{m+1,n} + \delta_{m,n} \lambda v(n), \quad (8.15)$$

where $v(n) = |\nu(n-1) - 1|$. The one dimensional Fibonacci quasicrystal is described by the Schrodinger equation

$$\psi_{n-1} + \psi_{n+1} + v(n)\psi_n = E\psi_n. \quad (8.16)$$

The Schrodinger equation can be rewritten using transfer matrices as

$$\begin{pmatrix} \psi_{n+1} \\ \psi_n \end{pmatrix} = T(n) \begin{pmatrix} \psi_n \\ \psi_{n-1} \end{pmatrix} = \begin{pmatrix} E - v(n) & -1 \\ 1 & 0 \end{pmatrix} \begin{pmatrix} \psi_n \\ \psi_{n-1} \end{pmatrix}. \quad (8.17)$$

This can be iterated, such that finding the eigenvectors ψ_n amounts to finding the product of n matrices $T(n)$, defined as

$$T_j = \prod_{i=1}^{F_j} T(i). \quad (8.18)$$

It is straightforward to show that for $T_j \in SL(2, \mathbb{C})$, the following recursion holds

$$T_{j+1} = T_{j-1} T_j. \quad (8.19)$$

Alternatively this relation on the transfer matrices can be rewritten in terms of the trace of the matrices as

$$\text{Tr}(T_{j+1}) = \text{Tr}(T_j) \text{Tr}(T_{j-1}) - \text{Tr}(T_{j-2}). \quad (8.20)$$

Therefore writing $x_j = \frac{1}{2}\text{Tr}(T_j)$, this defines a non-linear dynamical system whose expression is

$$x_{j+1} = 2x_j x_{j-1} - x_{j-2}. \quad (8.21)$$

For notational convenience, we further introduce $y_j = \frac{1}{2}\text{Tr}(T_{j+1})$ and $z_j = \frac{1}{2}\text{Tr}(T_{j+2})$. We can then define a discrete dynamical map \mathcal{T}

$$\mathcal{T} : \mathbb{R}^3 \rightarrow \mathbb{R}^3, \quad (x_i, y_i, z_i) \mapsto (y_i, z_i, 2y_i z_i - x_i). \quad (8.22)$$

This mapping has been introduced in the quasicrystal literature as the *Fibonacci trace map*. The mathematical structure of such a mapping has been studied in e.g [154, 155, 157–160]. A crucial property of the Fibonacci trace map is that it admits a quadratic invariant $I(x_j, y_j, z_j)$:

$$I(x_j, y_j, z_j) = x_j^2 + y_j^2 + z_j^2 - 2x_j y_j z_j - 1, \quad (8.23)$$

which is the same for any $j \in \mathbb{N}$. It is then natural to consider the cubic level surfaces

$$S_V = \{(x, y, z) \in \mathbb{R}^3 \mid I(x, y, z) = V\}. \quad (8.24)$$

The surfaces S_V have different topologies depending on the sign of V . The manifold is noncompact for $V > 0$. At $V = 0$ the middle part of the manifold is compact and touches the other 4 non compact components at a single point, and the resulting surface S_0 is called the Cayley cubic. For $V < 0$ the middle part is completely detached from the 4 noncompact components. These three different topologies are illustrated on Fig.8.4. In the case of the Fibonacci quasicrystal (8.15), the invariant is always positive and given by $V = \frac{\lambda^2}{4} \geq 0$. In other words, the trace maps of the Fibonacci quasicrystal leaves on a manifold that has a topology of the form of Fig. 8.4(a). One can then study the set of bounded orbits under infinite iterations of the Fibonacci trace map (8.22), starting from the initial point $(1, \frac{E}{2}, \frac{E-\lambda}{2})$. In order to make the connection between the orbits of the Fibonacci trace map and the spectrum E of the Fibonacci Hamiltonian, the following theorem has been proved in [157]:

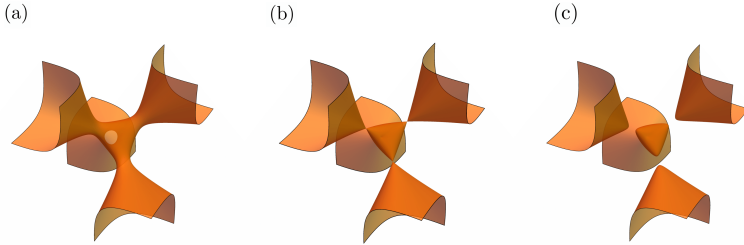


Figure 8.4: Three different types of topologies for the surface levels S_V . (a) $V = 0.5$ and the manifold is non-compact with the four quadrants connected at the center, (b) $V = 0$, in this case the four quadrants are connected through a single point to the compact manifold at the center, (c) $V = -0.1$, the compact manifold in the center is fully disconnected from the four quadrants.

Theorem 1 An energy $E \in \mathbb{R}$ belongs to the spectrum of the Fibonacci Hamiltonian (8.15) if and only if the positive semiorbit of the point $(1, \frac{E}{2}, \frac{E-\lambda}{2})$ under iterates of the trace map \mathcal{T} is bounded.

Therefore finding the set of bounded orbit under the Fibonacci trace map is sufficient to determine the spectrum of the Fibonacci quasicrystal (8.15). The study of the bounded orbits under the trace map led to the following result:

Theorem 2 The set of bounded orbits is a Cantor set for $\lambda > 0$.

This result leads to the conclusion that the spectrum (8.15) is a fractal set similar to a Cantor set, of measure zero in parameter space. It has been first proved for $\lambda \geq 4$ in [157], and then for any $\lambda > 0$ in [161].

Based on the fact that the time evolution of the quasiperiodic Fibonacci drive is encoded in products of $SL(2, \mathbb{C})$ matrices M_n obeying the Fibonacci sequence $M_{n+1} = M_{n-1}M_n$, we expect M_n to satisfy a trace relation analogous to (8.20). This implies that the trace of the matrix M_n encoding the time evolution after F_{n+1} iterations is completely determined by the orbit of the trace map (8.22). For the SSD quasiperiodic drive, The initial point is simply given by

$$\left(1, \cos\left(\frac{\pi T}{L}\right), \cos\left(\frac{\pi T}{L}\right) - \frac{\pi \tilde{T}}{L} \sin\left(\frac{\pi T}{L}\right)\right), \quad (8.25)$$

and the corresponding invariant is

$$I = \left[\frac{\pi \tilde{T}}{L}\right]^2 \sin^2\left(\frac{\pi T}{L}\right) > 0. \quad (8.26)$$

Clearly this invariant is strictly positive, and the associated manifold explored by the trace map is

$$\left\{(x, y, z) \in \mathbb{R}^3 \mid I(x, y, z) = \left[\frac{\pi \tilde{T}}{L}\right]^2 \sin^2\left(\frac{\pi T}{L}\right)\right\}. \quad (8.27)$$

This manifold is thus noncompact, as in the case of the Fibonacci quasicrystal, as shown in Fig. 8.4(a). As we iterate the trace map, orbits typically originate

in the central region of the manifold and escape to infinity with a particular escape rate. As in the Fibonacci chain, a sufficient condition for an orbit to escape to infinity is that at some step j one satisfies [154]

$$\begin{cases} |x_j| > 1, \\ |x_{j-1}| > 1, \\ |x_{j-1}| |x_j| > |x_{j-2}|. \end{cases} \quad (8.28)$$

A particular case of a bounded orbit is the trivial fixed point $(1, 1, 1)$ of the trace map (8.22), which corresponds to the limits $T/L = \tilde{T}/L = 0$ for the Fibonacci drive. This fixed point acts as a saddle point: some points in its vicinity will stay bounded for a very large number of iterations of the trace map, whereas some other points will be strongly repelled, i.e., their orbit will escape quickly. This is characteristic of the high frequency limit $T/L, \tilde{T}/L \ll 1$: if $T > 0$, $(1, 1, 1)$ acts as an attractor and the trace of the M_n stays bounded under T for a large number of iterations, as seen on Fig. 8.5. The system thus avoids heating for times which are longer than physically relevant timescales. In the case $T < 0$, or equivalently taking $H = -H[1]$, the orbits diverge away from $(1, 1, 1)$ and the system heats up only after a few iterations of n . Consequently, due to its proximity to the fixed point $(1, 1, 1)$ of the Fibonacci trace map, we expect a robust high-frequency expansion for the Fibonacci quasiperiodically driven problem. A second particular case is the family of transition lines $T/L \in \mathbb{N}$, with arbitrary \tilde{T}/L , for which the initial point is $(1, \pm 1, \pm 1)$, which orbit is bounded. Therefore at those particular lines $\text{Tr}(M_n)$ stays bounded, however as discussed in the previous section the oscillatory term in Eq. (8.13) is not negligible anymore and the energy grows quadratically, as for a single quench with the Hamiltonian \tilde{H} .

The case for arbitrary T/L and \tilde{T}/L is more subtle. The trace map discussed above helps us make the following identifications between the driven case and the one dimensional quasicrystal:

$$\begin{cases} E = 2 \cos\left(\frac{\pi T}{L}\right), \\ \lambda = \frac{2\pi\tilde{T}}{L} \sin\left(\frac{\pi T}{L}\right). \end{cases} \quad (8.29)$$

Note that in the Fibonacci crystal, the spectrum E of the system for any positive λ is a Cantor set. This means that for a given λ , any $E \in \text{spec}(H) \cap [-2, 2]$ specifies a particular value of T/L and \tilde{T}/L such that $\text{Tr}(M_n)$ stays bounded for an *infinite* number of iterations of the trace map, i.e., infinite stroboscopic and Fibonacci times. The spectrum E for a given value of the coupling λ defines the points in the T, \tilde{T} phase diagram at which no heating takes place under the quasiperiodic driving at Fibonacci steps n , as illustrated on Fig. 8.6. The non-heating regime forms a Cantor set for a fixed value of T and have sub-dimensional line-like locus in the parameter space. We refer to these as the *non-heating lines*. This also explains the fractal structure of the phase diagram where the Lyapunov exponents approach 0 (8.22). Gaps in $E(\lambda)$ correspond to regions with high Lyapunov exponents in Fig. 8.2, concomitant with strong heating. In this regime, the orbits of the trace map or equivalently, $\text{Tr}(M_n)$ diverges super-exponentially once it leaves the bounded central zone. A correct numerical evaluation of the Lyapunov exponent (8.10) requires that we consider

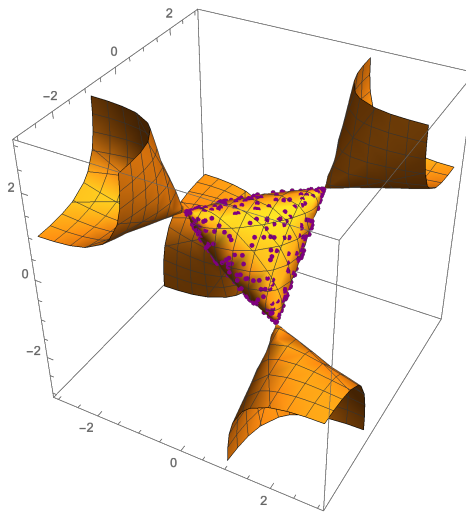


Figure 8.5: Flow of the Fibonacci trace map in the high frequency phase, for $L = 100$ and $T = \tilde{T} = 1$, for 500 iterations of the trace map. In this region, the trace map (8.22) stays bounded within the central part of the manifold (8.27) determined by the invariant (8.26) for a very large number of iterations. In the other regimes, this map will typically be unbounded, apart from a set of parameters of measure 0.

n for which $\text{Tr}(M_n)$ has already escaped, i.e., satisfies the conditions (8.28). To summarize, we see that since non-heating points constitute a Cantor set of measure zero, the quasiperiodically driven CFT will typically heat up for arbitrary (T, \tilde{T}, L) .

8.5 EXCEPTIONS TO HEATING

We have seen in the previous sections that in the case of a Fibonacci quasiperiodic drive between a homogeneous and a SSD Hamiltonian the parameter space comprises fractal lines that escape exponential growth of the energy. However, by the fractal nature of such lines, finding studying the dynamics exactly at these fine-tuned points is challenging. We will now provide another class of quasiperiodic drive where the dynamics at a single point in parameter space can be studied analytically. This class of drives alternates between the homogeneous Hamiltonian H and the class of elliptic (or ‘‘Möbius’’) deformations

$$\tilde{H}_\theta = \int_0^L \left[1 - \tanh(2\theta) \cos\left(\frac{2\pi x}{L}\right) \right] T_{00}(x) dx. \quad (8.30)$$

The resulting phase diagrams displaying the Lyapunov exponent for a few choices of θ are shown in Fig. 8.7. We note that the phase diagrams are periodic both in T/L as well as \tilde{T}/L directions, in contrast with the SSD quasiperiodic drive which is only periodic in the T/L directions, as the periodicity induced by the SSD Hamiltonian is infinite, which is recovered by taking the limit $\theta \rightarrow \infty$.

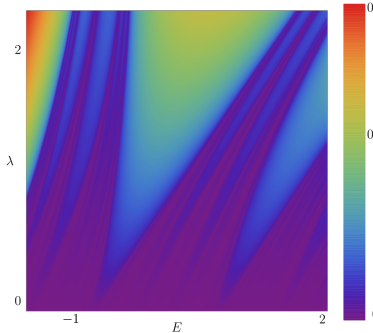


Figure 8.6: Lyapunov exponent as a function of the spectrum E and the parameter λ , using the correspondence (8.29). This Figure exactly reproduces the Figure for the spectrum $E(\lambda)$ of the Fibonacci quasicrystal, which can be found in [162]. Here, regions of non-zero Lyapunov exponent are dense for $\lambda > 0$ and correspond to gaps in the spectrum. The spectrum itself consists in regions of vanishing Lyapunov exponent, of measure zero. In that view, the spectrum of the quasicrystal maps to the non-heating lines of the quasiperiodically driven system, and spectral gaps map to the heating phase.

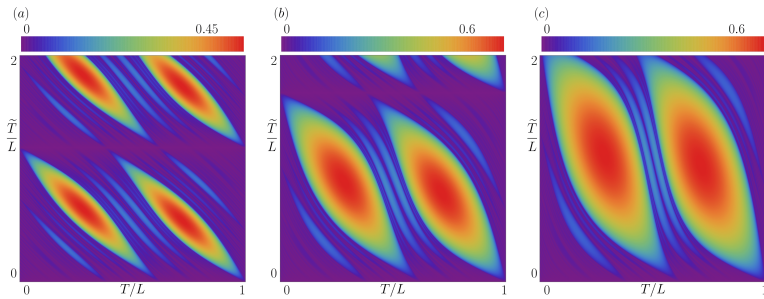


Figure 8.7: Möbius phase diagrams obtained from the Lyapunov exponent given by Eq. (8.10) for the Fibonacci quasiperiodic drive between H and \tilde{H}_θ for (a) $\theta = 0.3$, (b) $\theta = 0.55$, (c) $\theta = 0.7$.

These phase diagrams also display an emergent fractal structure where the Lyapunov exponent takes arbitrary small values. We also note that one can compute the invariant of the Fibonacci trace map associated, which is

$$I = \sin^2\left(\frac{\pi T}{L}\right) \sin^2\left(\frac{\pi \tilde{T}}{L} \operatorname{sech}(2\theta)\right) \sinh(2\theta)^2. \quad (8.31)$$

It is straightforward to verify that in the SSD limit one recovers the invariant (8.26). Once again the invariant is positive for any choice of driving parameters, and therefore the set of bounded orbits under the Fibonacci trace map still forms a fractal set, which will get denser as $\theta \rightarrow 0$. We note that the explicit mapping to the Fibonacci quasi-crystal, given by Eq. (8.29) for

the SSD quasiperiodic drive, cannot be explicitly found in the case of finite θ . However, the center of the unit cell of the phase diagram, $[0, 1] \times [0, \tanh(2\theta)]$, given by the exceptional point

$$\left(\frac{T}{L}, \frac{\tilde{T}}{L}\right) = \left(\frac{1}{2}, \frac{\tanh 2\theta}{2}\right), \quad (8.32)$$

belongs to the fractal set whose orbits are bounded under the Fibonacci trace map. Studying the properties of this point thus enables us to unravel the physics *exactly* at the lines that avoid exponential growth of energy. One finds that at this special point, the energy grows as a power law (instead of the usual exponential growth) at non-Fibonacci times, and the Loschmidt echo decays as a power law of the same power. On the other hand, at the exact Fibonacci times F_n , both energy and Loschmidt echo are periodic of period 6, $E(F_n) = E(F_{n+6})$ and $F(F_n) = F(F_{n+6})$. This directly implies that at such exceptional points, there always exist arbitrarily long times at which the system goes back to its initial state, despite the polynomial growth of energy at the most of the other times. We note that such exceptional points can always be found as long as the two Hamiltonians forming the Fibonacci words belong to the elliptic $\mathfrak{sl}(2)$ class.

8.6 QUASIPARTICLE PICTURE AND LATTICE CALCULATIONS

In this section, we discuss the physical significance of the fractality of the phase diagram and the associated flows of the Möbius transformations presented previously. As seen earlier, in the three representative cases for the Lyapunov exponents, the growth of energy as well as the Loschmidt echo manifest important differences stemming from the nature of the flows. We will now show that the structure of these flows are indeed crucial to understanding the nature of the heating. This is easily done in the quasiparticle picture, where one can track the time evolution of spatial distribution of the excitations. First, note that as we are dealing with a CFT, during time evolution with the uniform Hamiltonian \mathcal{H} , the excitations which are ballistic trace straight lines in spacetime. Choosing $T = \tilde{T}$, a quasiparticle located at x_0 at $t = 0$ will reach $\pm x(T) = x_0 \pm T$ at $t = T$, where the \pm corresponds to right and left movers respectively (the velocity has been set to one). Similarly, for a time evolution with the SSD Hamiltonian $\tilde{\mathcal{H}}$, the excitations follow null geodesics in a curved spacetime determined by the spatial inhomogeneity [121],

$$\pm x_N = \frac{L}{\pi} \text{arccot} \left(\mp \frac{2\pi T}{L} + \cot \left(\frac{\pi x_{N-1}}{L} \right) \right), \quad (8.33)$$

where we denote $x_N := x(t = NT)$. The stroboscopic position x_N of the quasiparticles for any initial position x_0 can now be obtained by concatenating the curved space geodesics and the straight lines in a sequence fixed by the Fibonacci drive.

We find three representative behaviours depending on the values of $T = \tilde{T}$. In the high frequency regime where the flow is periodic and does not have fixed points and the Lyapunov exponent $\lambda_L \sim 0$, the excitations evolve periodically in time akin to the energy for accessible time scales as seen on Fig. 8.8(a1). In the opposing regime of large λ_L , we see that after a few cycles of the quasiperiodic drive, the trajectories of the excitations collapse onto a unique trajectory

independent of the choice of initial conditions, leading to a localization effect. This trajectory alternates between a finite number of fixed points at stroboscopic times, as seen on Fig. 8.8(c1). Such fixed points of the stroboscopic trajectories of the quasiparticles are given by the flow of \tilde{z}_n on Fig. 8.3(c1). This is similar to the coherent heating phase of the periodic drive, for which the excitations at stroboscopic times localize at two points in space, understood as horizons. The energy grows exponentially with time at these fixed points, whose positions depend on the parameters of the drive.

However, in the fractal region of the phase diagram for the quasiperiodic drive, Fig. 8.8(b1), the situation is more complex. As before, the propagation of the excitations depends on the initial conditions upto a transient time t_0 , and the total energy in the system does not increase significantly. After this transient period, the excitations all follow the same trajectory independently of their initial position and localize, but the principal difference with the high Lyapunov case is the manifestation of a large number of recurring points at stroboscopic times see Fig. 8.8(b1). As one approaches a point in the Cantor set where $\lambda_L = 0$ the flow diagram Fig. 8.8(b1) is densely filled. Here, we expect this transient time $t_0 \rightarrow \infty$ concomitant with very slow increase of the energy. This slow dynamical evolution can be understood by noting that at the Cantor points the trace map remains bounded for all times. Since $\text{Tr}(M_n)^2$ also remains bounded, the energy given by (8.11), cannot diverge at Fibonacci steps. To summarise, we see that by tuning the parameters of the drive T and \tilde{T} we can encounter regions with fast heating, with a localization of the excitations, as well as regions with very slow heating, where excitations remain delocalized for large times, as opposed to a purely random drive.

We now present numerical results on the free fermion chain for the Loschmidt echo. The quasiperiodic drive is induced by the two Hamiltonians given by

$$\begin{cases} H = \frac{1}{2} \sum_{i=1}^{L-1} c_i^\dagger c_{i+1} + \text{h.c.}, \\ \tilde{H} = \sum_{i=1}^{L-1} \sin^2\left(\frac{\pi i}{L}\right) c_i^\dagger c_{i+1} + \text{h.c.}, \end{cases} \quad (8.34)$$

where c_i and c_i^\dagger are fermionic operators satisfying the usual anticommutation rules. Then, following the strategy of [123], one can get the stroboscopic time evolution under the quasiperiodic drive, starting from the ground state with open boundary conditions $|G\rangle$. The Loschmidt echo can then be computed numerically, $F(NT) = |\langle G|U(NT)|G\rangle|^2$, and we compare it to the CFT prediction, given by Eq. (8.9). The explicit comparison is shown in Fig. 8.8. In the high-frequency domain, Fig. 8.8(a2) as well as in the high Lyapunov region, Fig. 8.8(c2), the agreement between the CFT predictions and the free fermion numerics is remarkable for a large number of steps. In the fractal region, characterized by low Lyapunov exponent, the agreement is less striking as observed on Fig. 8.8(b2). Indeed in this region the Loschmidt echo scales very differently depending on the size of the system, making the explicit comparison with the CFT more complicated, even though the overall scaling of the Loschmidt echo is correctly captured by the CFT. This strong dependence on the system size in the fractal region of the phase diagram can be explained by the strong dependence of the Lyapunov exponent with T . Changing the size of the system L while keeping T/L fixed has the effect of redefining T . On the lattice such a redefinition can lead to non negligible changes in the Lyapunov exponent in the fractal region, changing the scaling of the Loschmidt echo.

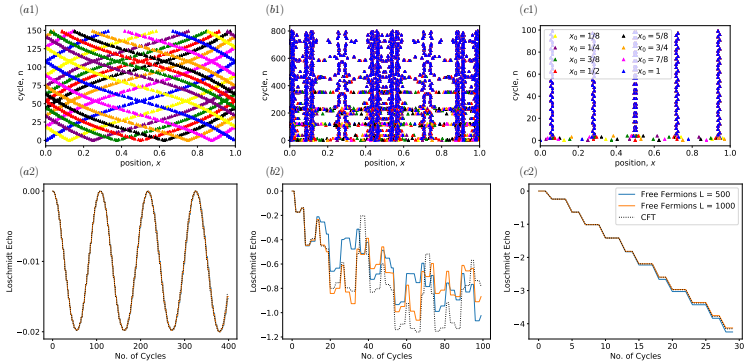


Figure 8.8: Top: Stroboscopic quasiparticle evolution as a function of both space and time predicted by the CFT for a variety of initial conditions. (a1) High frequency phase, $T/L = 0.01$, where the quasiparticle excitations evolve ballistically in an effective curved spacetime (b1) Fractal region, $T/L = 0.55101$. Beyond a transient time of approximately 400 stroboscopic steps, the quasiparticle trajectories collapse onto a unique trajectory independent of the initial conditions. The quasiparticles stroboscopically explore more and more regions of space as one approaches the Cantor line. (c1) High Lyapunov region, $T/L = 0.78$. Here, for all initial conditions and after very few time steps the time evolution collapses onto a single trajectory alternating between a few fixed points. Bottom: A comparison between CFT prediction for the Loschmidt echo (Eq. (8.9)) for the quasiperiodically driven CFT and the analogous quantity for free fermions hopping on a lattice, given by Eq. (8.34), for the three different regimes. In the high-frequency regime (a2) both completely agree. In the strongly heating (c2) regime they agree for a large number of stroboscopic steps. In the slow-heating regime (b2), because of the fractal structure of the phase diagram the numerical results strongly depend on the number of lattice sites.

The CFT and the free fermion chain are in good agreement for the total energy $E(t = NT)$ in the high-frequency regime, as the energy only oscillates and does not grow exponentially. However as long as the system starts to heat up, the description of the CFT might deviate at long times as it describes the low energy sector of the free fermion chain.

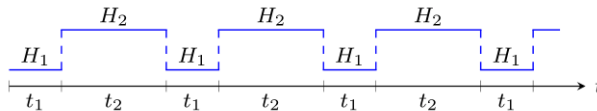
A GEOMETRIC APPROACH TO INHOMOGENEOUS
FLOQUET DYNAMICS

9.1 SETTING AND GENERAL APPROACH

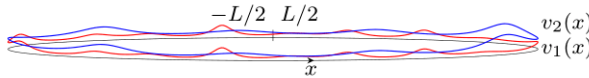
In this chapter we now turn to the study of Floquet dynamics for *arbitrary* deformations $v(x)$ of the energy density, provided such deformations are positive and smooth. This provides a generalization of the approach of the previous chapters, where the deformations of the energy density were always defined from a single Fourier mode, such that the underlying algebra of the Floquet problem was $\mathfrak{su}(1,1)$. For simplicity, we present our approach by using it to study 2-step Floquet drives for general smoothly deformed CFTs with periodic boundary conditions. The time evolution is under a Hamiltonian that equals H_1 or H_2 for times $T_1, T_2 \in \mathbb{R}$ ¹, respectively, see Fig. 9.1(a). The associated Floquet operator is

$$U_F = e^{-iH_1T_1}e^{-iH_2T_2} \quad (9.1)$$

and the period for a full cycle is $t_{\text{cyc}} = |T_1| + |T_2|$. Here, H_1 and H_2 are given by any smooth deformation of standard Minkowskian CFT on the cylinder $\mathbb{R} \times [-L/2, L/2]$.



(a) 2-step Floquet drive between Hamiltonians H_1 and H_2 .



(b) Inhomogeneous smooth velocities $v_{1,2}(x)$ of $H_{1,2}$.

Figure 9.1: Illustrations for our inhomogeneous Floquet drive.

We refer to the above general smoothly deformed CFT as *inhomogeneous CFT* [163–165]. They are defined by

$$H_{1,2} = \int_{-L/2}^{L/2} dx v_{1,2}(x) [T_+(x) + T_-(x)] \quad (9.2)$$

for smooth velocity functions $v_{1,2}(x) = v_{1,2}(x + L) > 0$, see Fig. 9.1(b), where $T_{\pm}(x) = T_{\pm}(x + L)$ are the usual light-cone components of the energy-momentum tensor of a 2-dimensional Minkowskian CFT. We stress that in this chapter only we make use of the notation T_{\pm} instead of T and \bar{T} to denote the

¹ One could restrict to $t_{1,2} \geq 0$ but our results will be true for all $t_{1,2} \in \mathbb{R}$.

holomorphic and antiholomorphic parts of the stress tensor, as we make use of Minkowskian CFT instead of Euclidean CFT. The latter satisfy

$$\begin{aligned} [T_{\pm}(x), T_{\pm}(y)] &= \mp 2i\delta'(x-y)T_{\pm}(y) \pm i\delta(x-y)T'_{\pm}(y) \\ &\quad \pm (c/24\pi)i\delta'''(x-y) \end{aligned} \quad (9.3)$$

and $[T_{\pm}(x), T_{\mp}(y)] = 0$, where c is the central charge of the CFT and the subscript $(-)$ denotes the right- (left-) moving component. These commutation relations correspond to two commuting copies of the Virasoro algebra. Using the conventions of this chapter, the Virasoro generators L_n^{\pm} , $n \in \mathbb{Z}$, are formally given by

$$T_{\pm}(x) = \frac{2\pi}{L^2} \sum_{n=-\infty}^{\infty} e^{\pm \frac{2\pi i n x}{L}} \left(L_n^{\pm} - \frac{c}{24} \delta_{n,0} \right) \quad (9.4)$$

and satisfy

$$[L_n^{\pm}, L_m^{\pm}] = (n-m)L_{n+m}^{\pm} + \frac{c}{12}(n^3 - n)\delta_{n+m,0} \quad (9.5)$$

and $[L_n^+, L_m^-] = 0$.

The deformations in our inhomogeneous CFTs are contained in $v_{1,2}(x)$, with constant velocity corresponding to standard homogeneous CFT. It is convenient to write $v_{1,2}(x) = v_{1,2}w_{1,2}(x/L)$ for constants $v_{1,2} > 0$ and dimensionless functions $w_{1,2}(\xi)$ of $\xi = x/L$, see Table 9.1 for a selection of examples. We also introduce dimensionless times $\tau_{1,2} = v_{1,2}t_{1,2}/L$ as the true independent parameters used to plot phase diagrams, see Fig. 9.2. The general structure of such phase diagrams is as follows: There are *leaf-shaped regions* where the system heats up, characterized by fixed or higher-periodic points of coordinate transformations encoding the time evolution, surrounded by regions where the system does not heat up. Moreover, the diagrams are invariant under:

1. changing (τ_1, τ_2) to $(-\tau_1, -\tau_2)$,
2. translations in τ_1 by $1/k_2 w_{1,0}$,
3. translations in τ_2 by $1/k_1 w_{2,0}$,

where $w_{j,0}^{-1}$ is given by $w_{j,0}^{-1} = \int_{-1/2}^{1/2} d\xi w_j(\xi)^{-1}$ and k_j^{-1} is the period of $w_j(\xi)$ for $j = 1, 2$. [If $w_j(\xi)$ is constant, we set $k_j = 1$.] The above follow from general properties for our periodic points that we will prove.

The geometric approach we propose is precisely the above mentioned reduction to studying coordinate transformations. Here, the latter will be shown to be given by orientation-preserving diffeomorphisms of the circle obtained directly from the velocities $v_{1,2}(x)$. We stress that the choice of a 2-step drive is for concreteness and simplicity: Our geometric approach is straightforwardly applicable to more general drives, including multi-step, random, chaotic, and quasi-periodic ones, cf., e.g., [24, 128, 131]. Indeed, how to use our tools to study random deformations was recently demonstrated in [164]. It can also be generalized to several coupled or uncoupled CFTs with different deformations and drives (the case here is equivalent to two uncoupled chiral CFTs with the same drive). As is well known, an inescapable issue is that a CFT description of a given condensed matter system, in general, starts to lose validity as it heats

Example	$w(\xi)$	Parameters
Ex. 1	$1 + g[2 \cos^2(\pi\xi) - 1]$	$g \in [0, 1)$
Ex. 2	$Ae^{-(\xi/d)^2}$	$A, d \in \mathbb{R}^+$
Ex. 3	$1/[1 - g \cosh(\xi/d)^{-2}]$	$g \in (-1, 1), d \in \mathbb{R}^+$
Ex. 4	$a/[b + \sin(2\pi k\xi) + \cos(2\pi\xi)]$	$a > 0, b > 2, k \in \mathbb{Z}^+$

Table 9.1: Examples of deformations $w(\xi)$ for $\xi = x/L$, including SSD CFT (obtained from Ex. 1 as $g \rightarrow 1^-$) and by a Gaussian (Ex. 2). Periodicity is imposed at $\xi = \pm 1/2$ if not manifest.

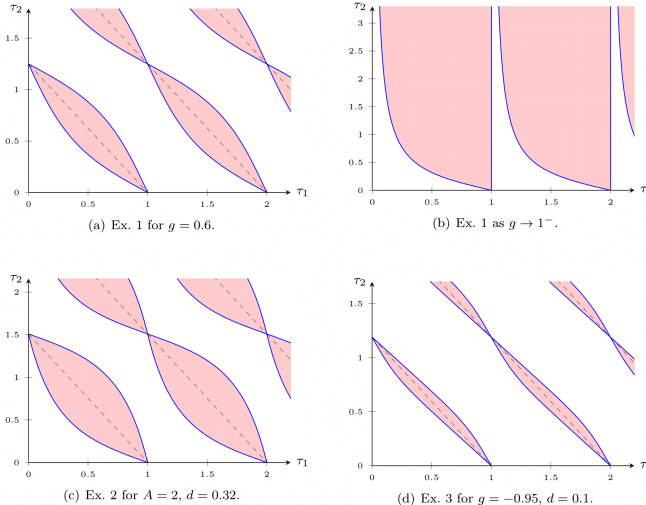


Figure 9.2: Phase diagrams in (τ_1, τ_2) -space for H_1 with $v_1(x) = v_1$ and H_2 with $v_2(x) = v_2 w_2(x/L)$ in Table 9.1: (a)–(b) Ex. 1, (c) Ex. 2, and (d) Ex. 3. Blue lines signify transitions between non-heating (white regions) and heating (pink regions), obtained by solving (9.6)–(9.7) analytically. Black dashed lines are given by $\tau_2 = m/k_1 w_{2,0} - (k_2 w_{1,0}/k_1 w_{2,0})\tau_1$ for $m \in \mathbb{Z}$.

up since the system leaves the low-temperature regime. Nonetheless, we expect that our approach and underlying ideas have wider applicability, even beyond CFT. For instance, periodic points in the CFT description may prove to be robust to higher excitations, or the latter may be taken into account by other means. Our approach is also suitable for numerical implementations, and we hope that it can be adapted or serve as inspiration for a wide range of other Floquet systems, e.g., for driven Bose-Einstein condensates [166–168] or fields in modulated cavities [169].

The key step is to establish an exact correspondence with dynamical systems on the circle, see, e.g., [170], in the sense that the Floquet time evolution can be fully encoded into coordinate transformations given by orientation-preserving diffeomorphisms of the circle, see Sec. 9.2. These diffeomorphisms $f_{\pm}(x)$ are

obtained directly from the velocity functions $v_{1,2}(x)$. We specifically show that the system can be either non-heating or heating, with heating phases characterized by periodic points x_{*p}^\mp of f_\pm with period $p \in \mathbb{Z}^+$:

$$x_{*p}^\mp = f_\pm^p(x_{*p}^\mp), \quad f_\pm^p = f_\pm \circ \dots \circ f_\pm, \quad (9.6)$$

where the function composition \circ is repeated p times. Of these, x_{*1}^\mp are fixed points of f_\pm , while x_{*p}^\mp for $p > 1$ can be viewed as fixed points of f_\pm^p for the smallest possible p . On general grounds, since the deformations are the same in both terms in (9.2), f_\pm have equally many periodic points with stable and unstable ones coming in pairs. Mergers of such pairs correspond to critical values $x_{cp}^\mp = x_{*p}^\mp$ denoting periodic points that also satisfy

$$1 = f_\pm^{p'}(x_{cp}^\mp) = \frac{d}{dx} f_\pm^p(x) \Big|_{x=x_{cp}^\mp}. \quad (9.7)$$

Unstable points play a predominant role as their presence will imply that the system is heating up: The picture is that energy and excitations flow to these points, which follows from exact analytical results for the evolution of the energy density and correlation functions.

Let $2N_p$ be the number of periodic points $x_{*p,i}^\mp$ of f_\pm with period p ($i = 1, \dots, 2N_p$). We will show that the heating rate ν is given by ²

$$\nu = \max_{p \in \mathbb{Z}^+, r=\pm, i \in \{1, \dots, 2N_p\}} 2t_{\text{cyc}}^{-1} p^{-1} \log[f_r^{p'}(x_{*p,i}^{-r})]. \quad (9.8)$$

If all $N_p = 0$, then $\nu = 0$, corresponding to non-heating, while $\nu > 0$ indicates heating. Thus, knowledge of f_\pm and (9.8) is all one needs to draw phase diagrams in (τ_1, τ_2) -space, such as in Figs. 9.2 and 9.3. We stress that Fig. 9.2(b) is obtained as $g \rightarrow 1^-$ for Ex. 1 in Table 9.1 ³ and agrees perfectly with Fig. 1(c) in [23], which can be verified analytically.

The heating rate serves as the natural order parameter for phase transitions between heating and non-heating. However, we will also show that regions with different numbers of unstable periodic points can be distinguished by kinks in the entanglement entropy, reminiscent of Lifshitz phase transitions. To better understand the entanglement pattern, we will also compute the so-called mutual information, and these results show that only neighboring unstable periodic points share linearly growing entanglement in the heating phase.

We emphasize that, due to the maximum in (9.8) over essentially $\sum_p 4N_p$ different functions of (τ_1, τ_2) , both smooth and nonanalytic behaviors are possible. Crucially, one can have cusps in ν also within the overall heating phase, see Fig. 9.3, and this possibility can also be demonstrated analytically, but in general there can also be paths that avoid such cusps. Finally, we note that heating phases, since they are given by periodic points, correspond precisely to so-called Arnold tongues, well known in the study of classical dynamical systems [170].

² The maximum in (9.8) is over all periodic points for each $r = \pm$ to avoid labeling which are stable or unstable.

³ The limit is taken after the phase-transition lines are computed. Note that the height $1/w_{2,0}$ of the pink leaves for $g < 1$, cf. Fig. 9.2(a), diverges as $g \rightarrow 1^-$. Hence, the lower phase-transition lines in Fig. 9.2(a) correspond to the curved ones in Fig. 9.2(b) while the upper lines correspond to the straight vertical ones. Similarly, the black dashed lines become vertical.

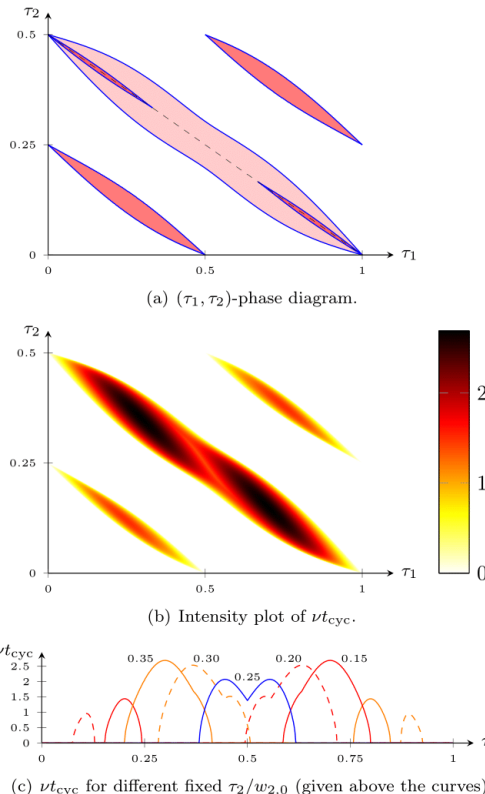


Figure 9.3: Phase diagram and heating rate for H_1 given by homogeneous CFT and H_2 by Ex. 4 in Table 9.1 with $a = 6$, $b = 3$, and $k = 2$. (a) Phase diagram in $(\tau_1, \tau_2) \in [0, 1] \times [0, 1/w_{2,0}]$ (cf. Fig. 9.2) due to fixed points (center leaf) computed analytically and periodic points with period 2 (leaves on each side of the center) computed numerically. Regions with two and four unstable periodic points are light and dark pink, respectively. (There are regions due to periodic points with period 3 not shown, and possibly also due to ones with period $p > 3$.) (b)–(c) Rescaled heating rate νt_{cyc} as function of (τ_1, τ_2) and along rays with fixed τ_2 .

9.2 FLOQUET DYNAMICS FROM CIRCLES MAPS

In this section we will introduce tools in [165, 171] to analytically study the Floquet drive given by (9.1) and (9.2).

First, we introduce

$$f_j(x) = \int_0^x dx' \frac{v_{j,0}}{v_j(x')}, \quad \frac{1}{v_{j,0}} = \frac{1}{L} \int_{-L/2}^{L/2} \frac{dx'}{v_j(x')} \quad (9.9)$$

for $j = 1, 2$. These are diffeomorphisms satisfying $f_j(x + L) = f_j(x) + L$ and $f'_j(x) > 0$. More specifically, f_j lie in the covering group $\widetilde{\text{Diff}}_+(S^1)$ of orientation-preserving diffeomorphisms of the circle S^1 such that

$$U_+(f_j)U_-(f_j)H_jU_-(f_j)^{-1}U_+(f_j)^{-1} = \int_{-L/2}^{L/2} dx v_{j,0} [T_+(x) + T_-(x)] + \text{const} \quad (9.10)$$

using the projective unitary representations $U_\pm(f)$ of $f \in \widetilde{\text{Diff}}_+(S^1)$ in [165, 171]. We note that their generators are precisely the energy-momentum components $T_\pm(x)$:

$$U_\pm(f) = I \mp i\epsilon \int_{-L/2}^{L/2} dx \zeta(x) T_\pm(x) + o(\epsilon) \quad (9.11)$$

for infinitesimal $f(x) = x + \epsilon\zeta(x)$.

Second, similar to [165], the diffeomorphisms in (9.9) can be used to compute exact analytical results for the Floquet time evolution of local observables

$$\mathcal{O}(x; t) = U_F^{-n} \mathcal{O}(x) U_F^n, \quad t = nt_{\text{cyc}}, \quad n \in \mathbb{Z}. \quad (9.12)$$

It follows from (9.10) and known results for the adjoint action of $U_\pm(f_j)$ ⁴ that the time evolution is encoded into generalized light-cone coordinates $x_t^\mp(x)$ given by⁵

$$x_{t+t_{\text{cyc}}}^\mp(x) = f_\pm(x_t^\mp(x)), \quad x_0^\mp(x) = x \quad (9.13)$$

using

$$f_\pm(x) = f_2^{-1}(f_2(f_1^{-1}(f_1(x) \mp v_{1,0}T_1)) \mp v_{2,0}T_2). \quad (9.14)$$

By definition, $f_\pm \in \widetilde{\text{Diff}}_+(S^1)$, and this also implies that $f_\pm^p \in \widetilde{\text{Diff}}_+(S^1)$ for f_\pm^p defined in (9.6).

⁴ For instance, for any $f \in \widetilde{\text{Diff}}_+(S^1)$,

$$U_\pm(f)T_\pm(x)U_\pm(f)^{-1} = f'(x)^2 T_\pm(f(x)) - \frac{c}{24\pi} \{f(x), x\},$$

$$U_\pm(f)T_\mp(x)U_\pm(f)^{-1} = T_\mp(x).$$

⁵ The new coordinates $x_t^\mp(x)$ are the analogues of those in Eq. (4) in [23]

For instance, for a primary field $\Phi(x) = \Phi(x, x)$ with conformal weights (Δ^+, Δ^-) ⁶,

$$\Phi(x; t) = \left[\frac{\partial x_t^-(x)}{\partial x} \right]^{\Delta^+} \left[\frac{\partial x_t^+(x)}{\partial x} \right]^{\Delta^-} \Phi(x_t^-(x), x_t^+(x)), \quad (9.15)$$

and for the components of the energy-momentum tensor,

$$T_{\pm}(x; t) = \left[\frac{\partial x_t^{\mp}(x)}{\partial x} \right]^2 T_{\pm}(x_t^{\mp}(x)) - \frac{c}{24\pi} \{ x_t^{\mp}(x), x \}, \quad (9.16)$$

where $\partial x_t^{\mp}(x)/\partial x = \prod_{m=0}^{n-1} f'_{\pm}(x_{mt_{\text{cyc}}}(x))$ for $n > 0$ and $\{f(x), x\}$ denotes the Schwarzian derivative of $f(x)$ with respect to x . Both results are important as they will allow us to compute correlation functions and the heating rate. Periodic points are solutions x_{*p}^{\mp} to (9.6) and correspond to intersections between the straight line $y = x$ and curves $y = f_{\pm}^p(x)$ (up to integer multiples of L since we are on the circle). This is illustrated in Fig. 9.4 using the case in Fig. 9.3 as an example. Note that a periodic point of f_{\pm}^p with period $p > 1$ can be viewed as a fixed point of f_{\pm}^p , and vice versa. The following definition will

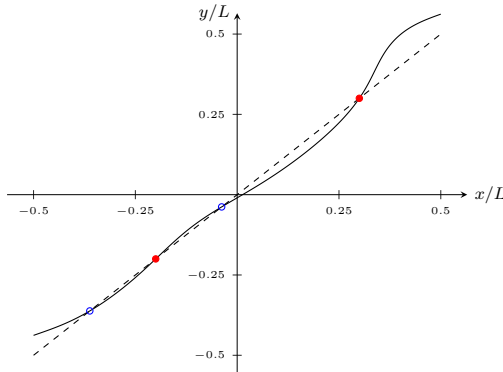


Figure 9.4: Illustration of fixed points as intersections between the (black solid) curve $y = f_+(x)$ and the straight (black dotted) line $y = x$ (up to integer multiples of L). Stable and unstable fixed points are indicated by empty blue and filled red circles, respectively. [The plotted curve is for the case in Fig. 9.3 at $(\tau_1, \tau_2) = (0.10, 0.45)$, which corresponds to a point in one of the darker leaves within the center leaf in Fig. 9.3(a), see also column (i) in Figs. 9.5 and 9.7.]

be important: Assuming x_{*p}^{\mp} solves (9.6), we say that it is

1. *stable* if $f_{\pm}^{p'}(x_{*}^{\mp}) < 1$,
2. *unstable* if $f_{\pm}^{p'}(x_{*}^{\mp}) > 1$, or
3. a *tangent point* if $f_{\pm}^{p'}(x_{*}^{\mp}) = 1$.

⁶ The first (second) argument in $\Phi(x, x)$ is for the right- (left-) moving component and corresponds to Δ^+ (Δ^-).

As a trivial example, note that $T_1 = T_2 = 0$, or equivalently $\tau_1 = \tau_2 = 0$, corresponds to a tangent point.

In Sec. 9.2 we state a number of general properties for our periodic points. In particular, apart from tangent points, they must come in pairs, one stable and one unstable. Their existence dramatically affects the dynamics, see Fig. 9.5 for typical examples. To understand this, suppose that x is a periodic point x_{*p}^{\mp} , then $\partial x_t^{\mp}(x)/\partial x = f_{\pm}^{p'}(x_{*p}^{\mp})^{n/p}$ for $t = nt_{\text{cyc}}$ with n a multiple of p . Thus, if $f_{\pm}^{p'}(x_{*p}^{\mp}) > 1 (< 1)$, this factor diverges (vanishes) exponentially as $t \rightarrow \infty$.

At (τ_1, τ_2) where pairs of stable and unstable periodic points merge, the straight line and the f_{\pm}^p -curve are tangent at some $x_{cp}^{\mp} = x_{*p}^{\mp}$ solving (9.6) and (9.7). This yields an equation system for τ_1 and τ_2 for each tangent point. Crucially, such tangent points correspond to curves separating regions in (τ_1, τ_2) -space with different numbers of periodic points. These regions (accounting for the symmetries illustrated in Fig. 9.2) typically have the shape of nested leaves and together give the overall heating phase, see, e.g., Figs. 9.2 and 9.3.

PROPERTIES OF PERIODIC POINTS The solutions x_{*p}^{\mp} to (9.6) have the following properties:

1. For each of the two f_{\pm} , stable and unstable periodic points come in pairs. Moreover, up to tangent points (which can be viewed as a pair), periodic points must alternate between stable and unstable, i.e., there is always a stable point between two unstable ones and vice versa.
2. The convergence of $x_t^{\mp}(x)$ to a stable periodic point x_{*p}^{\mp} (viewed as the evolution under f_{\pm}^p covering p integer time steps) is exponentially fast, with the rate given by $\log[f_{\pm}^p(x_{*p}^{\mp})]$.
3. For each solution of (9.6) for given (T_1, T_2) , there is also a solution for $(-T_1, -T_2)$.
4. Shifts of T_1 by $L/k_2 v_{1,0}$ and T_2 by $L/k_1 v_{2,0}$ leave (9.6) invariant, where L/k_j for $k_j \in \mathbb{Z}^+$ are the periods of $v_j(x)$; we set $k_j = 1$ if $v_j(x)$ is constant.

We provide a proof of such properties in App. b.1. We stress that Properties 3 and 4 imply the symmetries illustrated in Fig. 9.2 by considering $\tau_{1,2} = v_{1,2} t_{1,2}/L$ instead of $t_{1,2}$. For regions in (τ_1, τ_2) -space with periodic points with period p , it is sometimes natural to consider the evolution in units of p integer time steps. Note that, on general grounds, since we work with smooth deformations defining circle diffeomorphisms, a given region in the phase diagram cannot have periodic points with different periods [170].

9.3 DYNAMICS OF ENERGY AND ENTANGLEMENT

In this section The time-evolved energy density corresponding to H_1 in (9.2) is

$$\mathcal{E}_1(x; t) = v_1(x)[T_+(x; t) + T_-(x; t)]. \quad (9.17)$$

For simplicity, we will use this quantity to study the flow of energy in our Floquet system. Note that we may as well use $\mathcal{E}_2(x; t)$ with $v_1(x)$ replaced by $v_2(x)$; indeed, for our purposes, the exact choice is less important as long as it is a linear combination of both $T_{\pm}(x; t)$.

The properties of our periodic points and (9.17) together with (9.16) imply that the energy density $\mathcal{E}_1(x; t)$ grows (decays) exponentially in time at unstable (stable) such points. Moreover, if there are periodic points, all x except the unstable points flow exponentially fast to the stable ones, see Figs. 9.5(a)–(b) for typical examples of this behavior. This follows from the general properties of our periodic points in Sec. 9.2. As a consequence, the whole system is cooling apart from the exceptions which are heating exponentially, see Fig. 9.5(c) where we plot $\mathcal{E}_1(x; t)$ in (9.17) up to the Schwarzian-derivative terms; the latter do not affect the existence or location of periodic points, cf. [165, 171, 172] for discussions of similar Schwarzian-derivative contributions. It follows by integrating $\mathcal{E}_1(x, t)$ over $x \in [-L/2, L/2]$ that the presence of unstable points leads to an overall heating of the system with the heating rate ν determined by the unstable point with the steepest slope, which implies (9.8). On the other hand, the absence of periodic points implies $\nu = 0$ by definition, which characterizes the non-heating phase, and pseudoperiodic evolution of all trajectories⁷.

Lastly, by computing 2-point correlation functions for primary fields one can study the flow of excitations in the system. The former follow from (9.15) and known results for homogeneous CFT: To compute correlation functions for any primary field, all that is needed is knowledge about the corresponding correlation function for homogeneous CFT, cf. [165, 171]. For simplicity, consider the ground state $|0\rangle$ of the homogeneous theory. Then, under our Floquet time evolution, the results for 2-point correlation functions with respect $|0\rangle$ are

$$\begin{aligned} \langle 0 | \Phi(x; t)^\dagger \Phi(x'; t') | 0 \rangle &= \left[\frac{\partial x_t^-(x)}{\partial x} \frac{\partial x_{t'}^-(x')}{\partial x'} \right]^{\Delta^+} \left[\frac{\partial x_t^+(x)}{\partial x} \frac{\partial x_{t'}^+(x')}{\partial x'} \right]^{\Delta^-} \\ &\times \left(\frac{i\pi}{L \sin(\pi[x_t^-(x) - x_{t'}^-(x')] + i0^+)/L} \right)^{2\Delta^+} \\ &\times \left(\frac{-i\pi}{L \sin(\pi[x_t^+(x) - x_{t'}^+(x')] - i0^+)/L} \right)^{2\Delta^-} \end{aligned} \quad (9.18)$$

for finite L . This result together with the properties in Sec. 9.2 shows that, while almost all $x_t^\mp(x)$ -trajectories flow to stable periodic points in the heating phase, the probability density of excitations flow exponentially fast to the unstable ones, see Fig. 9.5(d) for examples of this.

We now turn to the stroboscopic time evolution of entanglement entropy after our general two-step drive protocol. As is commonplace, the von-Neumann entanglement entropy $S_A(t)$ for the subsystem on the interval $A = [x, y]$ with the rest can be computed from correlation functions for twist fields [69, 173]. We obtain that the entanglement grows as

$$\begin{aligned} S_A(t) &= \frac{c}{12} [S_+(t) + S_-(t)], \\ S_\pm(t) &= -\log \left[\frac{\partial x_t^\mp}{\partial x} \frac{\partial y_t^\mp}{\partial y} \left(\frac{\pm i\pi}{L \sin(\frac{\pi}{L}[x_t^\mp - y_t^\mp] \pm i0^+)} \right)^2 \right] \end{aligned} \quad (9.19)$$

⁷ The trajectories are said to be pseudoperiodic instead of periodic since, in general, their (pseudo)periodicity is not a multiple of t_{cyc} . Here, this behavior follows from our periodic boundary conditions in the absence of periodic points, but similar behavior would be true for, e.g., Dirichlet or Neumann boundary conditions.

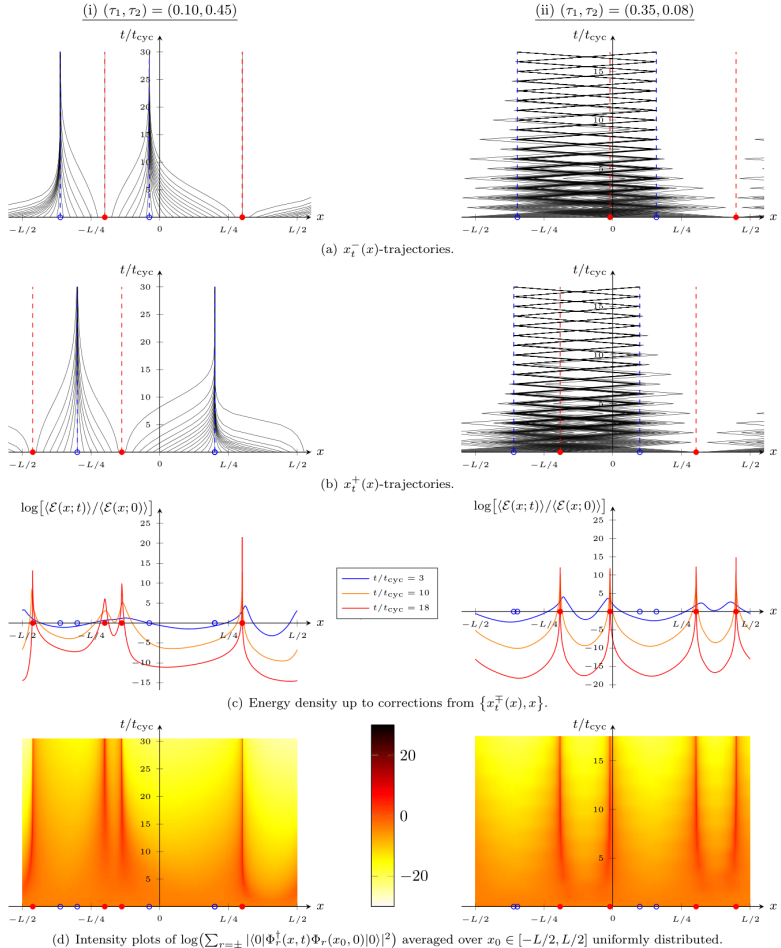


Figure 9.5: Plots for the case in Fig. 9.3 at (i) $(\tau_1, \tau_2) = (0.10, 0.45)$ in the left column and (ii) $(\tau_1, \tau_2) = (0.35, 0.08)$ in the right column. In (i) and (ii) there are eight fixed points and eight periodic points with period 2, respectively. (a)–(b) $x_t^\mp (x)$ -trajectories. (c) Energy-density expectation $\langle \mathcal{E}(x; t) \rangle$ for $\mathcal{E}(x; t) = \mathcal{E}_1(x; t) + (cv_1/24\pi)[\{x_t^-(x), x\} + \{x_t^+(x), x\}]$ given by (9.17) with respect to an arbitrary translation-invariant state. (d) Correlation functions $\langle 0|\Phi_r^\dagger(x, t)\Phi_r(x_0, 0)|0\rangle$ with respect to the ground state $|0\rangle$ of H_1 for primary fields $\Phi_r(x, t)$ with $\Delta_r^\pm = \delta_{r,\pm}$ for $r = \pm$, averaged over $x_0 \in [-L/2, L/2]$ uniformly distributed, setting $L = 50$. Stable and unstable periodic points are indicated by empty blue and filled red circles, respectively.

with $x_t^\mp = x_t^\mp(x)$ and $y_t^\mp = x_t^\mp(y)$. Its behavior is different depending on the absence or presence of periodic points. In the non-heating phase, as mentioned, there is an underlying pseudoperiodicity in time. On the other hand, when heating, the situation is drastically different. Using the properties of our periodic points in Sec. 9.2, we can study the behavior of $S_A(t)$ in the heating phase. We consider the following two cases, illustrated in Fig. 9.6: A contains (a) at least one of (but not all) the unstable periodic points or (b) no (or all) unstable periodic points. (Containing “no” or “all” points are equivalent due to our periodic boundary conditions.) For simplicity, and without loss of generality since the two \pm -components commute, we consider only the right-moving (+) component:

(a) Due to Property 1 in Sec. 9.2, x_t^- and y_t^- flow to two different stable periodic points, denoted x_{*p}^- and y_{*p}^- , respectively. (For simplicity, we consider the flow in units of p integer time steps.) Since $x_{*p}^- \neq y_{*p}^-$, the difference $x_t^- - y_t^-$ in (9.19) remains finite as $t \rightarrow \infty$, while the derivative factors decay exponentially to 0 as x_t^- and y_t^- flow to their respective stable periodic points. It follows that the leading contribution to $S_+(t)$ is

$$-\frac{\log[f_+^{p'}(x_{*p}^-)] + \log[f_+^{p'}(y_{*p}^-)]}{pt_{\text{cyc}}} t. \quad (9.20)$$

I.e., $S_+(t)$ grows linearly in time for large t .

(b) Due to the same property as in (a), x_t^- and y_t^- flow to the same stable periodic point, denoted $x_{*p,A}^-$. It follows from this and Property 2 in Sec. 9.2 that $x_t^- - y_t^-$ in (9.19) decays exponentially at a rate that exactly cancels the exponential decay of the derivative factors, implying that $S_+(t)$ becomes constant for large t .

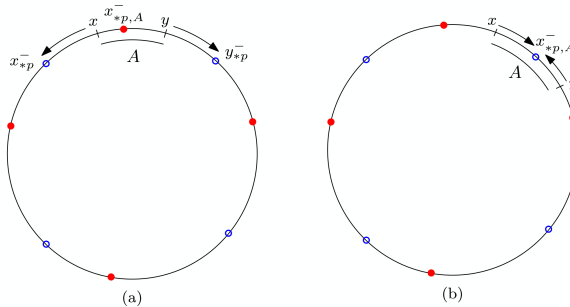


Figure 9.6: Illustrations of the two cases (a) and (b) described in the text for the entanglement entropy $S_A(t)$ in the heating phase. Stable and unstable periodic points are indicated by empty blue and filled red circles, respectively. For simplicity, we illustrate only the contribution from the right-moving component. (Flows to periodic points with period p should be interpreted as those under f_+^p .)

Note that, for all cases, if $t = 0$, then $x_0^\mp(x) = x$, which means that (9.19) yields

$$S_A(0) = \frac{c}{3} \log[(L/\pi) \sin(\pi\ell/L)] \quad (9.21)$$

for $\ell = x - y > 0$. This is precisely the usual equilibrium result in the case of periodic boundary conditions.

The exact analytical results in (9.19) give rise to a remarkable structure of kinks in the entanglement entropy $S_{[-L/2,x]}(t)$ that brings to mind Lifshitz phase transitions [174], see Fig. 9.7 for examples of such structures. Indeed, when crossing a transition line between regions with different numbers of unstable periodic points, cf. Fig. 9.3(a), the number of kinks in $S_{[-L/2,x]}(t)$ changes by an even integer. This can be viewed as a nonequilibrium analogue of a Lifshitz phase transition: Instead of jumps or cusps [174] there are, in general, kinks in the entanglement entropy induced by the unstable periodic points. Note that such transitions within the heating phase are local and do not affect global properties such as the heating rate.

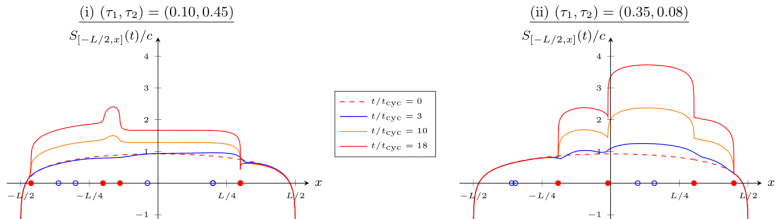


Figure 9.7: Plots of the entanglement entropy $S_{[-L/2,x]}(t)$ given by (9.19), setting $L = 50$, for the case in Fig. 9.3 at (i) $(\tau_1, \tau_2) = (0.10, 0.45)$ and (ii) $(\tau_1, \tau_2) = (0.35, 0.08)$. See the caption to Fig. 9.5 for further details.

To understand the entanglement-entropy pattern, we study the mutual information $I_{A;B}(t) = S_A(t) + S_B(t) - S_{A \cup B}(t)$ for two intervals $A = [x_1, x_2]$ and $B = [x_3, x_4]$. One can show that $I_{A;B}(t)$ evolves nontrivially in time if and only if A and B contain at least one unstable periodic point each, separated by a single stable point (with respect to the same component). Without loss of generality, we consider only the contributions from the right-moving component. We compute $I_{A;B}(t)$ for the following two cases, illustrated in Fig. 9.8:

(a) Suppose that A and B are neighbors, i.e., that there is only one stable periodic point, denoted $x_{*,p,AB}^-$, between them, see Fig. 9.8(a). It follows that $x_t^-(x_2)$ and $x_t^-(x_3)$ flow to $x_{*,p,AB}^-$, while $x_t^-(x_1)$ and $x_t^-(x_4)$ flow to two other different stable periodic points, denoted $x_{*,p,1}^-$ and $x_{*,p,4}^-$, respectively. In this case, we show that the leading contribution to $I_{A;B}(t)$ from the right-moving component is

$$-\frac{c}{6} \frac{\log[f_+^{p'}(x_{*,p,AB}^-)]}{pt_{\text{cyc}}} t. \quad (9.22)$$

I.e., it grows linearly in time with a rate given by the stable periodic point between A and B .

(b) Suppose that A and B are not neighbors, i.e., there is not only a single stable periodic point separating them, see Fig. 9.8(b). (Such a situation can only occur if there are at least four unstable periodic points for each component.) In this case, all $x_t^-(x_j)$ ($j = 1, 2, 3, 4$) flow to four different stable periodic points. We show that this leads to a cancellation between $S_{A \cup B}(t)$ and $S_A(t) + S_B(t)$ such that the contribution from the right-moving component to $I_{A;B}(t)$ does not change with time for large t .

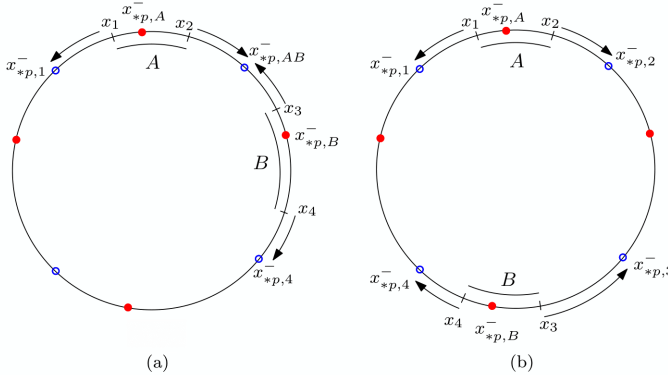


Figure 9.8: Illustrations of the two cases (a) and (b) described in the text for the mutual information $I_{A;B}(t)$ in the heating phase. See the caption to Fig. 9.6 for further details.

Below we compute the mutual information $I_{A;B}(t) = S_A(t) + S_B(t) - S_{A \cup B}(t)$ for two intervals $A = [x_1, x_2]$ and $B = [x_3, x_4]$. We give details only for the right-moving component (without loss of generality, since the two \pm -components commute). Moreover, it follows from the entanglement entropy computation that the result is nontrivial if and only if A and B contain at least one unstable periodic point each, denoted $x_{*p,A}^-$ and $x_{*p,B}^- \neq x_{*p,A}^-$, respectively, see Fig. 9.8; we will assume this in what follows.

Computing $S_A(t)$ and $S_B(t)$ can be done using (9.19). To compute $S_{A \cup B}(t)$ requires a 4-point correlation function of twist fields of the form

$$\left(\prod_{j=1}^4 \left[\frac{\partial x_t^-(x_j)}{\partial x} \right]^{\Delta_m^+} \right) \times \left(\frac{i\pi}{L \sin(\pi[x_t^-(x_1) - x_t^-(x_4) + i0^+]/L)} \right)^{2\Delta_m^+} \times \left(\frac{i\pi}{L \sin(\pi[x_t^-(x_2) - x_t^-(x_3) + i0^+]/L)} \right)^{2\Delta_m^+} \times \mathcal{F}(u), \quad (9.23)$$

where $\mathcal{F}(u)$ is the conformal block, which depends on the operator content of the theory, and

$$u = \frac{\sin(\pi[x_t^-(x_1) - x_t^-(x_4) + i0^+]/L)}{\sin(\pi[x_t^-(x_1) - x_t^-(x_2) + i0^+]/L)} \times \frac{\sin(\pi[x_t^-(x_2) - x_t^-(x_3) + i0^+]/L)}{\sin(\pi[x_t^-(x_4) - x_t^-(x_3) + i0^+]/L)} \quad (9.24)$$

is the so-called cross ratio. We will use that the conformal block $\mathcal{F}(u)$ does not contribute if u tends to a constant finite value different from 1, see, e.g., Appendix B of [125]. Let us now treat the cases (a) and (b) described above:

(a) Since $x_t^-(x_2)$ and $x_t^-(x_3)$ flow to $x_{*p,AB}^-$, while $x_t^-(x_1)$ and $x_t^-(x_4)$ flow to two other different stable periodic points $x_{*p,1}^-$ and $x_{*p,4}^-$, it follows that

u tends to 0, implying that $\mathcal{F}(u)$ does not contribute for large t and can be neglected in what follows. Due to Property 2 in Sec. 9.2, the contributions to the von-Neumann entanglement entropy $S_{A \cup B}(t)$ from $x_t^-(x_2)$ and $x_t^-(x_3)$ cancel, and thus the leading contribution from the right-moving component to $S_{A \cup B}(t)$ is

$$-\frac{c}{12} \log \left[\frac{\partial x_t^-(x_1)}{\partial x} \frac{\partial x_t^-(x_4)}{\partial x} \times \left(\frac{i\pi}{L \sin(\pi[x_t^-(x_1) - x_t^-(x_4)]/L) + i0^+} \right)^2 \right]. \quad (9.25)$$

The derivative factors above decay exponentially as $x_t^-(x_1)$ and $x_t^-(x_4)$ flow to their respective stable periodic points, which implies that (9.25) goes as

$$-\frac{c}{12} \frac{\log[f_+^{p'}(x_{*p,1}^-)] + \log[f_+^{p'}(x_{*p,4}^-)]}{pt_{\text{cyc}}} t + o(t) \quad (9.26)$$

for large t . This and the results for $S_A(t)$ and $S_B(t)$ [cf. (9.20)] imply that the leading contribution to $I_{A;B}(t)$ from the right-moving component is given by (9.22).

(b) We can repeat the argument in (a), recalling that $x_t^-(x_j)$ ($j = 1, 2, 3, 4$) flow to four different stable periodic points. Again, u tends to a constant different from 1, and thus $\mathcal{F}(u)$ does not contribute for large t , as before. The derivative terms in (9.23) will all decay exponentially, while the denominators stay finite. It follows that the leading contribution to $S_{A \cup B}(t)$ is canceled by the corresponding ones to $S_A(t) + S_B(t)$, meaning that the contribution from the right-moving component to $I_{A;B}(t)$ does not change with time for large t .

To summarize, the intervals A and B have to contain at least one unstable periodic point each and to be separated by a single stable periodic point for $I_{A;B}(t)$ to grow linearly in time for large t . As a special case, suppose that A and B contain exactly one unstable point each. Our results then imply that only neighboring unstable periodic points share entanglement that grows linearly at late times. This generalizes previous results obtained in [125] for the special case of $\mathfrak{sl}(2)$ -deformations to inhomogeneous CFT with general smooth deformations. Moreover, if the number of such points for each component is even, then the entanglement entropy is “bipartite”.

9.4 FLOQUET HAMILTONIAN AND CRITICAL EXPONENTS

In chapter 7, we have focused our attention on the dynamics of energy and entanglement under a generic type of drive that only involved the $\mathfrak{sl}(2)$ algebra of the full Virasoro algebra. In this case, writing down a Floquet Hamiltonian H_F was analytically reachable from the finite dimension of the underlying symmetry algebra. However, in this chapter we are dealing with an infinite dimensional symmetry algebra, for which obtaining an effective description is in principle cumbersome as the number of different terms in the Baker–Campbell–Hausdorff (BCH) formula will keep growing to infinity, even when starting from a relatively small set of Virasoro generators, such as for instance $\{L_0, L_1, L_{-1}, L_2, L_{-2}\}$. A first but slightly unsatisfactorily approach would be to consider regimes of high-frequency drives, where higher-order commutators in the BCH formula can safely be neglected. Such an approach is often referred to as Magnus expansion. However we propose here to capitalize on the properties of circle

diffeomorphisms to heavily constrain the form of the Floquet Hamiltonian in any regime of driving parameters.

Our goal is to obtain for a two-step drive between two generic inhomogeneous CFTs an effective Hamiltonian H_F such that

$$e^{-iH_F n t_{\text{cyc}}} = (e^{-iH_2 T_2} e^{-iH_1 T_1})^n, \quad t_{\text{cyc}} = t_1 + t_2, \quad (9.27)$$

which generically would assume the form

$$H_F = \int_0^L dx (v_{\text{eff}}^+(x) T_+(x) + v_{\text{eff}}^-(x) T_-(x)). \quad (9.28)$$

The problem reduces to finding an expression for v_{eff}^\pm . Such effective velocities can be obtained from the one-cycle diffeomorphism encoding the time evolution of (quasi-)primary fields. Let us first concentrate on the non-heating phase. In this case, the diffeomorphisms f_\pm have an irrational Poincaré number. This implies that it is conjugate to a rotation, i.e., $f_\pm = g_\pm \circ R_\pm \circ g_\pm$, for some diffeomorphism g_\pm . As a consequence, the invariant measure on the circle is simply $(g_\pm^{-1})'(x)dx$. The effective velocities are then given by the logarithm of the diffeomorphism f_\pm , i.e., the vector field $v_\pm(x)\partial_x$ whose flow at time one coincides with f_\pm . Recalling that the flow of v_\pm is the one-parameter family of diffeomorphisms spanned by the solutions of $\dot{x} = v(x(t))$, the statement $v_{\text{eff}}^\pm = \log f_\pm$ can be restated as

$$\int_x^{f_\pm(x)} \frac{dy}{v_{\text{eff}}^\pm(y)} = 1 \quad \text{for all } x. \quad (9.29)$$

Differentiating with respect to x , this leads to

$$v_{\text{eff}}^\pm(f_\pm(x)) = f'_\pm(x) v_{\text{eff}}^\pm(x) \quad \text{for all } x. \quad (9.30)$$

In order to find $v_{\text{eff}}^\pm(x)$ under the assumption that the one-cycle diffeomorphism $f_\pm(x)$ is known, we make use of the ergodic theorem, stating that the spatial average of $v_{\text{eff}}^\pm(x)$ with respect to the invariant measure of $f_\pm(x)$ coincides with the time-average, i.e.,

$$\int_0^{2\pi} \frac{dy}{2\pi} v_{\text{eff}}^\pm(g_\pm(y)) = \lim_{n \rightarrow \infty} \frac{1}{n} \sum_{k=0}^{n-1} v_{\text{eff}}^\pm(f_\pm^{(k)}(x)), \quad (9.31)$$

where x is any point on the circle. This reduces to a Fredholm integral equation of the second kind,

$$v_{\text{eff}}^\pm(x) = \frac{1}{\lim_{n \rightarrow \infty} \frac{1}{n} \sum_{k=0}^{n-1} (f_\pm^{(k)})'(x)} \int_0^{2\pi} \frac{dy}{2\pi} v_{\text{eff}}^\pm(g_\pm(y)). \quad (9.32)$$

As $g_\pm(x)$ is unknown, the numerator of (9.32) is an unknown constant, which can be found by plugging the solution for (9.32) into the constraint (9.29). This approach is based on the ergodicity of the non-heating phase, i.e., on the fact that under the iteration of the one-cycle Floquet map that has an irrational Poincaré number one covers densely the unit circle. However, in the heating phase the diffeomorphisms f_\pm have a rational Poincaré number. In this case, the ergodic theorem cannot be used because of fixed or higher-order periodic

points, but the Floquet Hamiltonian can still be approximated around the zeros of the effective profile $v_{\text{eff}}^\pm(x)$ associated to fixed points of $f_\pm(x)$. Nevertheless, reconstructing the entire Floquet Hamiltonian H_F in the heating phase is out of analytical reach.

We now study the criticality of the phase transition from the heating to the non-heating phase from a general perspective using circle diffeomorphisms. We have found in chapter 7 that the order parameter of such transition in the $\mathfrak{sl}(2)$ case was given by the (pseudo-)periodicity of the n -cycle Möbius transformation encoding stroboscopic time evolution, while such parameter was given by the inverse heating rate in the heating phase. The rate at which both parameters are diverging when crossing the phase boundary was given by a critical exponent of $\frac{1}{2}$. We now revisit this computation of the critical exponent, this time for arbitrary inhomogeneous Floquet drives. Stated in mathematical terms, we let f_ϵ be a one-parameter family of circle maps, with ϵ belonging to some open interval that contains $\epsilon = 0$. For each value of ϵ , we consider the dynamical system given by

$$x_{n+1} = f_\epsilon(x_n). \quad (9.33)$$

We shall assume that f_ϵ has no fixed points for $\epsilon > 0$, develops a fixed point x_c at $\epsilon = 0$, then has at least two fixed points at $\epsilon < 0$ (see Fig. 9.9). The point $\epsilon = 0$ in parameter space is a (saddle-node) bifurcation; following our usual terminology, the regime with $\epsilon > 0$ (resp. $\epsilon < 0$) is referred to as a non-heating phase (resp. heating phase). Our goal is to describe the scaling laws satisfied by certain measures of the ergodicity (or lack thereof) of this dynamical system in the limit $\epsilon \rightarrow 0$. In the non-heating phase, the Poincaré rotation number of f_ϵ satisfies such a scaling law: it goes to zero as $\epsilon^{1-\frac{1}{n}}$ for an integer n determined by the behaviour of $f_0(x)$ near x_c (typically $n = 2$). In the heating phase, the Poincaré rotation number vanishes identically, but the heating rate, i.e. the divergence rate away from the unstable fixed point, behaves as $-\epsilon^{1-1/n}$. In both cases, the computation rests on universal properties of $f_\epsilon(x)$ near x_c . For simplicity, in what follows we set $x_c = 0$ without loss of generality.

In the heating phase $\epsilon < 0$, the Poincaré rotation number of f_ϵ vanishes since f_ϵ has a fixed point. The transition from the heating to the non-heating phase ($\epsilon \rightarrow 0^-$) is a standard saddle-node bifurcation of one-dimensional dynamical systems, where a stable and an unstable fixed point merge and annihilate. Let us therefore describe the behaviour of the heating rate ν in the limit $\epsilon \rightarrow 0^-$. For small $\epsilon < 0$ and near $x_c = 0$, one can Taylor-expand $f_\epsilon(x) - x \sim \epsilon + \alpha x^n$ (with $n \in 2\mathbb{N}^*$ and $\alpha > 0$ without loss of generality). Then the unstable fixed point of f_ϵ is approximately located at $x^* = (-\epsilon/\alpha)^{1/n}$. The divergence rate away from that point is $\nu = \log f'(x^*) \sim n(-\epsilon)^{1-1/n} \alpha^{1/n}$. (This is also the convergence rate to the stable fixed point in the limit $\epsilon \rightarrow 0^+$.) The same scaling $\nu \sim |\epsilon|^{1-1/n}$ would be found for any other smooth parametrization of the ‘distance’ of f_ϵ away from the bifurcation.

In the non-heating phase $\epsilon > 0$, there is no notion of ‘convergence to fixed points’ since there are no fixed points to begin with, but there is a non-zero Poincaré rotation number θ . In fact, the dynamical system $x_{n+1} = f_\epsilon(x_n)$ then is ergodic in general, with a measure $\mu_\epsilon(x)dx$ that is normalized ($\int_0^{2\pi} \mu(x)dx = 2\pi$) and invariant under f_ϵ in the sense that

$$\mu_\epsilon(f_\epsilon(x))f'_\epsilon(x) = \mu_\epsilon(x). \quad (9.34)$$

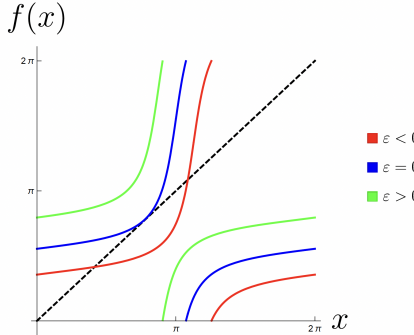


Figure 9.9: A typical plot of $f_\epsilon \bmod 2\pi$ on the interval $x \in [0, 2\pi]$. For $\epsilon > 0$, f_ϵ has no fixed points and has a non-zero (typically irrational) Poincaré rotation number θ . As $\epsilon \rightarrow 0^+$, the function f_ϵ (in green) gets closer to the identity line $f(x) = x$, and its Poincaré rotation number decreases until finally reaching $\theta = 0$ when $\epsilon = 0$ (in blue). The function $f_0(x)$ then has a single fixed point, x_c . As ϵ decreases further, f_ϵ (in red) develops a pair of fixed points (one stable, the other unstable), and the convergence rate ϵ to the stable fixed point increases. Our goal here is to describe the universal behaviour of θ and ν near $\epsilon = 0$.

In these terms, the Poincaré rotation number of f_ϵ is

$$\theta_\epsilon = \frac{1}{2\pi} \int_{-\pi}^{\pi} dx \mu_\epsilon(x) (f_\epsilon(x) - x). \quad (9.35)$$

Let us describe the behaviour of θ_ϵ in the limit $\epsilon \rightarrow 0^+$. For small $\epsilon > 0$, the dynamical system goes through a ‘bottleneck’ near x_c (many iterations of f_ϵ are needed for the dynamical system to move from $x \approx -\pi$ to $x \approx +\pi$). As a result, the invariant measure μ_ϵ appearing in (9.35) tends to localize near $x_c = 0$. Let us show this explicitly: Taylor-expanding $f_\epsilon(x) - x \sim \epsilon + \alpha x^n$ (with $\alpha > 0$ and $n \in 2\mathbb{N}^*$ without loss of generality) near $x_c = 0$, the invariance property (9.34) yields the differential equation

$$(\epsilon + \alpha x^n) \mu'_\epsilon(x) \sim -n \alpha x^{n-1} \mu_\epsilon(x) \quad (9.36)$$

as $\epsilon \rightarrow 0$ and $x \rightarrow 0$. The solution is $\mu_\epsilon(x) = C/(\epsilon + \alpha x^n)$ for some integration constant C . The latter is fixed by the normalization $\int_{-\pi}^{\pi} dx \mu_\epsilon(x) = 2\pi$ which yields

$$\mu_\epsilon(x) \sim \frac{n \sin(\pi/n) \epsilon^{1-1/n} \alpha^{1/n}}{\epsilon + \alpha x^n}, \quad \text{as } \epsilon \rightarrow 0^+. \quad (9.37)$$

The localization near $x = 0$ is manifest here, and the Poincaré rotation number (9.35) becomes

$$\theta_\epsilon \sim \frac{1}{2\pi} \int_{-\pi}^{\pi} dx \frac{C}{\epsilon + \alpha x^n} (\epsilon + \alpha x^n) = C \sim n \sin(\pi/n) \epsilon^{1-1/n} \alpha^{1/n} \quad (9.38)$$

in the limit $\epsilon \rightarrow 0^+$, where we used once more the Taylor expansion $f_\epsilon(x) - x \sim \epsilon + \alpha x^n$. This is the aforementioned scaling law. Note that the dependence of θ

on α and ϵ is the same as that of ν in the heating phase, save for a difference in the overall prefactor. Again, the scaling $\theta \sim \epsilon^{1-1/n}$ is universal in that it would hold for any smooth reparametrization of ϵ .

We conclude that the critical exponent is given by $1 - \frac{1}{n}$ by approaching the phase boundary from either phases. We stress that non-fine-tuned cases will be given by $n = 2$, leading to an exponent of $\frac{1}{2}$, generalizing the results from the $\mathfrak{sl}(2)$ drives to any drive where the one-cycle dynamics can be encoded in a dynamical map of the form (9.33).

THE THERMAL AND DISSIPATIVE EFFECTS ON FLOQUET DYNAMICS

10.1 INTRODUCTION

Recent years have seen much progress in the understanding of out of equilibrium properties of many-body quantum systems. Two broad categories which have been explored extensively are (i) the dissipative dynamics of open-systems [175] and (ii) the dynamics of periodically driven systems [176–178]. Dissipation, in general, engenders an irreversible non-unitary evolution of the quantum system towards a steady state. The interplay between unitary Hamiltonian evolution and dissipation can lead to dissipative phase transitions via nonanalyticities in the steady state [179]. Understanding the role of dissipation is especially relevant for quantum simulation platforms which permit the realization of a multitude of theoretical phenomena and out of equilibrium phases not accessible in standard solid state systems [180–182]. Tailored dissipation can also be used as a resource for quantum state engineering of many-body phases [183–192]. In these light, an important question is whether the phenomenology of inhomogeneous Floquet CFTs survives the onset of dissipation and whether dissipation suffices to eliminate the “integrable heating”, as opposed to usual ergodic heating.

In this chapter we address this question by studying the driven-dissipative dynamics of a critical free fermion chain that is periodically driven following the SSD drive protocol and can exchange particles with an external bath, as illustrated on Fig. 10.1. We first introduce initial thermal states in Sec. 10.2, for which we compute the stroboscopic time evolution of energy analytically using CFT, and then compute numerically the time evolution of the correlation matrix, from which we infer energy density evolution as well as entanglement entropy evolution. We explicitly compare predictions from periodically driven CFTs at finite temperature to results on the fermionic chain, and find that remarkably the CFT predictions about the existence of heating and non-heating phases, as well as the precise scaling across the transition, are still valid for relatively large initial temperatures. The spatial structure inherent to the heating phase of this Floquet drive at zero temperature is also present at finite temperatures, and can be observed both as signatures in energy density and entanglement entropy. We then study the effect of dissipation in Sec. 10.3, by putting two dissipators at the end of the chain, which can exchange particles with an external bath or that can act as a source of dephasing. In these two driven-dissipative scenarios, energy as well as entanglement increase rapidly, but clear signatures of the emergent horizons are observed in the high-frequency regime, where particles entering the system from the bath get stuck at the first horizon they encounter. Away from the high-frequency limit, though signatures of the horizons are not as easily observable in the energy/particle density, the specific kink structure of the mutual information between the two horizons survives a wide range of dissipation strengths.

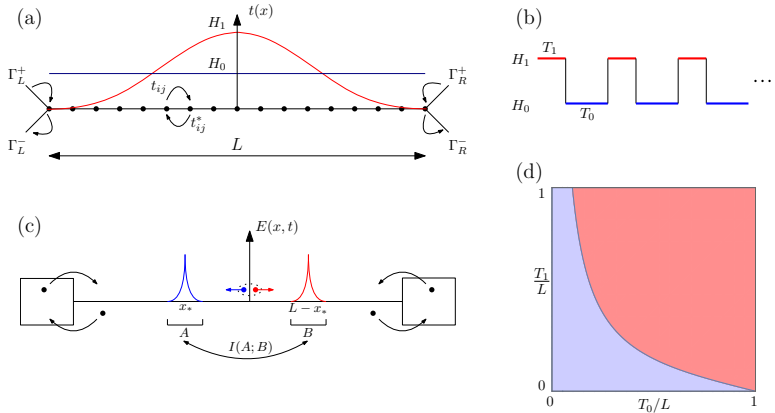


Figure 10.1: (a) Two Hamiltonians used to construct the Floquet drive: homogeneous Hamiltonian H_0 and sine-square deformed Hamiltonian H_1 on a free fermion chain of length L , with dissipators placed at the boundaries of the chain and characterised by dissipation rates $\Gamma_{L/R}^\pm$. (b) Illustration of the two step drive $H(t)$ between H_0 and H_1 . (c) Sketch of the emergent spatial structure in the energy density $E(x,t)$ in the heating phase, with two hotspots x_* and $L - x_*$, interpreted as emergent horizons in a stroboscopic curved spacetime [193]. At each Floquet cycle entangled pairs of quasiparticles are created, which accumulate at each of the two peaks, leading to a linear growth of mutual information $I(A;B)$ between the two horizons. We want to understand the robustness of this phenomenology to the introduction of dissipation and thermal initial states. (d) Phase diagram between heating and non-heating phases in the case without dissipation at zero temperature.

10.2 THERMAL EFFECTS ON THE HEATING DYNAMICS

In this first section we first generalize the results from Chapter 7 and Chapter 9 on the time evolution of total energy $E(t)$ in the case of finite temperature β^{-1} and finite system size L , and compare these CFT predictions with explicit lattice calculations on a non-interacting fermionic chain.

THERMAL FLOQUET CFT We now provide an analytical expression for the stroboscopic time evolution of the total energy $E(t)$ after n -cycles of the SSD Floquet drive (see Chapter 7), starting from an initial thermal state at temperature β^{-1} . This entails the computation of the following:

$$E(t) = \frac{2\pi}{L} \text{Tr}(e^{-\beta H_0} (U_F^n)^\dagger (L_0 + \bar{L}_0) U_F^n), \quad (10.1)$$

where $U_F = e^{-iH_0T_0} e^{-iH_1T_1}$. We provide two alternative routes to compute $E(t)$. The first approach makes use of the underlying $\mathfrak{su}(1,1)$ algebra spanned by $\{L_0, L_{-1}, L_1\}$, while the second approach relies on diffeomorphisms of the circle presented in Chapter 9.

We first evaluate the stroboscopic time evolution operator

$$(U_F^n)^\dagger L_0 U_F^n = e^{in(T_0+T_1)H_F} L_0 e^{-in(T_0+T_1)H_F}, \quad (10.2)$$

with the Floquet Hamiltonian assuming the form (7.63) from Chapter 7. The time evolution of the operator L_0 in the Heisenberg picture then takes the form

$$e^{in(T_0+T_1)H_F} L_0 e^{-in(T_0+T_1)H_F} = \theta_1 L_0 + \theta_2 L_1 + \theta_3 L_{-1}. \quad (10.3)$$

Using the fact that only L_0 has a non-zero expectation in a thermal state, we obtain

$$\text{Tr}[(L_0 + L_1 + L_{-1})e^{-\beta H_0}] = \text{Tr}[L_0 e^{-\beta H_0}], \quad (10.4)$$

Note that the non-zero modes of the stress tensor do not contribute since $L_{\pm 1}$ acting on the ket (or bra) creates a descendant state of a different level, which is orthogonal to the bra (or ket). From this argument, it is clear that $\langle L_1 \rangle_\beta = \langle L_{-1} \rangle_\beta = 0$, thus we simply need to evaluate θ_1 in (10.3). To do so, we make use of the non-unitary 2×2 representation of the $\mathfrak{su}(1,1)$ algebra, given by

$$L_0 \Big|_{2 \times 2} = \begin{pmatrix} -1/2 & 0 \\ 0 & 1/2 \end{pmatrix}, \quad L_{-1} \Big|_{2 \times 2} = \begin{pmatrix} 0 & 0 \\ -1 & 0 \end{pmatrix}, \quad L_1 \Big|_{2 \times 2} = \begin{pmatrix} 0 & 1 \\ 0 & 0 \end{pmatrix}. \quad (10.5)$$

We thus deduce that

$$\begin{aligned} \langle e^{iH_F t} L_0 e^{-iH_F t} \rangle_\beta &= \theta_1 \langle L_0 \rangle_\beta \\ &= \left(\frac{\sigma_0^2 - (\sigma_+^2 + \sigma_-^2) \cos \left[\sqrt{\sigma_0^2 - \sigma_+^2 - \sigma_-^2} \frac{2\pi t}{L} \right]}{\sigma_0^2 - \sigma_+^2 - \sigma_-^2} \right) \langle L_0 \rangle_\beta, \end{aligned} \quad (10.6)$$

The remaining thermal expectation value is a time-independent equilibrium one, thus the full stroboscopic time evolution is encoded in θ_1 . Restricting to the $c = 1$ free boson CFT we can use the following standard result on the torus for a Luttinger liquid at Luttinger parameter $K = 1$,

$$\langle L_0 \rangle_\beta = -\frac{L}{4\pi} \frac{\partial \log \Theta(\beta/L)}{\partial \beta} + \sum_{m>0} \frac{m}{e^{2\pi m\beta/L} - 1}, \quad (10.7)$$

where Θ is the Siegel theta function, explicitly defined as

$$\Theta = \sum_{m,\omega \in \mathbb{Z}} \exp \left[-\frac{\pi\beta}{L} \left(\frac{m^2}{2} + 2\omega^2 \right) \right]. \quad (10.8)$$

Using the above results in (7.63), we obtain the following general result for the stroboscopic energy evolution after n cycles,

$$E(n) = \frac{\gamma_1 \gamma_2 - 4 \cosh \left(\log \xi \frac{\sqrt{\gamma_1 \gamma_2} \sqrt{\gamma_1 \gamma_2 - 4}}{\gamma_1 - \gamma_2} n \right)}{\gamma_1 \gamma_2 - 4} \times \left[-\frac{L}{4\pi} \frac{\partial \log \Theta(\beta/L)}{\partial \beta} + \sum_{m>0} \frac{m}{e^{2\pi m\beta/L} - 1} \right]. \quad (10.9)$$

The principal effect of temperature manifests via an overall temperature dependent prefactor stemming from the equilibrium thermal expectation value $\langle L_0 \rangle_\beta$. Consequently, both the periodicity of the energy oscillations and the heating rate remain unaltered. Though this factor depends on the specific theory at hand, temperature effectively decreases the energy amplitudes in both phases. The universal critical exponent characterising the non-heating-to-heating phase transition is still $\frac{1}{2}$, as the order parameters (the periodicity and the heating rate) are identical with respect to the zero temperature case.

We note that the above derivation only holds for deformation profiles that belong to the $\mathfrak{sl}(2)$ subalgebra of the full Virasoro algebra. We can also derive the finite-temperature evolution of the energy-momentum tensor after the 2-step Floquet drive for generic deformations based on the geometric approach from [165]. In this case, the evolution of the holomorphic part of the stress tensor is given by

$$\langle T(x, t) \rangle_\beta = \left(\frac{\partial \tilde{x}_n^-}{\partial x} \right)^2 \langle T(\tilde{x}_n^-(x)) \rangle_\beta - \frac{c}{24\pi} \{ \tilde{x}_n^-, x \}, \quad (10.10)$$

where $\tilde{x}_n^-(x)$ is given by (9.13), and $\{ \tilde{x}_n^-, x \}$ is the Schwarzian derivative of $x_n^-(x)$. Combining the holomorphic and anti-holomorphic parts of the stress tensor, we conclude that the energy density is

$$E(x, t) = \left[\left(\frac{\partial \tilde{x}_n^-}{\partial x} \right)^2 + \left(\frac{\partial \tilde{x}_n^+}{\partial x} \right)^2 \right] \langle T \rangle_\beta - \frac{c}{24\pi} [\{ \tilde{x}_n^-, x \} + \{ \tilde{x}_n^+, x \}]. \quad (10.11)$$

We can then use the fact that the equilibrium one-point function of the stress tensor $\langle T(\tilde{x}_n^-(x)) \rangle_\beta = \langle \bar{T}(\tilde{x}_n^+(x)) \rangle_\beta = \langle T \rangle_\beta$ is independent of x , and is simply

given by the derivative of the partition function on the torus with respect to β . For a $c = 1$ CFT corresponding to the $K = 1$ Luttinger liquid, we find

$$\langle T \rangle_\beta = \langle \bar{T} \rangle_\beta = -\frac{\partial \log Z}{\partial \beta}, \quad (10.12)$$

with the partition function of the free boson at $K = 1$ given by

$$Z(\beta) = \frac{1}{|\xi(i\beta/L)|^2} \sum_{m,w \in \mathbb{Z}} \exp \left[-\pi \frac{\beta}{L} \left(\frac{m^2}{2} + 2w^2 \right) \right] = \frac{\Theta(\beta/L)}{|\xi(i\beta/L)|^2}, \quad (10.13)$$

where ξ is the Dedekind eta function. This formula enables one (by integrating over space) to obtain $E(t)$,

$$E(t) = \int_0^L E(x, t) dx. \quad (10.14)$$

For the case of the SSD drive, the 1-cycle diffeomorphisms introduced in the previous chapter are expressed as

$$f_\pm(x) = f^{-1}(f(x) \mp T_0) \mp T_1 = \frac{L}{\pi} \arctan \left[\tan \left(\frac{\pi x}{L} \right) \mp 2\pi \frac{T_0}{L} \right] \mp \frac{T_1}{L}. \quad (10.15)$$

This approach thus leads to the stroboscopic evolution of energy density and total energy after n -cycles for general deformation profiles. However, the result does not have a closed form and must be iterated for each Floquet cycle. In the rest of the chapter, we concentrate on the SSD drive protocol for which we have a closed form expression for (10.9).

THERMAL INITIAL STATES ON THE LATTICE We now turn to lattice calculations at finite temperature. We consider the following initial thermal correlation matrix

$$C_{ij} = \frac{1}{\text{tr}(e^{-\beta H_0})} \text{tr}(c_i^\dagger c_j e^{-\beta H_0}), \quad (10.16)$$

where H_0 is the uniform chain defined in Eq. (10.19). This expression reduces to evaluating

$$C_{ij} = \sum_k U_{ki}^* U_{kj} \langle n_k \rangle, \quad (10.17)$$

where U is the unitary diagonalizing the matrix h_0 . In the large $N = \sum_k \langle n_k \rangle$ limit, we can use the Fermi-Dirac distribution

$$\langle n_k \rangle = \frac{1}{e^{\beta(\epsilon_k - \mu)} + 1}. \quad (10.18)$$

The time evolution of the correlation matrix is then obtained by solving Eq. (10.27) numerically for zero dissipation, which then reduces to the Heisenberg equation.

We extended previous CFT results at $\beta^{-1} = 0$ at thermal initial states in Sec. 10.2, in the case of a $c = 1$ compactified free boson CFT on a radius $R = 2$ (or equivalently with the Luttinger parameter $K = 1$), which describes the low-energy dynamics of our lattice model. We conclude that the physical

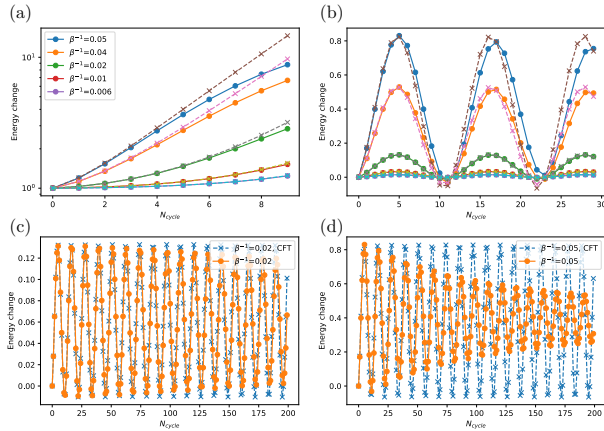


Figure 10.2: Energy change $E(t) - E(0)$ in heating phase (a) and non-heating phase (b), for different initial temperatures, for a one dimensional chain of length $L = 1000$ with periodic boundary conditions and $|T_0/L| = |T_1/L| = 0.05$. Comparison with the CFT time evolution at finite temperature is shown (dashed lines). The long time limit of the energy evolution is shown in the non-heating phase on the lattice (orange), compared to the CFT predictions (blue), both at initial temperature $\beta^{-1} = 0.02$ (c) and $\beta^{-1} = 0.05$ (d).

behaviour predicted by thermal Floquet CFT in the heating and non-heating phases does not depend crucially on the choice of (pure) initial state, which simply changes the amplitude of the total energy evolution, c.f. (10.9). In order to verify the CFT predictions, we revert to the lattice model and compute the energy, $E(t) = \sum_i \langle c_{i+1}^\dagger c_i \rangle + h.c.$. Our results for different temperatures and a comparison with the CFT predictions are shown in Fig. 10.2. In the heating phase, an exponential growth of energy with higher energy absorption at finite temperature is seen, as predicted by the finite temperature CFT predictions, that agree for a few Floquet cycles with the lattice calculations. Surprisingly, the actual heating rate on the lattice compared to the one predicted by CFT, $\frac{2\pi}{T_0+T_1} |\log(\xi)|$, slightly decreases with increasing temperature. The non-heating phase persists: the periodicity, formally defined as the inverse of the heating rate of the heating phase, $T_E = \frac{T_0+T_1}{2\pi|\log(\xi)|}$, grows with temperature in the same way that the heating rate decreases with temperature in the heating phase, while the amplitude of the oscillations gets larger, as predicted from CFT. From a CFT perspective, the change in periodicity and heating rate cannot be explained by the introduction of finite temperature, as seen explicitly from (10.9). This effect is a consequence of the full cosine dispersion of the lattice Hamiltonian, as taking higher initial temperatures will imply access to high-energy states away from the linearized regime around the Fermi points. We finally note that at long times on the lattice in the non-heating phase, the energy oscillations eventually decay, as shown in Fig. 10.2(c-d), while CFT predicts persistent oscillations up to infinite times. The speed of such a decay depends non-universally on the initial temperature β^{-1} as well as the choice of

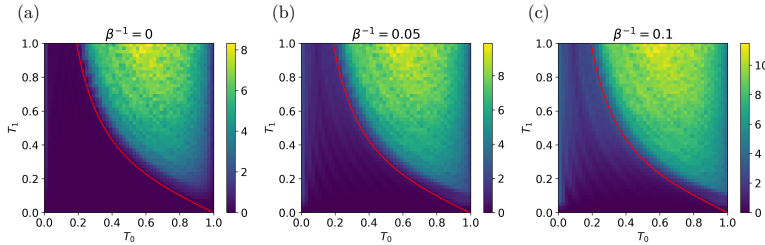


Figure 10.3: Total energy after 10 cycles as a function of T_0 and T_1 for $L = 200$, for (a) $\beta^{-1} = 0$, (b) $\beta^{-1} = 0.05$, (c) $\beta^{-1} = 0.1$. The phase boundary between heating and non-heating phases predicted by CFT (at finite and zero temperature) is shown in red and given by the solution of $\Delta = 0$ in Eq. (7.16). We note that a higher number of Floquet cycles leaves the phase diagram qualitatively unchanged, although the resulting energy deviate from CFT predictions in the heating phase at non-zero initial temperature.

driving parameters $(T_0/L, T_1/L)$. However it does not depend on the choice of system size L , for fixed T_0/L and T_1/L .

To study the robustness of the phase diagram to temperature, we plot $E(t = 10T)$ as a function of the driving parameters T_0 and T_1 , as shown in Fig. 10.3. At zero temperature, this approximates well the analytically obtained phase diagram of the CFT. At $\beta^{-1} = 0.1$ (to be compared with the cosine bandwidth of 2), the phase diagram remains unaffected and the transition between oscillating and exponentially growing total energy is still clear. This observation is consistent with the expectations from the CFT: in principle, the long time Floquet dynamics should be independent of the initial state as it only involves time evolution of operators in Heisenberg picture, such that both heating and non-heating phases should remain well-defined. This conclusion is further strengthened by the scaling behaviour of the order parameter $\frac{T_0+T_1}{2\pi|\log(\xi)|}$, the (pseudo-)periodicity of the energy $E(t)$. For pure states, CFT predicts a divergence of this order parameter with a critical exponent $\frac{1}{2}$ [123] as one approaches the boundary to the heating phase. In Fig. 10.4, we plot the scaling behaviour of the periodicity of the energy as one approaches the heating phase. At zero temperature, the lattice numerics are well-fitted by the CFT predictions. At finite temperature, though the periodicity is modified by temperature as we have observed in Fig. 10.2, the scaling across the phase transition remains the same and we can still extract a critical exponent of $\frac{1}{2}$ [123], as predicted by thermal Floquet CFT. This indicates that the transition is robust to thermal states as long as $\beta^{-1} < 0.1$, after which broadening effects stemming from the full lattice dispersion become relevant, as observed on Fig. 10.3.

The hallmark of the heating phase is the emergence of entangled black-hole horizons, where the mutual information $I(A, B)$ between the two horizons x_* and $L - x_*$ grows linearly in time, i.e., $I(A, B) \sim \frac{1}{3} \log(\xi)n$, with n the cycle number, provided A and B both contain one of the two horizons. Using Peschel's method for non-interacting lattice systems [194], we extract the entanglement entropy from the correlation matrix C_{ij} of the lattice problem. The stroboscopic evolution of the mutual information for $A = [0, x]$ and $B = (x, L]$ for $n = 15$ Floquet cycles with the concomitant energy density $E(x, t)$ are shown in

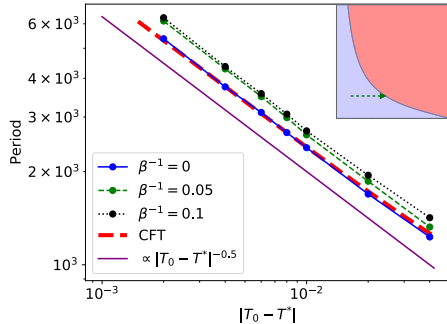


Figure 10.4: Scaling of the periodicity of total energy $E(t)$ in the non-heating phase when approaching phase transition at $T_0 = T_*$, for $T_1/L = 0.05$, and for different initial states β^{-1} . Explicit comparison with the CFT scaling (which is independent of temperature) is shown. While the periodicity changes as we increase initial temperature, its scaling near the phase transition agrees with the CFT prediction giving a critical exponent $\frac{1}{2}$ for any initial temperature.

Figs. 10.5(a) and (b) (heating phase away from the high-frequency limit). At zero temperature, the mutual information displays a clear kink structure at x_* and $L - x_*$, with a linear growth of mutual information if $x \in (x_*, L - x_*)$, and saturation to a constant otherwise. We find that this spatial structure of entanglement is robust to the introduction of initial temperatures, as long as $\beta^{-1} \approx 0.05$, after which the emergent entanglement structure starts to break down, and the energy horizons disappear. We note that this regime of driving parameters corresponds to large micromotion of the order of the system size, such that deviations from the linear dispersion are crucial. We conclude that the CFT predictions for the phase diagram and the structure characterising the heating-to-non-heating transition in the driven lattice model are robust to the introduction of temperatures up to $\beta^{-1} \sim 0.05$.

10.3 EFFECTS OF DISSIPATION ON THE HEATING TRANSITION

In the previous section, we discussed how heating in a generic class of critical driven closed systems emerges via with formation of entangled energy hotspots. We now explore whether this rich phenomenology survives in an open system setting, a situation of great relevance to experiments where dissipation is ubiquitous. Typically, the study of a dissipative and driven interacting lattice model at criticality requires highly complex computational tools which might be poorly convergent in the long time limit. However, here we can harness the fact that the main physical features are universal and solely characterized by the central charge of the critical lattice model to simplify our task of the study of the dissipative system. Hence, in this section, as a representative example, we consider a system of free fermions hopping on a one-dimensional lattice of length L at half-filling, whose low energy theory is a $c = 1$ free boson CFT. This model permits an exact derivation of the time evolution of the system in

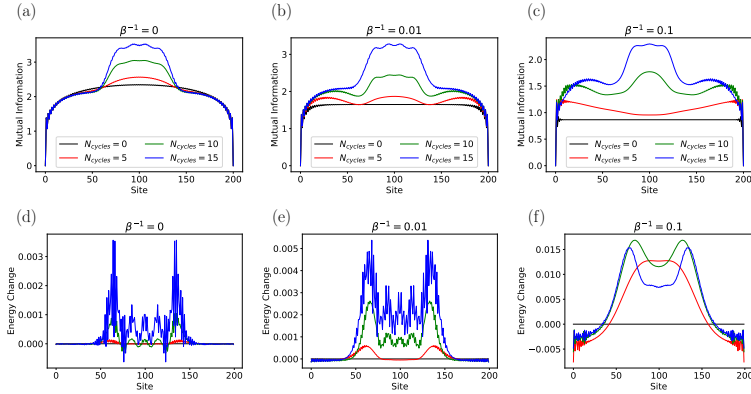


Figure 10.5: (a-c) Scaling of mutual information $I([0, x], (x, L])$ in the heating phase, $T_0/L = 0.95$, $T_1/L = 0.05$, $L = 200$ for different initial temperatures, $\beta^{-1} = 0, 0.01, 0.1$. A kink structure is observed at the position of the two horizons $x_* \approx 55$ and $L - x_*$, as predicted by CFT. (d-f) Energy density $E(x, t) - E(x, 0)$ in the heating phase $T_0/L = 0.95$, $T_1/L = 0.05$, $L = 200$ for different initial temperatures, $\beta^{-1} = 0, 0.01, 0.1$. We observe at x_* and $L - x_*$ two hotspots in energy density that are building up exponentially in time.

the presence of both dissipation and drive. The Hamiltonians corresponding to the two-step drive in Eq. (13.44) are given by

$$\begin{aligned} H_0 &= \frac{1}{2} \sum_{i=1}^{L-1} c_i^\dagger c_{i+1} + \text{h.c.}, \\ H_1 &= \sum_{i=1}^{L-1} \sin^2\left(\frac{\pi i}{L}\right) c_i^\dagger c_{i+1} + \text{h.c..} \end{aligned} \quad (10.19)$$

The dynamics of the system density matrix ρ is governed by the Gorini-Kossakowski-Sudarshan-Lindblad master equation [175, 195–199]

$$\frac{\partial \rho}{\partial t} = -i[H(t), \rho] + \sum_{\mu} \left(2L_{\mu}\rho L_{\mu}^\dagger - \{L_{\mu}^\dagger L_{\mu}, \rho\} \right). \quad (10.20)$$

For the situation where the Hamiltonian $H(t)$ and the bath operators L_{μ} are respectively quadratic and linear in the fermionic operators (c and c^\dagger), a general solution can be exactly obtained [200].

We first map the fermionic operators to Hermitian Majorana operators

$$w_{2m-1} = c_m^\dagger + c_m, \quad w_{2m} = i(c_m - c_m^\dagger) \quad (10.21)$$

which satisfy the anti-commutation relations

$$\{w_j, w_k\} = 2\delta_{j,k}. \quad (10.22)$$

In the Majorana representation, the Hamiltonian and the bath operators can be expressed as

$$\begin{aligned} H &= \sum_{lm} w_l H_{lm} w_m, \\ L_\mu &= \sum_n l_{\mu,n} w_n, \end{aligned} \quad (10.23)$$

where H_{lm} is a $2L$ by $2L$ anti-symmetric matrix. In this chapter, we consider the following bath operators attached at the two ends of the chain as shown in Fig. 10.1(a):

$$L_{L/R} = \Gamma_{+/-}^{L/R} c_{L/R}^\dagger + \Gamma_{-/+}^{L/R} c_{L/R}, \quad (10.24)$$

where L (R) refers to the site on the left (right) edge of the chain. For this chapter, we fix $\Gamma^L = \Gamma^R$ and define

$$\Gamma_+ = \gamma, \quad \Gamma_- = \mathcal{R}\gamma. \quad (10.25)$$

In a non-interacting system, all observables can be obtained from the correlation matrix

$$C_{lm} = \text{tr}(w_l w_m \rho). \quad (10.26)$$

Using the anti-commutativity of the Majorana operators (10.22) and the Lindblad equation (10.20), it can be shown that the correlation matrix obeys [201]

$$\frac{dC}{dt} = -4C(t) \left[iH(t) + iH(t)^T + M_r + M_r^T \right] - 8iM_i, \quad (10.27)$$

where M_r (M_i) is the real (imaginary) part of the matrix $M_{ij} = \sum_\mu l_{\mu,i} l_{\mu,j}^*$. We now use the fact that the Floquet Hamiltonian $H(t)$ is piecewise constant in time, such that Eq. (10.27) is a Lyapunov matrix ordinary differential equation of the form $\dot{C} = -XC(t) - C(t)X^T - iY$, whose explicit solution takes the closed form [202]

$$\begin{aligned} C_{il}(t) &= \sum_{j,k} V_{ij} \left[\left(e^{t(\alpha_j + \beta_k)} \right) \left(V^{-1} C(t_0) (W^\dagger)^{-1} \right)_{jk} \right. \\ &\quad \left. + \left(\int_{t_0}^t ds e^{(t-s)(\alpha_j + \beta_k)} \right) \left(V^{-1} (-iY) (W^\dagger)^{-1} \right)_{jk} \right] W_{kl}^\dagger, \end{aligned} \quad (10.28)$$

where $C(t_0)$ is the initial correlation matrix, V and W are the unitaries diagonalizing $-X$ and $-X^T$, and α_i, β_i are their respective eigenvalues. The full stroboscopic time evolution $C(n(T_0 + T_1))$ can be obtained numerically via a sequential evolution by resetting the initial condition to $C(nT_1 + (n-1)T_0)$.

This analysis can be extended to include dissipation quadratic in fermion operators, such as on-site dephasing, for which $L_\mu = \sqrt{\gamma_\mu} c_\mu^\dagger c_\mu$. By taking expectation values of Eq. (10.20) one finds the evolution equation for the (now complex) correlation matrix $\Gamma_{ij}(t) = \text{Tr}\{\rho(t)c_i^\dagger c_j\}$ to be of the form

$$\partial_t \Gamma_{ij}(t) = i \left[h^T(t), \Gamma(t) \right]_{ij} + \sum_\mu \gamma_\mu (2\delta_{ij}\delta_{\mu i} - \delta_{\mu i} - \delta_{\mu j}) \Gamma_{ij}(t), \quad (10.29)$$

where $h(t)$ is defined by $H = \sum_{ij} h_{ij}(t) c_i^\dagger c_j$. Closed equations similar to Eq. (10.29) can be easily integrated numerically, and hold for generic dephasing terms as long as the jump operators are hermitian. As before, the correlation matrix contains enough information to compute quantities such as the energy density. However, in contrast to single particle loss and gain, the resulting density matrix is in general non-gaussian, which prevents us from directly computing entanglement entropies [203].

Dephasing is also often generated by unitary evolution in the presence of white noise [204], or in quantum state diffusion models [203]. Here we take the former approach by adding an additional Hamiltonian term $V_i = \xi_i(t)n_i$, where $\xi_i(t)$ is gaussian white noise whose variance is fixed by the dephasing strength via $\overline{\xi_i(t)\xi_i(t')} = \delta(t-t')\gamma_i$. After averaging over different noise realizations the unitary dynamics is equivalent to Eq. (10.20) with $L_\mu = \sqrt{\gamma_\mu} c_\mu^\dagger c_\mu$, which can be seen by averaging over the trotterized equations of motion for the density matrix. This endows the dephasing with a physical interpretation and allows us to study the entanglement dynamics within each noise realization. The average dynamics of the entanglement entropy $\overline{S_A(t)} = -\text{Tr}\rho_A \log \rho_A \neq -\text{Tr}\bar{\rho}_A \log \bar{\rho}_A$ generally differs from the entanglement of the average density matrix, and can exhibit more interesting features such as entanglement phase transitions [205]. In the following we will focus on the dynamics of $\overline{S_A(t)}$ and the energy density for boundary noise where

$$L_{L,R} = \sqrt{\gamma_{L,R}} c_{L,R}^\dagger c_{L,R} = L_{L,R}^\dagger \quad (10.30)$$

Whether coherent non-equilibrium dynamics remains stable to external baths is an interesting —and in general open— question. The difficulty in open systems stems from the fact that the system can now exchange energy and information with a dissipative environment, which can irreversibly alter fragile quantum states. Typically, one can expect that a contact with the environment acts as a mitigating influence on the energy absorbed by the system from the drive, thereby stabilising non-heating phases in larger parts of the phase diagram. To test this heuristic picture, we consider boundary dissipation in the finite chain. We will not be interested in the steady state reached by the system at large times, but rather in the robustness of the features of the heating phase to dissipation, as well as the transition between different phases at short times, of the order of tens of Floquet cycles.

We first consider the case where the driven free fermion chain exchanges particles with an external bath at its boundaries. All observables can be computed from the correlation matrix (10.26). The time dependent correlation matrix for dissipative particle exchange is explicitly given by Eq. (10.28), for a piecewise constant Floquet Hamiltonian $H(t)$.

As a first step, we consider the high-frequency regime of the drive, i.e. $|T_0| + |T_1| \ll L$. For $T_0, T_1 > 0$, this corresponds to the non-heating phase in the dissipationless case, as seen in Fig. 10.1(d). Dissipation washes out the oscillating structure of energy and entanglement entropy of the non-heating phase. We will therefore focus our analysis on the heating phase. Note that addition of temporal disorder already erases the non-heating phase in the dissipationless setting [131]. Given the periodicity of the phase diagram along the $\frac{T_0}{L}$ axis, we can also explore a heating phase in the high-frequency limit if $T_0 < 0$. This is equivalent to switching the sign of the homogeneous Hamiltonian. In this case the quasiparticles propagating with local velocities $v_0(x)$ for time T_0 and $v_1(x)$ for time T_1 , change their direction between the two steps of the drive,

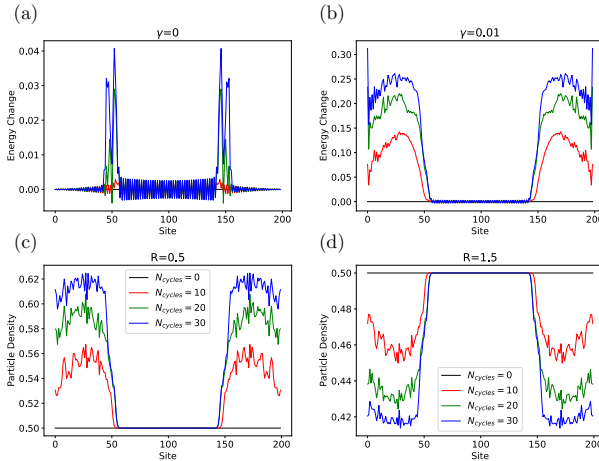


Figure 10.6: High-frequency regime for the driving parameters, $|T_0|/L = |T_1|/L = 0.05$. (a,b): Energy density time evolution $E(x,t) - E(x,0)$ in the case without dissipation, $\gamma = 0$, as well as the case with dissipation $\gamma = 0.01$. (c) Particle density evolution, for $\gamma = 0.01$, for different number of Floquet cycles, with $\mathcal{R} = 0.5$, leading to an overall particle gain. (d) Same as (c) but for $\mathcal{R} = 1.5$, leading to an overall particle loss.

and the micro-motion of left (right) movers oscillates around x_* ($L - x_*$). This regime will be particularly resistant to the introduction of dissipation at the two edges of the chain as due to reduced micromotion, the energy horizons survive not only at stroboscopic times but all times. Consequently, no information can propagate from one edge of the system to the other. Therefore, adding or removing particles (depending on the ratio \mathcal{R} between $\Gamma_+^{L/R}$ and $\Gamma_-^{L/R}$) at the edges of the chain does not affect the particle density between x_* and $L - x_*$, which remains pinned at $\frac{1}{2}$, as seen in Fig. 10.6(c–d) .

Energy accumulation is seen in the regions $[0, x_*]$ and $[L - x_*, L]$ for non-zero dissipation strength, see Fig. 10.6(b). Although the energy density ultimately becomes larger at the edges of the chain, the horizons act as an energy blockade, preventing any energy growth in the central region ($x_*, L - x_*$). We conclude that in such a regime the dissipative system will not tend to a steady state with uniform density, where particle density is 1 (0) if $\mathcal{R} < 1$ ($\mathcal{R} > 1$) (see Eq. (10.25)) , because of the persistence of the horizons which effectively decouple the system into three pieces: the left and right edges $[0, x_*]$ and $(L - x_*, L]$ where particles accumulate or deplete because of the exchange with the bath, and the middle piece $(x_*, L - x_*)$ where the dynamics is unaffected by the dissipative couplings to the baths. This decoupling is understood via the quasiparticle picture, where the micromotion of quasiparticles is concentrated around the horizons, and the system is effectively quenched with a deformed Hamiltonian with a velocity profile $v_{\text{eff}}(x)$ such that $v_{\text{eff}}(x_*) = v_{\text{eff}}(L - x_*) = 0$, leading to such decoupling [193]. We note that this quenched dynamics is only a good approximation in the high-frequency limit $|T_0| + |T_1| \ll L$. Besides exponential energy accumulation, horizons also share mutual information $I(A, B)$ which

grows linearly in time. This linear growth of mutual information is shown in Fig. 10.7(a). The extent of this linear regime increases with system size L , as clearly shown in Fig. 10.7(b). We see that the physics of entangled horizons persist for a substantial range of dissipation in large enough systems. However, we note that above a certain dissipation threshold of about $\gamma \sim 0.1$, we lose this linear regime of entanglement growth in the high-frequency regime.

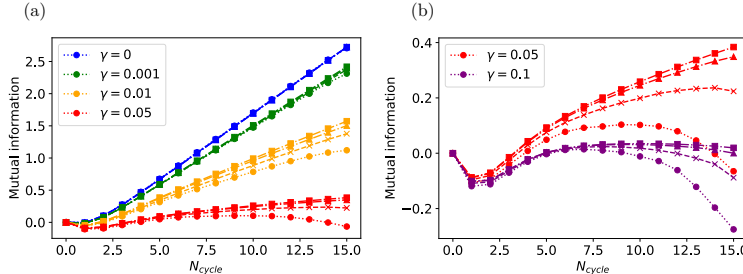


Figure 10.7: (a) Growth of half-system mutual information $I([0, L/2], [L/2, L])$ for $|T_0/L| = 0.05$, $T_1/L = 0.05$, with different dissipations, and system sizes $L = \{100, 200, 500, 800\}$ (circle, cross, triangle, square). (b) Same plot for different values of γ .

Away from such a high-frequency limit, micro-motion is not negligible anymore [126] and quasiparticles can travel through the whole system in a single Floquet period, which makes the horizon picture only valid at stroboscopic times, and cannot decouple the system completely at all times. The energy density will ultimately, at long enough times, increase uniformly in the system instead of being confined to the horizons as we increase dissipation. Our results for the mutual information for the case $\Gamma_+^{L/R} = \Gamma_-^{L/R} =: \gamma$ are summarized in Fig. 10.8. We find that the mutual information is robust to small enough dissipation $\gamma < 0.005$, indicating that the entangled horizons survive for a range of times, even in cases where $|T_0| + |T_1| \sim L$. We stress that such a structure is not observed as clearly in the entanglement entropy, as it does not integrate out entanglement shared with the bath contrary to mutual information.

An important question concerns whether the transition from the heating to the non-heating phase is modified or smeared by dissipation. The heating phase is characterised by linearly growth of mutual information in time, as long as the subsystems A and B contain one of the two horizons each, while the non-heating phase has an oscillatory mutual information. Therefore we analyse the scaling of the half-system mutual information $I\left([0, \frac{L}{2}], \left(\frac{L}{2}, L\right)\right)$ after 10 Floquet cycles across the phase transition predicted by CFT across the $\frac{T_0}{L} = \frac{T_1}{L}$ line in Fig. 10.9(a). In the non-heating phase mutual information oscillates by varying the driving parameters, while it suddenly grows as a function of $\frac{T_0}{L}$ after $\frac{T_*}{L} \approx 0.415$, as predicted by CFT in the non-dissipative case, and then increases as a function of driving parameters in the heating phase. Although the critical exponent cannot be extracted clearly in the dissipative case, we still clearly observe a non-analyticity at $\frac{T_*}{L}$, signalling the persistence of the phase transition, for values of the dissipation rate γ smaller than 0.005. After this threshold, dissipation dephases quasi-particles which makes it impossible to

Floquet cycles across the phase transition predicted by CFT across the $\frac{T_0}{L} = \frac{T_1}{L}$ line in Fig. 10.9(a). In the non-heating phase mutual information oscillates by varying the driving parameters, while it suddenly grows as a function of $\frac{T_0}{L}$ after $\frac{T_*}{L} \approx 0.415$, as predicted by CFT in the non-dissipative case, and then increases as a function of driving parameters in the heating phase. Although the critical exponent cannot be extracted clearly in the dissipative case, we still clearly observe a non-analyticity at $\frac{T_*}{L}$, signalling the persistence of the phase transition, for values of the dissipation rate γ smaller than 0.005. After this threshold, dissipation dephases quasi-particles which makes it impossible to

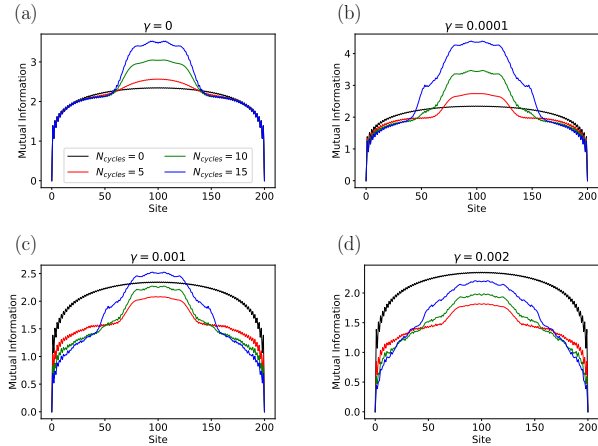


Figure 10.8: Scaling of mutual information in the heating phase $T_0/L = 0.9$, $T_1/L = 0.1$ and $L = 200$, for different values of dissipation $\gamma = \Gamma_+^L = \Gamma_+^R$, with $\Gamma_+^{L/R} = R\Gamma_-^{L/R}$ with $R = 0.1$, (a) no dissipation, $\gamma = 0$, (b) $\gamma = 0.0001$, (c) $\gamma = 0.001$, (d) $\gamma = 0.002$.

correctly observe entangled pairs of quasiparticles forming at the two horizons x_* and $L - x_*$ at each Floquet cycles, leading to entanglement growth between left and right regions in the dissipationless case.

We now consider dephasing at the boundaries of the chain instead of letting particle exchange with an external bath. In contrast to the previous case, here the dissipation conserves particle number and the particle density will not show any signature of the horizons. We therefore focus on the energy density $E(x, t)$, computed from the correlation matrix, as well as the mutual information averaged over the Gaussian white noise realizations $\xi_i(t)$ in the presence of a boundary potential $V_i = \xi_i(t)n_i$. We show the half-system mutual information after 10 drive cycles in Fig. 10.9 (b). While dephasing is expected to partially suppress the generation of entanglement since it drives the system into a trivial mixed state, we find that the half-chain entanglement entropy grows with increasing dephasing strength for several driving cycles. This shows that fluctuations induced by our dephasing protocol at the edges of the system dominate the dynamics on the time scales we are considering. Our results show that the entanglement dynamics introduced by the dephasing smoothens out the sharp transition from the heating-to-non-heating phase compared to the previous dissipation scheme. This growth in entanglement is also connected to the rapid growth of energy density across the whole system, as shown in Fig. 10.10. This dynamics of the total energy stems from the injection of quasiparticle excitations due to the fluctuations at the edges and is generally found to be exponential in time [203, 206].

Although there is no sharp transition between the heating and non-heating phase, the energy density $E(x, t)$ in the heating phase still forms robust peak structures, similar to the heating phase in the closed system, see Fig. 10.10. The horizon structure persists for more than 10 driving cycles, despite dephasing

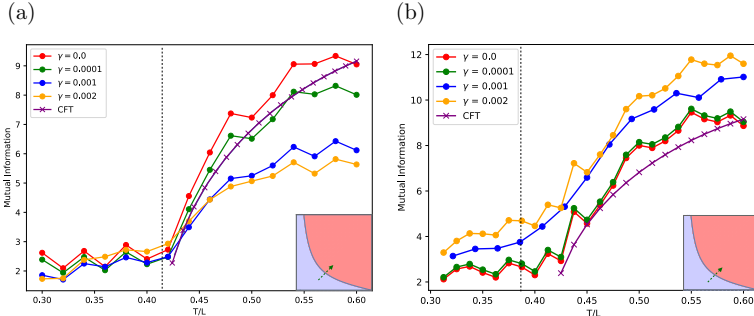


Figure 10.9: (a) Half-system mutual information $I([0, \frac{L}{2}), (\frac{L}{2}, L])$ after 10 Floquet cycles as a function of $\frac{T_0}{L} = \frac{T_1}{L} =: \frac{T}{L}$ for different values of the dissipation γ , and $L = 100$. The phase transition in the CFT model occurs at $\frac{T_*}{L} = 0.415$. We also display the scaling predicted by the CFT for the mutual information in the dissipationless case. We observe a kink in the mutual information around $\frac{T_*}{L}$, signalling the persistence of the heating and non-heating phases in the entanglement structure of the system, even for non-zero dissipation. (b) Same figure but with dephasing instead of particle exchange with the bath.

strengths of the order of $\gamma = 0.001$. Furthermore, the horizons remain at the positions x_* and $L - x_*$ predicted by the CFT, despite the sizable change in the total energy, as shown in Fig. 10.10(b).

We finally note that studying the interplay between dissipation and dephasing could lead to even richer physics. In systems without any Floquet driving, for example the XXZ chain, it has been shown that the interplay between edge dissipators and local dephasing terms can indeed result in varied regimes of heat and spin transport, for instance unidirectional heat flow, or heat flowing from both edge reservoirs towards the middle. Transitions from a ballistic regime to diffusive regime can be generated by such dissipators [207]. When coupled with periodic driving, it is highly likely that interesting regimes of behaviour, especially from a quantum thermodynamics perspective, might arise. It will be interesting to study in detail these effects.

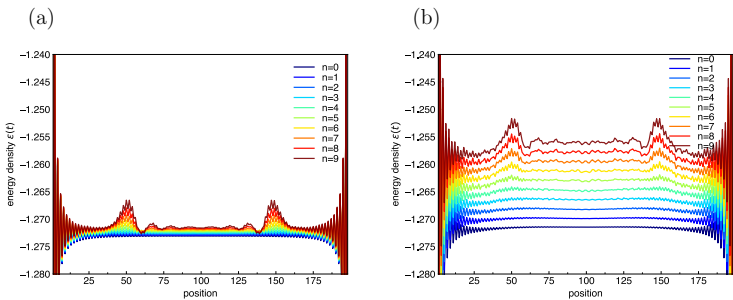


Figure 10.10: Time evolved energy density $E(x, t)$ in the heating phase with driving parameters $T_0/L = 0.95$, $T_1/L = 0.05$ for the dephasing protocol on the boundaries, with dephasing strengths (a) $\gamma = 0.0001$ and (b) $\gamma = 0.001$. The horizon structure of the heating phase persists in presence of dissipation.

FLOQUET ENGINEERED INHOMOGENEOUS QUANTUM CHAOS

11.1 INTRODUCTION

This chapter delves into the investigation of scrambling properties exhibited by periodically driven inhomogeneous critical systems. As explored in Chapter 7 and 9, these Floquet systems showcase diverse heating and non-heating phases, owing to the presence of fixed points in the one-cycle Floquet map that captures the time evolution of primary fields. Although the effective curved spacetime [see Sec. 7.4] related to the non-heating phase is devoid of singularities, the heating phase displays emergent spacetime horizons that absorb all quasiparticles and share growing non-local quantum information. The peculiar nature of this “integrable heating phase” suggests that the emergent Floquet horizons could contribute to the emergence of quantum chaotic features. While minimal models and rational CFTs do not exhibit chaotic features, holographic CFTs at thermal equilibrium have been shown to be maximally chaotic [208].

The primary objective of this chapter is to understand how the emergence of Floquet horizons affects chaotic features at large central charge far from thermal equilibrium. We demonstrate that inhomogeneous periodic drives in the heating phase result in the inhomogeneous scrambling of quantum information, as indicated by out-of-time-order correlators (OTOC) [see Sec. 4.3]. The Hawking temperature of the Floquet horizons serves as an effective temperature at which the driven large- c CFT thermalizes, thereby restoring the limit on quantum chaos at thermal equilibrium. Furthermore, the inhomogeneous nature of this scrambling implies that continuous tuning of the driving parameters results in transitions from chaotic to non-chaotic regimes, which cannot be the case for homogeneous chaotic CFTs at equilibrium [208].

The remainder of this chapter is structured as follows. In Sec. 11.2, we provide a brief review of OTOC computation for large central charge CFTs at thermal equilibrium, as outlined in [208]. In Sec. 11.3, we extend this computation to the case of periodically driven inhomogeneous CFTs with large central charge, with a focus on the $\mathfrak{sl}(2)$ class of drives. Additionally, in Sec. 11.4, we investigate another class of periodic drives based on Rindler deformations and demonstrate how tuning the driving parameters can induce transitions in the OTOC behavior between chaotic and non-chaotic dynamics. Finally, in Sec. 11.5 we propose a simple measurement protocol for OTOCs, which is based on a stroboscopic backward time evolution approach that is suitable for any driven inhomogeneous CFT.

11.2 PRELUDE: QUANTUM CHAOS AT LARGE CENTRAL CHARGE

In this section we review the derivation of the time evolution of out-of-time-order correlators (OTOCs) for a homogeneous CFTs at a temperature β^{-1} [208]. In particular, we rederive the result that the OTOC of holographic CFTs (i.e., CFTs with central charge $c \rightarrow \infty$) in the Virasoro identity block shows an early time exponential growth with a Lyapunov exponent λ_L that saturates

the bound on quantum chaos. As discussed in Sec. 4.3, the OTOC defines a useful diagnose of early time quantum chaos, and is generally defined, for two operators V and W , as

$$C(t) \sim \langle W(t)VW(t)V \rangle_\beta, \quad (11.1)$$

such that $[V, W] = 0$ at time $t = 0$. By the growing non-commutativity of operators in quantum chaotic systems, one would expect at large times a small overlap by comparing a state on which we apply V and then $W(t)$ or first $W(t)$ and then V , thus leading to non-trivial time evolution evolution of OTOCs. This chaotic property of OTOC was uncovered from the gravity sector of holographic theories [209], and led to the assumption that there is a bound on the exponential growth of OTOC [210].

We consider a (1+1)-dimensional CFT, such that the computation of the OTOC reduces to a four-point function of primary fields $V(z, \bar{z})$ and $W(z, \bar{z})$, on a Euclidean thermal cylinder at finite temperature β^{-1} and infinite system size. In such a setting, time evolution of primary fields on the thermal cylinder amounts to computing vacuum expectations,

$$\langle \Phi(x, t) \dots \rangle_\beta = \left(\frac{2\pi z}{\beta} \right)^h \left(\frac{2\pi \bar{z}}{\beta} \right)^{\bar{h}} \langle \Phi(z, \bar{z}) \dots \rangle, \quad (11.2)$$

with

$$z(t) = e^{\frac{2\pi}{\beta}(x+t)}, \quad \text{and} \quad \bar{z}(t) = e^{\frac{2\pi}{\beta}(x-t)}. \quad (11.3)$$

We are thus left with evaluating a vacuum four point function, of the form

$$\langle W(z_1, \bar{z}_1)W(z_2, \bar{z}_2)V(z_3, \bar{z}_3)V(z_4, \bar{z}_4) \rangle = \frac{1}{z_{12}^{2h_v} z_{34}^{2h_w}} \frac{1}{\bar{z}_{12}^{2\bar{h}_v} \bar{z}_{34}^{2\bar{h}_w}} \mathcal{F}(\eta, \bar{\eta}), \quad (11.4)$$

with the cross ratio $\eta = \frac{z_{12}z_{34}}{z_{13}z_{24}}$. In fact, as explained in Sec. 3.2, four-point functions of primary fields cannot be fixed solely by conformal invariance, and require the knowledge of the full operator content of the theory at hand, which is encoded in the conformal blocks \mathcal{F} . On general grounds, this function can be expanded in terms of global conformal blocks for any CFT, taking the form of a sum over the conformal dimension of all global $SL(2)$ primary fields of Gauss hypergeometric functions $F(h, h, 2h, \eta)$. This implies a common feature of \mathcal{F} to all CFTs: it has a branch cut on $[1, \infty)$. While such an expression is not analytically tractable in most cases, we will focus on the Virasoro identity block of the large central charge limit, in which case it can be approximated for small h_w/c and large h_v/c [211]. The whole task is thus to correctly analytically continue the correlator (11.4) from a Euclidean to a Lorentzian correlator, while preserving the correct time-ordering prescription to reproduce the desired out-of-time-order (OTO) ordering. The prescription amounts to first giving a small imaginary time component $i\epsilon_j$ to all four fields $j = 1, 2, 3, 4$, then time evolve with real time evolution the W fields, and then take the limit of zero imaginary time, $\epsilon_j \rightarrow 0$, in such a way that $\epsilon_1 > \epsilon_3 > \epsilon_2 > \epsilon_4$. The cross ratio, for the W field inserted at x_1 at $t = 0$, and V inserted at x_2 , thus reads

$$\eta = \frac{\left(e^{\frac{2\pi}{\beta}(x_1+t+i\epsilon_1)} - e^{\frac{2\pi}{\beta}(x_1+t+i\epsilon_2)} \right) \left(e^{\frac{2\pi}{\beta}(x_2+i\epsilon_3)} - e^{\frac{2\pi}{\beta}(x_2+i\epsilon_4)} \right)}{\left(e^{\frac{2\pi}{\beta}(x_1+t+i\epsilon_1)} - e^{\frac{2\pi}{\beta}(x_2+i\epsilon_3)} \right) \left(e^{\frac{2\pi}{\beta}(x_1+t+i\epsilon_2)} - e^{\frac{2\pi}{\beta}(x_2+i\epsilon_4)} \right)}, \quad (11.5)$$

and similarly for the anti-holomorphic cross ratio. Different orderings of the imaginary times ϵ_j leads to different paths in the complex plane for the cross-ratio as a function of t , even in the limit $\epsilon_j \rightarrow 0$. In the case of the OTO ordering prescription, one readily shows that η crosses the branch cut $[1, \infty)$ for a finite time t_* that is given by

$$t_* = \frac{\epsilon_{12}\epsilon_{34}}{\epsilon_{13}\epsilon_{24}}, \quad (11.6)$$

with $\epsilon_{ij} = i(e^{\frac{2\pi}{\beta}i\epsilon_i} - e^{\frac{2\pi}{\beta}i\epsilon_j})$. The crossing of this branch cut, by the monodromy properties of \mathcal{F} around $\eta = 1$, leads to the following expression for the holomorphic conformal block in the limit of large central charge, with h_w/c fixed and small and h_v/c fixed and large,

$$\mathcal{F}(\eta) \approx \left(\frac{1}{1 - \frac{24\pi i h_w}{c\eta}} \right)^{2h_v}, \quad (11.7)$$

while $\bar{\mathcal{F}}(\bar{\eta}) \approx 1$ as the antiholomorphic cross ratio does not cross the branch cut¹. In the late time limit, the holomorphic cross ratio is shown to saturate to

$$\eta \sim -e^{\frac{2\pi}{\beta}(x_2 - x_1 - t)} \epsilon_{12}^* \epsilon_{34}. \quad (11.8)$$

This late time expression for the cross ratio leads to the following late-time expression of the OTOC [208],

$$\begin{aligned} & \langle W(x_1, t + i\epsilon_1) V(x_2, i\epsilon_2) W(x_1, t + i\epsilon_3) V(x_2, i\epsilon_4) \rangle_\beta \\ & \sim \left(\frac{1}{1 + \frac{24\pi i h_w}{\epsilon_{12}^* \epsilon_{34}}} e^{\frac{2\pi}{\beta}(t - t_* - x_2 + x_1)} \right)^{2h_v}, \end{aligned} \quad (11.9)$$

where we defined the scrambling time

$$t_* = \frac{\beta}{2\pi} \log(c), \quad (11.10)$$

which leads to an exponential decrease of the OTOC as t is larger than the scrambling time. In particular, the Lyapunov exponent of such an exponential decrease is given by

$$\lambda_L = \frac{2\pi}{\beta}, \quad (11.11)$$

which exactly saturates the bound on quantum chaos [210], as is also the case for black holes. This result is expected because of the existence of a gravitational AdS₃ dual to holographic CFTs containing a black hole. While such a maximally exponentially decaying behaviour is not expected for rational CFTs at finite central charge, because of their integrability properties, it has been shown that irrational CFTs also exhibit exponential decay at a smaller Lyapunov exponent. Another example of a CFT displaying non-trivial OTOC at finite temperature is the compactified free boson $c = 1$ at an irrational radius, that may be realized in the low energy physics of the XXZ model for irrational values of the anisotropy Δ .

¹ We note that this condition is necessary to obtain the desired non-trivial evolution of the OTOC: if both the holomorphic and antiholomorphic cross ratio would cross the branch cut, the obtained total time evolution would be trivial. This subtlety will become crucial in the rest of the chapter.

11.3 OTOCS FOR INHOMOGENEOUS FLOQUET CFTS

We have seen in Sec. 11.2 that CFTs at large central charge and at thermal equilibrium are maximally chaotic as their OTOCs saturate the bound on quantum chaos (11.11). On the other hand, we have studied in Chapter 7 the emergence of “integrable heating phases” in periodically driven inhomogeneous CFTs, when starting from either pure or thermal initial states. These heating phases are characterized by a strongly inhomogeneous growth of energy and entanglement, such that all entangled pairs of quasiparticles accumulate at single points at stroboscopic times, interpreted as emergent Floquet horizons. Such classes of driven inhomogeneous CFTs apply to arbitrary values of the central charge, and is in particular valid in the holographic limit, and possess a holographic dual (see [212] for an investigation of the holographic dual of the $\mathfrak{sl}(2)$ quenched CFTs). This emergence of Floquet horizons thus raises the question of how it impacts the scrambling properties of CFTs at large central charge, fast scrambling properties of quantum systems are believed to be inherent to black hole horizons.

In order to diagnose such possibly inhomogeneous scrambling properties of driven CFTs, we compute the OTOC at stroboscopic time after the drive, based on a Floquet Hamiltonian approach². Our arguments rely on the knowledge of the form of the Floquet Hamiltonian (7.62) for $\mathfrak{sl}(2)$ Floquet drives, which is independent of the details of the drive, e.g., the numbers of driving steps in one cycle, and applies to both discrete step drives as well as continuous drives. We consider a quantum quench with H_F , starting from the $\mathfrak{sl}(2)$ vacuum $|0\rangle$. In practice, we need to compute the time evolution of the four point function

$$\frac{1}{\mathcal{N}} \langle 0 | e^{iH_F t} W(z_1, \bar{z}_1) e^{-iH_F t} e^{iH_F t} W(z_2, \bar{z}_2) e^{-iH_F t} V(z_3, \bar{z}_3) V(z_4, \bar{z}_4) | 0 \rangle, \quad (11.12)$$

where, as in Sec. 11.2, V and W are primary fields of weights (h_v, \bar{h}_v) , (h_w, \bar{h}_w) , and \mathcal{N} a normalization factor accounting for two-point factorization $\langle VV \rangle \langle WW \rangle$. The time evolution of primary fields with H_F in Heisenberg picture is given by the continuous time Möbius transformation (7.65). Thus, the four point function can be expressed as

$$\frac{1}{\mathcal{N}} \left(\frac{\partial \bar{z}_1}{\partial z} \frac{\partial \bar{z}_2}{\partial z} \right)^{h_w} \left(\frac{\partial \bar{z}_1}{\partial \bar{z}} \frac{\partial \bar{z}_2}{\partial \bar{z}} \right)^{\bar{h}_w} \langle 0 | W(\bar{z}_1, \tilde{z}_1) W(\bar{z}_2, \tilde{z}_2) V(z_3, \bar{z}_3) V(z_4, \bar{z}_4) | 0 \rangle. \quad (11.13)$$

We note that the derivative factors in front of the four-point function will not contribute to the time evolution of the OTOC, as they are cancelled by the normalization \mathcal{N} . Therefore, time evolution after a quantum quench with H_F amounts to an equilibrium four-point with time-dependent change of coordinates. We will thus follow the strategy outline in Sec. 11.2 to compute this four-point function with the correct OTO ordering. More specifically, OTO ordering is obtained by using the correct *ie* prescription, where we introduce the complexified time $t_i = it_i + \epsilon_i$. Such prescription is given by the ordering of limits $\epsilon_1 > \epsilon_3 > \epsilon_2 > \epsilon_4 \rightarrow 0$. The non-trivial behaviour of the OTOC is

² We consider a quantum quench with the Floquet Hamiltonian H_F in order to circumvent possible ambiguities with defining analytic continuation at discrete stroboscopic times.

then obtained as the cross-ratio crosses such branch cut, leading to the second sheet effect. We now choose to restrict our analysis to pure initial states, as considering the OTOC computation from a thermal initial at finite system size L is beyond the scope of this chapter. We note that the similar approach from [213] has an ambiguity due to the fact that the time is only evaluated at discrete stroboscopic values, such that it makes it difficult to judge whether or not the cross-ratio η or $\bar{\eta}$ has crossed the real axis in between two stroboscopic times $n(T_0 + T_1)$ and $(n+1)(T_0 + T_1)$, and the analytic continuation to a complexified of a discrete stroboscopic time is unclear. This motivates the use of the Floquet Hamiltonian H_F , such that time is continuous and the crossing of the real axis can explicitly be observed. The final result for the OTOC will then only be valid for stroboscopic times in order to agree with the OTOC evolution for a Floquet drive.

We can now explicitly compute the time evolution of the cross-ratios η and $\bar{\eta}$ after the quantum quench, with the correct $i\epsilon$ prescription of the OTOC. Let us without loss of generality suppose that the driving parameters are chosen such that $0 < \xi < 1$, i.e., that γ_1 is the stable fixed point, and γ_2 is unstable. The cross-ratio is

$$\eta = \frac{8z_1 z_2 \gamma_1 (z_1 + z_1^* - \gamma_1 - \gamma_1^*) (-z_2 - z_2^* + \gamma_1 + \gamma_1^*) \sin \pi \Theta_H \epsilon_{13} \sin \pi \Theta_H \epsilon_{24}}{[A \cosh \pi \Theta_H (t + i\epsilon_{13}) + B \sinh \pi \Theta_H (t + i\epsilon_{13})][\epsilon_{13} \rightarrow \epsilon_{24}]}, \quad (11.14)$$

with

$$A = -(z_1 - z_2)(\gamma_1^2 - 1), \quad B = ((z_1 + z_2)(1 + \gamma_1) - 2\gamma_1(1 + z_1 z_2)), \quad (11.15)$$

introducing the notation $\epsilon_{ij} = \epsilon_i - \epsilon_j$. Note that the anti-holomorphic cross-ratio $\bar{\eta}$ can similarly be computed. In order for the cross-ratio to be $\mathcal{O}(1)$, and cross the branch cut, we arrive to the condition

$$\tanh(\pi \Theta_H t) = \frac{(z_2 - z_1)(\gamma_1 - \gamma_2)}{(z_1 + z_2)(\gamma_1 + \gamma_2) - 2(z_1 z_2 + \gamma_1 \gamma_2)}. \quad (11.16)$$

Conversely the condition for $\bar{\eta}$ to cross the branch cut reads

$$\tanh(\pi \Theta_H t) = \frac{(\bar{z}_2 - \bar{z}_1)(\gamma_1^* - \gamma_2^*)}{(\bar{z}_1 + \bar{z}_2)(\gamma_1^* + \gamma_2^*) - 2(\bar{z}_1 \bar{z}_2 + \gamma_1^* \gamma_2^*)}. \quad (11.17)$$

Let us now assume that η crosses the branch cut but not $\bar{\eta}$, as illustrated on Fig. 11.1(a-b). The large time asymptotics in this case reads

$$\eta \sim e^{-2\pi \Theta_H t} 2\pi^2 \Theta_H^2 \epsilon_{12} \epsilon_{34} \frac{\sin \frac{\pi}{L} (x_1 - x_{*,2}) \sin \frac{\pi}{L} (x_2 - x_{*,1})}{\sin \frac{\pi}{L} (x_1 - x_{*,1}) \sin \frac{\pi}{L} (x_2 - x_{*,2})}. \quad (11.18)$$

Following the strategy from Sec. 11.2, we can now restrict to the Virasoro identity block, and consider the large central charge limit with the constraint that h_w/c is small and fixed, and h_v/c is large and fixed. This leads to the late-time expression for the OTOC

$$C(t) \sim \frac{i\pi}{2 \log(e^{-2\pi \Theta_H t} \epsilon_{12} \epsilon_{34} \pi^2 \Theta_H^2 v_*(x_1, x_2))}, \quad (11.19)$$

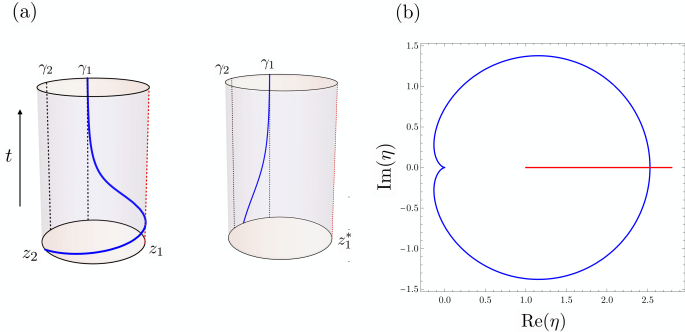


Figure 11.1: (a) Flow of the primary field $W(z_2, \bar{z}_2)$ under the continuous time evolution with H_F generated by the maps (7.65). Left: Flow of the chiral part, that crosses the chiral part of $V(z_1, \bar{z}_1)$ at a time given by (11.16). Right: Flow of the anti-chiral part, that does not cross V . (b) In this case, the cross-ratio η crosses the branch cut with the OTOC ordering at the time of the crossing between W and V .

with

$$v_*(x_1, x_2) = \frac{\sin \frac{\pi}{L}(x_1 - x_{*,2}) \sin \frac{\pi}{L}(x_2 - x_{*,1})}{\sin \frac{\pi}{L}(x_1 - x_{*,1}) \sin \frac{\pi}{L}(x_2 - x_{*,2})}. \quad (11.20)$$

We conclude that the OTOC displays an exponential decay given by the Lyapunov exponent

$$\lambda_L = \frac{2\pi}{\Theta_H}, \quad (11.21)$$

where Θ_H is the Hawking temperature associated to the emergent Floquet horizon. In other words, we have found an out-of-equilibrium analog to the thermal bound on quantum chaos, $\lambda_L = 2\pi\beta^{-1}$ [210]. Although our system is initialized in a pure state at $t = 0$, but the emergent Floquet horizons of the heating phase provide an emergent local temperature Θ_H characterizing scrambling of quantum information. Thus, a quantum quench with the Floquet Hamiltonian H_F is equivalent to a thermal chaotic CFT, up to the identification $\beta^{-1} = \Theta_H$.

From (11.18) it is clear that the Lyapunov exponent is $\lambda_L = 2\pi\Theta_H$. The inhomogeneous butterfly velocity $v_B(x)$ reads [213]

$$\begin{aligned} v_B(x) &\equiv \lambda_L v_*(x_2, x_1) \left(\frac{\partial v_*(x_1, x_2)}{\partial x_2} \right)^{-1} \\ &= 2L\Theta_H \frac{\sin \frac{\pi}{L}(x - x_{*,1}) \sin \frac{\pi}{L}(x - x_{*,2})}{\sin \frac{\pi}{L}(x_{*,1} - x_{*,2})}. \end{aligned} \quad (11.22)$$

Thus, the butterfly velocity associated to the crossing of the holomorphic cross-ratio equals the holomorphic part of the effective velocity for the Floquet drive (7.62),

$$v_B(x) = v_{\text{eff}}^+(x). \quad (11.23)$$

For completeness, let us now assume that $\bar{\eta}$ crosses the branch cut, such that the long time asymptotics read (upon replacement $x_{*,1} \mapsto L - x_{*,2}$, $x_{*,2} \mapsto L - x_{*,1}$)

$$\bar{\eta} = \sim e^{-2\pi\Theta_H t} 2\pi^2 \Theta_H^2 \epsilon_{12} \epsilon_{34} \frac{\sin \frac{\pi}{L} (x_1 + x_{*,1}) \sin \frac{\pi}{L} (x_2 + x_{*,2})}{\sin \frac{\pi}{L} (x_1 + x_{*,2}) \sin \frac{\pi}{L} (x_2 + x_{*,1})}. \quad (11.24)$$

Thus it becomes clear that in this case (7.62),

$$v_B(x) = v_{\text{eff}}^-(x). \quad (11.25)$$

We thus conclude that the Butterfly velocity is equal to the chiral or antichiral Floquet velocity, depending on whether η or $\bar{\eta}$ crosses the branch cut after the quantum quench with H_F . In other words, the inhomogeneous scrambling of quantum information is carried by the chiral or the antichiral part of the Floquet Hamiltonian depending on the initial positions of the fields V and W .

The generalization of the $\mathfrak{sl}(2)$ Floquet drive to any smooth velocity profiles $v(x) > 0$ was discussed in Chapter 9. In this case, the deformed Hamiltonians do not only involve the global conformal algebra spanned by $\{L_0, L_1, L_{-1}\}$, but the full Virasoro algebra. While the Virasoro algebra is infinite dimensional, a similar strategy still holds to solve the Floquet dynamics: one can write down a one-cycle diffeomorphism f_{\pm} (\pm stands for the chiral and anti-chiral components respectively) whose n -th iteration encodes the stroboscopic evolution of any (quasi-)primary field. For simplicity let us consider a two-step drive between a homogenous Hamiltonian H_0 and an arbitrary deformed Hamiltonian H_1 with velocity $v_1(x)$. Such one-cycle transformation takes the form

$$f_{\pm} = f_1^{-1}(f_1(x \mp T_0) \mp v_1 T_1), \quad (11.26)$$

where the diffeomorphism associated to the velocity profile $v_1(x)$ of H_1 reads

$$f_1(x) = \int_0^x dx' \frac{v_1}{v_1(x')}, \quad \frac{1}{v_1} = \frac{1}{L} \int_0^L \frac{dx}{v_1(x)}. \quad (11.27)$$

The heating phase is diagnosed by fixed points of f_{\pm} , or higher periodic points, i.e., fixed points of the m -th iteration of f_{\pm} for any m , denoted by f_{\pm}^m . The number of such fixed points can be arbitrary, leading to many emergent Floquet horizons at positions $x_{*,m}^{\mp}$, each characterized by a local Hawking temperature, or heating rate, $\frac{1}{m(T_0+T_1)} \log f_{\pm}^m(x_{*,m}^{\mp})$. While it is tempting to generalize the reasoning detailed in this section to this general class of drives, we stress that our approach based on the Floquet Hamiltonian hardly applies in this case. The reason is that deriving a Floquet Hamiltonian in the general case is a complicated task as the Virasoro algebra is infinite dimensional. On the other hand, dealing with iterations of the diffeomorphisms f_{\pm} does not allow for an analytic continuation to a complexified time, as time n only appears through n -th composition of f_{\pm} , i.e., there is no closed form for the n -th iteration of a general diffeomorphism of the circle. Nonetheless it is clear that the fixed point picture for OTOC evolution will also hold in such a general case, and is illustrated in Fig. 11.2. If the operator V is inserted at time $t = 0$ close to a Floquet horizon at position $x_{*,i}^{+}$, the Floquet velocity will scale as

$$v_{\text{eff}}(x) \sim \frac{|\log(f'_-(x_{*,i}^{+}))|}{T} (x - x_{*,i}^{+}), \quad (11.28)$$

where T is the period of the drive, and f'_- is the one-cycle diffeomorphism. We thus conclude that the Butterfly velocity will vanish close to the emergent fixed points. From the above considerations it is clear that the decay of the OTOC will be governed by the local Hawking temperature of the horizon $x_{*,i}^+$, given

$$\text{by } \Theta_{H,i} = \frac{|\log(f'_{-}(x_{*,i}^+))|}{T}.$$

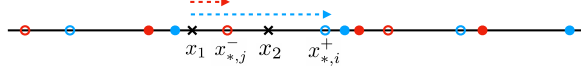


Figure 11.2: General geometric picture for the operator evolution under a Floquet drive made of arbitrary steps and arbitrary velocity profiles $v_i(x) > 0$. The stable (unstable) fixed points of the chiral sector are shown as blue filled (hollow) circles, while they are illustrated in red for the anti-chiral sector. The blue (red) dashed arrow illustrates the flow generated by the n -th composition of 1-cycle diffeomorphism f_- (f_+). Note that the alternating structure between stable and unstable fixed points within a given sector is a general property of 1-cycle diffeomorphisms [25]. Here, a non-trivial winding of η is shown as x_1 goes through to x_2 when flowing to the stable fixed point $x_{*,i}^+$. On the other hand, $\bar{\eta}$ will not cross the branch cut as the anti-chiral sector flows to the stable fixed point $x_{*,j}^-$ in between x_1 and x_2 . The obtained OTOC will be governed by the local Hawking temperature associated to the fixed point $x_{*,i}^+$.

11.4 CHAOS TO NON-CHAOS TRANSITIONS

In this section, we consider another class of Floquet drives on the infinite line, i.e., $L \rightarrow \infty$. One advantage of considering such type of setup is that it readily generalizes to finite temperatures. Concretely, we consider a 2-step drive between the two Hamiltonians H_0 and

$$H_R = \int_{-\infty}^{\infty} h x T_{00}(x) dx. \quad (11.29)$$

The Rindler Hamiltonian H_R has a horizon at $x = 0$, where the local velocity of gapless quasiparticles goes linearly to zero. In order to obtain the time evolution with this new Hamiltonian, we employ an $SL(2)$ symmetry in the generators of Lorentz transformations. In the limit of high-frequency, the Floquet drive can be seen as a single quantum quench with a new Hamiltonian H_F that has one horizon at position

$$x_* = \frac{T_0}{2} \left(1 - \frac{1}{\tanh \frac{T_1}{2}} \right). \quad (11.30)$$

The conformal map that encodes the time evolution of the coordinates of (quasi-)primary fields is given by

$$\tilde{z}(t) = x_0 e^{-h\lambda t} - \frac{2(1-\lambda)}{h\lambda} e^{-h\lambda t/2} \sinh \frac{h\lambda t}{2}, \quad (11.31)$$

$$\tilde{\bar{z}}(t) = x_0 e^{h\lambda t} + \frac{2(1-\lambda)}{h\lambda} e^{h\lambda t/2} \sinh \frac{h\lambda t}{2}, \quad (11.32)$$

where x_0 is the position of the primary field at time $t = 0$, and $\lambda = T_1/(T_0+T_1)$. It is straightforward to understand the flow as $t \rightarrow \infty$ of $\tilde{z}(t)$ and $\tilde{\bar{z}}(t)$:

$$\lim_{t \rightarrow \infty} \tilde{z}(t) = x_*, \quad \lim_{t \rightarrow \infty} \tilde{\bar{z}}(t) = \infty \quad \text{if } x_0 > x_*, \quad \lim_{t \rightarrow \infty} \tilde{\bar{z}}(t) = -\infty \quad \text{if } x_0 < x_*, \quad (11.33)$$

i.e., x_* is a stable fixed point for the holomorphic part, and an unstable fixed point for the anti-holomorphic part. With this in mind, we now consider that the maps (11.31), (11.32) encode the continuous time evolution with the Floquet Hamiltonian H_F in the high-frequency limit, and consider a quantum quench with H_F . Doing so, the analytic continuation for the cross-ratio is the same as described in Sec. 11.3: we simply need to replace $t \rightarrow t + i\epsilon_i$, where ϵ_i will satisfy the correct OTO ordering in order to have the correct analytic continuation. Then, we compute the cross ratio η for the holomorphic part and $\bar{\eta}$ for the anti-holomorphic part. We conclude that non-trivial OTOC time evolution only happens if x_1 and x_2 , the initial positions of the two fields at time $t = 0$, are on the same side of the Floquet horizon x_* . This directly implies that by changing continuously T_1 , or equivalently the parameter λ , one changes tunes continuously the position of the horizon on the real line, such that for fixed positions of the operators V and W at $t = 0$, one can have transition from chaotic behaviours in the OTOC to non-chaotic behaviours, as illustrated on Fig. 11.3.

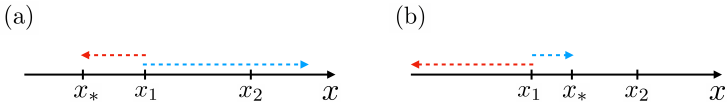


Figure 11.3: We consider the two operators W and V to be inserted at time $t = 0$ at positions x_1 and x_2 respectively. In order for the OTOC to have a non-trivial evolution, the operator W needs to pass through the position x_2 during the continuous time evolution with H_F . By changing continuously the driving parameters we can tune between a situation where the cross ratio crosses the branch cut (a), or a situation where the cross ratio cannot cross the branch cut as the emergent horizon x_* is between x_1 and x_2 (b).

Let us now proceed with the computation of the late-time value of the cross-ratio, which determines the time-evolution of the OTOC after the Floquet drive. Essentially, in the large t limit, the cross ratio takes the form

$$\eta \sim \frac{\epsilon_{12}\epsilon_{34}}{\epsilon_{13}\epsilon_{24}} e^{-ht\lambda} \frac{1 + \lambda(hx_2 - 1)}{1 + \lambda(hx_1 - 1)} \quad (11.34)$$

From this value of the cross-ratio at late times we deduce that the OTOC will decay exponentially with a heating rate given by $h\lambda$. However, we again identify a butterfly velocity, by defining

$$v_*(x_1, x_2) = \frac{1 + \lambda(hx_2 - 1)}{1 + \lambda(hx_1 - 1)} \quad (11.35)$$

We deduce that the Butterfly velocity is precisely given by

$$v_B(x) = h\lambda x + (1 - \lambda) \quad (11.36)$$

Note that again this expression for the inhomogeneous Butterfly velocity coincides with the Floquet velocity of the 2-step driven problem in the high frequency limit: In this case, the Floquet Hamiltonian is the convex combination of H_0 and H_R , with the interpolation parameter λ such that $\lambda = 0$ corresponds to H_0 and $\lambda = 1$ corresponds to the Rindler case,

$$H_F = \lambda H_R + (1 - \lambda) H_0 \quad (11.37)$$

Geometrically, this simply moves the horizon from $-\infty$ at $\lambda = 0$ to 0 at $\lambda = 1$. The stroboscopic horizon of the Floquet drive is thus located at $x_* = h^{-1}(1 - \frac{1}{\lambda})$ for $\lambda \in [0, 1]$. Note that in the case $\lambda = 1$, i.e., $T_0 = 0$, our result for the cross-ratio coincides with the results for a quantum quench with the Rindler Hamiltonian H_R . In this case, the OTOC displays an exponential decay with a rate given h , as expected. In the case $\lambda = 0$ we however do not find any exponential behaviour of the OTOC, which is expected as the initial state for the OTOC computation is the conformal vacuum, such that time evolution is simply trivial in this case, such that no chaotic feature in the OTOC is expected when starting from the ground state.

11.5 OTOC MEASUREMENTS AND BACKWARD TIME EVOLUTION

In order to measure the inhomogeneous scrambling of the OTOC for driven critical spin chains, we propose a concrete protocol involving an effective backward time evolution, illustrated on Fig. 11.4. Our protocol is based on

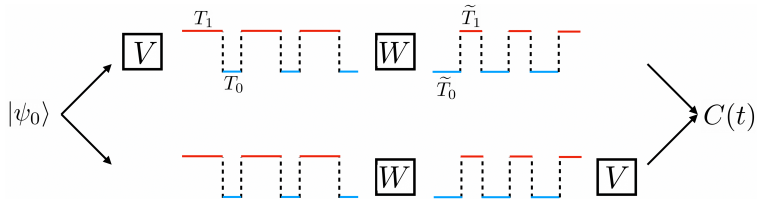


Figure 11.4: Proposed setup to measure an OTOC in a periodically driven critical inhomogeneous system. We consider two copies of the system to be prepared in an initial state $|\psi_0\rangle$ at time $t = 0$. This initial state is then evolved as $\tilde{U}_F^n W U_F^n V |\psi_0\rangle$ and $V \tilde{U}_F^n W U_F^n |\psi_0\rangle$, such that the overlap between both protocols leads to the OTOC $C(t) = \langle \tilde{U}_F^n W U_F^n V \tilde{U}_F^n W U_F^n V \rangle$.

engineering a stroboscopic backward Floquet time evolution simply by switching the sign of the *unphysical* Floquet Hamiltonian (7.61). A natural way to achieve this for $\mathfrak{sl}(2)$ drives is to switch the driving parameters (T_0, T_1) to $(\tilde{T}_0, \tilde{T}_1)$ after driving the system for N cycles, and switch the order of the unitaries U_0 and U_1 , as illustrated on Fig. 11.4. The parameters $(\tilde{T}_0, \tilde{T}_1)$ are defined such that only the stable and unstable fixed points swap, $x_{*,1} \leftrightarrow x_{*,2}$, leading to

$$\tilde{U}_F = e^{-i\tilde{H}_F(\tilde{T}_0 + \tilde{T}_1)} = e^{iH_F(T_0 + T_1)} = U_F^\dagger, \quad (11.38)$$

i.e., the new driving parameters effectively reverse time evolution at stroboscopic times³. We stress that this time-reversing protocol applies to *any* two-step drives with $v_i(x) > 0$ for $i = 0, 1$, as we will show below. In the heating phase this leads to an effective “evaporation” of the emergent Floquet horizons (see [212] for a SSD quantum quench analogue), with the entanglement entropy linearly decreasing back to the initial state entanglement. We note that this procedure works for both pure and thermal initial states.

We now prove the existence of driving parameters $(\tilde{T}_0, \tilde{T}_1)$ that satisfy (11.38) for a two step drive between two inhomogeneous CFTs. We first consider the case of $\mathfrak{sl}(2)$ drives, and consider a two step drive between two Hamiltonians H_0 and H_1 of the form (7.5) for durations T_0 and T_1 , with the constraint that $v_0(x)$ and $v_1(x)$ are both strictly positive. In this case choose our driving parameters $(\tilde{T}_0/L, \tilde{T}_1/L)$ in such a way that

$$\tilde{\gamma}_1 = \gamma_2, \quad \tilde{\gamma}_2 = \gamma_1, \quad \text{stable fixed point} \leftrightarrow \text{unstable fixed point.} \quad (11.39)$$

To prove that this implies (11.38), we simply need to show that the Floquet Hamiltonian of the new driving sequence flips sign $\tilde{H}_F = -H_F$ as we exchange $\gamma_1 \leftrightarrow \gamma_2$. The change of driving parameters (11.39) corresponds to interchanging the “sources” and “sinks” of energy and entanglement. From a quasiparticle standpoint, the quasiparticles which were accumulating at the unstable fixed points $x_{*,2} = \frac{L}{2\pi i} \log \gamma_2$, $L - x_{*,2} = \frac{L}{2\pi i} \log \gamma_2^*$ are suddenly repelled as these become stable fixed points, and are attracted by the new unstable fixed points $x_{*,1} = \frac{L}{2\pi i} \log \gamma_1$, $L - x_{*,1} = \frac{L}{2\pi i} \log \gamma_1^*$. While ultimately new horizons will form at these two new positions, there is an intermediate time-scale at which all quasiparticles emitted at time $t = 0$ at all spatial positions go back to their initial position, reinitializing the system. From a geometric point of view the unit cell of the phase diagram is $(T_0/L, T_1/L) \in [0, 1/\mathcal{C}_0] \times [0, 1/\mathcal{C}_1]$, with \mathcal{C}_i being the absolute value of the Casimir invariant. Solving the equation (11.39) is equivalent to choosing the new driving parameters $(\tilde{T}_0/L, \tilde{T}_1/L)$ to be

$$\tilde{T}_0/L = 1/\mathcal{C}_0 - T_0/L, \quad \tilde{T}_1/L = 1/\mathcal{C}_1 - T_1/L. \quad (11.40)$$

This is easily understood by looking at γ_2 and $\tilde{\gamma}_1$, see Fig. 11.5. For such choice of driving parameters, the condition (11.38) is fulfilled as this provides a representation of the inverse Floquet unitary U_F^\dagger .

We now design a stroboscopic time-reversal operation for the two-step drive protocol between two general inhomogeneous Hamiltonian with smooth positive deformations, as studied in Chap. 9. Following the strategy outlined in the $\mathfrak{sl}(2)$ case, we take \tilde{T}_0/L and \tilde{T}_1/L to be (assuming that $(T_0/L, T_1/L) \in [0, v_0^{-1}] \times [0, v_1^{-1}]$)

$$\tilde{T}_0/L = v_0^{-1} - T_0/L, \quad \tilde{T}_1/L = v_1^{-1} - T_1/L, \quad (11.41)$$

such that $(\tilde{T}_0/L, \tilde{T}_1/L) \in [0, v_0^{-1}] \times [0, v_1^{-1}]$. Let us denote the map associated to the new one-cycle diffeomorphism $\tilde{f}_\pm(x)$, defined as [25]

$$\tilde{f}_\pm(x) = f_0^{-1}(f_0(f_1^{-1}(f_1(x) \mp v_1 \tilde{T}_1)) \mp v_0 \tilde{T}_0). \quad (11.42)$$

³ Similar backward evolution protocols were discussed in the context of electromagnetic fields in periodically driven cavities [169].

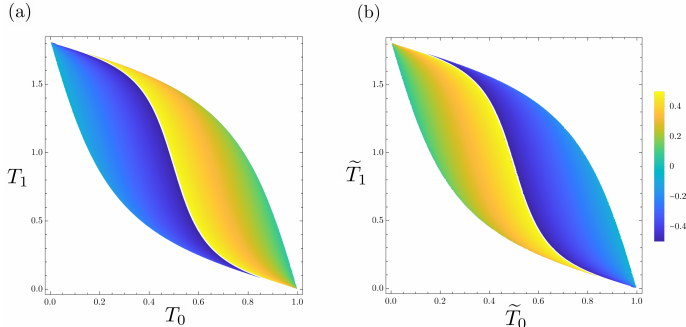


Figure 11.5: (a) Unstable fixed point $x_{*,2}$ as function of the driving parameters (T_0, T_1) for the first sequence of the drive. Only the heating phase is shown, in which case $|\gamma_{1,2}| = 1$. (b) Stable fixed point $x_{*,1}$ as function of the new driving parameters $(\tilde{T}_0, \tilde{T}_1)$ for the second sequence of the drive. We show a single unit cell of the phase diagram, and take a drive between $v_0(x) = 1$ and $v_1(x) = 1 - \frac{1}{2} \tanh(0.8) \cos(2\pi x/L)$, $L = 1$, such that $\frac{L}{2\pi i} \gamma_{1,2} \in [-0.5, 0.5]$ with periodic boundaries. In both subfigures we normalized L to one.

Plugging (11.41) into (11.42) and using properties of the circle diffeomorphism $f_{\pm}(x)$, we can readily show that

$$\tilde{f}_{\pm} = f_{\pm}^{-1}(x), \quad (11.43)$$

which directly implies (11.38), as the one-cycle diffeomorphism encodes the stroboscopic time evolution of any primary field. In other words, the double quench protocol with driving parameters $(T_0/L, T_1/L)$ followed by $(\tilde{T}_0/L, \tilde{T}_1/L)$ leads to a perfect time-reversal of primary fields, just like in the $\mathfrak{sl}(2)$ case. This result shows that the time-reversal procedure (11.41) is not simply limited to a finite-dimensional class of spatial deformations, but apply to any smooth deformation of the stress tensor $T_{00}(x)$. In order to gain a geometric understanding of this time-reversal procedure we will make use of the properties of the fixed (or in general, periodic) points associated to the 1-cycle diffeomorphism f_{\pm} in the heating phase. The periodic points of f_{\pm} , $\{x_{*,p}^{\mp}\}$ of period p , come in pairs of stable and unstable periodic points [25]. The new map \tilde{f}_{\pm} effectively interexchanges each stable and unstable fixed point within each pair, as can be seen from Fig. 11.6, for a choice of velocity profile $v_1(x)$ that involves the full Virasoro algebra and not only the $\mathfrak{sl}(2)$ subalgebra. Thus, from a quasiparticle perspective, the source, pumping entangled quasiparticles pairs at each driving cycle, and the sink at which they flow are exchanged, and thus each horizon evaporates until the system relaxes back to its initial state.

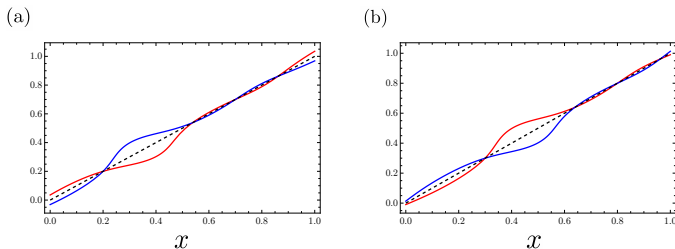


Figure 11.6: Left: One cycle diffeomorphism $f_+(x)$ (blue) and its time-reversal partner $\tilde{f}_+(x)$ (red). The choice of velocity profiles is $v_0(x) = 1$ and $v_1(x) = 6/(3 + \sin 4\pi x + \cos 2\pi x)$, and $T_0/L = 0.1$, $T_1/L = 0.45$. We observe four fixed points, two of which are stable and two are unstable. The stability (the sign of $f'_+(x_*) - 1$ for a fixed point x_*) is reversed between the first driving sequence and the second, as a direct consequence of (11.43). Right: Same, but for the anti-chiral part, $f_-(x)$ (blue) and $\tilde{f}_-(x)$ (red).

BERRY PHASES FROM ADIABATIC DRIVES

In this concluding chapter on the non-equilibrium dynamics of inhomogeneous critical systems, we discuss potential applications of our formalism to extract a new class of Berry phases unique to systems with an underlying conformal symmetry. While the results presented in this chapter need further investigation, they form a solid basis for a careful study of the emergence of Berry phases in adiabatically driven inhomogeneous systems, that could be verified in adiabatically deformed critical spin chains.

We first introduce Berry phases on Virasoro orbits in Sec 12.1, based on the results of [214], and then discuss in Sec. 12.2 a dynamical protocol to extract them, that is applicable to any critical lattice described in its low energy limit by a gapless field theory.

12.1 PRELUDE: BERRY PHASES OF VIRASORO ORBITS

In this section we review results from [214] on the Berry phases arising in two dimensional conformal field theories subject to adiabatic changes of coordinates, implemented by unitary transformations. On general grounds, with consider a quantum system with a symmetry provided by a Lie group G , and a unitary representation $U[f]$ on a Hilbert space \mathcal{H} , for any $f \in G$. We assume the existence of a particular element X_0 in the Lie algebra of G , such that $U[e^{tX_0}]$ can be interpreted as the unitary evolution operator of the system. As time translations belong to the symmetry group, the choice of Hamiltonian is not unique, and any element f of the symmetry group G can be associated to a change of reference frame, defining a new Hamiltonian $U[f]HU[f]^{-1}$. The symmetry group G thus defines a manifold on which a family of Hamiltonians live. As a direct consequence, a closed adiabatic sequence in such a space of Hamiltonian should result to Berry phases. In other words, we consider a closed path $f(t)$ on G , $f(t) : [0, T] \rightarrow G : t \mapsto f(t)$, and define a one-parameter family of Hamiltonians as $U[f(t)]HU[f(t)]^{-1}$. We consider as an initial state $U[f]|h\rangle$, with $|h\rangle$ being an eigenstate of H , with eigenvalue E . The final state $e^{i\theta(T)}U[f(T)]|h\rangle$ acquires a phase given by

$$\theta(T) = -ET + i \int_0^T dt \langle h | U[f(t)]^\dagger \partial_t U[f(t)] | h \rangle, \quad (12.1)$$

with a dynamical piece and a non-trivial geometric piece.

We now apply these ideas to the two dimensional CFTs, in which case the symmetry group G is given by the Virasoro group of the diffeomorphisms of the circle, with associated algebra $\{L_n\}_{n \in \mathbb{Z}}$. The Hilbert space is constructed by considering finitely many towers of primary states $|h\rangle$, with energy eigenvalues $L_0|h\rangle = h|h\rangle$, that are annihilated by the generators L_n , $n \leq 0$ [see Sec. 3.2]. The descendant states in each such tower are given by

$$L_{-m_1} \dots L_{-m_N} |h\rangle, \quad 1 \leq m_1 \leq \dots \leq m_N. \quad (12.2)$$

The stabilizer of $|h\rangle$ is a $U(1)$ subgroup of the Virasoro group $\text{Diff}(S^1)$ generated by L_0 . We will thus consider adiabatic closed cycles in the coadjoint orbits of

the Virasoro group $\text{Diff}(S^1)/S^1$. More concretely, let us take a path in such coadjoint orbits parametrized by $f(t, \phi)$, that associates to each $t \in [0, T]$ a circle diffeomorphism $\phi \mapsto f(t, \phi) \in \text{Diff}(S^1)$. The Berry phase for a closed path parametrized by such a one-parameter family of diffeomorphisms is [214]

$$\begin{aligned} \theta_B = & -\frac{1}{2\pi} \int_0^T dt \int_0^{2\pi} d\phi \frac{\dot{f}}{f'} \left[h - \frac{c}{24} + \frac{c}{24} \left(\frac{f''}{f'} \right)' \right] \\ & + \left(h - \frac{c}{24} \right) f^{-1}(0, f(0, T)). \end{aligned} \quad (12.3)$$

This is the holonomy of the Berry connection on the infinite dimensional manifold $\text{Diff}(S^1)/S^1$.

In particular, considering paths restricted to the subalgebra $\{L_0, L_n, L_{-n}\}$, generally parametrized by

$$e^{inf(\phi)} = \frac{\alpha e^{in\phi} + \beta}{\beta^* e^{in\phi} + \alpha^*}. \quad (12.4)$$

For circular paths given by $\alpha = \cosh \lambda/2$, $\beta = \sinh \lambda/2$, the Berry phase can be shown to simplify to

$$\theta_B = -2\pi \left(h + \frac{c}{24} (n^2 - 1) \right) (\cosh \lambda - 1). \quad (12.5)$$

We note that this results extends to the combination of both chiral and anti-chiral sectors, both giving independent contributions to the Berry phase in the adiabatic limit.

12.2 ADIABATIC DEFORMATIONS OF CRITICAL SYSTEMS

The aim of this section is to show that the Berry phases discussed in the previous section can emerge in the thermodynamic limit by driving adiabatically a CFT with a time dependent Hamiltonian $H(t)$. We will first consider orbits of the $\mathfrak{sl}(2)$ subalgebra of the Virasoro algebra, such that the time dependent Hamiltonian is a combination of $\{L_0, L_1, L_{-1}\}$. A natural choice for such a continuous path on the orbit of the uniform Hamiltonian $H_0 = \frac{2\pi}{L} (L_0 + \bar{L}_0)$ is the following Hamiltonian

$$H(t) = \frac{2\pi}{L} \left[\alpha L_0 + \sqrt{\alpha^2 - 1} \left(\cos \left(\frac{2\pi t}{T} \right) L_+ + \sin \left(\frac{2\pi t}{T} \right) L_- \right) \right], \quad (12.6)$$

with L_+ and L_- defined as sum and difference of L_1 and L_{-1} . For $\alpha > 1$, it is straightforward to show that at each time the instantaneous Hamiltonian lies on the orbit of H_0 , and the total trajectory encircles a finite area, as seen on Fig. 12.1. The associated spacetime deformation of the stress tensor reads

$$v(x, t) = \alpha + \sqrt{\alpha^2 - 1} [\cos(2\pi t/T) \cos(2\pi x/L) + \sin(2\pi t/T) \sin(2\pi x/L)], \quad (12.7)$$

such that it is essentially is a periodic spatial deformation travelling through the whole system of size L . In particular, the initial Hamiltonian at time $t = 0$ takes the form

$$H(t=0) = \frac{2\pi}{L} \left[\alpha L_0 + \sqrt{\alpha^2 - 1} \frac{L_1 + L_{-1}}{2} \right] + \text{anti-holomorphic}. \quad (12.8)$$

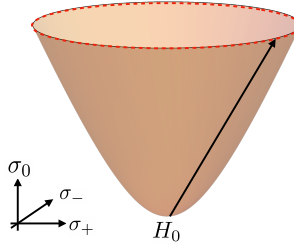


Figure 12.1: Trajectory along a path in the $SL(2, \mathbb{R})$ orbit of the uniform Hamiltonian H_0 , defined as the (connected component of the) set of $\mathfrak{sl}(2)$ -deformed Hamiltonians with quadratic Casimir $c^{(2)} = -\sigma_0^2 + \sigma_+^2 + \sigma_-^2 = -1$. The height of the orbit (dashed red curve) is provided by the value of α in (12.6).

In order to compute the Berry phase associated to this dynamical evolution with a deformed and time-dependent Hamiltonian, we first need to define the initial state at time $t = 0$. Following the strategy outlined in [214], one should start with a primary state $|h\rangle$ of H_0 and boost it so that it becomes an eigenstate of the Hamiltonian $H(t=0)$. In other words, we need to find a unitary transformation such that

$$UL_0U^\dagger = \alpha L_0 + \sqrt{\alpha^2 - 1} \frac{L_1 + L_{-1}}{2}, \quad (12.9)$$

and similarly for the anti-holomorphic part. The unitary operator U can be constructed by using basic properties of the $\mathfrak{su}(1, 1)$ algebra, such that it reads

$$U = e^{i \cosh^{-1}(\alpha) \frac{L_1 - L_{-1}}{2i}}. \quad (12.10)$$

It is straightforward to show that the associated transformation is

$$\tilde{z} = \frac{\sqrt{\frac{\alpha+1}{2}}z + \sqrt{\frac{\alpha-1}{2}}}{\sqrt{\frac{\alpha-1}{2}}z + \sqrt{\frac{\alpha+1}{2}}}, \quad \bar{\tilde{z}} = \frac{\sqrt{\frac{\alpha+1}{2}}\bar{z} - \sqrt{\frac{\alpha-1}{2}}}{-\sqrt{\frac{\alpha-1}{2}}\bar{z} + \sqrt{\frac{\alpha+1}{2}}}. \quad (12.11)$$

The second step is to carry out the time evolution with $H(t)$. This is a continuous drive whose Floquet unitary evolution operator is given by

$$U_F = \mathcal{T} e^{-i \int_0^T dt' H(t')}. \quad (12.12)$$

The time evolution of primary fields with such a unitary operator is given by a Möbius transformation whose coefficients will be determined exactly in the following of the section. The goal is to finally compute the Loschmidt amplitude, i.e.,

$$\langle \Phi | U_F | \Phi \rangle = \langle h | U^\dagger U_F U | h \rangle. \quad (12.13)$$

In order to compute the Möbius transformation $z'(z)$ associated to U_F , we devide the interval $[0, T]$ into M subintervals of length $\frac{T}{M}$. The exact discretization of the Floquet unitary is

$$U_F = \lim_{M \rightarrow \infty} \prod_{j=0}^M e^{-iH(jT/M)T/M}. \quad (12.14)$$

At the step j , the Möbius map reads

$$f_j(z) = \frac{A_j z + B_j}{B_j^* z + A_j^*}, \quad (12.15)$$

with coefficients

$$A_j = \cos\left(\frac{\pi T}{ML}\right) + i\alpha \sin\left(\frac{\pi T}{ML}\right), \quad B_j = i\sqrt{\alpha^2 - 1} \sin\left(\frac{\pi T}{ML}\right) e^{2\pi ij/M}. \quad (12.16)$$

The total Möbius transformation is obtained by composing each transformation associated to each of the M steps, $[0, \frac{T}{M}, 2\frac{T}{M}, \dots, T]$, and then taking the continuous limit $M \rightarrow \infty$. In other words, we need to compute

$$\begin{pmatrix} A & B \\ B^* & A^* \end{pmatrix} = \lim_{M \rightarrow \infty} \prod_{j=0}^M \begin{pmatrix} A_j & B_j \\ B_j^* & A_j^* \end{pmatrix}. \quad (12.17)$$

We now use a standard trick from linear algebra: consider a general matrix of the form

$$A_j = \begin{pmatrix} a & be^{-i\phi j} \\ b^* e^{i\phi j} & a^* \end{pmatrix}, \quad (12.18)$$

for $a, b \in \mathbb{C}$ and $\phi \in \mathbb{R}$. Noting that

$$A_j = \begin{pmatrix} 0 & e^{-i(\phi/2)j} \\ e^{i(\phi/2)j} & 0 \end{pmatrix} \begin{pmatrix} a^* & b^* \\ b & a \end{pmatrix} \begin{pmatrix} 0 & e^{-i(\phi/2)j} \\ e^{i(\phi/2)j} & 0 \end{pmatrix} = S_j B S_j, \quad (12.19)$$

and defining $D = S_{j-1} S_j = \text{diag}(e^{i\phi/2}, e^{-i\phi/2})$, products of A_j 's can be written

$$A_0 A_1 \dots A_M = S_0 (BD)^M B S_M. \quad (12.20)$$

Thanks to this identity, we can write explicitly the product of the M matrices by using matrix diagonalization of general $\mathfrak{su}(1, 1)$ matrices. Then, we can safely take the limit $M \rightarrow \infty$ to obtain a meaningful limit for the Floquet operator (12.12). The final result, providing the one-cycle Möbius transformation that encodes time evolution for a single period T of the continuous drive, is given by the Möbius transformation

$$z'(z) = \frac{Az + B}{B^* z + A^*}, \quad (12.21)$$

where

$$A = -\cos\left(\pi\sqrt{1 + \left(\frac{T}{L}\right)^2 + 2\alpha\frac{T}{L}}\right) - i\left(1 + \alpha\frac{T}{L}\right) \frac{\sin\left(\pi\sqrt{1 + \left(\frac{T}{L}\right)^2 + 2\alpha\frac{T}{L}}\right)}{\sqrt{1 + \left(\frac{T}{L}\right)^2 + 2\alpha\frac{T}{L}}},$$

(12.22)

$$B = -i \frac{T}{L} \sqrt{\alpha^2 - 1} \frac{\sin \left(\pi \sqrt{1 + \left(\frac{T}{L} \right)^2 + 2\alpha \frac{T}{L}} \right)}{\sqrt{1 + \left(\frac{T}{L} \right)^2 + 2\alpha \frac{T}{L}}}. \quad (12.23)$$

There are a few features to appreciate in the obtained transformation (12.21): the trace squared of the associated matrix, which gives the stability of the Floquet problem, is bounded by 4 for the chiral part, i.e., there is no heating phase. This is expected, as heating phase would necessarily mean going far away from any adiabatic limit. More specifically, the trace squared is

$$\text{Tr}^2 \begin{pmatrix} A & B \\ B^* & A^* \end{pmatrix} = 4 \cos^2 \left(\pi \sqrt{1 + \left(\frac{T}{L} \right)^2 + 2\alpha \frac{T}{L}} \right). \quad (12.24)$$

As a last remark, we note that from (12.21), it is straightforward to derive the effective Hamiltonian encoding the time evolution for one cycle. Such Hamiltonian, here defined as $U_F = e^{-iH_F T}$, is given by $H_F = \frac{2\pi}{L}(\sigma_0 L_0 + \sigma_+ L_+ + \sigma_- L_-)$, with

$$\sigma_0 = \frac{L}{T} + \alpha, \quad \sigma_+ = \sqrt{\alpha^2 - 1}, \quad \sigma_- = 0. \quad (12.25)$$

Remarkably, in the adiabatic limit $\frac{T}{L} \rightarrow \infty$, one obtains that the effective Hamiltonian is the original Hamiltonian,

$$H_F = \frac{2\pi}{L} \left[\alpha L_0 + \sqrt{\alpha^2 - 1} \frac{L_1 + L_{-1}}{2} \right] = H(t=0). \quad (12.26)$$

We now compute the Loschmidt amplitude for the chiral part,

$$\langle h | \mathcal{U} | h \rangle = \langle h | e^{\tilde{\sigma}_0 L_0 + \tilde{\sigma}_+ (L_1 + L_{-1})} | h \rangle, \quad (12.27)$$

where

$$\tilde{\sigma}_0 = -2\pi i \left(\alpha + \frac{T}{L} (2\alpha^2 - 1) \right), \quad \tilde{\sigma}_+ = -2\pi i \sqrt{\alpha^2 - 1} \left(1 + 2\alpha \frac{T}{L} \right). \quad (12.28)$$

In order to make progress, we write the exponential of the sum of generators as a product of exponentials of generators [215],

$$e^{\tilde{\sigma}_0 L_0 + \tilde{\sigma}_+ (L_1 + L_{-1})} = e^{\theta_{-1} L_{-1}} e^{\theta_0 L_0} e^{\theta_1 L_1}, \quad (12.29)$$

with

$$\theta_0 = \log \left((\cosh \phi - \tilde{\sigma}_0 / (2\phi) \sinh \phi)^{-2} \right), \quad \theta_1 = \theta_{-1} = \frac{\tilde{\sigma}_+}{\phi} \frac{\sinh \phi}{\cosh \phi - \frac{\tilde{\sigma}_0}{2\phi} \sinh \phi}, \quad (12.30)$$

where $\phi = \frac{1}{2} \sqrt{\tilde{\sigma}_0^2 - 4\tilde{\sigma}_+^2}$. The rest of the computation amounts to evaluating

$$\langle h | e^{\theta_{-1} L_{-1}} e^{\theta_0 L_0} e^{\theta_1 L_1} | h \rangle = e^{\theta_0 h}, \quad (12.31)$$

by using the fact that $L_1 |h\rangle = 0$ for primary states. We thus conclude that

$$\langle \Phi | U_F | \Phi \rangle^{1/(2h)} = - \frac{i\Delta}{i\Delta \cos(\pi\sqrt{\Delta}) - \sqrt{\Delta}(-\alpha - \alpha^2 \frac{T}{L} + \frac{T}{L}(\alpha^2 - 1)^2) \sin(\pi\sqrt{\Delta})}, \quad (12.32)$$

with $\Delta = 1 + \left(\frac{T}{L}\right)^2 + 2\alpha \frac{T}{L}$. It directly follows that the Loschmidt echo goes to one as $\frac{T}{L} \rightarrow \infty$, providing a well-defined adiabatic limit, as clearly shown on Fig. 12.2(a). Furthermore, the phase of the Loschmidt amplitude in the adiabatic limit reads

$$\lim_{T/L \rightarrow \infty} \langle \Phi | U_F | \Phi \rangle = e^{i\theta} = e^{2\pi i h T / L} \times e^{2\pi i h(\alpha - 1)}. \quad (12.33)$$

While the first piece is the dynamical phase picked up by the time evolution, of the form e^{iET} , with the energy of the initial state $E = \frac{2\pi}{L}h$, the second phase is of geometric origin, and can be identified as the Berry phase associated to the closed path we performed in the coadjoint orbits of $\mathfrak{sl}(2)$ with $H(t)$. In the adiabatic limit it emerges as a periodicity-independent piece, as seen on Fig. 12.2(b).

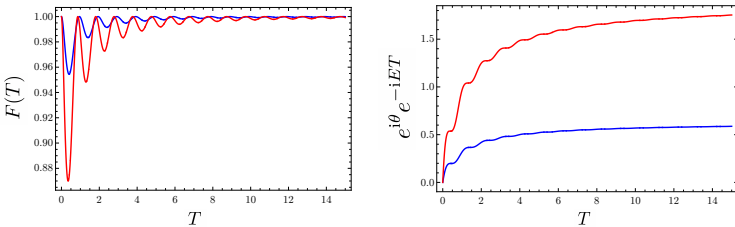


Figure 12.2: (a) Loschmidt echo $F(T)$ as a function of the driving period T , for a system size L normalized to one, for $\alpha = 1.1$ (blue) and $\alpha = 1.4$ (red), for the chiral sector only. The convergence to a unit probability, defining an adiabatic limit as $T \rightarrow \infty$, is manifest. (b) The geometric contribution to the phase as a function of the driving period T . In the adiabatic limit, the geometric part (i.e., removing the dynamical contribution to the phase e^{iET}) becomes constant and independent of the period T , thus depending only the parameter α .

Similarly, similar steps can be carried out for the anti-chiral sector, by noting that at the step j , the map reads

$$\bar{f}_j(\bar{z}) = \frac{\bar{A}_j \bar{z} + \bar{B}_j}{\bar{B}_j^* \bar{z} + \bar{A}_j^*}, \quad (12.34)$$

with coefficients

$$\begin{aligned}\bar{A}_j &= \cos\left(\frac{\pi T}{ML}\right) + i\alpha \sin\left(\frac{\pi T}{ML}\right), \\ \bar{B}_j &= i\sqrt{\alpha^2 - 1} \sin\left(\frac{\pi T}{ML}\right) e^{2\pi i \omega t_j} = i\sqrt{\alpha^2 - 1} \sin\left(\frac{\pi T}{ML}\right) e^{-2\pi i j/M}.\end{aligned}\quad (12.35)$$

Note that the chiral and the anti-chiral transformations are different, as they involve a non-trivial σ_- component. Repeating similar steps as for the chiral sector, one obtains the one-cycle transformation as

$$\bar{z}'(\bar{z}) = \frac{\bar{A}\bar{z} + \bar{B}}{\bar{B}^*\bar{z} + \bar{A}^*} \quad (12.36)$$

where

$$\bar{A} = -\cos\left(\pi\sqrt{1 + \left(\frac{T}{L}\right)^2 + 2\alpha\frac{T}{L}}\right) - i\left(1 + \alpha\frac{T}{L}\right) \frac{\sin\left(\pi\sqrt{1 + \left(\frac{T}{L}\right)^2 + 2\alpha\frac{T}{L}}\right)}{\sqrt{1 + \left(\frac{T}{L}\right)^2 + 2\alpha\frac{T}{L}}}, \quad (12.37)$$

$$\bar{B} = -i\frac{T}{L}\sqrt{\alpha^2 - 1} \frac{\sin\left(\pi\sqrt{1 + \left(\frac{T}{L}\right)^2 + 2\alpha\frac{T}{L}}\right)}{\sqrt{1 + \left(\frac{T}{L}\right)^2 + 2\alpha\frac{T}{L}}}. \quad (12.38)$$

It is important to note that the trace-squared associated to the anti-chiral Möbius transformation is

$$\text{Tr}^2 \begin{pmatrix} \bar{A} & \bar{B} \\ \bar{B}^* & \bar{A}^* \end{pmatrix} = 4 \cosh^2 \left(\pi\sqrt{-1 - \left(\frac{T}{L}\right)^2 + 2\frac{T}{L}\alpha} \right). \quad (12.39)$$

As opposed to (12.24), the trace squared (12.39) is larger than 4 for any $\frac{T}{L} \in [\alpha - \sqrt{\alpha^2 - 1}, \alpha + \sqrt{\alpha^2 + 1}]$. This implies that a heating phase is reached for the antichiral sector for a finite range of driving parameters, while the chiral sector never heats up. This breaking of the symmetry between both sectors is a direct consequence of the particular form of the driving Hamiltonian $H(t)$. In particular, the Loschmidt amplitude can be computed in the antichiral sector, leading to

$$\langle \Phi | U_F | \Phi \rangle^{1/(2\hbar)} = -\frac{\sqrt{\bar{\Delta}}}{\sqrt{\bar{\Delta}} \cosh(\pi\sqrt{\bar{\Delta}}) - i\left[-\alpha + \alpha^2\frac{T}{L} + \frac{T}{L}(\alpha^2 - 1)^2\right] \sinh(\pi\sqrt{\bar{\Delta}})}, \quad (12.40)$$

where $\bar{\Delta} = -1 - \left(\frac{T}{L}\right)^2 + 2\alpha\frac{T}{L}$. In this case, as opposed to the chiral Loschmidt amplitude, no adiabatic limit can be reached, even in the limit $\frac{T}{L} \rightarrow \infty$. We

conclude that the Berry phase would be observable starting from chiral initial states, with conformal weights $(h, 0)$, in order to reach the adiabatic limit, with a unit probability to reach the intial state after one period up to the phase (12.33). As a natural next step, it would be fascinating to observe this Berry phase in a critical lattice model. In particular, one would need to consider a time evolution with the time-dependent Hamiltonian

$$H(t) = -\frac{1}{2} \sum_{i=1}^L v(i, t)(c_{i+1}^\dagger c_i + \text{h.c.}). \quad (12.41)$$

Starting from a purely chiral state of the Hamiltonian at $t = 0$. Identifying such chiral state on the lattice can be achieved using the methods from [216–218]. In particular, our predictions apply to any CFT, and could thus be adapted to any critical lattice.

We now consider adiabatic deformations of the Hamiltonian involving the Virasoro generators L_0 , L_n , and L_{-n} with $n > 1$, which leads to Berry phases that directly involve the central charge of the underlying CFT, as discussed in the previous section. In fact, we can repeat all the steps of the calculation in the case of $n = 1$ by simply replacing $L \mapsto \frac{L}{n}$. The unitary transformation that maps L_0 to $H(t = 0)$ now reads

$$U = e^{i \frac{\cosh^{-1}(\alpha)}{n} \frac{L_n - L_{-n}}{2i}}, \quad (12.42)$$

for which the Möbius transformation is again given by (12.11). We again need to compute $\langle h|U|h\rangle$, where $U = U^\dagger U_F U$. More specifically, we write

$$U = e^{-2\pi i (\sigma_0 L_0 + \sigma_+ (L_n + L_{-n})/2) T/L}, \quad (12.43)$$

with $\sigma_0 = (L\alpha/(nT) + 1)$, and $\sigma_+ = -\sqrt{\alpha^2 - 1}$. Further, we can use the isomorphism between $\mathfrak{sl}(2)$ and its n -fold cover by introducing the transformations

$$M_0 = \frac{1}{n}(L_0 + \frac{c}{24}(n^2 - 1)), \quad M_n = \frac{1}{n}L_n, \quad M_{-n} = \frac{1}{n}L_{-n}. \quad (12.44)$$

It is straightforward to verify that the new set of generators follow the usual $\mathfrak{su}(1, 1)$ algebra. We need to evaluate

$$\begin{aligned} U^\dagger |0\rangle &= e^{2\pi i \frac{c}{24} \frac{T}{L} (n^2 - 1)\sigma_0} e^{-2\pi n i (\sigma_0 M_0 + \sigma_+ (M_n + M_{-n})/2) T/L} |0\rangle \\ &= e^{2\pi i \frac{c}{24} \frac{T}{L} (n^2 - 1)\sigma_0} e^{\tilde{\sigma}_0 M_0 + \tilde{\sigma}_+ (M_n + M_{-n})} |0\rangle. \end{aligned} \quad (12.45)$$

We again split the exponential of a sum of generators to a product of exponentials,

$$e^{\tilde{\sigma}_0 M_0 + \tilde{\sigma}_+ (M_n + M_{-n})} = e^{\theta_{-n} M_{-n}} e^{\theta_0 M_0} e^{\theta_n M_n}, \quad (12.46)$$

with θ_0 and $\theta_{-n} = \theta_n$ given by (12.30). Using the action of the Virasoro generators on primary states, we deduce that

$$\langle h|U|h\rangle = \frac{e^{2\pi i \frac{c}{24} \frac{T}{L} (n^2 - 1)\sigma_0} e^{\frac{1}{n}\theta_0 \frac{c}{24}(n^2 - 1)}}{(\cosh \phi - \tilde{\sigma}_0/(2\phi) \sinh \phi)^2}, \quad (12.47)$$

where we used that $e^{L_n}|h\rangle = |h\rangle$. This provides a direct generalization of the computation $n = 1$, which only differs by an extra piece in the Berry phase that explicitly makes appear the central charge c .

Part IV

MARGINAL DEFORMATIONS OF TOMONAGA-LUTTINGER LIQUIDS

In the last part of this thesis we study Tomonaga-Luttinger liquids thrown out of equilibrium by marginal deformations in the form of interaction modulations. This is modeled by quenching or periodically driving the Luttinger parameter or, equivalently, the compactification radius of the free boson conformal field theory between two different values. We obtain exact analytical results for the evolution of the Loschmidt echo and observables such as the particle and energy densities. Starting from generic initial states, the quench dynamics are shown to exhibit revivals and temporal orthogonalities. For the periodic drive, we show stability or instability of time-evolved physical quantities dependent on the drive parameters. We also compare the corresponding marginally deformed thermal density matrices by non-perturbatively evaluating their Rényi divergence as a Euclidean quench. All the dynamics are shown to be crucially dependent on the ratio of the Luttinger parameters, which corresponds to the Zamolodchikov distance in the space of marginal deformations.

The content of this part of the thesis is based on [27].

MARGINAL QUENCHES AND DRIVES IN
TOMONAGA-LUTTINGER LIQUIDS

13.1 INTRODUCTION

The last part of this thesis is devoted to the analytical study of non-equilibrium properties of Tomonaga-Luttinger liquids (TLLs), with time-dependent Luttinger parameter. In general, quenches of critical theories are categorized as massive or massless, depending on whether the initial state has correlations with exponential or power-law decay, respectively. Massive or short-range correlated states can be well-approximated by suitable conformal boundary states, consequently, massive quenches have been studied extensively using powerful techniques in boundary CFT [68, 69]. On the other hand, massless quenches pertain to initializing the system in a state that corresponds to one critical Hamiltonian and abruptly changing to another. Examples of works in this direction include interaction or marginal quenches in TLLs [73, 219–231], the sine-Gordon model [232], quantum spin chains [233–236], the one-dimensional Hubbard model [237], and the Lieb-Liniger model [238–243]. Despite much progress in the study of quench dynamics for CFTs, few exact results are known for quenches from arbitrary excited states. Furthermore, the role played by the geometry of the space of marginally deformed theories [244] in any non-equilibrium setting is yet to be identified.

In this chapter, we harness underlying symmetries to derive a number of exact analytical results for dynamical quantities for TLLs subjected to marginal quenches and drives. Among these are the evolution of particle and energy densities and the Loschmidt echo starting from arbitrary excited or thermal states. For the quench, we show that the results exhibit revivals and periodic orthogonality signaling dynamical quantum phase transitions [245]. For the periodic drive, we find stable and unstable dynamical phases and infer the critical exponents of natural order parameters at the phase boundary. A key feature common to all our results is a dependence through the ratio of the two Luttinger parameters. This ratio also corresponds to the well-known Zamolodchikov distance in the space of CFTs related by marginal deformations [244]. Besides studying dynamical properties, we also use and extend our formalism to evaluate the Rényi divergence [246] and relative entropy [247] between thermal states of two TLLs with different Luttinger parameters. The Rényi divergence is a one-parameter generalization of the relative entropy, which serves as an information-theoretic measure of the distance between two density matrices, and our result establishes a relation between this distance and the Zamolodchikov distance for marginally deformed TLLs.

This chapter is organized as follows. In Sec. 13.2, we discuss a number of applications of TLL theory to motivate the interpretation of our quench and drive protocols as interaction modulations. In Sec. 13.3, we provide the necessary technical background and tools used for computations in the subsequent sections, including justifications for interpreting changes in the Luttinger parameter or the compactification radius as marginal $J\bar{J}$ deformations. In Secs. 13.4 and 13.5, we present our main results for quantum quenches and Floquet drives,

respectively. In Sec. 13.6, we present the computation of the Rényi divergence and the relative entropy.

13.2 APPLICATIONS

To motivate the interpretation of our quench and drive protocols as effectively describing interaction modulations, we briefly discuss a number of applications of TLL theory and recall how the propagation velocity v and the Luttinger parameter K depend on model parameters. At the end of the section, we also briefly describe how our setup concretely translates to the dynamics of the bosonic string.

INTERACTING MASSLESS FERMIONS – THE LUTTINGER MODEL. The prototype for TLLs is the Luttinger model of interacting massless fermions in one spatial dimension [248–250]. The fermions are either right or left moving, described by fermionic fields $\psi_+(x)$ and $\psi_-(x)$, respectively, satisfying $\{\psi_r(x), \psi_{r'}(x')^\dagger\} = \delta_{r,r'}\delta(x-x')$ and $\{\psi_r(x), \psi_{r'}(x')\} = 0$ ($r, r' = \pm$) and suitable boundary conditions. The Hamiltonian can be written

$$\begin{aligned} H = & \sum_{r=\pm} \int_{-L/2}^{L/2} dx : \psi_r(x)^\dagger (-iv_F \partial_x) \psi_r(x) : \\ & + \sum_{r,r'=\pm} \int_{-L/2}^{L/2} dx \frac{\pi v_F}{2} (\delta_{r,-r'} g_2 + \delta_{r,r'} g_4) \\ & \times : \psi_r(x)^\dagger \psi_r(x) : : \psi_{r'}(x)^\dagger \psi_{r'}(x) :, \end{aligned} \quad (13.1)$$

where $v_F > 0$ denotes the Fermi velocity and $g_{2,4}$ are coupling constants satisfying $|g_2| < 2 + g_4$. The notation for the couplings is from ‘g-ology’ in condensed matter physics, see, e.g., [251], with g_2 and g_4 corresponding to different four-fermion interaction terms. The Luttinger model is well known to be exactly solvable by bosonization, using which H is mapped precisely to the TLL Hamiltonian in (13.10) with

$$v = v_F \sqrt{(1 + g_4/2)^2 - (g_2/2)^2}, \quad K = \sqrt{\frac{1 + g_4/2 - g_2/2}{1 + g_4/2 + g_2/2}}, \quad (13.2)$$

see, e.g., [251–253] and references therein. Modulating $g_{2,4}$ in time thus corresponds to our interaction quenches or drives changing K and v .

QUANTUM XXZ SPIN CHAIN IN THE GAPLESS REGIME. An example of a one-dimensional lattice model that falls into the TLL class is the spin-1/2 quantum XXZ Heisenberg chain for certain values of the anisotropy. This is a famous Bethe-ansatz integrable model of nearest-neighbor coupled spins described by spin operators S_j^x , S_j^y , and S_j^z that act on lattice site j and satisfy $[S_j^\alpha, S_{j'}^\beta] = i\delta_{j,j'}\epsilon_{\alpha\beta\gamma}S_j^\gamma$ ($\alpha, \beta, \gamma \in \{x, y, z\}$), where $\epsilon_{\alpha\beta\gamma}$ is the totally anti-symmetric tensor ($\epsilon_{xyz} = 1$), and periodic boundary conditions. The XXZ Hamiltonian is

$$H = -J \sum_{j=1}^N \left(S_j^x S_{j+1}^x + S_j^y S_{j+1}^y - \Delta S_j^z S_{j+1}^z \right) - h \sum_{j=1}^N S_j^z, \quad (13.3)$$

where J is the exchange-coupling strength, Δ is the anisotropy, h is an external magnetic field, and $L = Na$ with a the lattice spacing. We recall that the anisotropy term corresponds to four-fermion interactions after a Jordan-Wigner transformation. In fact, for $|\Delta| < 1$ and near (but not exactly at) half filling, applying this transformation to the Hamiltonian in (13.3) and taking a scaling limit effectively yields the Luttinger model in (13.1), see, e.g., [251, 252]. Indeed, in this regime, the low-energy description is given by TLL theory with

$$v = Ja \frac{\pi}{2} \frac{\sqrt{1-\Delta^2}}{\arccos(\Delta)}, \quad K = \frac{\pi}{2[\pi - \arccos(\Delta)]}, \quad (13.4)$$

obtained from the exact Bethe-ansatz solution when $h = 0$, see, e.g., [252]. As before, modulations in Δ corresponds to our interaction quenches or drives changing K and v .

INTERACTING MASSLESS BOSONS – THE LIEB-LINIGER MODEL. Another well-known example of a Bethe-ansatz integrable model is the Lieb-Liniger model of interacting bosons in one spatial dimension. In second quantization, the Hamiltonian is

$$H = \int_{-L/2}^{L/2} dx \left(\frac{1}{2m} \partial_x \Psi(x)^\dagger \partial_x \Psi(x) + c \Psi(x)^\dagger \Psi(x) \Psi(x)^\dagger \Psi(x) \right), \quad (13.5)$$

where m is the particle mass, $c \geq 0$ is a repulsive coupling constant, and $\Psi(x)$ is a bosonic field satisfying $[\Psi(x)^\dagger, \Psi(x')] = \delta(x - x')$. If we define the dimensionless coupling $\gamma = 2mc/\rho_0$, where ρ_0 is the density of particles, then $v = v(\gamma)$ and $K = K(\gamma)$ are functions of γ for which analytical expressions are not known in general but whose product must equal $v_F = \pi\rho_0/m$. As limiting cases for large and small γ ,

$$v = \frac{v_F}{K}, \quad K \sim \begin{cases} 1 + \frac{4}{\gamma} & \text{for } \gamma \gg 1, \\ \frac{\pi}{\sqrt{\gamma}} \left(1 - \frac{\sqrt{\gamma}}{2\pi}\right)^{-1/2} & \text{for } \gamma \ll 1, \end{cases} \quad (13.6)$$

see, e.g., [254, 255]. Once again, modulations in γ , or rather in c assuming ρ_0 is fixed, corresponds to our non-equilibrium protocols changing K and v .

TRAPPED ULTRA-COLD ATOMS. Besides its theoretical significance, TLL theory has direct experimental relevance to low-dimensional quantum many-body systems. Well-known and intensely studied examples are quasi-one-dimensional condensates of ultra-cold atoms. For a single condensate of bosons, such a system can be modeled by the Hamiltonian

$$H = \int_{-L/2}^{L/2} dx \left(\frac{1}{2m} \partial_x \Psi(x)^\dagger \partial_x \Psi(x) + \frac{g}{2} \Psi(x)^\dagger \Psi(x) \Psi(x)^\dagger \Psi(x) + [V(x) - \mu] \Psi(x)^\dagger \Psi(x) \right), \quad (13.7)$$

where m is the atom mass, $g \geq 0$ is the effective interaction strength, $V(x)$ is the trapping potential, and μ is the chemical potential, see, e.g., [254–257].¹ In the Thomas-Fermi regime, (13.7) can be approximated as an inhomogeneous TLL following the harmonic-fluid approach [258], setting $\Psi(x)^\dagger =$

¹ This model is that of a trapped Lieb-Liniger gas with $c = g/2$ using the notation in (13.5).

$\sqrt{\rho_0(x) + \pi\Pi(x)}e^{i\varphi(x)}$ and keeping only terms quadratic in the fields, with position-dependent

$$v(x) = \sqrt{\rho_0(x)g/m}, \quad K(x) = \pi\sqrt{\rho_0(x)/mg}, \quad (13.8)$$

where $\rho_0(x) = [\mu - V(x)]/g$ denotes the mean-atom-density distribution. The effect of $v(x)$ and $K(x)$ on non-equilibrium dynamics was recently studied in [259]. It would be interesting to study quenched or driven inhomogeneous TLLs modulating $v(x)$ and $K(x)$ in time, which would be directly applicable to trapped ultra-cold atoms. However, this is beyond the scope of the present analysis, as we only consider the homogeneous case, but which can be viewed as a first step in this direction. We remark that a related but different question concerns modulated tunnel couplings between pairs of quasi-one-dimensional condensates, see, e.g., [260, 261].

QUANTUM CIRCUITS. Another important application of TLL theory is to one-dimensional arrays of superconducting junctions. These have been proposed to simulate TLLs, the map between the parameters given by

$$v \sim a\sqrt{2E_{C_0}E_J}, \quad K \sim \frac{1}{2\pi}\sqrt{\frac{2E_{C_0}}{E_J}}, \quad (13.9)$$

to lowest order in the regime $E_J \gg E_{C_0}$, where E_J is the Josephson energy, E_{C_0} is the charging energy, and a is the array spacing, see, e.g., [262, 263]. It would be interesting if an array of driven junctions could be realized to simulate quenches and drives in TLLs.

STRING THEORY. The single compactified free boson in (13.11) also describes the closed bosonic string with target space being a circle of radius R . In this context, the bosonic field φ plays the role of the target-space coordinate while x and t are the worldsheet coordinates. A sudden change in the radius from R_1 to R_2 , with $R_2 > R_1$, realizes a toy scenario of sudden inflation. From a purely field-theoretic standpoint, one can imagine studying quenches caused by current-current deformations of more general sigma and WZW models [264]. These are integrable deformations and, therefore, the quench dynamics should be tractable. The analysis we are about to present is a first step in this direction.

13.3 ALGEBRAIC FRAMEWORK AND BOGOLIUBOV TRANSFORMATIONS

In TLL theory, all details are encapsulated in two parameters: The propagation velocity v and the Luttinger parameter K encoding the interactions of the original system. The Hamiltonian can be written as²

$$H_{v,K} = \frac{1}{2\pi} \int_{-L/2}^{L/2} dx : \left(\frac{v}{K} [\pi\Pi(x)]^2 + vK[\partial_x\varphi(x)]^2 \right) : - \frac{\pi v}{6L} \quad (13.10)$$

² We use units so that $\hbar = k_B = 1$.

for a bosonic field $\varphi(x) = \varphi(x) + 2\pi$ with x on the circle of length L , where $[\varphi(x), \Pi(y)] = i\delta(x-y)$ and $\cdots \cdot$ denotes Wick ordering. From a path integral perspective, this corresponds to the action³

$$S = \frac{R^2}{4\pi\alpha'} \int d^2x (\partial^\mu \varphi)(\partial_\mu \varphi) = \frac{1}{4\pi\alpha'} \int d^2x (\partial^\mu X)(\partial_\mu X) \quad (13.11)$$

describing free bosons $X = R\varphi$ with compactification radius R satisfying

$$K = \frac{R^2}{2\alpha'}, \quad (13.12)$$

where α' is referred to as the string tension in bosonic string theory [265]. We recall that α' has dimension length² and is commonly set as $\alpha' = 2$, which we will also do here for simplicity.

To establish our notation and conventions, following [55, 165, 171], we recall that the TLL Hamiltonian in (13.10) can equivalently be written as

$$H_{v,K} = \int_{-L/2}^{L/2} dx v [T_+(x) + T_-(x)] \quad (13.13)$$

using the right- and left-moving components $T_+(x)$ and $T_-(x)$ of the energy-momentum tensor in light-cone coordinates. The latter can, in turn, be expressed in terms of current operators

$$T_\pm(x) = \frac{\pi}{K} :J_\pm(x)^2: - \frac{\pi}{12L^2}, \quad (13.14)$$

where

$$J_\pm(x) = \frac{1}{2\pi} [\pi\Pi(x) \mp K\partial_x\varphi(x)] \quad (13.15)$$

are the right- and left-moving components of a conserved U(1) current in TLL theory. In general, consider a 1+1-dimensional CFT with central charge c (in our case $c = 1$) and a conserved U(1) current with K appearing as the current-algebra central charge. Passing to Fourier space,

$$T_+(x) = \frac{2\pi}{L^2} \sum_{n=-\infty}^{\infty} e^{+2\pi i n x/L} \left(L_n - \frac{c}{24} \delta_{n,0} \right), \quad (13.16)$$

$$J_+(x) = \frac{1}{L} \sum_{n=-\infty}^{\infty} e^{+2\pi i n x/L} J_n,$$

$$T_-(x) = \frac{2\pi}{L^2} \sum_{n=-\infty}^{\infty} e^{-2\pi i n x/L} \left(\bar{L}_n - \frac{c}{24} \delta_{n,0} \right), \quad (13.17)$$

$$J_-(x) = \frac{1}{L} \sum_{n=-\infty}^{\infty} e^{-2\pi i n x/L} \bar{J}_n,$$

³ Here $\varphi = \varphi(x, t)$ with $X = R\varphi$ taking values on the circle $[0, 2\pi R]$ for (x, t) on the cylinder $[-L/2, L/2] \times \mathbb{R}$. As usual, $x^0 = vt$, $x^1 = x$, $\partial_\mu = \partial/\partial x^\mu$ for $\mu = 0, 1$, and the metric is $\text{diag}(1, -1)$.

the operators L_n and J_n for $n \in \mathbb{Z}$ satisfy the commutation relations

$$\begin{aligned} [L_n, L_m] &= (n - m)L_{n+m} + \frac{c}{12}(n^3 - n)\delta_{n+m,0}, \\ [J_n, J_m] &= Kn\delta_{n+m,0}, \quad [L_n, J_m] = -mJ_{n+m}, \end{aligned} \quad (13.18)$$

and commute with all \bar{L}_n and \bar{J}_n , which in turn satisfy relations analogous to (13.18). We refer to [55] for an introduction to these and related topics.

Changes in the Luttinger parameter K or equivalently the compactification radius $R = 2\sqrt{K}$ correspond to marginal deformations of the TLL or free boson CFT.⁴ One way to arrive at this interpretation from a Lagrangian point of view is by identifying the marginal operator Φ responsible for changes in R , which by definition is a primary field with conformal weights $(h, \bar{h}) = (1, 1)$, see, e.g., [266]. The aim below is to identify this operator and explain how this gives a geometric interpretation to our space of marginal deformations.

An infinitesimal change from R to $R + \delta R$ implies the following change in the action (13.11):

$$\delta S = S_{R+\delta R} - S_R = \frac{R\delta R}{4\pi} \int d^2x (\partial^\mu \varphi)(\partial_\mu \varphi). \quad (13.19)$$

Therefore, the marginal operator is

$$\Phi = \frac{R\delta R}{4\pi} (\partial^\mu \varphi)(\partial_\mu \varphi) = \frac{1}{4\pi} \frac{\delta R}{R} J(z) \bar{J}(\bar{z}), \quad (13.20)$$

where we identified the currents

$$J(z) = -2\pi J_+(x^-)/\sqrt{K} \quad \text{and} \quad \bar{J}(\bar{z}) = -2\pi J_-(x^+)/\sqrt{K} \quad (13.21)$$

in complex coordinates $z = x + i\tau = x^-$ and $\bar{z} = x - i\tau = x^+$ with $\tau = it$ denoting imaginary time [cf. (13.15)]. The change is thus exactly in the form of a $J\bar{J}$ deformation.

The geometry of the ‘theory space’ generated by marginal deformations, known as the moduli space or conformal manifold, here denoted by \mathcal{M} , is given by the Zamolodchikov metric [244].⁵ This is obtained from the ground-state correlation function of a pair of marginal operators on the sphere (or the infinite plane):

$$\langle \Phi(z, \bar{z}) \Phi(0, 0) \rangle = \frac{ds_{\mathcal{M}}^2}{|z|^4}, \quad ds_{\mathcal{M}}^2 = \frac{1}{(4\pi)^2} \left(\frac{dR}{R} \right)^2. \quad (13.22)$$

Thus, up to an overall constant, the geodesic distance between two CFTs of compactification radii R_1 and R_2 in \mathcal{M} is

$$\int_{R_2}^{R_1} \frac{dR}{R} = \log \left(\frac{R_1}{R_2} \right), \quad (13.23)$$

which is exactly ν in (13.32), giving it the geometric interpretation as the Zamolodchikov distance. It will turn out that the dynamics of our non-equilibrium protocols will crucially depend on this parameter.

⁴ Recall that we set $\alpha' = 2$.

⁵ The moduli space of the free boson CFT is parametrized by the radius $R \in [\sqrt{\alpha'}, \infty]$, obtained by quotienting $[0, \infty]$ by the action of T-duality $R \leftrightarrow \alpha'/R$.

Given our non-equilibrium protocols featuring $H_1 = H_{v_1, K_1}$ and $H_2 = H_{v_2, K_2}$, we find it convenient to let H_1 be our ‘undeformed’ theory, i.e., we set $K = K_1$ in (13.14), (13.15), and (13.18), and view $H_2 = H_{v_2, K_2}$ as our ‘deformed’ theory. To this end, we introduce two commuting sets of bosonic operators a_n and \bar{a}_n , $n \in \mathbb{Z}$, for right- and left-moving excitations, respectively, satisfying $a_n^\dagger = a_{-n}$,

$$[a_n, a_m] = n\delta_{n+m,0} = [\bar{a}_n, \bar{a}_m], \quad [a_n, \bar{a}_m] = 0, \quad (13.24)$$

and

$$a_n|\Omega\rangle = \bar{a}_n|\Omega\rangle = 0 \quad \forall n \geq 0, \quad (13.25)$$

which also defines the vacuum $|\Omega\rangle$. The operators in the theory with $K = K_1$ can then be constructed as

$$J_n = \sqrt{K_1}a_n, \quad \bar{J}_n = \sqrt{K_1}\bar{a}_n \quad (13.26)$$

and

$$L_n = \frac{1}{2} \sum_{m=-\infty}^{\infty} :a_{n-m}a_m:, \quad \bar{L}_n = \frac{1}{2} \sum_{m=-\infty}^{\infty} :\bar{a}_{n-m}\bar{a}_m:, \quad (13.27)$$

where the Wick ordering $:\dots:$ is with respect to $|\Omega\rangle$. We recall that the latter identities are examples of the Sugawara construction, see, e.g., [55]. These operators can be shown to satisfy (13.18) with $K = K_1$ and $c = 1$. The Fourier modes of the bosonic fields $\varphi(x)$ and $\Pi(x)$ in (13.10) can then be constructed as

$$\varphi_n = \frac{1}{2\sqrt{K_1}} \frac{i}{n} (a_n - \bar{a}_{-n}), \quad \Pi_n = \sqrt{K_1} (a_{-n} + \bar{a}_n) \quad (13.28)$$

for all $n \neq 0$, satisfying $[\varphi_n, \Pi_m] = i\delta_{n,m}$ and $[\varphi_n, \varphi_m] = 0 = [\Pi_n, \Pi_m]$ for $n, m \neq 0$. As usual, the case $n = 0$ has to be handled separately. To fix our terminology, we will refer to a_n and \bar{a}_n for $n \neq 0$ as oscillator modes and a_0 and \bar{a}_0 as zero modes.

Given the above, we can express the undeformed Hamiltonian

$$H_1 = \frac{2\pi v_1}{L} (L_0 + \bar{L}_0) - \frac{\pi v_1}{6L} \quad (13.29)$$

in terms of the oscillator and zero modes: $H_1 = H_1^{(0)} + H_1^{(\text{osc})} - \pi v_1 / 6L$ with

$$\begin{aligned} H_1^{(\text{osc})} &= \frac{\pi v_1}{L} \sum_{n \neq 0} :(a_{-n}a_n + \bar{a}_{-n}\bar{a}_n):, \\ H_1^{(0)} &= \frac{\pi v_1}{L} (a_0^2 + \bar{a}_0^2). \end{aligned} \quad (13.30)$$

It follows that H_1 does not couple right and left movers and has $|\Omega\rangle$ in (13.25) as its ground state. Let us also write the deformed Hamiltonian H_2 using the modes of the undeformed theory:⁶ $H_2 = H_2^{(0)} + H_2^{(\text{osc})} - \pi v_2/6L$ with

$$\begin{aligned} H_2^{(\text{osc})} &= \frac{\pi v_2}{L} \sum_{n \neq 0} [\cosh(2\nu) : (a_{-n} a_n + \bar{a}_{-n} \bar{a}_n) : + 2 \sinh(2\nu) a_n \bar{a}_n] + E_2^0, \\ H_2^{(0)} &= \frac{\pi v_2}{L} [\cosh(2\nu) (a_0^2 + \bar{a}_0^2) + 2 \sinh(2\nu) a_0 \bar{a}_0] \end{aligned} \quad (13.31)$$

for the Zamolodchikov distance ν

$$\nu = \log \sqrt{K_1/K_2} = \log(R_1/R_2), \quad (13.32)$$

as a function of the two Luttinger parameters $K_{1,2}$ (or the two radii $R_{1,2}$), where $E_2^0 = -(2\pi v_2/L) \sum_{n>0} [\cosh(2\nu) - 1] n$ is a diverging constant due to Wick ordering with respect to $|\Omega\rangle$. We note the presence of terms that couple right and left movers if $\nu \neq 0$, which makes it manifest that H_2 is a $J\bar{J}$ deformation of H_1 [cf. (13.26)]. For completeness and future reference, we note the following analogue of (13.29) for the deformed Hamiltonian:

$$H_2 = \frac{2\pi v_2}{L} \cosh(2\nu) (L_0 + \bar{L}_0) + \frac{2\pi v_2 \sinh(2\nu)}{L} \sum_{n=-\infty}^{\infty} J_n \bar{J}_n - \frac{\pi v_2}{6L} + E_2^0, \quad (13.33)$$

where all ingredients are operators of the undeformed theory with $K = K_1$.⁷

The combinations of oscillator modes appearing in H_1 and H_2 in (13.30) and (13.31) can conveniently be written in terms of the generators of a countably infinite number of copies of the $\mathfrak{su}(1,1)$ algebra, labeled by $n \in \mathbb{Z}^+ = \{1, 2, \dots\}$. More precisely, for $n > 0$, let

$$K_0^{(n)} = \frac{1}{2n} (a_{-n} a_n + \bar{a}_{-n} \bar{a}_n + n), \quad K_-^{(n)} = \frac{1}{n} a_n \bar{a}_n, \quad K_+^{(n)} = \frac{1}{n} a_{-n} \bar{a}_{-n}, \quad (13.34)$$

which satisfy $(K_-^{(n)})^\dagger = K_+^{(n)}$ and

$$[K_-^{(n)}, K_+^{(m)}] = 2K_0^{(n)} \delta_{n,m}, \quad [K_0^{(n)}, K_\pm^{(m)}] = \pm K_\pm^{(n)} \delta_{n,m}, \quad (13.35)$$

see, e.g., [267]. For later reference, one can show that the associated Cartan-Killing form is

$$\mathcal{K}(X, Y) = \begin{pmatrix} x_0 & x_- & x_+ \end{pmatrix} \begin{pmatrix} 2 & 0 & 0 \\ 0 & 0 & -4 \\ 0 & -4 & 0 \end{pmatrix} \begin{pmatrix} y_0 \\ y_- \\ y_+ \end{pmatrix} \quad (13.36)$$

⁶ The expression in (13.31) can also be derived from (13.43). We note that the coefficients $\cosh(2\nu)$ and $\sinh(2\nu)$ can be interpreted as coupling constants and correspond to $1 + g_4/2$ and $g_2/2$ in the Luttinger model (13.1) respectively, if the latter are defined with respect to the theory with $K = K_1$ (instead of $K = 1$ as usual).

⁷ Under an infinitesimal change of the Luttinger parameter, $K_2 = K_1 + \delta K_1$, the deformed Hamiltonian (13.33) is related to the undeformed one as $H_2/v_2 \approx H_1/v_1 - (2\pi/L)(\delta K_1/K_1^2) \sum_n J_n \bar{J}_n$.

for $X = x_0 K_0^{(n)} + x_- K_-^{(n)} + x_+ K_+^{(n)}$ and $Y = y_0 K_0^{(n)} + y_- K_-^{(n)} + y_+ K_+^{(n)}$. We recall that the corresponding group, $\mathfrak{su}(1, 1)$, is non-compact and, therefore, all unitary irreducible representations are infinite dimensional, see, e.g., [267]. However, one can construct a non-unitary 2×2 -matrix representation of the generators:

$$\begin{aligned} K_0^{(n)}|_{2 \times 2} &= \begin{pmatrix} -1/2 & 0 \\ 0 & 1/2 \end{pmatrix}, & K_-^{(n)}|_{2 \times 2} &= \begin{pmatrix} 0 & 1 \\ 0 & 0 \end{pmatrix}, \\ K_+^{(n)}|_{2 \times 2} &= \begin{pmatrix} 0 & 0 \\ -1 & 0 \end{pmatrix}. \end{aligned} \quad (13.37)$$

Additionally, it is also useful to note the following commutation relations:

$$[K_-^{(n)}, a_m] = \delta_{n+m, 0} \bar{a}_{-m}, \quad [K_-^{(n)}, \bar{a}_m] = \delta_{n+m, 0} a_{-m}, \quad (13.38a)$$

$$[K_+^{(n)}, a_m] = -\delta_{n+m, 0} \bar{a}_{-m}, \quad [K_+^{(n)}, \bar{a}_m] = -\delta_{n+m, 0} a_{-m}. \quad (13.38b)$$

The Hamiltonians can also be written in terms of the $\mathfrak{su}(1, 1)$ generators as

$$H_1 = H_1^{(0)} + \frac{2\pi v_1}{L} \sum_{n>0} 2n \left(K_0^{(n)} - \frac{1}{2} \right) - \frac{\pi v_1}{6L} \quad (13.39)$$

and

$$\begin{aligned} H_2 &= \frac{2\pi v_2}{L} \sum_{n>0} 2n \left[\cosh(2\nu) \left(K_0^{(n)} - \frac{1}{2} \right) + \sinh(2\nu) \left(K_-^{(n)} + K_+^{(n)} \right) \right] \\ &\quad + H_2^{(0)} - \frac{\pi v_2}{6L} \end{aligned} \quad (13.40)$$

with ν in (13.32).

It is well-known that a TLL Hamiltonian can be ‘diagonalized’ by a Bogoliubov transformation, which effectively ‘rotates’ the oscillator modes by an ‘angle’ ν , for a suitable choice of the latter. Below, we discuss the operator that implements this transformation and show that the relevant choice of ν is exactly the one in (13.32).

As explained in [250], the Bogoliubov transformation is implemented by the unitary operator⁸

$$\mathcal{I}_\nu = \exp \left[\nu \sum_{n \neq 0} \frac{1}{n} a_n \bar{a}_n \right] = \prod_{n>0} \exp \left[\nu \left(K_-^{(n)} - K_+^{(n)} \right) \right], \quad (13.41)$$

defined for any $\nu \in \mathbb{R}$. The second equality rewrites the operator as it appears in [250] in terms of the $\mathfrak{su}(1, 1)$ generators, which will prove convenient later. Indeed, using (13.38), it is straightforward to show

$$\mathcal{I}_\nu a_n \mathcal{I}_\nu^\dagger = a_n \cosh(\nu) + \bar{a}_{-n} \sinh(\nu), \quad (13.42a)$$

$$\mathcal{I}_\nu \bar{a}_n \mathcal{I}_\nu^\dagger = \bar{a}_n \cosh(\nu) + a_{-n} \sinh(\nu) \quad (13.42b)$$

⁸ Note that we use a_n and \bar{a}_n of the undeformed theory with $K = K_1$ to define \mathcal{I}_ν rather than the usual choice corresponding to $K = 1$.

for $n \neq 0$. The inverse relations are obtained by noting that $\mathcal{I}_\nu^\dagger = \mathcal{I}_\nu^{-1} = \mathcal{I}_{-\nu}$. Note that one must take the latter as a definition of \mathcal{I}_ν^\dagger when using (13.41) with the non-unitary representation in (13.37). By picking ν as in (13.32), one can show that

$$\mathcal{I}_\nu^\dagger H_2^{(\text{osc})} \mathcal{I}_\nu = \frac{v_2}{v_1} H_1^{(\text{osc})} + E_2^0 \quad (13.43)$$

up to the diverging constant E_2^0 due to Wick ordering with respect to $|\Omega\rangle$. This allows us to write the Floquet operator

$$U_F = e^{-iH_1 t_1} e^{-iH_2 t_2}, \quad (13.44)$$

as

$$U_F = e^{-iE_2^0 t_2} e^{-iH_1 t_1} \mathcal{I}_\nu e^{-iH_1 \tilde{t}_2} \mathcal{I}_\nu^\dagger e^{-i[H_2^{(0)} t_2 - H_1^{(0)} \tilde{t}_2]}, \quad \tilde{t}_2 = (v_2/v_1)t_2, \quad (13.45)$$

where the overall phase $e^{-iE_2^0 t_2}$ will be of no consequence to the dynamical observables we study. The above expression for U_F is the key to most of our subsequent computations. (The quantum quench can be studied as a special case by setting $t_1 = 0$ and $t_2 = t$.) Note that \mathcal{I}_ν brings to mind interface operators in boundary CFT since it connects two different bosonic theories along time interfaces in our non-equilibrium protocols. One can also observe that this operator, as defined in (13.41), has the form of a two-mode squeeze operator [268]. This class of operators play an important role in quantum optics, where they are associated to degenerate parametric amplification. In our present setup, the two modes correspond to the right- and left-moving sets of oscillator modes.

We also find it useful to introduce the q -modified operator

$$\begin{aligned} \mathcal{I}_\nu^{(q)} &= q^{L_0 + \bar{L}_0} \mathcal{I}_\nu q^{-L_0 - \bar{L}_0} = \exp \left[\nu \sum_{n \neq 0} \frac{q^{-2n}}{n} a_n \bar{a}_n \right] \\ &= \prod_{n>0} \exp \left[\nu \left(q^{-2n} K_-^{(n)} - q^{2n} K_+^{(n)} \right) \right] \end{aligned} \quad (13.46)$$

for $q \in \text{U}(1)$. In the second equality, we used that

$$q^{L_0 + \bar{L}_0} a_n q^{-L_0 - \bar{L}_0} = a_n q^{-n}, \quad q^{L_0 + \bar{L}_0} \bar{a}_n q^{-L_0 - \bar{L}_0} = \bar{a}_n q^{-n}. \quad (13.47)$$

(The latter is nothing but the inverse time evolution of a_n and \bar{a}_n under H_1 in (13.30) if one sets $q = e^{-2\pi i v_1 t/L}$.) The q -modified operators transform the oscillator modes as

$$\mathcal{I}_\nu^{(q)} a_n (\mathcal{I}_\nu^{(q)})^\dagger = a_n \cosh(\nu) + \bar{a}_{-n} \sinh(\nu) q^{2n}, \quad (13.48a)$$

$$\mathcal{I}_\nu^{(q)} \bar{a}_n (\mathcal{I}_\nu^{(q)})^\dagger = \bar{a}_n \cosh(\nu) + a_{-n} \sinh(\nu) q^{2n}, \quad (13.48b)$$

generalizing (13.42). Moreover, it also allows us to further rewrite (13.45) as

$$U_F = e^{-iE_2^0 t_2} q_1^{L_0 + \bar{L}_0} \mathcal{I}_\nu \left(\mathcal{I}_\nu^{(q_2)} \right)^\dagger q_2^{L_0 + \bar{L}_0} e^{-i[H_2^{(0)} - (v_2/v_1) H_1^{(0)}] t_2} \quad (13.49)$$

for $q_{1,2} = e^{-2\pi i \tau_{1,2}}$, where we reiterate that the phase $e^{-iE_2^0 t_2}$ will be of no consequence in practice. Lastly, as for $\mathcal{I}_\nu = \mathcal{I}_\nu^{(1)}$, unitarity implies $(\mathcal{I}_\nu^{(q)})^\dagger = (\mathcal{I}_\nu^{(q)})^{-1} = \mathcal{I}_{-\nu}^{(q)}$, which must be taken as a definition when using (13.46) with the non-unitary representation in (13.37).

The Wick ordering \dots : we use is with respect to $|\Omega\rangle$ in (13.25) and is therefore the ordering of the Hilbert space of H_1 constructed from its primary states and their descendants. For bilinears of the form $a_n a_m$ and $\bar{a}_n \bar{a}_m$, this ordering is equivalent to subtracting the ground-state expectation value,

$$:a_n a_m: = a_n a_m - \langle \Omega | a_n a_m | \Omega \rangle = a_n a_m - \delta_{n+m,0} n \theta(n) \quad (13.50)$$

where $\theta(\cdot)$ is the Heaviside function, and similarly for $\bar{a}_n \bar{a}_m$.⁹

The constant E_2^0 in (13.31) and (13.43) appears due to re-ordering of the right-hand side, and diverges due to that the $J\bar{J}$ deformation affects all modes. A more rigorous approach would be to include an ultraviolet cutoff on the deformation, effectively a momentum dependence in the Luttinger parameter $K_2^{(n)}$ so that it tends to K_1 sufficiently fast for large $|n|$. As mentioned, this is related to making \mathcal{I}_ν well defined: This operator provides a map between the Hilbert spaces of our two theories with different Luttinger parameters, which strictly speaking become unitarily inequivalent in the absence of a cutoff, manifested by that the ‘true ground state’ of H_2 is separated from its ‘ground state’ $\mathcal{I}_\nu |\Omega\rangle$ in the Hilbert space of H_1 by a diverging constant. This necessitates an additive renormalization of $\mathcal{I}_\nu^\dagger H_2 \mathcal{I}_\nu$ for it to make sense on the Hilbert space of H_1 , see, e.g., [253] for further discussion. We remark, however, that the presence of a cutoff can be motivated by physical applications and that all steps in this chapter can be repeated with it in place since our quenched or driven theory corresponds to an infinite sequence of uncoupled (discrete-time) quantum (parametric) oscillators.

13.4 QUANTUM QUENCH

In this section, we study the dynamics of a TLL after an interaction quench, starting from an arbitrary eigenstate of H_1 , and switching the Luttinger parameter from K_1 to K_2 at time $t = 0$. As discussed in Sec. 13.3, this corresponds to quenching the original TLL Hamiltonian with a marginal ($J\bar{J}$) deformation. We compute the exact time-evolution after the quench of the following two quantities:

1. The Loschmidt echo, defined for a pure initial state $|\Psi\rangle$ as

$$F(t) = |\langle \Psi | e^{-iH_2 t} | \Psi \rangle|^2. \quad (13.51)$$

This quantifies the time-dependent return probability of a state and can thereby be used to measure the probability of quantum revivals. Moreover, non-analyticities in $\log[F(t)]$ after a quantum quench can reveal rich dynamics and are a typical signature of dynamical quantum phase transitions [245].

⁹ Starting from the usual definition of placing all creation operators to the left of all annihilation operators, (13.50) can be verified by identifying a_n and \bar{a}_n for $n < (>) 0$ as creation (annihilation) operators, meaning that the only non-trivial case is $n > 0 > m$, and using (13.24) and (13.25).

2. The energy-density expectation, defined for a pure initial state $|\Psi\rangle$ as

$$\mathcal{E}_\Psi(x, t) = \langle \Psi | e^{iH_2 t} v_1 [T_+(x) + T_-(x)] e^{-iH_2 t} |\Psi\rangle. \quad (13.52)$$

In addition to pure states, we also compute the time evolution of the energy-density expectation with respect to initial thermal states. For all the cases considered, the spatial-homogeneity of the initial state significantly simplifies the computations.

We note that, since the initial states we consider are spatially homogeneous, time evolution of the particle density would be trivial, which is why we do not study this observable in the present chapter. However, for spatially inhomogeneous initial states, the expectation value of particle density would generically have a non-trivial time evolution.

We first compute the Loschmidt echo after the quench from the ground state $|\Omega\rangle$ of H_1 ,

$$F_\Omega(t) = |\langle \Omega | e^{-iH_2 t} |\Omega\rangle|^2. \quad (13.53)$$

Using the framework introduced in Sec. 13.3, it can be shown that

$$\langle \Omega | e^{-iH_2 t} |\Omega\rangle = e^{-iE_2^0 t} \langle \Omega | \mathcal{I}_\nu (\mathcal{I}_\nu^{(q)})^\dagger |\Omega\rangle. \quad (13.54)$$

Indeed, since (13.44) implies $U_F = e^{-iH_2 t}$ for $t_1 = 0$ and $t_2 = t$, the above follows from (13.49) for $q_1 = 1$ and $q_2 = q = e^{-2\pi i v_2 t/L}$ and (13.25). Note that $F_\Omega(t)$ is insensitive to the overall phase $e^{-iE_2^0 t}$. Our strategy to compute the right-hand side of (13.54) is to use the decomposition of $\mathcal{I}_\nu (\mathcal{I}_\nu^{(q)})^\dagger$ in terms of the $\mathfrak{su}(1, 1)$ generators in (13.34):

$$\begin{aligned} & \langle \Omega | \mathcal{I}_\nu (\mathcal{I}_\nu^{(q)})^\dagger |\Omega\rangle \\ &= \prod_{n>0} \langle \Omega | \exp(\zeta_+^{(n)} K_+^{(n)}) \exp(\zeta_0^{(n)} K_0^{(n)}) \exp(\zeta_-^{(n)} K_-^{(n)}) |\Omega\rangle \\ &= \prod_{n>0} \langle \Omega | \exp(\zeta_0^{(n)} K_0^{(n)}) |\Omega\rangle = \prod_{n>0} \exp(\zeta_0^{(n)} / 2), \end{aligned} \quad (13.55)$$

where we used $\langle \Omega | K_+^{(n)} = 0 = K_-^{(n)} |\Omega\rangle$, which follows from (13.25). One efficient way to find the coefficients $\zeta_0^{(n)}$ and $\zeta_\pm^{(n)}$ is to use the non-unitary 2×2 -matrix representation of the $\mathfrak{su}(1, 1)$ in (13.37). In this representation, using (13.41) and (13.46) with $(\mathcal{I}_\nu^{(q)})^\dagger = \mathcal{I}_{-\nu}^{(q)}$ as a definition,¹⁰ we obtain

$$\begin{aligned} & \mathcal{I}_\nu (\mathcal{I}_\nu^{(q)})^\dagger \Big|_{2 \times 2}^{(n)} \\ &= \begin{pmatrix} \cosh^2(\nu) - \sinh^2(\nu) q^{2n} & \frac{1}{2} \sinh(2\nu) (1 - q^{-2n}) \\ \frac{1}{2} \sinh(2\nu) (1 - q^{2n}) & \cosh^2(\nu) - \sinh^2(\nu) q^{-2n} \end{pmatrix} \end{aligned} \quad (13.56)$$

¹⁰ At a practical level, this is done in order to bypass the unitarity requirement on the $\mathfrak{su}(1, 1)$ representation.

for the n th mode. Comparing this with the product

$$\begin{aligned} & e^{\zeta_+^{(n)} K_+^{(n)}} e^{\zeta_0^{(n)} K_0^{(n)}} e^{\zeta_-^{(n)} K_-^{(n)}} \Big|_{2 \times 2} \\ &= \begin{pmatrix} e^{-\zeta_0^{(n)}/2} & \zeta_-^{(n)} e^{-\zeta_0^{(n)}/2} \\ -\zeta_+^{(n)} e^{-\zeta_0^{(n)}/2} & e^{\zeta_0^{(n)}/2} - \zeta_-^{(n)} \zeta_+^{(n)} e^{-\zeta_0^{(n)}/2} \end{pmatrix}, \end{aligned} \quad (13.57)$$

we deduce that the Loschmidt echo after the quench starting from the ground state is

$$F_\Omega(t) = \prod_{n>0} \frac{1}{|\cosh^2(\nu) - \sinh^2(\nu) q^{2n}|^2}. \quad (13.58)$$

Considering all the modes by taking the infinite product in (13.58) into account, the resulting Loschmidt echo has a Dirac comb structure, i.e., it is zero at all times t apart from $t = kL/2v_2$ for $k \in \mathbb{N} = \{0, 1, 2, \dots\}$, at which there are exact quantum revivals. These can be understood from a quasiparticle picture [67]: Right- and left-moving quasiparticles emitted from any position meet again after half-integer multiples of L with periodic boundary conditions. A similar result was found in [71] for the Loschmidt echo by starting from a boundary state and quenching with a uniform CFT Hamiltonian, while we started from the ground state of a uniform compactified free boson CFT, and quenched with a $J\bar{J}$ deformed CFT. To compare with critical lattice systems, it is necessary to apply a cutoff on the number of momentum modes that appear in the infinite product. This in turn leads to a cutoff dependent Loschmidt echo, as shown in Fig. 13.1. Finally, we note that the Loschmidt echo starting from a primary state $|h, \bar{h}\rangle$ of conformal dimension (h, \bar{h}) is the same as starting from the ground state $|\Omega\rangle$. In order to show that, Let us first use the operator-state correspondence and write

$$\langle h, \bar{h} | \mathcal{I}_\nu \left(\mathcal{I}_\nu^{(q)} \right)^\dagger | h, \bar{h} \rangle = \lim_{\substack{z, \bar{z} \rightarrow 0 \\ \omega, \bar{\omega} \rightarrow 0}} \langle \Omega | O^\dagger(\omega, \bar{\omega}) \mathcal{I}_\nu \left(\mathcal{I}_\nu^{(q)} \right)^\dagger O(z, \bar{z}) | \Omega \rangle, \quad (13.59)$$

where $O(z, \bar{z})$ is a primary field with conformal weights (h, \bar{h}) . The following commutation relations can be derived from the OPEs of $O(z, \bar{z})$ with the conserved $U(1)$ currents $J(z)$ and $\bar{J}(\bar{z})$:

$$[a_n, O(z, \bar{z})] = q_O z^n O(z, \bar{z}), \quad (13.60)$$

$$[a_n \bar{a}_n, O(z, \bar{z})] = [\bar{q}_O \bar{z}^n a_n + q_O z^n \bar{a}_n - q_O \bar{q}_O (z\bar{z})^n] O(z, \bar{z}). \quad (13.61)$$

Here, q_O and \bar{q}_O are the charges of the $U(1)_+$ and $U(1)_-$ current algebras, respectively, for the primary field $O(z, \bar{z})$; equivalently, these are the right and left momenta of the vertex operators. As a consequence, it is clear that

$$\lim_{z, \bar{z} \rightarrow 0} [a_n \bar{a}_n, O(z, \bar{z})] = 0, \quad \lim_{z, \bar{z} \rightarrow 0} \left[\left(\mathcal{I}_\nu^{(q)} \right)^\dagger, O(z, \bar{z}) \right] = 0, \quad (13.62)$$

where we used (13.41), which implies

$$\langle h, \bar{h} | \mathcal{I}_\nu \left(\mathcal{I}_\nu^{(q)} \right)^\dagger | h, \bar{h} \rangle = \lim_{\substack{z, \bar{z} \rightarrow 0 \\ \omega, \bar{\omega} \rightarrow 0}} \langle \Omega | \mathcal{I}_\nu O^\dagger(\omega, \bar{\omega}) O(z, \bar{z}) \left(\mathcal{I}_\nu^{(q)} \right)^\dagger | \Omega \rangle. \quad (13.63)$$

Using the fact that the primary states of the compactified free boson CFT are vertex operators, we conclude that $\lim_{z, \bar{z} \rightarrow 0} \lim_{\omega, \bar{\omega} \rightarrow 0} O^\dagger(\omega, \bar{\omega})O(z, \bar{z}) = \mathbb{I}$ and thus one has

$$\langle h, \bar{h} | \mathcal{I}_\nu \left(\mathcal{I}_\nu^{(q)} \right)^\dagger | h, \bar{h} \rangle = \langle \Omega | \mathcal{I}_\nu \left(\mathcal{I}_\nu^{(q)} \right)^\dagger | \Omega \rangle. \quad (13.64)$$

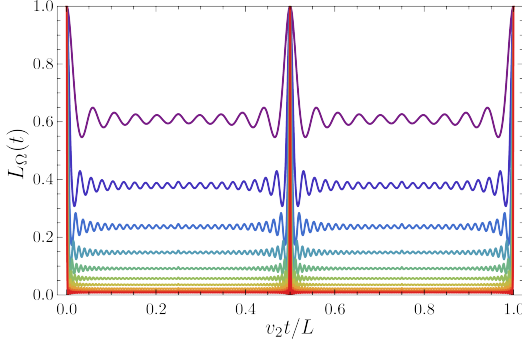


Figure 13.1: Time evolution of the Loschmidt echo $F_\Omega(t)$ in (13.58) following a quench with $K_1/K_2 = 7/6$ starting from the ground state. The results are plotted for a cutoff on the number of modes at $n = 10, 20, \dots, 100$ (top to bottom). We observe that by increasing the number of terms in the product, $F_\Omega(t)$ tends to the exact CFT result of a Dirac comb with revivals at $kL/2v_2$, $k \in \mathbb{N}$.

We now compute the exact time evolution of the Loschmidt echo starting from an initial state of the form

$$|\Psi_{\mathbf{p}, \bar{\mathbf{p}}} \rangle = \frac{1}{\sqrt{\mathcal{N}_{\mathbf{p}, \bar{\mathbf{p}}}}} \prod_{n=1}^{\infty} \bar{a}_{-n}^{\bar{p}_n} a_n^{p_n} |\Omega \rangle, \quad \mathcal{N}_{\mathbf{p}, \bar{\mathbf{p}}} = \prod_{n=1}^{\infty} (n^{p_n} p_n!) (n^{\bar{p}_n} \bar{p}_n!) \quad (13.65)$$

for $\mathbf{p} = (p_n)_{n=1}^{\infty}$ and $\bar{\mathbf{p}} = (\bar{p}_n)_{n=1}^{\infty}$ with $p_n, \bar{p}_n \in \mathbb{N}$, i.e., any possible descendant state from the ground state $|\Omega\rangle$. Following the above reasoning, the Loschmidt echo has the form

$$F_{\mathbf{p}, \bar{\mathbf{p}}}(t) = \left| \langle \Psi_{\mathbf{p}, \bar{\mathbf{p}}} | e^{-iH_2 t} | \Psi_{\mathbf{p}, \bar{\mathbf{p}}} \rangle \right|^2 = \frac{1}{\mathcal{N}_{\mathbf{p}, \bar{\mathbf{p}}}^2} |C_{\mathbf{p}, \bar{\mathbf{p}}}|^2, \quad (13.66)$$

where

$$C_{\mathbf{p}, \bar{\mathbf{p}}} = \langle \Omega | \left(\prod_{n=1}^{\infty} a_n^{p_n} \bar{a}_n^{\bar{p}_n} \right) \mathcal{I}_\nu \left(\mathcal{I}_\nu^{(q)} \right)^\dagger \left(\prod_{n=1}^{\infty} \bar{a}_{-n}^{\bar{p}_n} a_{-n}^{p_n} \right) |\Omega \rangle \quad (13.67)$$

is the non-trivial part we need to compute.

Let us start by considering the initial state $(1/\sqrt{n^p p!}) a_{-n}^p |\Omega\rangle$, writing $p = p_n$ to lighten the notation. We thus need to compute

$$C_p = \langle \Omega | a_n^p \mathcal{I}_\nu \left(\mathcal{I}_\nu^{(q)} \right)^\dagger a_{-n}^p |\Omega \rangle. \quad (13.68)$$

This can be achieved by using (13.42) and (13.48) to move one a_{-n} past $\mathcal{I}_\nu(\mathcal{I}_\nu^{(q)})^\dagger$, which yields

$$C_p = \langle \Omega | a_n^p (A_n a_{-n} + B_n \bar{a}_n) \mathcal{I}_\nu (\mathcal{I}_\nu^{(q)})^\dagger a_{-n}^{p-1} | \Omega \rangle \quad (13.69)$$

with $A_n = A_n(t)$ and $B_n = B_n(t)$ given by

$$A_n(t) = \cosh^2(\nu) - \sinh^2(\nu) q^{-2n}, \quad B_n(t) = \frac{1}{2} \sinh(2\nu) (1 - q^{-2n}) \quad (13.70)$$

using $q = e^{-2\pi i v_2 t/L}$. Noting that $\langle \Omega | a_n^p a_{-n} = p n \langle \Omega | a_n^{p-1}$, we obtain

$$C_p = np A_n C_{p-1} + B_n \langle \Omega | a_n^p \bar{a}_n \mathcal{I}_\nu (\mathcal{I}_\nu^{(q)})^\dagger a_{-n}^{p-1} | \Omega \rangle. \quad (13.71)$$

The second term can be simplified by moving \bar{a}_n to the right, leading to

$$\langle \Omega | a_n^p \bar{a}_n \mathcal{I}_\nu (\mathcal{I}_\nu^{(q)})^\dagger a_{-n}^{p-1} | \Omega \rangle = A_n \langle \Omega | a_n^p \mathcal{I}_\nu (\mathcal{I}_\nu^{(q)})^\dagger \bar{a}_n a_{-n}^{p-1} | \Omega \rangle - \overline{B_n} C_p \quad (13.72)$$

with the complex conjugated $\overline{B_n} = B_n(-t)$ given by (13.70). The first term vanishes and we conclude that C_p must satisfy the recursion relation

$$C_p = np \frac{A_n}{1 + |B_n|^2} C_{p-1}, \quad C_0 = \langle \Omega | \mathcal{I}_\nu (\mathcal{I}_\nu^{(q)})^\dagger | \Omega \rangle. \quad (13.73)$$

Solving this recursion relation, we conclude that

$$C_p = n^p p! \left(\frac{A_n}{1 + |B_n|^2} \right)^p \langle \Omega | \mathcal{I}_\nu (\mathcal{I}_\nu^{(q)})^\dagger | \Omega \rangle. \quad (13.74)$$

Thus, using (13.66) with $\mathcal{N}_{p_n} = n^{p_n} (p_n!)$, the Loschmidt echo starting from an initial state of the form $(1/\sqrt{n^{p_n} p_n!}) a_{-n}^{p_n} | \Omega \rangle$ is obtained by multiplying $F_\Omega(t)$ in (13.58) by a time-dependent factor. The result is

$$L_{p_n}(t) = F_\Omega(t) \left(\frac{|A_n(t)|}{1 + |B_n(t)|^2} \right)^{2p_n} \quad (13.75)$$

with $A_n(t)$ and $B_n(t)$ in (13.70). A direct consequence of (13.75) is that $L_{p_n}(t)$ decreases exponentially with p_n by starting from such an excited state instead of the ground state. However, the quantum revivals at times $t = kL/2v_2$ remain unchanged, see Fig. 13.2(a).

We now consider an initial state that mixes right- and left-moving excitations for a given mode n ,

$$|\Psi_{p,\bar{p}}\rangle = \frac{1}{\sqrt{(n^p p!) (n^{\bar{p}} \bar{p}!)}} \bar{a}_{-n}^{\bar{p}} a_{-n}^p |\Omega\rangle, \quad (13.76)$$

again writing $p = p_n$ and $\bar{p} = \bar{p}_n$ to lighten the notation. The Hamiltonian H_2 after the quench acts non-trivially on such an initial state because the marginal ($J\bar{J}$) deformation effectively repartitions excitations into right and left moving. As before, we compute

$$C_{p,\bar{p}} = \langle \Omega | a_n^p \bar{a}_n^{\bar{p}} \mathcal{I}_\nu (\mathcal{I}_\nu^{(q)})^\dagger \bar{a}_{-n}^{\bar{p}} a_{-n}^p | \Omega \rangle. \quad (13.77)$$

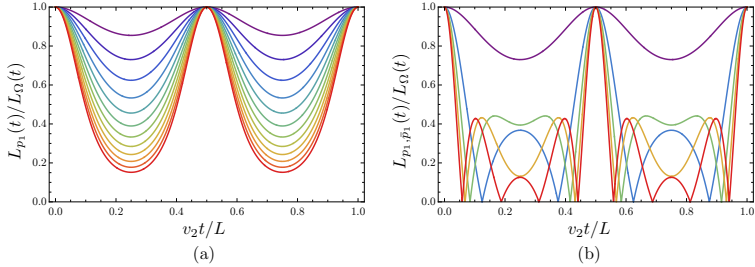


Figure 13.2: (a) Time evolution of the Loschmidt echo $L_{p_1}(t)/L_{\Omega}(t)$ in (13.75) following a quench with $K_1/K_2 = 4/3$ for initial states of the form $a_{-1}^{p_1}|\Omega\rangle$ for $p_1 = 1, 2, \dots, 12$ (top to bottom). (b) Time evolution of the Loschmidt echo $L_{p_1, \bar{p}_1}(t)/L_{\Omega}(t)$ in (13.84) following the same quench for initial states of the form $a_n^{p_1}\bar{a}_{-1}^{\bar{p}_1}|\Omega\rangle$ for $p_1 = 0, 1, 2, 3, 4$ (top to bottom) and $\bar{p}_1 = 2$. Temporal orthogonality and non-analyticities of the Loschmidt echo at discrete times can only be observed if the initial state mixes right- and left-moving excitations for a given mode n . On the other hand, quantum revivals at integer multiples of $L/2$ happen for any choice of pure initial state.

Once again, using (13.42) and (13.48) to move one \bar{a}_{-n} from the right to the left, we obtain

$$C_{p, \bar{p}} = n\bar{p}A_n C_{p, \bar{p}-1} + B_n \langle \Omega | a_n^{p+1} \bar{a}_n^{\bar{p}} \mathcal{I}_{\nu} \left(\mathcal{I}_{\nu}^{(q)} \right)^{\dagger} \bar{a}_{-n}^{\bar{p}-1} a_{-n}^p | \Omega \rangle \quad (13.78)$$

with $A_n = A_n(t)$ and $B_n = B_n(t)$ given by (13.70). The second term can be simplified by successively moving \bar{a}_n from the left to the right, eventually leading to

$$\begin{aligned} B_n \langle \Omega | a_n^{p+1} \bar{a}_n^{\bar{p}} \mathcal{I}_{\nu} \left(\mathcal{I}_{\nu}^{(q)} \right)^{\dagger} \bar{a}_{-n}^{\bar{p}-1} a_{-n}^p | \Omega \rangle \\ = -|B_n|^2 \sum_{j=0}^{\bar{p}-1} \frac{(\bar{p}-1)!}{(\bar{p}-j-1)!} (nA_n)^j C_{p+1, \bar{p}-1-j}. \end{aligned} \quad (13.79)$$

Plugging into (13.78), we find the following two-variable recursion relation for $C_{p, \bar{p}}$:

$$C_{p, \bar{p}} = n\bar{p}A_n C_{p, \bar{p}-1} - |B_n|^2 \sum_{j=0}^{\bar{p}-1} \frac{(\bar{p}-1)!}{(\bar{p}-j-1)!} (nA_n)^j C_{p+1, \bar{p}-1-j} \quad (13.80)$$

with (initial) conditions $C_{p, 0} = C_p$ and $C_{0, \bar{p}} = C_{\bar{p}}$ given by (13.74). The solution to (13.80) takes the general form

$$\begin{aligned} C_{p, \bar{p}} = & (n^p p!)(n^{\bar{p}} \bar{p}!) \left(\frac{A_n}{1 + |B_n|^2} \right)^{p+\bar{p}} \\ & \times \sum_{j=0}^{\min\{p, \bar{p}\}} \binom{p}{j} \binom{\bar{p}}{j} (-|B_n|^2)^j \langle \Omega | \mathcal{I}_{\nu} \left(\mathcal{I}_{\nu}^{(q)} \right)^{\dagger} | \Omega \rangle. \end{aligned} \quad (13.81)$$

Alternatively, this can be stated in terms of the hypergeometric function ${}_2F_1(a, b; c; z)$ as

$$\begin{aligned} C_{\mathbf{p}, \bar{\mathbf{p}}} &= (n^p p!)(n^{\bar{p}} \bar{p}!) \left(\frac{A_n}{1 + |B_n|^2} \right)^{p+\bar{p}} {}_2F_1(-p, -\bar{p}; 1; -|B_n|^2) \\ &\quad \times \langle \Omega | \mathcal{I}_\nu \left(\mathcal{I}_\nu^{(q)} \right)^\dagger | \Omega \rangle, \end{aligned} \quad (13.82)$$

from which the Loschmidt echo is obtained using (13.66). In conclusion, the final result starting from initial states of the form

$$(1/\sqrt{(n^{p_n} p_n!)(n^{\bar{p}_n} \bar{p}_n!)}) \bar{a}_{-n}^{\bar{p}_n} a_{-n}^{p_n} | \Omega \rangle \quad (13.83)$$

is

$$\begin{aligned} F_{p_n, \bar{p}_n}(t) &= F_\Omega(t) \left(\frac{|A_n(t)|}{1 + |B_n(t)|^2} \right)^{2(p_n + \bar{p}_n)} \\ &\quad \times \left| {}_2F_1(-p_n, -\bar{p}_n; 1; -|B_n(t)|^2) \right|^2 \end{aligned} \quad (13.84)$$

with $A_n(t)$ and $B_n(t)$ in (13.70). Note that this is consistent with (13.75) if $p_n = 0$ or $\bar{p}_n = 0$ since ${}_2F_1(0, b; c; z) = 1 = {}_2F_1(a, 0; c; z)$.

It follows from (13.84) that mixing right- and left-moving excitations in the initial state leads to an additional factor of ${}_2F_1(-p_n, -\bar{p}_n; 1; -|B_n|^2)$, which is a consequence of the repartitioning of the excitations due to the $J\bar{J}$ deformation in H_2 . Note that this hypergeometric function is a polynomial of order $\min\{p_n, \bar{p}_n\}$. Thus, if such a polynomial admits real zeros, the Loschmidt echo might in turn admit exact zeros at particular values of t , leading to non-analytic times in $\log[F(t)]$. In particular, we apply Theorem 2(v) in [269] to conclude that all zeros of ${}_2F_1(-p_n, -\bar{p}_n; 1; y)$ for the variable y are real and negative. On the other hand, in order for the Loschmidt echo to develop an exact zero at finite times, a given zero y_* of ${}_2F_1(-p_n, -\bar{p}_n; 1; y)$ is required to fulfill

$$y_* \in [-4 \cosh^2(\nu) \sinh^2(\nu), 0]. \quad (13.85)$$

In particular, in the limit where $\nu \rightarrow \infty$, all the $\min\{p_n, \bar{p}_n\}$ zeros correspond to different values of t for which the Loschmidt echo is exactly zero. As can be seen on Fig. 13.2(b), the Loschmidt echo is non-analytic in the vicinity of these exact zeros. Thus, we interpret our result for the Loschmidt echo as dynamical quantum phase transitions arising periodically in time. We stress that this phenomena of temporal orthogonality [270] can only be observed for our quench protocol if the initial state mixes right- and left-moving excitations for the same mode n , and can be seen as Lee-Yang-Fisher zeros [245] in the complex Loschmidt amplitude crossing the real time axis whenever the condition in (13.85) is fulfilled.

Finally, we note that the non-normalized return amplitude $C_{\mathbf{p}, \bar{\mathbf{p}}}$ in (13.67) for a general excited state of the form in (13.65) can be obtained as $C_{\mathbf{p}, \bar{\mathbf{p}}} = \prod_n C_{p_n, \bar{p}_n}$. Therefore, we conclude that the Loschmidt echo after a quantum quench starting from a general excited state is

$$F_{\mathbf{p}, \bar{\mathbf{p}}}(t) = F_\Omega(t) \prod_{n=1}^{\infty} \left(\frac{|A_n(t)|}{1 + |B_n(t)|^2} \right)^{2(p_n + \bar{p}_n)} \left| {}_2F_1(-p_n, -\bar{p}_n; 1; -|B_n(t)|^2) \right|^2$$

(13.86)

with $A_n(t)$ and $B_n(t)$ in (13.70). We note that the result would be unchanged by considering excited states in the form of descendant states from other primary states than the ground state. Consequently, (13.86) is the most general result for the Loschmidt echo after an interaction quench starting from any eigenstate of H_1 .

We now turn to the energy density of the system initialized in an arbitrary eigenstate or a thermal state of H_1 and subsequently evolved in time under H_2 . In each case, the initial state is spatially homogeneous and can be denoted by a density matrix $\hat{\rho}$. The corresponding energy density can be written as

$$\begin{aligned}\mathcal{E}_{\hat{\rho}}(x, t) &= \text{Tr} \left[\hat{\rho} e^{iH_2 t} v_1 [T_+(x) + T_-(x)] e^{-iH_2 t} \right] \\ &= \frac{2\pi v_1}{L^2} \sum_{n=-\infty}^{\infty} \text{Tr} \left[\hat{\rho} e^{iH_2 t} \left(L_n e^{2\pi i n x / L} + \bar{L}_n e^{-2\pi i n x / L} \right) e^{-iH_2 t} \right] \\ &\quad - \frac{\pi v_1}{6L^2},\end{aligned}\tag{13.87}$$

where we used (13.16). The basic problem is therefore to study the quenched time evolution of the Virasoro generators L_n and \bar{L}_n . For L_n , and analogously for \bar{L}_n , we can write

$$e^{iH_2 t} L_n e^{-iH_2 t} = \mathcal{U} \mathcal{I}_{\nu}^{(q)} \mathcal{I}_{\nu}^{\dagger} L_n \mathcal{I}_{\nu} \left(\mathcal{I}_{\nu}^{(q)} \right)^{\dagger} \mathcal{U}^{\dagger}\tag{13.88}$$

with

$$\mathcal{U} = q^{-(L_0 + \bar{L}_0)} e^{i[H_2^{(0)} - (v_2/v_1) H_1^{(0)}]t}\tag{13.89}$$

and $q = e^{-2\pi i v_2 t / L}$, where we used $e^{-iH_2 t} = U_F$ and (13.49) for $t_1 = 0$ and $t_2 = t$. Momentarily, neglecting \mathcal{U} , the remaining object $\mathcal{I}_{\nu}^{(q)} \mathcal{I}_{\nu}^{\dagger} L_n \mathcal{I}_{\nu} \left(\mathcal{I}_{\nu}^{(q)} \right)^{\dagger}$ can be computed using (13.42) and the decomposition of L_n into oscillator modes in (13.27). It takes the general form

$$\begin{aligned}\mathcal{I}_{\nu}^{(q)} \mathcal{I}_{\nu}^{\dagger} L_n \mathcal{I}_{\nu} \left(\mathcal{I}_{\nu}^{(q)} \right)^{\dagger} &= \frac{1}{2} \sum_{m=-\infty}^{\infty} \left[C_{aa}^{(n)}(m) a_{n-m} a_m \right. \\ &\quad \left. + C_{\bar{a}\bar{a}}^{(n)}(m) \bar{a}_{-n+m} \bar{a}_{-m} + C_{\bar{a}a}^{(n)}(m) \bar{a}_{-n+m} a_m + C_{a\bar{a}}^{(n)}(m) a_{n-m} \bar{a}_{-m} \right]\end{aligned}\tag{13.90}$$

for certain coefficients $C_{(\cdot)(\cdot)}^{(n)}(m)$, where the last term comes from undoing the Wick ordering using (13.50). One can explicitly show that, when taking the trace in (13.87) with a spatially homogeneous $\hat{\rho}$, that the contributions from $\bar{a}_{-n+m} a_m$ and $a_{n-m} \bar{a}_{-m}$ vanish for all n , while those from $a_{n-m} a_m$ and $\bar{a}_{-n+m} \bar{a}_{-m}$ vanish unless $n = 0$, a fact which \mathcal{U} in (13.89) cannot change. It follows that the only contributions we need to evaluate come from L_0 and \bar{L}_0 and that the energy density is constant in space. More concretely, $\mathcal{E}_{\hat{\rho}}(x, t) = \mathcal{E}_{\hat{\rho}}(t)$ with

$$\mathcal{E}_{\hat{\rho}}(t) = \frac{2\pi v_1}{L^2} \text{Tr} \left[\hat{\rho} \mathcal{U} \mathcal{I}_{\nu}^{(q)} \mathcal{I}_{\nu}^{\dagger} (L_0 + \bar{L}_0) \mathcal{I}_{\nu} \left(\mathcal{I}_{\nu}^{(q)} \right)^{\dagger} \mathcal{U}^{\dagger} \right] - \frac{\pi v_1}{6L^2},\tag{13.91}$$

where the only coefficients in (13.90) we need are

$$\begin{aligned} C_{aa}^{(0)}(m) &= \frac{1}{4} [(1 + q^{-2m})(1 + q^{2m}) + \cosh^2(2\nu)(1 - q^{-2m})(1 - q^{2m})], \\ C_{\bar{a}\bar{a}}^{(0)}(m) &= \frac{1}{4} \sinh^2(2\nu)(1 - q^{-2m})(1 - q^{2m}), \end{aligned} \quad (13.92)$$

which manifestly satisfy $C_{aa}^{(0)}(-m) = C_{aa}^{(0)}(m)$ and $C_{\bar{a}\bar{a}}^{(0)}(-m) = C_{\bar{a}\bar{a}}^{(0)}(m)$.

To proceed, we specialize to different choices of the state $\hat{\rho}$ in which the system is initialized.

Consider the position-independent energy density $\mathcal{E}_\Omega(t) = \mathcal{E}_{\hat{\rho}}(t)$ in (13.91) for $\hat{\rho} = |\Omega\rangle\langle\Omega|$ given by the ground state $|\Omega\rangle$ of the theory with $K = K_1$. In this case, the contributions from \mathcal{U} in (13.89) vanish since $a_0|\Omega\rangle = 0 = \bar{a}_0|\Omega\rangle$ and $L_0|\Omega\rangle = 0 = \bar{L}_0|\Omega\rangle$. It follows that

$$\text{Tr}[\hat{\rho} \mathcal{U} \mathcal{I}_\nu^{(q)} \mathcal{I}_\nu^\dagger L_0 \mathcal{I}_\nu (\mathcal{I}_\nu^{(q)})^\dagger \mathcal{U}^\dagger] = \langle \Omega | \mathcal{I}_\nu^{(q)} \mathcal{I}_\nu^\dagger L_0 \mathcal{I}_\nu (\mathcal{I}_\nu^{(q)})^\dagger | \Omega \rangle = \langle L_0 \rangle_\Omega(t), \quad (13.93)$$

which defines the time-dependent expectation

$$\begin{aligned} \langle L_0 \rangle_\Omega(t) &= \frac{1}{2} \sum_m [C_{aa}^{(0)}(m) \langle \Omega | a_{-m} a_m | \Omega \rangle + C_{\bar{a}\bar{a}}^{(0)}(m) \langle \Omega | \bar{a}_m \bar{a}_{-m} | \Omega \rangle] \\ &= \frac{1}{2} \sum_{m>0} m [C_{aa}^{(0)}(m) + C_{\bar{a}\bar{a}}^{(0)}(m) - 1] \\ &= \frac{1}{2} \sum_{m>0} m [\cosh^2(2\nu) - \sinh^2(2\nu) \cos(4\pi m v_2 t / L) - 1], \end{aligned} \quad (13.94)$$

where we used (13.92) and $q = e^{-2\pi i v_2 t / L}$ in the last step. The corresponding expectation $\langle \bar{L}_0 \rangle_\Omega(t)$ can be shown to be exactly the same.

We stress that the result in (13.94), in general, is not convergent when summing over m and needs to be regularized. The appropriate regularization in this case is provided by the Lerch zeta function, $\zeta(s|v, w)$.¹¹ This function satisfies the required finiteness and periodicity properties and is a natural generalization of the Riemann zeta function $\zeta(s)$ used in the regularization of the Casimir energy of the undeformed TLL theory. Using this function,

$$\begin{aligned} \langle L_0 \rangle_\Omega(t) &= \frac{1}{2} [\cosh^2(2\nu) - 1] \zeta(-1) \\ &\quad - \frac{1}{4} \sinh^2(2\nu) [\zeta(-1|0, 2v_2 t / L) + \zeta(-1|0, -2v_2 t / L)], \end{aligned} \quad (13.95)$$

where $\zeta(-1) = -1/12$ through analytic continuation. Inserting the above into (13.91), it follows that the ground-state energy density after the quantum quench is

$$\mathcal{E}_\Omega(t) = -\frac{\pi v_1}{6L^2} (\cosh^2(2\nu) + 6 \sinh^2(2\nu) [\zeta(-1|0, 2v_2 t / L) + \zeta(-1|0, -2v_2 t / L)]).$$

¹¹ We are grateful to Pierre Vanhove for discussions on this.

(13.96)

At $t = 0$, the function $\zeta(-1|0, \pm 2v_2 t/L)$ reduces to the Riemann zeta function, since $\zeta(-1|0, 0) = \zeta(-1)$. This implies that the energy density at $t = 0$ is the familiar ground-state energy density of a TLL theory:

$$\mathcal{E}_\Omega(0) = -\frac{\pi v_1}{6L^2}. \quad (13.97)$$

We note that the revivals observed in the Loschmidt echo at $t = kL/2v_2$ for $k \in \mathbb{N}$ are also present in the energy density. These lead to discontinuities at these discrete times, as seen in Fig. 13.3(a). Physically, the discontinuity in the vicinity of $t = 0$ appear due to the abrupt nature of the interaction quench, while the periodic revivals occur due to the integrability of the system.

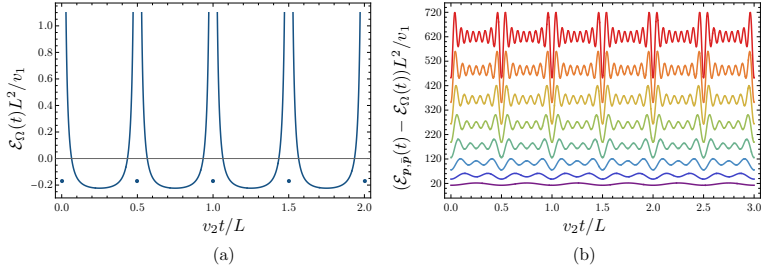


Figure 13.3: (a) Time evolution of the ground-state energy density $\mathcal{E}_\Omega(t)$ in (13.96) following a quench with $K_1/K_2 = 4/3$. We observe discontinuities in the evolution at $v_2 t/L = k/2$, $k \in \mathbb{N}$, where the energy density goes back to its equilibrium value. (b) Time evolution of the excitation contribution $\mathcal{E}_{\mathbf{p},\bar{\mathbf{p}}}(t) - \mathcal{E}_\Omega(t)$ given by (13.101) following the same quench for initial states of the form $a_{-m}\bar{a}_{-m}|\Omega\rangle$, $m = 1, \dots, 8$ (bottom to top).

Consider now instead the system initialized in the state $\hat{\rho} = |\Psi_{\mathbf{p},\bar{\mathbf{p}}}\rangle\langle\Psi_{\mathbf{p},\bar{\mathbf{p}}}|$ with $|\Psi_{\mathbf{p},\bar{\mathbf{p}}}\rangle$ of the form in (13.65). As for the computation of the ground-state energy density, the contributions from \mathcal{U} and \mathcal{U}^\dagger given by (13.89) can be shown to cancel each other. Thus, similar to before,

$$\begin{aligned} \text{Tr}\left[\hat{\rho} \mathcal{U} \mathcal{I}_\nu^{(q)} \mathcal{I}_\nu^\dagger L_0 \mathcal{I}_\nu \left(\mathcal{I}_\nu^{(q)}\right)^\dagger \mathcal{U}^\dagger\right] &= \langle \Psi_{\mathbf{p},\bar{\mathbf{p}}} | \mathcal{I}_\nu^{(q)} \mathcal{I}_\nu^\dagger L_0 \mathcal{I}_\nu \left(\mathcal{I}_\nu^{(q)}\right)^\dagger | \Psi_{\mathbf{p},\bar{\mathbf{p}}}\rangle \\ &= \langle L_0 \rangle_{\mathbf{p},\bar{\mathbf{p}}}(t) \end{aligned} \quad (13.98)$$

with

$$\begin{aligned} \langle L_0 \rangle_{\mathbf{p},\bar{\mathbf{p}}}(t) &= \frac{1}{2} \sum_{m>0} \left[C_{aa}^{(0)}(m)(2p_m + 1)m + C_{\bar{a}\bar{a}}^{(0)}(m)(2\bar{p}_m + 1)m - m \right] \\ &= \langle L_0 \rangle_\Omega(t) + \sum_{m>0} m \left[C_{aa}^{(0)}(m)p_m + C_{\bar{a}\bar{a}}^{(0)}(m)\bar{p}_m \right]. \end{aligned} \quad (13.99)$$

In the second step, we used $\langle \Omega | a_m^{p_n} a_{-n} a_n a_{-n}^{p_n} | \Omega \rangle = n p_n (n^{p_n} p_n!)$ for $n > 0$ to show that

$$\begin{aligned} \langle \Psi_{\mathbf{p},\bar{\mathbf{p}}} | a_{-m} a_m | \Psi_{\mathbf{p},\bar{\mathbf{p}}}\rangle &= m p_m, & \langle \Psi_{\mathbf{p},\bar{\mathbf{p}}} | a_m a_{-m} | \Psi_{\mathbf{p},\bar{\mathbf{p}}}\rangle &= m(p_m + 1), \\ \langle \Psi_{\mathbf{p},\bar{\mathbf{p}}} | \bar{a}_m \bar{a}_{-m} | \Psi_{\mathbf{p},\bar{\mathbf{p}}}\rangle &= m(\bar{p}_m + 1), & \langle \Psi_{\mathbf{p},\bar{\mathbf{p}}} | \bar{a}_{-m} \bar{a}_m | \Psi_{\mathbf{p},\bar{\mathbf{p}}}\rangle &= m\bar{p}_m \end{aligned}$$

$$(13.100)$$

for all $m \in \mathbb{Z}^+$, as well as the symmetry properties of the coefficients in (13.92). The first term in (13.99) is the ground-state contribution in (13.95), while the second term is the additional contribution depending on the occupation numbers of the excited initial state in (13.65). For the corresponding expectation $\langle \bar{L}_0 \rangle_{\mathbf{p}, \bar{\mathbf{p}}}(t)$ one simply needs to swap the roles of C_{aa} and $C_{\bar{a}\bar{a}}$.

It follows by inserting the above into (13.91) that the position-independent energy density $\mathcal{E}_{\mathbf{p}, \bar{\mathbf{p}}}(t) = \mathcal{E}_{\hat{\rho}}(t)$ for $\hat{\rho} = |\Psi_{\mathbf{p}, \bar{\mathbf{p}}}\rangle \langle \Psi_{\mathbf{p}, \bar{\mathbf{p}}}|$ given by (13.65) is

$$\begin{aligned} \mathcal{E}_{\mathbf{p}, \bar{\mathbf{p}}}(t) &= \mathcal{E}_\Omega(t) + \frac{2\pi v_1}{L^2} \sum_{m>0} \left[C_{aa}^{(0)}(m) + C_{\bar{a}\bar{a}}^{(0)}(m) \right] m(p_m + \bar{p}_m) \\ &= \mathcal{E}_\Omega(t) + \frac{2\pi v_1}{L^2} \sum_{m>0} [\cosh^2(2\nu) - \sinh^2(2\nu) \cos(4\pi mv_2 t/L)] \\ &\quad \times m(p_m + \bar{p}_m) \end{aligned} \quad (13.101)$$

with $\mathcal{E}_\Omega(t)$ in (13.96), where we used (13.92) and $q = e^{-2\pi i v_2 t/L}$. We plot the time evolution of the excitation contribution $\mathcal{E}_{\mathbf{p}, \bar{\mathbf{p}}}(t) - \mathcal{E}_\Omega(t)$ in Fig. 13.3(b). The energy density still oscillates in time with period $L/2v_2$ and reaches its minimum at the energy density of the given level $\sum_{m>0} m(p_m + \bar{p}_m)$. In contrast to the Loschmidt echo, the time evolution of the energy density does not crucially depend on whether or not the initial state mixes right- and left-moving excitations. As a remark, note that we only considered initial states that are descendants of the ground state $|\Omega\rangle$. Non-zero contributions from the zero modes appear if one considers initial states that are descendants of other primary states than the ground state. These are, however, constant shifts of the energy density corresponding to the conformal dimensions of the primary states and are sub-leading in the system size.

Lastly, we study the position-independent energy density $\mathcal{E}_\beta(t) = \mathcal{E}_{\hat{\rho}}(t)$ for an initial thermal state given by $\hat{\rho} = Z_1^{-1} e^{-\beta H_1}$, where $Z_1 = \text{Tr}(e^{-\beta H_1})$ is the partition function of the undeformed theory with $K = K_1$. To compute $\mathcal{E}_\beta(t)$, it follows from (13.90) and (13.91) (and the discussion between them) that we need to evaluate

$$\begin{aligned} &\text{Tr} \left[\hat{\rho} \mathcal{U} \mathcal{I}_\nu^{(q)} \mathcal{I}_\nu^\dagger L_0 \mathcal{I}_\nu \left(\mathcal{I}_\nu^{(q)} \right)^\dagger \mathcal{U}^\dagger \right] \\ &= \frac{1}{2} \sum_m \left(C_{aa}^{(0)}(m) \frac{\text{Tr}[e^{-\beta H_1} a_{-m} a_m]}{\text{Tr}[e^{-\beta H_1}]} + C_{\bar{a}\bar{a}}^{(0)}(m) \frac{\text{Tr}[e^{-\beta H_1} \bar{a}_m \bar{a}_{-m}]}{\text{Tr}[e^{-\beta H_1}]} \right) \end{aligned} \quad (13.102)$$

together with the corresponding expectation for \bar{L}_0 . In the second line, we used that \mathcal{U} and \mathcal{U}^\dagger given by (13.89) cancel due to cyclicity of the trace. The remaining traces appearing in (13.102) are thermal expectation values of bosonic occupation numbers and can be calculated using the following manipulation for the oscillator modes ($m \neq 0$):

$$\begin{aligned} \text{Tr} \left[a_{-m} a_m z^{L_0 + \bar{L}_0} \right] &= z^m \text{Tr} \left[a_{-m} z^{L_0 + \bar{L}_0} a_m \right] = z^m \text{Tr}[a_m a_{-m} z^{L_0 + \bar{L}_0}] \\ &= mz^m \text{Tr} \left[z^{L_0 + \bar{L}_0} \right] + z^m \text{Tr} \left[a_{-m} a_m z^{L_0 + \bar{L}_0} \right]. \end{aligned} \quad (13.103)$$

Setting $z = e^{-2\pi v_1 \beta / L}$ in the above, we obtain

$$\frac{\text{Tr} [e^{-\beta H_1} a_{-m} a_m]}{\text{Tr} [e^{-\beta H_1}]} = \frac{m}{e^{2\pi m v_1 \beta / L} - 1} = \langle a_{-m} a_m \rangle_{v_1 \beta / L} \quad (13.104)$$

for $m \neq 0$, which reproduces the expected Bose-Einstein occupation number $\langle a_{-m} a_m \rangle_{v_1 \beta / L}$. The same result is true for $\langle \bar{a}_m \bar{a}_{-m} \rangle_{v_1 \beta / L}$. The corresponding time-dependent expectation of L_0 can therefore be expressed as

$$\langle L_0 \rangle_{v_1 \beta / L}(t) = \text{Tr} \left[\hat{\rho} \mathcal{U} \mathcal{I}_\nu^{(q)} \mathcal{I}_\nu^\dagger L_0 \mathcal{I}_\nu \left(\mathcal{I}_\nu^{(q)} \right)^\dagger \mathcal{U}^\dagger \right] = \langle L_0^{(0)} \rangle_{v_1 \beta / L} + \langle L_0^{(\text{osc})} \rangle_{v_1 \beta / L}, \quad (13.105)$$

where $\langle L_0^{(0)} \rangle_{v_1 \beta / L}$ and $\langle L_0^{(\text{osc})} \rangle_{v_1 \beta / L}(t)$ are the contributions to the expectation value from the zero- and oscillator-mode parts of L_0 , respectively. The zero-mode part is constant in time and sub-leading in the system size L , and thus not relevant to the post-quench dynamical properties. However, we present it here for completeness:

$$\begin{aligned} \langle L_0^{(0)} \rangle_{v_1 \beta / L} &= \frac{1}{4\Theta(v_1 \beta / L)} \sum_{n, w \in \mathbb{Z}} \left(\frac{n^2}{2K_1} + 2w^2 K_1 \right) \\ &\times \exp \left[-\pi \frac{v_1 \beta}{L} \left(\frac{n^2}{2K_1} + 2w^2 K_1 \right) \right] = -\frac{L}{4\pi v_1} \frac{\partial \ln \Theta(v_1 \beta / L)}{\partial \beta}, \end{aligned} \quad (13.106)$$

where Θ is the Siegel theta function [cf. (13.177)]. On the other hand, the oscillator part depends non-trivially on time:

$$\langle L_0^{(\text{osc})} \rangle_{v_1 \beta / L}(t) = \frac{1}{2} \sum_{m \neq 0} \left[C_{aa}^{(0)}(m) \langle a_{-m} a_m \rangle_{v_1 \beta / L} + C_{\bar{a}\bar{a}}^{(0)}(m) \langle \bar{a}_m \bar{a}_{-m} \rangle_{v_1 \beta / L} \right] \quad (13.107)$$

with $C_{aa}^{(0)}(m)$ and $C_{\bar{a}\bar{a}}^{(0)}(m)$ in (13.92) and $q = e^{-2\pi i v_2 t / L}$. From (13.50), we have $\langle :a_{-m} a_m: \rangle_{v_1 \beta / L} = \langle a_{-m} a_m \rangle_{v_1 \beta / L} + m\theta(-m)$, where

$$\langle :a_{-m} a_m: \rangle_{v_1 \beta / L} = \frac{|m|}{e^{2\pi|m|v_1 \beta / L} - 1}, \quad (13.108)$$

which implies

$$\langle L_0^{(\text{osc})} \rangle_{v_1 \beta / L}(t) = \langle L_0 \rangle_\Omega(t) + \sum_{m>0} \frac{m [\cosh^2(2\nu) - \sinh^2(2\nu) \cos(4\pi m v_2 t / L)]}{e^{2\pi m v_1 \beta / L} - 1}, \quad (13.109)$$

where the first term $\langle L_0 \rangle_\Omega(t)$ is given in (13.94). By inserting the above together with the analogous expressions for $\langle \bar{L}_0^{(0)} \rangle_{v_1 \beta / L}$ into (13.91), we obtain the final result:

$$\begin{aligned} \mathcal{E}_\beta(t) &= \mathcal{E}_\Omega(t) - \frac{1}{L} \frac{\partial \ln \Theta(v_1 \beta / L)}{\partial \beta} \\ &+ \frac{4\pi v_1}{L^2} \sum_{m>0} \frac{m [\cosh^2(2\nu) - \sinh^2(2\nu) \cos(4\pi m v_2 t / L)]}{e^{2\pi m v_1 \beta / L} - 1} \end{aligned} \quad (13.110)$$

with $\mathcal{E}_\Omega(t)$ in (13.96).

As a consistency check, the equilibrium expectation value can be obtained from (13.106) and (13.109) by setting $t = 0$, yielding

$$\langle L_0 \rangle_{v_1\beta/L}(0) = -\frac{L}{4\pi v_1} \frac{\partial \ln \Theta(v_1\beta/L)}{\partial \beta} + \sum_{m>0} \frac{m}{e^{2\pi m v_1 \beta/L} - 1}, \quad (13.111)$$

which is consistent with $\langle L_0 \rangle_{v_1\beta/L}$ obtained from (13.27) using (13.108).¹² The oscillator part can be expressed using a quasimodular form $E_2(\tau)$ known as the Eisenstein series of weight 2:

$$\langle L_0^{(\text{osc})} \rangle_{v_1\beta/L}(0) = \sum_{m>0} \frac{m}{e^{2\pi m v_1 \beta/L} - 1} = \sum_{m>0} \frac{mz^m}{1-z^m} = -\frac{E_2(\tau)}{24} + \frac{1}{24}, \quad (13.112)$$

where $z = e^{2\pi i \tau}$ and $\tau = iv_1\beta/L$. The S-modular transformation

$$E_2(\tau) = (-1/\tau)^2 E_2(-1/\tau) - 6/\pi i \tau \quad (13.113)$$

can be used to extract the asymptotic behavior of (13.112) for $L/v_1\beta \gg 1$:

$$E_2(iv_1\beta/L) \approx -\frac{L^2}{v_1^2 \beta^2} + \frac{6L}{\pi v_1 \beta} \approx -\frac{L^2}{v_1^2 \beta^2}, \quad (13.114)$$

which yields

$$\langle L_0^{(\text{osc})} \rangle_{v_1\beta/L} \approx \frac{L^2}{24v_1^2 \beta^2}. \quad (13.115)$$

This gives the expected equilibrium energy density in the thermodynamic limit $L \rightarrow \infty$. Indeed, by inserting the above into (13.91), it follows that

$$\lim_{t \rightarrow 0} \lim_{L \rightarrow \infty} \mathcal{E}_\beta(t) = \frac{\pi}{6v_1\beta^2}, \quad (13.116)$$

which is exact in the thermodynamic limit.

The evolution of the energy density from the thermal state can be evaluated analytically in the thermodynamic limit by replacing the sums over m in (13.109) by integrals with respect to the dimensionless variable $\xi = 2\pi m v_1 \beta/L$. The integrals can then be performed by using the following identities:

$$\int_0^\infty d\xi \frac{\xi}{e^\xi - 1} = \frac{\pi^2}{6}, \quad \int_0^\infty d\xi \frac{\xi \cos(w\xi)}{e^\xi - 1} = \frac{1}{2w^2} - \frac{\pi^2}{2 \sinh^2(\pi w)}. \quad (13.117)$$

In our case, $w = 2v_2 t/v_1\beta$. We conclude that

$$\begin{aligned} \langle L_0^{(\text{osc})} \rangle_{v_1\beta/L}(t) - \langle L_0 \rangle_\Omega(t) &\approx \frac{L^2 \cosh^2(2\nu)}{24v_1^2 \beta^2} - \frac{L^2 \sinh^2(2\nu)}{8v_1^2 \beta^2} \\ &\times \left[\left(\frac{v_1\beta}{2\pi v_2 t} \right)^2 - \operatorname{csch}^2 \left(\frac{2\pi v_2 t}{v_1\beta} \right) \right] \end{aligned} \quad (13.118)$$

¹² This is also consistent with the relation between the torus one-point function of the holomorphic stress tensor and the partition function: $\langle L_0 - c/24 \rangle_\tau = (2\pi i)^{-1} \partial_\tau \log Z(\tau, \bar{\tau})$. For our case $\tau = iv_1\beta/L$ and the partition function is given in (13.177).

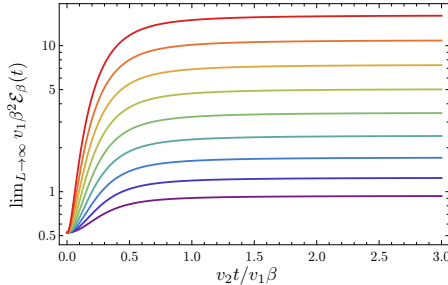


Figure 13.4: Time evolution of the thermal-state energy density $\lim_{L \rightarrow \infty} \mathcal{E}_\beta(t)$ in (13.119) in the thermodynamic limit following a quench with $K_1/K_2 = e^{2\nu}$, $\nu = 0.4, 0.5, \dots, 1.2$ (from bottom to top). We observe that the TLL equilibrates to different energies depending on ν according to (13.120) with the effective temperature β_{eff}^{-1} in (13.121).

in the regime $L/v_1\beta \gg \infty$ with the same result for $\langle \bar{L}_0^{(\text{osc})} \rangle_{v_1\beta/L}(t)$. In the thermodynamic limit, at which point the results become exact, it finally follows from (13.91) that the energy density for the quenched thermal state is

$$\lim_{L \rightarrow \infty} \mathcal{E}_\beta(t) = \frac{\pi \cosh^2(2\nu)}{6v_1\beta^2} - \frac{\pi \sinh^2(2\nu)}{2v_1\beta^2} \left[\left(\frac{v_1\beta}{2\pi v_2 t} \right)^2 - \operatorname{csch}^2 \left(\frac{2\pi v_2 t}{v_1\beta} \right) \right], \quad (13.119)$$

where we used that $\langle L_0 \rangle_\Omega(t)$, $\langle \bar{L}_0 \rangle_\Omega(t)$, and the zero modes give sub-leading contributions in the system size L . In particular, the late-time asymptotic behavior in this regime is¹³

$$\lim_{t \rightarrow \infty} \lim_{L \rightarrow \infty} \mathcal{E}_\beta(t) = \frac{\pi}{6v_1\beta_{\text{eff}}^2}, \quad (13.120)$$

where we defined the effective temperature

$$\beta_{\text{eff}}^{-1} = \beta^{-1} \cosh(2\nu) = \beta^{-1} \frac{K_1/K_2 + K_2/K_1}{2}. \quad (13.121)$$

We thus observe, in the thermodynamic limit, an equilibration of the original TLL following the quench from an initial temperature β^{-1} to an emergent temperature: The time evolution of the energy-density expectation reaches that of a steady state at an effective temperature β_{eff}^{-1} given by (13.121), as seen in Fig. 13.4. We note that a similar large-scale equilibration to an effective temperature was observed in quenched TLLs in [271] for a different type of quenching protocol and through different physical observables.

13.5 FLOQUET DRIVE

In this section, we study a two-step driven TLL whose Hamiltonian switches periodically between H_1 and H_2 with periods t_1 and t_2 . We recall that the two

¹³ Note that (13.116) is also recovered from (13.119) using that $\operatorname{csch}(\xi) = \xi^{-1} - \xi/6 + O(\xi^3)$ for small ξ .

Hamiltonians H_1 and H_2 are particular combinations of the $\mathfrak{su}(1, 1)$ generators $K_0^{(n)}$ and $K_{\pm}^{(n)}$ in (13.34) for each individual mode $n > 0$. It follows that the Floquet operator $U_F^{(n)}$, for the n th mode can be expressed as $U_F^{(n)} = e^{-iH_F^{(n)}(t_1+t_2)}$ using a Floquet Hamiltonian $H_F^{(n)}$ that is also a combination of the $\mathfrak{su}(1, 1)$ generators:

$$H_F^{(n)} = \frac{i}{t_1 + t_2} C_F^{(n)}, \quad C_F^{(n)} = c_0^{(n)} K_0^{(n)} + c_-^{(n)} K_-^{(n)} + c_+^{(n)} K_+^{(n)} \quad (13.122)$$

for certain coefficients $c_0^{(n)}$ and $c_{\pm}^{(n)}$. Our driven TLL thus corresponds to an infinite sequence of uncoupled discrete-time quantum parametric oscillators labeled by n . Consequently, as for harmonic oscillators with continuously and periodically driven frequency, see, e.g., [272, 273], famously leading to the Mathieu equation, similar algebraic stability arguments can be employed here. Namely, for each mode, a characterization into stable or unstable can be deduced from the different classes of orbits of $\mathfrak{su}(1, 1)$, see Table 13.1. These are delineated by the value $\mathcal{K}(H_F^{(n)}, H_F^{(n)}) = -2(t_1 + t_2)^{-2} \left[(c_0^{(n)})^2 - 4c_+^{(n)}c_-^{(n)} \right]$ of the Cartan-Killing form $\mathcal{K}(\cdot, \cdot)$ in (13.36), or equivalently by the squared trace $\sigma_n = (\text{Tr}[U_F^{(n)}])^2$, which are related through

$$\sigma_n = 4 \cosh^2 \left(\sqrt{\mathcal{K}(C_F^{(n)}, C_F^{(n)})/8} \right) = 4 \cos^2 \left((t_1 + t_2) \sqrt{\mathcal{K}(H_F^{(n)}, H_F^{(n)})/8} \right). \quad (13.123)$$

Using the 2×2 -matrix representation of the $\mathfrak{su}(1, 1)$ generators in (13.37), the coefficients in (13.122) can be computed, which inserted into (13.123) yields exactly

$$\sigma_n = \left(\frac{(q_1^n + q_1^{-n})(q_2^n + q_2^{-n}) + (q_1^n - q_1^{-n})(q_2^n - q_2^{-n}) \cosh(2\nu)}{2} \right)^2, \quad (13.124)$$

with $q_{1,2}$ defined as $e^{-2\pi i \tau_{1,2}}$. This can be rewritten as

$$\sigma_n = 4\omega_n^2, \quad \omega_n = \cos(2\pi n \tau_1) \cos(2\pi n \tau_2) - \sin(2\pi n \tau_1) \sin(2\pi n \tau_2) \cosh(2\nu), \quad (13.125)$$

which shows the explicit dependence on the dimensionless times $(\tau_1, \tau_2) = (v_1 t_1 / L, v_2 t_2 / L)$ and the Zamolodchikov distance ν . Note that ω_n and σ_n are manifestly invariant under change of sign in n .

Dynamical phase diagrams in the parameter space (τ_1, τ_2) can be straightforwardly drawn using (13.125) for a given mode n and Zamolodchikov distance ν , computed for a pair of Luttinger parameters (K_1, K_2) or radii (R_1, R_2) through (13.32). Note that the phase diagram for any mode $n \in \mathbb{Z}^+$ is simply a rescaling of the phase diagram of that for $n = 1$, obtained by replacing L by L/n , with each of its individual unstable regions having the shape of a leaf that shrinks to a line as $\nu \rightarrow 0$ and grows to approximate a square as $|\nu| \rightarrow \infty$, as illustrated in Fig. 13.5. The total phase diagram is obtained by overlaying the phase diagrams of each individual mode, with the unstable phase being the union of the unstable regions, see Fig. 13.6. Any remaining stable phase

Class	$\mathcal{K}(H_F^{(n)}, H_F^{(n)})$	σ_n	Stability characterization
Elliptic	> 0	< 4	Stable phase
Parabolic	$= 0$	$= 4$	Phase boundary
Hyperbolic	< 0	> 4	Unstable phase

Table 13.1: Classes for a given mode $n \in \mathbb{Z}^+$ depending on the value $\mathcal{K}(H_F^{(n)}, H_F^{(n)})$ of the Cartan-Killing form or the squared trace σ_n in (13.123) along with the corresponding stability characterization.

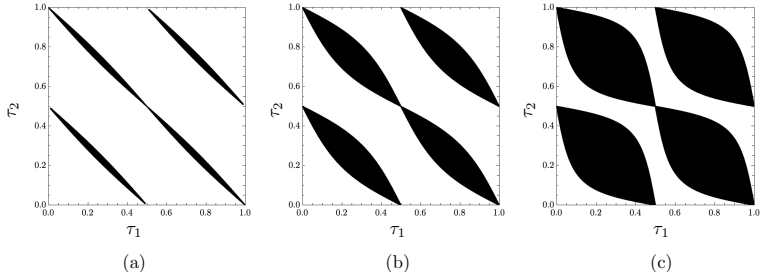


Figure 13.5: Dynamical phase diagrams in (τ_1, τ_2) space for a single mode $n = 1$ and (a) $K_1/K_2 = 16/15$, (b) $K_1/K_2 = 7/5$, and (c) $K_1/K_2 = 7/3$.

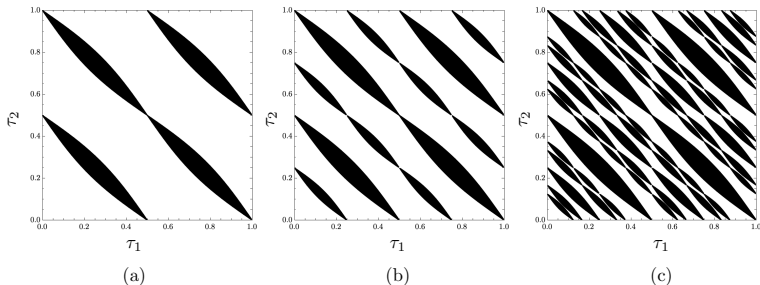


Figure 13.6: Dynamical phase diagrams in (τ_1, τ_2) space for $K_1/K_2 = 1.2$ for a finite number of modes. The unstable regions are colored black. (a) Single mode $n = 1$. (b) Two modes $n = 1, 2$. (c) Four modes $n = 1, \dots, 4$. Note that the lines $(k/2, \tau_2)$ and $(\tau_1, k/2)$, $k \in \mathbb{N}$ remain critical or stable even when an arbitrary number of modes are included. The phase diagrams are plotted for $(\tau_1, \tau_2) \in [0, 1] \times [0, 1]$ since they repeat themselves outside this domain.

thus depends crucially on ν and the number of modes included. In particular, imposing a (physical) cutoff on the total number of allowed modes would ensure that an extended stable phase remains.

Below we investigate the physical consequences of the dynamical phases in Table 13.1 on certain physical quantities, specifically the Loschmidt echo and the particle and energy densities. We also identify natural order parameters and study their critical behavior near the phase boundary when approaching from the stable or the unstable phase. In a nutshell, we will show that the evolution of these physical quantities in stroboscopic time $M(t_1 + t_2)$ enters through factors of the form $(\lambda_n^\pm)^M$ with

$$\lambda_n^\pm = \omega_n \pm \text{sgn}(\omega_n) \sqrt{\omega_n^2 - 1} = \text{sgn}(\omega_n) \frac{\sqrt{\sigma_n} \pm \sqrt{\sigma_n - 4}}{2}, \quad (13.126)$$

which depends on (τ_1, τ_2) and ν through σ_n and ω_n in (13.125). The factors λ_n^\pm can be interpreted as eigenvalues of a 2×2 -matrix representation of our Floquet drive and have distinct behaviors for the following three cases:¹⁴

1. If $\sigma_n < 4$, then $\lambda_n^\pm = \text{sgn}(\omega_n) e^{\pm i\phi}$ for $\phi = \arctan(\sqrt{(4 - \sigma_n)/\sigma_n})$.
2. If $\sigma_n = 4$, then $\lambda_n^\pm = \text{sgn}(\omega_n)$.
3. If $\sigma_n > 4$, then $|\lambda_n^+| > 1 > |\lambda_n^-| > 0$.

In other words, λ_n^\pm lie on segments of the unit circle in the complex plane when $0 < \sigma_n < 4$, starting at $\pm i \text{sgn}(\omega_n)$ for $\sigma_n = 0^+$ and moving toward $\text{sgn}(\omega_n)$ as σ_n grows toward 4, coinciding at $\text{sgn}(\omega_n)$ exactly when $\sigma_n = 4$, and then moving on the real line in $\pm \text{sgn}(\omega_n)$ directions as σ_n grows beyond 4, see Fig. 13.7. Given that the stroboscopic time evolution enters as $(\lambda_n^\pm)^M$, this agrees with our stability discussion for individual modes based on classes of $\mathfrak{su}(1, 1)$, see Table 13.1. In particular, if $\sigma_n > 4$, there are parametric instabilities since $|\lambda_n^+|^M$ diverges as M increases, while if $\sigma_n < 4$, there are oscillations of the form $e^{\pm i M \phi}$ with M .

The above stability analysis is analogous to the well-known discussion of the quantum parametric oscillator, see, e.g., [273]. Indeed, while our periodic drive is step-like and not continuous, we can identify the corresponding quantities to construct phase diagrams of the same form as in [274] obtained from the Mathieu equation for a continuously driven TLL, see Fig. 13.8. In particular, the Mathieu characteristic exponent is identified with $\phi = \arctan(\sqrt{(4 - \sigma_n)/\sigma_n})$ introduced above, see Fig. 13.8(b), and the amplitude of the drive with the ratio of Luttinger parameters, see Fig. 13.8(a).

The first quantity we study is the Loschmidt echo for the system initialized in the ground state or any excited state of H_1 . We recall that the Floquet operator in (13.44) can be written as in (13.49). Similarly, it will also be convenient to express the M -cycle Floquet operator as a concatenation of several q -modified operators:

$$U_F^M = q_1^{L_0 + \bar{L}_0} \left[\prod_{j=0}^{M-1} \mathcal{I}_\nu^{(q_1^j q_2^j)} \left(\mathcal{I}_\nu^{(q_1^j q_2^{j+1})} \right)^\dagger \right] (q_1^{M-1} q_2^M)^{L_0 + \bar{L}_0} \times e^{-iM[H_2^{(0)} - (v_2/v_1)H_1^{(0)}]t_2} \quad (13.127)$$

¹⁴ In the last case, we use that $\partial \lambda_n^\pm / \partial \sigma_n < 0$.

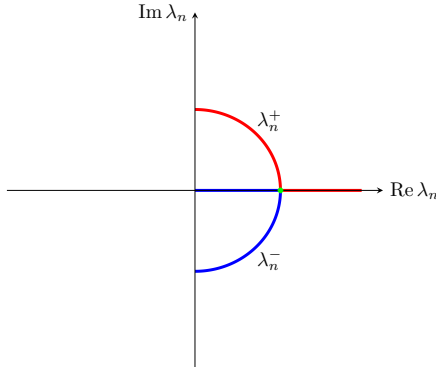


Figure 13.7: Eigenvalues λ_n^+ (red curve) and λ_n^- (blue curve) in (13.126) as functions of σ_n for the case $\text{sgn}(\omega_n) > 0$. If $\sigma_n < (>) 4$, the eigenvalues lie on the unit circle (real line) and the n th-mode contribution is stable (unstable). The green dot corresponds to $\sigma_n = 4$, i.e., the value where λ_n^\pm coincide.

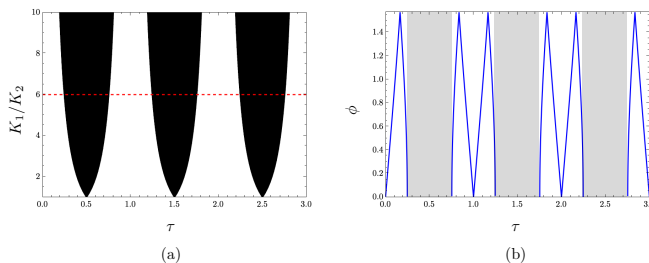


Figure 13.8: (a) Phase diagram for $n = 1$ when $\tau_1 = \tau_2$ parametrized in terms of $\tau = \tau_1 + \tau_2$ and K_1/K_2 , interpreted as the period and the amplitude of the drive, respectively. The unstable regions are colored black. (b) Plot of $\phi = \arctan\left(\sqrt{(4 - \sigma_1)/\sigma_1}\right)$, interpreted as the Mathieu characteristic exponent, using σ_1 in (13.125) as a function of $\tau = \tau_1/2 = \tau_2/2$ along the red dashed line ($K_1/K_2 = 6$) in (a). The blue curves give the plotted values when ϕ is real, and the shaded areas correspond to the unstable regions.

for $M = 1, 2, \dots$, generalizing (13.49). We recall that the overall phase $e^{-iME_2^0 t_2}$ will be of no consequence to our computations.

We begin by computing the Loschmidt echo $L_\Omega(M[t_1 + t_2]) = |\langle \Omega | U_F^M | \Omega \rangle|^2$ for the ground state $|\Omega\rangle$ of H_1 after M cycles. Using (13.127) and the fact that L_0 , \bar{L}_0 , and $H_{1,2}^{(0)}$ annihilate $|\Omega\rangle$, we have

$$L_\Omega(M[t_1 + t_2]) = \left| \langle \Omega | \prod_{j=0}^{M-1} \mathcal{I}_\nu^{(q_1^j q_2^j)} \left(\mathcal{I}_\nu^{(q_1^j q_2^{j+1})} \right)^\dagger | \Omega \rangle \right|^2. \quad (13.128)$$

As in the previous section, our strategy to compute the product of the q -modified operators $\mathcal{I}_\nu^{(q)}$ is to first decompose them in terms of exponentials of the $\mathfrak{su}(1,1)$ generators in (13.34):

$$\begin{aligned} & \langle \Omega | \prod_{j=0}^{M-1} \mathcal{I}_\nu^{(q_1^j q_2^j)} \left(\mathcal{I}_\nu^{(q_1^j q_2^{j+1})} \right)^\dagger | \Omega \rangle \\ &= \prod_{n>0} \langle \Omega | \exp \left(\xi_+^{(n)} K_+^{(n)} \right) \exp \left(\xi_0^{(n)} K_0^{(n)} \right) \exp \left(\xi_-^{(n)} K_-^{(n)} \right) | \Omega \rangle \\ &= \prod_{n>0} \exp \left(\xi_0^{(n)} / 2 \right), \end{aligned} \quad (13.129)$$

repeating the same steps as for the quench. Again, one efficient way to find the coefficients $\xi_0^{(n)}$ and $\xi_\pm^{(n)}$ is to use the 2×2 -matrix representation of the $\mathfrak{su}(1,1)$ generators in (13.37). In this representation, using (13.41) and (13.46) with $(\mathcal{I}_\nu^{(q)})^\dagger = \mathcal{I}_\nu^{(q)}$ as a definition, we find that the j th factor in the product of q -modified operators has the form

$$\mathcal{I}_\nu^{(q_1^j q_2^j)} \left(\mathcal{I}_\nu^{(q_1^j q_2^{j+1})} \right)^\dagger \Big|_{2 \times 2}^{(n)} = \begin{pmatrix} a & b \\ b^* & a^* \end{pmatrix}, \quad (13.130)$$

with

$$a = \cosh^2(\nu) - \sinh^2(\nu) q_2^{2n}, \quad b = \frac{1}{2} \sinh(2\nu) \left(1 - q_2^{-2n} \right) q_2^{-2jn} q_1^{-2jn}, \quad (13.131)$$

for the n th mode. In analogy with (13.57), we have

$$\begin{aligned} & e^{\xi_+^{(n)} K_+^{(n)}} e^{\xi_0^{(n)} K_0^{(n)}} e^{\xi_-^{(n)} K_-^{(n)}} \Big|_{2 \times 2} \\ &= \begin{pmatrix} e^{-\xi_0^{(n)}/2} & \xi_-^{(n)} e^{-\xi_0^{(n)}/2} \\ -\xi_+^{(n)} e^{-\xi_0^{(n)}/2} & e^{-\xi_0^{(n)}/2} - \xi_-^{(n)} \xi_+^{(n)} e^{-\xi_0^{(n)}/2} \end{pmatrix}, \end{aligned} \quad (13.132)$$

meaning that, at a practical level, we only need the $(1,1)$ -component in the 2×2 -matrix representation to determine $\exp(\xi_0^{(n)}/2)$ and thereby evaluate (13.129). Let us denote

$$\prod_{j=0}^{M-1} \mathcal{I}_\nu^{(q_1^j q_2^j)} \left(\mathcal{I}_\nu^{(q_1^j q_2^{j+1})} \right)^\dagger \Big|_{2 \times 2}^{(n)} = \begin{pmatrix} I_{1,1}^{(n,M)} & I_{1,2}^{(n,M)} \\ I_{2,1}^{(n,M)} & I_{2,2}^{(n,M)} \end{pmatrix}, \quad (13.133)$$

which implies, using (13.129) and (13.132),

$$\langle \Omega | \prod_{j=0}^{M-1} \mathcal{I}_\nu^{(q_1^j q_2^j)} \left(\mathcal{I}_\nu^{(q_1^j q_2^{j+1})} \right)^\dagger | \Omega \rangle = \prod_{n>0} \frac{1}{I_{1,1}^{(n,M)}}. \quad (13.134)$$

From (13.130) and (13.133), we obtain the following recursion relation:

$$\begin{pmatrix} I_{1,1}^{(n,M)} & I_{1,2}^{(n,M)} \\ I_{2,1}^{(n,M)} & I_{2,2}^{(n,M)} \end{pmatrix} = \begin{pmatrix} I_{1,1}^{(n,M-1)} & I_{1,2}^{(n,M-1)} \\ I_{2,1}^{(n,M-1)} & I_{2,2}^{(n,M-1)} \end{pmatrix} \begin{pmatrix} a & b' \\ b'^* & a^* \end{pmatrix}, \quad (13.135)$$

with

$$b' = \frac{1}{2} \sinh(2\nu) \left(1 - q_2^{-2n} \right) q_2^{-2(M-1)n} q_1^{-2(M-1)n}. \quad (13.136)$$

This can be solved for $I_{1,1}^{(n,M)}$, see Appendix c. The result is

$$I_{1,1}^{(n,M)} = (q_2^n q_1^n)^M \left| \frac{(1 - \varepsilon_n)(\lambda_n^-)^M + (1 + \varepsilon_n)(\lambda_n^+)^M}{2} \right|^2 \quad (13.137)$$

with λ_n^\pm in (13.126) and

$$\varepsilon_n = - \frac{2[\sin(2\pi n\tau_1)\cos(2\pi n\tau_2) + \cos(2\pi n\tau_1)\sin(2\pi n\tau_2)\cosh(2\nu)]}{\sqrt{4 - \sigma_n^2}} \quad (13.138)$$

using σ_n in (13.125). In conclusion, the Loschmidt echo after M cycles for the ground state is

$$\begin{aligned} L_\Omega(M[t_1 + t_2]) &= \prod_{n>0} L_\Omega^{(n)}(M[t_1 + t_2]), \\ L_\Omega^{(n)}(M[t_1 + t_2]) &= \left| \frac{2}{(1 - \varepsilon_n)(\lambda_n^-)^M + (1 + \varepsilon_n)(\lambda_n^+)^M} \right|^2 \end{aligned} \quad (13.139)$$

with λ_n^\pm in (13.126) and ε_n in (13.138).

We now restrict our analysis to the ground-state Loschmidt echo $L_\Omega^{(n)}(M[t_1 + t_2])$ for a single mode n . Its behavior as a function of the stroboscopic time $M(t_1 + t_2)$ depends crucially on the driving parameters (τ_1, τ_2) and the Zamolodchikov distance ν between H_1 and H_2 due to the different properties of λ_n^\pm in (13.126). Indeed, if $\sigma_n < 4$, we recall that $\lambda_n^\pm = \text{sgn}(\omega_n)e^{\pm i\phi}$ for $\phi \in (0, \pi/2]$, which leads to an overall oscillation with M of the form

$$L_\Omega^{(n)}(M[t_1 + t_2]) = \left| \frac{2}{(1 - \varepsilon_n)e^{-iM\phi} - (1 + \varepsilon_n)e^{iM\phi}} \right|^2. \quad (13.140)$$

On the other hand, if $\sigma_n > 4$, we recall that $|\lambda_n^\pm|$ is larger than one, which implies that $L_\Omega^{(n)}(M[t_1 + t_2])$ decays exponentially,

$$L_\Omega^{(n)}(M[t_1 + t_2]) \sim e^{-\lambda_L M(t_1 + t_2)} \quad (13.141)$$

with the rate

$$\lambda_L = \frac{\log |\lambda_n^+|}{t_1 + t_2}. \quad (13.142)$$

These two distinct dynamical behaviors of the single-mode Loschmidt echo can be observed in Fig. 13.9(a) and compared with the stability characterizations in Table 13.1.

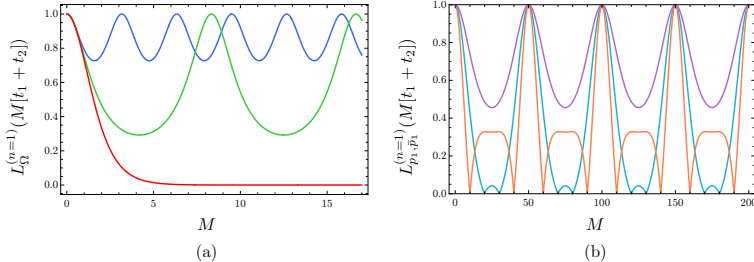


Figure 13.9: (a) Stroboscopic time evolution of the single-mode Loschmidt echo $L_{\Omega}^{(n=1)}(M[t_1 + t_2])$ in (13.139) for the ground state $|\Omega\rangle$ of H_1 in a two-step drive with $K_1/K_2 = 4/3$ and different driving parameters $\tau_1 = \tau_2 = 8/50, 9.8/50, 12/50$ (blue, green red). In the stable phase, the Loschmidt echo displays periodic revivals with a period that depends on the driving parameters. In the unstable phase, the Loschmidt echo decays exponentially to zero. (b) Stroboscopic time evolution of the single-mode Loschmidt echo $L_{p_1, p_2}^{(n=1)}(M[t_1 + t_2])$ in (13.158) for different initial states of the form $a_{-1}^{p_1} \bar{a}_{-1}^{p_2} |\Omega\rangle$ with $p_1 = 0, 1, 3$ (purple, cyan, orange) in a two-step drive with $K_1/K_2 = 4/3$ and driving parameters $(\tau_1, \tau_2) = (0.5, 0.51)$. The periodicity of the Loschmidt echo does not depend on the initial state, but temporal orthogonality can be observed for more general initial states.

We stress that the Loschmidt echo $L_{\Omega}(M[t_1 + t_2])$ is a product over all possible modes n , such that it would generically decay exponentially in time when all modes are taken into account. However, as discussed previously, one usually needs to impose a cutoff on the number of modes in order to connect with physical applications. Depending on the value of such a cutoff and the value of the Zamolodchikov distance, $\nu = \log \sqrt{K_1/K_2}$, some extended regions in the parameter space (τ_1, τ_2) may still be stable, leading to non-trivial phase diagrams with phase transitions between oscillating and exponentially decaying Loschmidt echo.

As a final consideration, we study the behavior of the Loschmidt echo for a single mode when approaching the phase boundary from the stable phase. As can be observed in Fig. 13.9(a), the period T_L of the Loschmidt echo in the stable phase increases as we approach the boundary and can be interpreted as a natural order parameter. We can explicitly write the period as

$$T_L = \frac{\pi(t_1 + t_2)}{\arg(\lambda_n^+)}. \quad (13.143)$$

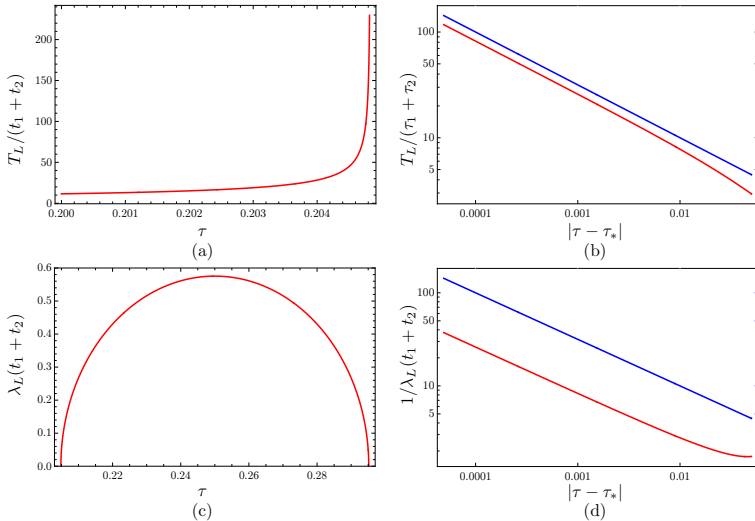


Figure 13.10: Critical properties of the order parameters in a two-step drive with $K_1/K_2 = 4/3$ when approaching the phase boundary from the stable or the unstable phase for a single mode $n = 1$. (a) The period $T_L/(t_1 + t_2)$ as a function of $\tau = \tau_1 = \tau_2$ when approaching the phase boundary at $\tau_* \approx 0.2048$ from the stable phase. (b) Red curve: $T_L/(t_1 + t_2)$ as a function of $|\tau - \tau_*|$. Blue curve: Expected scaling as $|\tau - \tau_*|^{-1/2}$. (c) The rate $(t_1 + t_2)\lambda_L$ as a function of $\tau = \tau_1 = \tau_2$ in the unstable phase. (d) Red curve: $1/\lambda_L(t_1 + t_2)$ as a function of $|\tau - \tau_*|$ when approaching the phase boundary at $\tau_* \approx 0.2048$ from the unstable phase. Blue curve: Expected scaling as $|\tau - \tau_*|^{-1/2}$.

As we approach the phase boundary, say by varying $\tau = \tau_1 = \tau_2$,¹⁵ the period diverges as a power law

$$T_L \sim |\tau - \tau_*|^{-\beta_T}, \quad (13.144)$$

where τ_* lies on the phase boundary and β_T is the critical exponent at the transition, as seen in Fig. 13.10(a). By fitting the critical exponent, we infer that $\beta_T = 1/2$, see Fig. 13.10(b). Alternatively, the phase boundary can be approached from the unstable phase, in which case the natural order parameter is the rate λ_L , which is understood formally as the inverse of T_L by comparing (13.143) and (13.142). Close to the phase boundary, see Fig. 13.10(c), λ_L approaches zero as

$$\lambda_L \sim |\tau - \tau_*|^{\beta_\lambda}, \quad (13.145)$$

with the critical exponent $\beta_\lambda = 1/2$ inferred from Fig. 13.10(d). In conclusion, the rate λ_L and the inverse period $1/T_L$ for the Loschmidt echo are natural order parameters for the stable-to-unstable transition in the respective phases and have the same critical exponent $\beta_T = \beta_\lambda = 1/2$ when approaching the phase boundary from each side. We note that such a critical scaling for the period in the stable phase and for the rate in the unstable phase has been observed in other classes of integrable Floquet systems [124].

We now study the stroboscopic time evolution of the Loschmidt echo for general excited states of the form in (13.65).

First, we consider the state $(1/\sqrt{n^p p!})a_{-n}^p |\Omega\rangle$, as before writing $p = p_n$ to lighten the notation. The Loschmidt echo after M cycles is

$$L_p(M[t_1 + t_2]) = \frac{1}{\mathcal{N}_p^2} \left| \langle \Omega | a_n^p U_F^M a_{-n}^p | \Omega \rangle \right|^2, \quad \mathcal{N}_p = n^p p!. \quad (13.146)$$

Analogous to the quench case, the computation reduces to evaluating

$$C_p^{(M)} = \langle \Omega | a_n^p \prod_{j=0}^{M-1} \mathcal{I}_\nu^{(q_1^j q_2^j)} \left(\mathcal{I}_\nu^{(q_1^j q_2^{j+1})} \right)^\dagger a_{-n}^p | \Omega \rangle. \quad (13.147)$$

To this end, we consider the following generalized rotation relations:

$$\begin{aligned} \mathcal{I}_\nu^{(q_1^j q_2^j)} \left(\mathcal{I}_\nu^{(q_1^j q_2^{j+1})} \right)^\dagger a_{-n} \mathcal{I}_\nu^{(q_1^j q_2^{j+1})} \left(\mathcal{I}_\nu^{(q_1^j q_2^j)} \right)^\dagger &= A_n a_{-n} + (q_1 q_2)^{-2n} B_n \bar{a}_n, \\ \mathcal{I}_\nu^{(q_1^j q_2^j)} \left(\mathcal{I}_\nu^{(q_1^j q_2^{j+1})} \right)^\dagger \bar{a}_n \mathcal{I}_\nu^{(q_1^j q_2^{j+1})} \left(\mathcal{I}_\nu^{(q_1^j q_2^j)} \right)^\dagger &= \overline{A_n} \bar{a}_n + (q_1 q_2)^{2n} \overline{B_n} a_{-n}, \end{aligned} \quad (13.148)$$

with $A_n = A_n(q_2)$, $\overline{A_n} = A_n(\overline{q_2})$, $B_n = B_n(q_2)$, and $\overline{B_n} = B_n(\overline{q_2})$ given by

$$A_n(q_2) = \cosh^2(\nu) - \sinh^2(\nu) q_2^{-2n}, \quad B_n(q_2) = \frac{1}{2} \sinh(2\nu)(1 - q_2^{-2n}). \quad (13.149)$$

¹⁵ Note that τ here should not be confused with a modular parameter, such as the one in (13.112).

Written in matrix form, this amounts to an $\mathfrak{su}(1, 1)$ rotation:

$$\mathsf{T}_j \begin{pmatrix} a_{-n} \\ \bar{a}_n \end{pmatrix} = \begin{pmatrix} A_n & (q_1 q_2)^{-2nj} B_n \\ (q_1 q_2)^{2nj} \bar{B}_n & \bar{A}_n \end{pmatrix} \begin{pmatrix} a_{-n} \\ \bar{a}_n \end{pmatrix}. \quad (13.150)$$

The rotation in the other direction is given by

$$\mathsf{T}_j^{-1} \begin{pmatrix} a_{-n} \\ \bar{a}_n \end{pmatrix} = \begin{pmatrix} \bar{A}_n & -(q_1 q_2)^{-2nj} B_n \\ -(q_1 q_2)^{2nj} \bar{B}_n & A_n \end{pmatrix} \begin{pmatrix} a_{-n} \\ \bar{a}_n \end{pmatrix}. \quad (13.151)$$

For M cycles, we need to apply these rotations M times. The matrices implementing these rotations can be written

$$\prod_{j=M-1}^0 \mathsf{T}_j = \begin{pmatrix} \mathcal{A}_n & \mathcal{B}_n \\ \bar{\mathcal{B}}_n & \bar{\mathcal{A}}_n \end{pmatrix}, \quad \prod_{j=0}^{M-1} \mathsf{T}_j^{-1} = \begin{pmatrix} \bar{\mathcal{A}}_n & -\mathcal{B}_n \\ -\bar{\mathcal{B}}_n & \mathcal{A}_n \end{pmatrix}, \quad (13.152)$$

which define $\mathcal{A}_n = \mathcal{A}_n(M)$ and $\mathcal{B}_n = \mathcal{B}_n(M)$ as functions of M .

It follows from the above that

$$\begin{aligned} C_p^{(M)} &= np \mathcal{A}_n \langle \Omega | a_n^{p-1} \prod_{j=0}^{M-1} \mathcal{I}_\nu^{(q_1^j q_2^j)} \left(\mathcal{I}_\nu^{(q_1^j q_2^{j+1})} \right)^\dagger a_{-n}^{p-1} | \Omega \rangle \\ &\quad + \mathcal{B}_n \langle \Omega | a_n^p \bar{a}_n \prod_{j=0}^{M-1} \mathcal{I}_\nu^{(q_1^j q_2^j)} \left(\mathcal{I}_\nu^{(q_1^j q_2^{j+1})} \right)^\dagger a_{-n}^{p-1} | \Omega \rangle. \end{aligned} \quad (13.153)$$

By moving \bar{a}_n from the left to the right in the second term, we obtain the recursion relation

$$C_p^{(M)} = np \frac{\mathcal{A}_n}{1 + |\mathcal{B}_n|^2} C_{p-1}^{(M)}, \quad C_0^{(M)} = \langle \Omega | \prod_{j=0}^{M-1} \mathcal{I}_\nu^{(q_1^j q_2^j)} \left(\mathcal{I}_\nu^{(q_1^j q_2^{j+1})} \right)^\dagger | \Omega \rangle. \quad (13.154)$$

This has the solution

$$C_p^{(M)} = n^p p! \left(\frac{\mathcal{A}_n}{1 + |\mathcal{B}_n|^2} \right)^p \langle \Omega | \prod_{j=0}^{M-1} \mathcal{I}_\nu^{(q_1^j q_2^j)} \left(\mathcal{I}_\nu^{(q_1^j q_2^{j+1})} \right)^\dagger | \Omega \rangle. \quad (13.155)$$

We conclude that the Loschmidt echo after M cycles for the state

$$(1/\sqrt{n^{p_n} p_n!}) a_{-n}^{p_n} | \Omega \rangle \quad (13.156)$$

is

$$L_{p_n}(M[t_1 + t_2]) = \left(\frac{|\mathcal{A}_n(M)|}{1 + |\mathcal{B}_n(M)|^2} \right)^{2p} L_\Omega(M[t_1 + t_2]) \quad (13.157)$$

with $\mathcal{A}_n(M)$ and $\mathcal{B}_n(M)$ given by (13.149)–(13.152). The result in (13.157) is a generalization of the quench result in (13.75) to our Floquet drive. The Loschmidt echo after a quantum quench can be obtained as a special case by

setting $q_1 = 1$, $q_2 = q = e^{-2\pi i v_2 t/L}$, and $M = 1$, for which $\mathcal{A}_n(M = 1) = A_n(t)$ and $\mathcal{B}_n(M = 1) = B_n(t)$ given by (13.70).

Finally, following the derivation of the previous section for excited states, we can write down the Loschmidt echo for the most general excited state of the form in (13.65). The result is

$$\begin{aligned} L_{\mathbf{p}, \bar{\mathbf{p}}}(M[t_1 + t_2]) &= \frac{1}{N_{\mathbf{p}, \bar{\mathbf{p}}}^2} \left| \langle \Omega | \prod_{n=1}^{\infty} a_n^{p_n} \bar{a}_n^{\bar{p}_n} U_F^M \prod_{n=1}^{\infty} \bar{a}_{-n}^{\bar{p}_n} a_{-n}^{p_n} | \Omega \rangle \right|^2 \\ &= \prod_{n=1}^{\infty} L_{p_n, \bar{p}_n}^{(n)}(M[t_1 + t_2]), \\ L_{p_n, \bar{p}_n}^{(n)}(M[t_1 + t_2]) &= L_{\Omega}^{(n)}(M[t_1 + t_2]) \left(\frac{|\mathcal{A}_n(M)|}{1 + |\mathcal{B}_n(M)|^2} \right)^{2(p_n + \bar{p}_n)} \\ &\quad \times \left| {}_2F_1(-p_n, -\bar{p}_n; 1; -|\mathcal{B}_n(M)|^2) \right|^2 \end{aligned} \quad (13.158)$$

with $\mathcal{A}_n(M)$ and $\mathcal{B}_n(M)$ given by (13.149)–(13.152). As was the case for (13.157), the result in (13.158) generalizes that in (13.86), which can be seen as a special case with $q_1 = 1$, $q_2 = q = e^{-2\pi i v_2 t/L}$, and $M = 1$. It thus provides the most general form of the stroboscopic time evolution of the Loschmidt echo under a periodic drive starting from any eigenstate of the theory with $K = K_1$. As shown in Fig. 13.9(b), the periodicity of the Loschmidt echo is independent of the choice of initial state, and the discussion of the critical exponents of T_L and λ_L across the transition is thus unchanged. As already discussed in the quench case, by considering general initial states that mix right- and left-moving excitations, the stroboscopic Loschmidt echo can display non-analytic behavior. However, we note that the Loschmidt echo is now evaluated at discrete times $M(t_1 + t_2)$, and thus the zeros in the return probability are only approximate, showing a pseudo-orthogonality at stroboscopic times.

In TLL theory, the total particle density is

$$\rho(x) = J_+(x) + J_-(x), \quad (13.159)$$

which is expressible in terms of a_n and \bar{a}_n using (13.16) and (13.26). Thus, to study the Floquet time evolution of the particle density, it suffices to consider the evolution of the oscillator modes. It should be noted that (13.24) implies conservation of the particle-number charges $J_0 = \sqrt{K_1} a_0$ and $\bar{J}_0 = \sqrt{K_1} \bar{a}_0$, since they commute with all modes and thus with H_1 and H_2 . However, in general, at the level of operators, the chiral densities $J_{\pm}(x)$ evolve non-trivially, unless evaluated with respect to a spatially homogeneous state, in which case trivially, since only the zero modes J_0 and \bar{J}_0 contribute.

To this end, consider the evolution of the operators a_n and \bar{a}_{-n} under one full cycle of the Floquet drive. (The change of sign in the subscript for the latter is for convenience, due to the way our drive mixes the modes.) From (13.42), (13.45), and (13.47), it follows that

$$U_F^{-1} \begin{pmatrix} a_n \\ \bar{a}_{-n} \end{pmatrix} U_F = C(n) \begin{pmatrix} a_n \\ \bar{a}_{-n} \end{pmatrix} \quad (13.160)$$

with the 2×2 matrix

$$C(n) = \begin{pmatrix} [q_2^n \cosh^2(\nu) - q_2^{-n} \sinh^2(\nu)] q_1^n & (q_2^n - q_2^{-n}) \cosh(\nu) \sinh(\nu) q_1^n \\ (q_2^{-n} - q_2^n) \cosh(\nu) \sinh(\nu) q_1^{-n} & [q_2^{-n} \cosh^2(\nu) - q_2^n \sinh^2(\nu)] q_1^{-n} \end{pmatrix}.$$

(13.161)

This matrix lies in $\mathfrak{su}(1, 1)$ and is non-trivial unless $n = 0$, in which case it is the identity matrix, consistent with particle-number conservation. It follows that the result after M cycles is obtained by multiplication by $C(n)^M$,

$$U_F^{-M} \begin{pmatrix} a_n \\ \bar{a}_{-n} \end{pmatrix} U_F^M = C(n)^M \begin{pmatrix} a_n \\ \bar{a}_{-n} \end{pmatrix}, \quad (13.162)$$

meaning that all information can be obtained by studying the properties of $C(n)$.

One can show that the eigenvalues of $C(n)$ are precisely $\lambda_n^\pm = \omega_n \pm \text{sgn } \omega_n \sqrt{\omega_n^2 - 1}$ in (13.126) in terms of ω_n in (13.125). As direct consequences,

$$\det[C(n)] = \lambda_n^+ \lambda_n^- = 1, \quad \text{tr}[C(n)] = \lambda_n^+ + \lambda_n^- = 2\omega_n = \text{Tr} [U_F^{(n)}] \quad (13.163)$$

for $U_F^{(n)} = e^{-iH_F^{(n)}(t_1+t_2)}$ with $H_F^{(n)}$ in (13.122). More importantly, the effect of the M -cycle drive in (13.162) enters precisely through factors of the form $(\lambda_n^\pm)^M$. Thus, following the discussion below (13.126), the stability characterizations in Table 13.1 are directly observable in the particle density $\rho(x)$. Indeed, the n th-mode contribution exhibits parametric instability if $\sigma_n = 4\omega_n^2 > 4$, since this implies exponential growth in discrete time $M(t_1 + t_2)$ with the same rate $\lambda_L = (t_1 + t_2)^{-1} \log |\lambda_n^+|$ as in (13.142). Similarly, if $\sigma_n < 4$, one can deduce that it features oscillations with the same period $T_L = \pi(t_1 + t_2)/\arg(\lambda_n^+)$ as in (13.143).

A related quantity of interest are density fluctuations in $\rho(x)$, or phrased differently, density-density correlations in the form of expectations of $\rho(x_1)\rho(x_2)$. Again, it follows from (13.16) and (13.26) that the relevant objects in Fourier space are the bilinears $a_n a_m$, $a_n \bar{a}_{-m}$, $\bar{a}_{-n} a_m$, and $\bar{a}_{-n} \bar{a}_{-m}$. From (13.160) and elementary linear algebra, the evolution of these under one full cycle is given by the Kronecker product $C(n) \otimes C(m)$, whose eigenvalues are

$$\lambda_{n,m}^1 = \lambda_n^+ \lambda_m^+, \quad \lambda_{n,m}^2 = \lambda_n^+ \lambda_m^-, \quad \lambda_{n,m}^3 = \lambda_n^- \lambda_m^+, \quad \lambda_{n,m}^4 = \lambda_n^- \lambda_m^- \quad (13.164)$$

with λ_n^\pm in (13.126). As before, it follows that

$$\det[C(n) \otimes C(m)] = 1, \quad \text{tr}[C(n) \otimes C(m)] = 4\omega_n \omega_m = \text{Tr} [U_F^{(n)}] \text{Tr} [U_F^{(m)}]. \quad (13.165)$$

Crucially, the discussion on stability involving λ_n^\pm translates directly to $\lambda_{n,m}^j$ for $j = 1, 2, 3, 4$. The above results for $C(n) \otimes C(m)$ are particularly important when considering expectations with respect to homogeneous states, since not only zero modes but also expectations of $a_n a_{-n}$ and $\bar{a}_{-n} \bar{a}_n$ ($n \neq 0$) then contribute, meaning that the eigenvalues $\lambda_{n,n}^1 = (\lambda_n^+)^2$ and $\lambda_{n,n}^4 = (\lambda_n^-)^2$ for $n \neq 0$ are always relevant to study. This implies that the stability characterizations in Table 13.1, including the exponential growth with M for $\sigma_n > 4$ indicating parametric instability, are always observable in density-density correlations, which were the objects considered in [274, 275] as probes of instabilities.

As seen earlier, the energy density can be expressed as

$$\mathcal{E}(x) = v_1 [T_+(x) + T_-(x)] \quad (13.166)$$

at an operator level. Using (13.16) and (13.27), it follows that the relevant objects to study in order to understand its Floquet time evolution are : $a_{n-m}a_m$: and : $\bar{a}_{-n+m}\bar{a}_{-m}$: (Again, the change of signs in the subscripts for the latter is for convenience.) However, as seen for particle-density fluctuations, under individual cycles, our drive generates contributions of the form $a_{n-m}\bar{a}_{-m}$ and $\bar{a}_{-n+m}a_m$. It is thus necessary to consider all four of these bilinears. By the same argument as before, it follows from (13.160) that

$$U_F^{-1} \begin{pmatrix} :a_{n-m}a_m: \\ a_{n-m}\bar{a}_{-m} \\ \bar{a}_{-n+m}a_m \\ :\bar{a}_{-n+m}\bar{a}_{-m}: \end{pmatrix} U_F = \mathbf{A}(n, m) \begin{pmatrix} :a_{n-m}a_m: \\ a_{n-m}\bar{a}_{-m} \\ \bar{a}_{-n+m}a_m \\ :\bar{a}_{-n+m}\bar{a}_{-m}: \end{pmatrix} + \delta_{n,0}|m|\mathbf{B}(m) \quad (13.167)$$

with the 4×4 matrix

$$\mathbf{A}(n, m) = \mathbf{C}(n - m) \otimes \mathbf{C}(m) \quad (13.168)$$

obtained as the Kronecker product of two 2×2 matrices of the form in (13.161) and the vector

$$\mathbf{B}(m) = \begin{pmatrix} (q_2^m - q_2^{-m})(q_2^m - q_2^{-m})\cosh^2(\nu)\sinh^2(\nu) \\ [q_2^{-m}\cosh^2(\nu) - q_2^m\sinh^2(\nu)][(q_2^{-m} - q_2^m)\cosh(\nu)\sinh(\nu)q_1^{-2m}] \\ [q_2^m\cosh^2(\nu) - q_2^{-m}\sinh^2(\nu)][(q_2^m - q_2^{-m})\cosh(\nu)\sinh(\nu)q_1^{2m}] \\ (q_2^{-m} - q_2^m)(q_2^m - q_2^{-m})\cosh^2(\nu)\sinh^2(\nu) \end{pmatrix}. \quad (13.169)$$

We note that the presence of $\mathbf{B}(m)$ is due to re-ordering of the right-hand side using (13.50).

As before, the result of our Floquet drive after M cycles can be understood from the properties of the matrix in (13.168). More precisely,

$$U_F^{-M} \begin{pmatrix} :a_{n-m}a_m: \\ a_{n-m}\bar{a}_{-m} \\ \bar{a}_{-n+m}a_m \\ :\bar{a}_{-n+m}\bar{a}_{-m}: \end{pmatrix} U_F^M = \mathbf{A}(n, m)^M \begin{pmatrix} :a_{n-m}a_m: \\ a_{n-m}\bar{a}_{-m} \\ \bar{a}_{-n+m}a_m \\ :\bar{a}_{-n+m}\bar{a}_{-m}: \end{pmatrix} + \delta_{n,0}|m| \sum_{j=0}^{M-1} [\mathbf{A}(0, m)]^j \mathbf{B}(m). \quad (13.170)$$

Note that the second term still contributes even if the above expression is evaluated with respect to the ground state $|\Omega\rangle$ of the theory with $K = K_1$. Indeed,

$$\begin{aligned} \langle\Omega|U_F^{-M}L_nU_F^M|\Omega\rangle &= \delta_{n,0}\langle\Omega|U_F^{-M}L_0U_F^M|\Omega\rangle \\ &= \delta_{n,0}\sum_{m=-\infty}^{\infty}\frac{|m|}{2}\begin{pmatrix} 1 & 0 & 0 & 0 \end{pmatrix}\sum_{j=0}^{M-1}[\mathbf{A}(0,m)]^j\mathbf{B}(m), \\ \langle\Omega|U_F^{-M}\bar{L}_nU_F^M|\Omega\rangle &= \delta_{n,0}\langle\Omega|U_F^{-M}\bar{L}_0U_F^M|\Omega\rangle \\ &= \delta_{n,0}\sum_{m=-\infty}^{\infty}\frac{|m|}{2}\begin{pmatrix} 0 & 0 & 0 & 1 \end{pmatrix}\sum_{j=0}^{M-1}[\mathbf{A}(0,m)]^j\mathbf{B}(m), \end{aligned} \quad (13.171)$$

where the vectors $\begin{pmatrix} 1 & 0 & 0 & 0 \end{pmatrix}$ and $\begin{pmatrix} 0 & 0 & 0 & 1 \end{pmatrix}$ were inserted to project the results to give the energies of right- and left-moving excitations. We recall the need to renormalize the above expressions, as discussed in the previous section, unless an ultraviolet cutoff is imposed on the interaction modulation.

From the above, it is clear that we are interested in the eigenvalues $\lambda_{n-m,m}^j$ of $\mathbf{A}(n,m)$ in (13.168) as well as those of $\sum_{j=0}^{M-1}[\mathbf{A}(0,m)]^j$. As before, using standard properties for Kronecker products, $\lambda_{n-m,m}^j$ are given by (13.164) and thus directly obtained from the eigenvalues of $\mathbf{C}(n)$. Setting $n = 0$, the eigenvalues of $\mathbf{A}(0,m)^M$ are

$$(\lambda_{-m,m}^1)^M = (\lambda_m^+)^{2M}, \quad (\lambda_{-m,m}^{2,3})^M = 1, \quad (\lambda_{-m,m}^4)^M = (\lambda_m^-)^{2M}, \quad (13.172)$$

which also implies that the eigenvalues of $\sum_{j=0}^{M-1}[\mathbf{A}(0,m)]^j$ are¹⁶

$$\begin{aligned} \sum_{j=0}^{M-1}(\lambda_{-m,m}^1)^j &= \frac{1 - (\lambda_m^+)^{2M}}{1 - (\lambda_m^+)^2}, & \sum_{j=0}^{M-1}(\lambda_{-m,m}^{2,3})^j &= M, \\ \sum_{j=0}^{M-1}(\lambda_{-m,m}^4)^j &= \frac{1 - (\lambda_m^-)^{2M}}{1 - (\lambda_m^-)^2}, \end{aligned} \quad (13.173)$$

in terms of λ_m^\pm in (13.126). Again, this results in the same stability characterizations depending on σ_m as described in the beginning of this section, see Table 13.1 and Fig. 13.7: If $\sigma_m > 4$, there are parametric instabilities observable in the m th-mode contribution to (the L_0 - and \bar{L}_0 -parts of) the energy density in the form of exponential growth with the rate in (13.142), while if $\sigma_m < 4$, there are oscillations with the period in (13.143).

13.6 RÉNYI DIVERGENCE AND RELATIVE ENTROPY

In this section we turn to a Euclidean setup. We consider a measure from quantum information theory, the so-called Rényi divergence, which quantifies the difference between thermal states of the undeformed Hamiltonian H_1 and

¹⁶ Clearly, all four eigenvalues in (13.173) are equal to M if $\lambda_m^\pm = 1$.

the deformed Hamiltonian H_2 . It is defined as the one-parameter generalization of the relative entropy, in the same way that Rényi entropy is the one-parameter generalization of von Neumann entropy. For any two normalized density matrices $\hat{\rho}_1$ and $\hat{\rho}_2$, the Rényi divergence $D_\alpha(\hat{\rho}_1||\hat{\rho}_2)$ is defined as [246]

$$D_\alpha(\hat{\rho}_1||\hat{\rho}_2) = \frac{1}{\alpha - 1} \log \text{Tr} \left[\hat{\rho}_1^\alpha \hat{\rho}_2^{1-\alpha} \right]. \quad (13.174)$$

The quantity $D_\alpha = D_\alpha(\hat{\rho}_1||\hat{\rho}_2)$ possesses several mathematical properties: (i) it is positive, $D_\alpha \geq 0$, (ii) monotonic, $D_{\alpha_1} \geq D_{\alpha_2}$ if $\alpha_1 > \alpha_2$, (iii) continuous, and (iv) $(1-\alpha)D_\alpha$ is concave in α . Furthermore, the limit $\alpha \rightarrow 1$ enables us to recover the relative entropy or Kullback-Leibler divergence

$$S(\hat{\rho}_1||\hat{\rho}_2) = \text{Tr} [\hat{\rho}_1 \log \hat{\rho}_1] - \text{Tr} [\hat{\rho}_1 \log \hat{\rho}_2], \quad (13.175)$$

which defines a measure of the distance between two density matrices that is of importance in quantum information [247], holography [276, 277], and CFT [278–280]. The concept of Rényi divergence recently attracted attention in the context of holography, where it was used to put additional constraints than the second law of thermodynamics using the monotonicity of D_α [281, 282]. In this context, the Rényi divergence for two-dimensional CFTs was computed from Euclidean quenches in a path integral formalism, and its computation amounts to evaluating new classes of generalized partition functions of deformed theories.

The goal of this section is to derive expressions for the Rényi divergence and the relative entropy between a thermal state $\hat{\rho}_1 = e^{-\beta H_1}/Z_1(\beta)$ with $Z_1(\beta) = \text{Tr}[e^{-\beta H_1}]$ of the TLL or compactified free boson theory H_1 with Luttinger parameter K_1 or radius R_1 and a thermal state $\hat{\rho}_2 = e^{-\beta H_2}/Z_2(\beta)$ with $Z_2(\beta) = \text{Tr}[e^{-\beta H_2}]$ of the marginally deformed theory H_2 with Luttinger parameter K_2 or radius R_2 . The Rényi divergence as a measure of the distance between two TLLs at finite temperature is defined in (13.174). As mentioned earlier, existing calculations of (13.174) in QFTs have been perturbative, namely, order-by-order in the deformation parameter μ if $S_2 = S_1 + \mu \int d^2x \mathcal{O}$ for actions S_1 and S_2 , where \mathcal{O} is some operator. Here we will demonstrate that the TLL or compactified free boson CFT offers an example to evaluate the object in (13.174) non-perturbatively as a function of K_1 and K_2 , i.e., by taking \mathcal{O} to be the marginal operator $\Phi \sim J\bar{J}$ in Sec. 13.3 [cf. (13.11), (13.20), and (13.33)].

For simplicity we set $v_1 = v_2 = 1$ throughout this section.

For convenience, we introduce $\tilde{\alpha} = 1 - \alpha$. The Rényi divergence in (13.174) for the thermal density matrices $\hat{\rho}_1$ and $\hat{\rho}_2$ then takes the form

$$D_\alpha(\hat{\rho}_1||\hat{\rho}_2) = -\frac{1}{\tilde{\alpha}} \log \left(\frac{Z(\tilde{\alpha}, \beta)}{Z_2(\beta)^{\tilde{\alpha}} Z_1(\beta)^{1-\tilde{\alpha}}} \right), \quad (13.176)$$

where $Z_j(\beta) = \text{Tr}[e^{-\beta H_j}]$ for $j = 1, 2$ is the partition function of the TLL or compactified free boson Hamiltonian H_j and $Z(\tilde{\alpha}, \beta) = \text{Tr}[e^{-\tilde{\alpha}\beta H_2} e^{-(1-\tilde{\alpha})\beta H_1}]$. The former are given by [see (3.27)] [265]

$$Z_j(\beta) = \frac{1}{|\eta(i\beta/L)|^2} \sum_{m,w \in \mathbb{Z}} \exp \left[-\pi \frac{\beta}{L} \left(\frac{m^2}{2K_j} + 2w^2 K_j \right) \right] = \frac{\Theta_j(\beta/L)}{\eta(i\beta/L)^2}, \quad (13.177)$$

where $\eta(\cdot)$ denotes the Dedekind eta function¹⁷ and $\Theta_j(\cdot)$ is the Siegel theta function with j indicating the dependence on the Luttinger parameter K_j . Therefore, the crucial object to evaluate is the generalized partition function $Z(\tilde{\alpha}, \beta)$ in the numerator of the logarithm in (13.176). In terms of path integrals, this quantity is a Euclidean quench amplitude, see [281] for more details. The evolution in the (periodic) imaginary time direction is under H_2 for a duration $\tilde{\alpha}\beta$ and under H_1 for the remaining time $(1 - \tilde{\alpha})\beta$. We can write this quantity as

$$Z(\tilde{\alpha}, \beta) = \text{Tr} \left[\mathcal{I}_\nu (\mathcal{I}_\nu^{(q^{\tilde{\alpha}})})^\dagger q^{\left(L_0^{(\text{osc})} + \bar{L}_0^{(\text{osc})} + \tilde{\alpha}H_2^{(0)} + (1 - \tilde{\alpha})H_1^{(0)} \right)} \right] q^{-1/12} \quad (13.178)$$

for $q = e^{-2\pi\beta/L}$, where we have used (13.49) along with the cyclicity of the trace.¹⁸ The above trace can be conveniently factorized into contributions from the primaries and their descendants, analogous to the usual torus partition function of the compactified free boson CFT. The quantity above then takes the form

$$\tilde{\Theta}(\tilde{\alpha}, \beta) = \tilde{\Theta}(\beta/L) \Xi(\beta/L) \langle \Omega | \mathcal{I}_\nu (\mathcal{I}_\nu^{(q^{\tilde{\alpha}})})^\dagger | \Omega \rangle e^{\pi\beta/6L}. \quad (13.179)$$

We now spell out the factors of the above expression in turn.

The contribution from the primary states is $\tilde{\Theta}(\beta/L)$, where we take into account zero modes from H_1 as well as H_2 in (13.31):

$$\tilde{\Theta}(\beta/L) \quad (13.180)$$

$$= \sum_{m,w \in \mathbb{Z}} \exp \left[-\pi \frac{\tilde{\alpha}\beta}{L} \left(\frac{m^2}{2K_2^2} + 2K_2^2 w^2 \right) - \pi \frac{(1 - \tilde{\alpha})\beta}{L} \left(\frac{m^2}{2K_1^2} + 2K_1^2 w^2 \right) \right]. \quad (13.181)$$

Meanwhile, the contribution $\Xi(\beta/L)$ from the descendant states is given by the following: We introduce

$$\begin{aligned} \Xi(z, \bar{z}) &= \frac{\text{Tr}_{\mathcal{V}_{m,w}} \left[\mathcal{I}_\nu (\mathcal{I}_\nu^{(q^{\tilde{\alpha}})})^\dagger z^{L_0^{(\text{osc})}} \bar{z}^{\bar{L}_0^{(\text{osc})}} \right]}{\langle \Omega | \mathcal{I}_\nu (\mathcal{I}_\nu^{(q^{\tilde{\alpha}})})^\dagger | \Omega \rangle} \\ &= \sum_{\bar{\mathbf{p}}, \bar{\mathbf{p}}} \frac{\langle \Psi_{\mathbf{p}, \bar{\mathbf{p}}} | \mathcal{I}_\nu (\mathcal{I}_\nu^{(q^{\tilde{\alpha}})})^\dagger | \Psi_{\mathbf{p}, \bar{\mathbf{p}}} \rangle}{\langle \Omega | \mathcal{I}_\nu (\mathcal{I}_\nu^{(q^{\tilde{\alpha}})})^\dagger | \Omega \rangle} z^{\sum n p_n} \bar{z}^{\sum n \bar{p}_n}, \end{aligned} \quad (13.182)$$

where the trace is over a single Verma module, $\mathcal{V}_{m,w}$, of a primary operator with momentum m and winding number w . The quantity above is the generating function for normalized and analytically continued return amplitudes for descendant states; we have $q^{\tilde{\alpha}} = e^{-2\pi\tilde{\alpha}\beta/L}$ as opposed to $q = e^{-2\pi i t/L}$. This can be explicitly computed using (13.67) and (13.82), yielding

$$\begin{aligned} \Xi(z, \bar{z}) &= \prod_{n=1}^{\infty} \sum_{p_n, \bar{p}_n=0}^{\infty} \left(\frac{A_n}{1 + B_n B_{-n}} \right)^{p_n + \bar{p}_n} \\ &\quad \times {}_2F_1(-p_n, -\bar{p}_n; 1; -B_n B_{-n}) z^{n p_n} \bar{z}^{n \bar{p}_n}, \end{aligned} \quad (13.183)$$

¹⁷ We recall that $\eta(\tau) = e^{i\pi\tau/12} \prod_{n=1}^{\infty} (1 - e^{2\pi n i \tau})$ for complex τ satisfying $\text{Im}(\tau) > 0$.

¹⁸ The E_2^0 contribution is omitted since the computations conspire to cancel it for $D_\alpha(\hat{\rho}_1 || \hat{\rho}_2)$.

where

$$A_n = \cosh^2(\nu) - \sinh^2(\nu)e^{4\pi\tilde{\alpha}\beta n/L}, \quad B_n = \frac{1}{2} \sinh(2\nu)(1 - e^{4\pi\tilde{\alpha}\beta n/L}). \quad (13.184)$$

Using the definition of the hypergeometric function ${}_2F_1(a, b; c; z)$ as well as properties of the binomial coefficients, the generating function in (13.183) simplifies to the infinite product

$$\begin{aligned} \Xi(z, \bar{z}) &= \prod_{n=1}^{\infty} \sum_{p_n, \bar{p}_n=0}^{\infty} \sum_{j=0}^{\infty} \binom{p_n}{j} \zeta_n^{p_n} \binom{\bar{p}_n}{j} \bar{\zeta}_n^{\bar{p}_n} \beta_n^j \\ &= \prod_{n=1}^{\infty} \frac{1}{(1 - \zeta_n)(1 - \bar{\zeta}_n) - \beta_n \zeta_n \bar{\zeta}_n}, \end{aligned} \quad (13.185)$$

where $\zeta_n = z^n A_n / (1 - \beta_n)$ and $\beta_n = -B_n B_{-n}$. The standard undeformed generating function for the descendant states is thus recovered by setting $\nu = 0$, leading to $\prod_{n=1}^{\infty} \frac{1}{(1-z^n)(1-\bar{z}^n)}$. On the other hand, the analytically continued generating function $\Xi(\beta/L)$ for $z = \bar{z} = e^{-2\pi\beta/L}$ in (13.185), which takes into account the contribution from the deformed descendant states, takes the form

$$\Xi(\beta/L) = \prod_{n=1}^{\infty} \frac{1}{(1 - \zeta_n)(1 - \bar{\zeta}_n) - \beta_n \zeta_n \bar{\zeta}_n}, \quad (13.186)$$

where

$$\zeta_n = \bar{\zeta}_n = \frac{A_n}{1 - \beta_n} e^{-2\pi\beta n/L}, \quad \beta_n = \sinh^2(2\nu) \sinh^2(2\pi\tilde{\alpha}\beta n/L) \quad (13.187)$$

with A_n in (13.184). Finally, we recall that the analytically continued ground-state return amplitude appearing in (13.179) is

$$\langle \Omega | \mathcal{I}_{\nu} (\mathcal{I}_{\nu}^{(q\tilde{\alpha})})^\dagger | \Omega \rangle = \prod_{n=1}^{\infty} \frac{1}{\cosh^2(\nu) - \sinh^2(\nu)e^{-4\pi\tilde{\alpha}\beta n/L}}. \quad (13.188)$$

Putting everything together in (13.179), one can readily verify that (13.176) implies that the trivial limit of two identical TLLs ($\nu \rightarrow 0$) consistently yields $\lim_{\nu \rightarrow 0} D_{\alpha}(\hat{\rho}_1 || \hat{\rho}_2) = 0$.

As a first step toward the evaluation of the Rényi divergence between two different TLLs, let us find the contribution from the zero modes to (13.176). To this end, we compute

$$\begin{aligned} &\frac{\tilde{\Theta}(\beta/L)}{\Theta_2(\beta/L)^{\tilde{\alpha}} \Theta_1(\beta/L)^{1-\tilde{\alpha}}} \\ &= \frac{\vartheta_3\left(i\pi \frac{\beta}{2L} \left[\frac{\tilde{\alpha}}{K_2} + \frac{1-\tilde{\alpha}}{K_1}\right]\right) \vartheta_3\left(i\pi \frac{2\beta}{L} [\tilde{\alpha}K_2 + (1-\tilde{\alpha})K_1]\right)}{\left[\vartheta_3\left(i\pi \frac{\beta}{2L} \frac{1}{K_2}\right) \vartheta_3\left(i\pi \frac{2\beta}{L} K_2\right)\right]^{\tilde{\alpha}} \left[\vartheta_3\left(i\pi \frac{\beta}{2L} \frac{1}{K_1}\right) \vartheta_3\left(i\pi \frac{2\beta}{L} K_1\right)\right]^{1-\tilde{\alpha}}}, \end{aligned} \quad (13.189)$$

where we used the Jacobi theta function $\vartheta_3(\cdot)$.¹⁹ This allows us to use its modular properties to derive the high-temperature limit of the zero-mode contribution to the Rényi divergence: Using the S-modular transformation

$$\vartheta_3(\tau) = (-i\tau)^{-1/2} \vartheta_3(-1/\tau), \quad (13.190)$$

we find that in the high-temperature regime $\beta/L \ll 1$, (13.189) simplifies to

$$\frac{\tilde{\Theta}(\beta/L)}{\Theta_2(\beta/L)^{\tilde{\alpha}} \Theta_1(\beta/L)^{1-\tilde{\alpha}}} \approx \left(\cosh^2(\nu) - (1-2\tilde{\alpha})^2 \sinh^2(\nu) \right)^{-1/2}, \quad (13.191)$$

which yields

$$\begin{aligned} D_{\alpha}^{(0)}(\hat{\rho}_1 || \hat{\rho}_2) &= -\frac{1}{\tilde{\alpha}} \log \left(\frac{\tilde{\Theta}(\beta/L)}{\Theta_2(\beta/L)^{\tilde{\alpha}} \Theta_1(\beta/L)^{1-\tilde{\alpha}}} \right) \\ &\approx \frac{\log \left(\cosh^2(\nu) - (1-2\tilde{\alpha})^2 \sinh^2(\nu) \right)}{2\tilde{\alpha}}. \end{aligned} \quad (13.192)$$

In particular, taking the limit $\alpha \rightarrow 1$, i.e., $\tilde{\alpha} \rightarrow 0$, gives the zero-mode contribution

$$S^{(0)}(\hat{\rho}_1 || \hat{\rho}_2) \approx 2 \sinh^2(\nu) \quad (13.193)$$

to the relative entropy. Since this contribution does not scale with temperature, it will be sub-leading and can thus be ignored in the high-temperature regime.

We now consider the contribution from the oscillator modes. Their contribution to $Z(\tilde{\alpha}, \beta) e^{-\pi\beta/6L}$ is

$$\begin{aligned} &\Xi(\beta/L) \langle \Omega | \mathcal{I}_{\nu}(\mathcal{I}_{\nu}^{(q\tilde{\alpha})})^\dagger | \Omega \rangle \\ &= \prod_{n=1}^{\infty} \frac{1}{[(1-\zeta_n)^2 - \beta_n \zeta_n^2] [\cosh^2(\nu) - \sinh^2(\nu) e^{-4\pi\tilde{\alpha}\beta n/L}]} \end{aligned} \quad (13.194)$$

For $\alpha = 1$, i.e., $\tilde{\alpha} = 0$, this yields

$$\Xi(\beta/L) \langle \Omega | \mathcal{I}_{\nu}(\mathcal{I}_{\nu}^{(q)})^\dagger | \Omega \rangle e^{\pi\beta/6L} = \frac{1}{\eta(i\beta/L)^2}, \quad (13.195)$$

where $q = e^{-2\pi\beta/L}$, in which case this cancels with the contribution from the oscillator modes to $Z_2(\beta)^{\tilde{\alpha}} Z_1(\beta)^{1-\tilde{\alpha}}$ in (13.176) for the Rényi divergence, cf. (13.177) and (13.179). It follows that

$$\begin{aligned} &D_{\alpha}^{(\text{osc})}(\hat{\rho}_1 || \hat{\rho}_2) \\ &= -\frac{1}{\tilde{\alpha}} \left[\log \left(\frac{Z(\tilde{\alpha}, \beta)}{Z_2(\beta)^{\tilde{\alpha}} Z_1(\beta)^{1-\tilde{\alpha}}} \right) - \log \left(\frac{\tilde{\Theta}(\beta/L)}{\Theta_2(\beta/L)^{\tilde{\alpha}} \Theta_1(\beta/L)^{1-\tilde{\alpha}}} \right) \right] \\ &= -\frac{1}{\tilde{\alpha}} \log \left(\eta(i\beta/L)^2 \Xi(\beta/L) \langle \Omega | \mathcal{I}_{\nu}(\mathcal{I}_{\nu}^{(q\tilde{\alpha})})^\dagger | \Omega \rangle e^{\pi\beta/6L} \right) \\ &= \frac{1}{\tilde{\alpha}} \sum_{n=1}^{\infty} \log \left(\frac{[(1-\zeta_n)^2 - \beta_n \zeta_n^2] [\cosh^2(\nu) - \sinh^2(\nu) e^{-4\pi\tilde{\alpha}\beta n/L}]}{[1 - e^{-2\pi\beta n/L}]^2} \right) \end{aligned} \quad (13.196)$$

¹⁹ We recall that $\vartheta_3(\tau) = \sum_{n \in \mathbb{Z}} e^{\pi i \tau n^2}$ for complex τ satisfying $\text{Im}(\tau) > 0$.

with ζ_n and β_n in (13.187), where we recall that $\tilde{\alpha} = 1 - \alpha$. Similar to previous results in this chapter, since individual terms in the sum in (13.196) tends to $\log \cosh^2(\nu)$ for large n , the sum must be renormalized unless an ultraviolet cutoff is imposed. In Fig. 13.11(a), we plot the result for the oscillator part of the Rényi divergence for a fixed cutoff on the number of modes. Its properties of positivity, monotonicity, and continuity are clearly visible in the figure. Furthermore, the concavity of $(1 - \alpha)D_\alpha^{(\text{osc})}(\hat{\rho}_1 \parallel \hat{\rho}_2)$ is shown in Fig. 13.11(b). We stress that the formula in (13.196) for the Rényi divergence was obtained non-perturbatively.

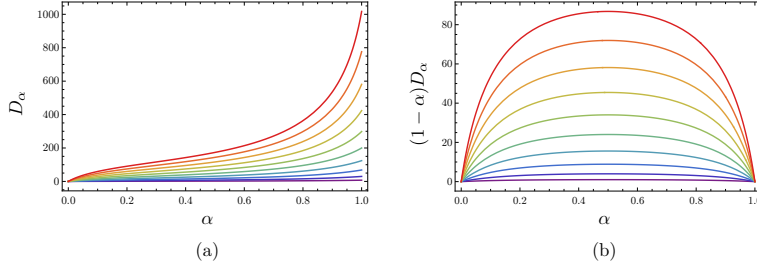


Figure 13.11: Plots of (a) the oscillator part of the Rényi divergence $D_\alpha = D_\alpha^{(\text{osc})}(\hat{\rho}_1 \parallel \hat{\rho}_2)$ in (13.196) and (b) the corresponding $(1 - \alpha)D_\alpha$ as functions of $\alpha \in (0, 1)$. The positivity, monotonicity, and continuity of D_α and the concavity of $(1 - \alpha)D_\alpha$ are clearly visible. The parameters used in both (a) and (b) are $\beta/L = 0.01$ and $K_1/K_2 = e^{2\nu}$ for $\nu = 0.1, 0.2, \dots, 1$ (bottom to top), and the results are plotted for a cutoff on the number of modes at $n = 100$.

As a last step, we take the limit $\alpha \rightarrow 1$ for $D_\alpha^{(\text{osc})}(\hat{\rho}_1 \parallel \hat{\rho}_2)$ in (13.196) to compute the oscillator part of the relative entropy between two TLLs. Formally taking the limit inside the sum and recalling that $\tilde{\alpha} = 1 - \alpha$, one obtains

$$S^{(\text{osc})}(\hat{\rho}_1 \parallel \hat{\rho}_2) = \sum_{n=1}^{\infty} \frac{4\pi\beta n}{L} \sinh(\nu^2) \coth(\pi\beta n/L). \quad (13.197)$$

This sum can be regularized by writing it as

$$S^{(\text{osc})}(\hat{\rho}_1 \parallel \hat{\rho}_2) = \sum_{n=1}^{\infty} \frac{4\pi\beta n}{L} \sinh^2(\nu) [\coth(\pi\beta n/L) - 1] + \frac{4\pi\beta}{L} \sinh^2(\nu) \zeta(-1), \quad (13.198)$$

where $\zeta(-1) = -1/12$ through analytic continuation. In the high-temperature regime $\beta/L \ll 1$, the sum in (13.198) can be approximated by an integral with respect to the dimensionless variable $\xi = \pi\beta n/L$ and computed analytically, yielding

$$\begin{aligned} S^{(\text{osc})}(\hat{\rho}_1 \parallel \hat{\rho}_2) &\approx \frac{4L}{\pi\beta} \sinh^2(\nu) \int_0^\infty d\xi \xi [\coth(\xi) - 1] - \frac{\pi\beta}{3L} \sinh^2(\nu) \\ &= \frac{\pi L}{3\beta} \left(1 - \frac{\beta^2}{L^2}\right) \sinh^2(\nu). \end{aligned} \quad (13.199)$$

Recalling that the zero-mode contribution in (13.193) is sub-leading in L , we conclude that the relative entropy between two TLLs with Luttinger parameters K_1 and K_2 is

$$S(\hat{\rho}_1 || \hat{\rho}_2) \approx \frac{\pi L}{3\beta} \sinh^2(\nu) \quad (13.200)$$

for large system sizes $L \gg 1$.

As a consistency check of our results for the Rényi divergence and the formula in (13.200) for the relative entropy as its $\alpha \rightarrow 1$ limit, we now provide a direct calculation of the latter. We start with the definition in (13.175). Since $\hat{\rho}_1$ and $\hat{\rho}_2$ are normalized thermal density matrices, we can rewrite the relative entropy as

$$S(\hat{\rho}_1 || \hat{\rho}_2) = \beta \left(\text{Tr} [\hat{\rho}_1 H_2] - \text{Tr} [\hat{\rho}_1 H_1] \right) - \log \left(\frac{Z_2(\beta)}{Z_1(\beta)} \right). \quad (13.201)$$

As before, we are interested in results for large system sizes. The last term vanishes due to the universality of high-temperature partition functions for CFTs: $Z(\beta) \approx \exp(\pi cL/6\beta)$ for $\beta/L \ll 1$. The trace $\text{Tr} [\hat{\rho}_1 H_1]$ appearing in (13.201) is simply the total energy of the undeformed theory at high temperatures. From (13.116), this is

$$\text{Tr}[\hat{\rho}_1 H_1] = L\mathcal{E}_\beta \approx \frac{\pi L}{6\beta^2}. \quad (13.202)$$

We are then left to calculate the trace $\text{Tr}[\hat{\rho}_1 H_2]$ at high temperatures. In order to proceed, we use the expression of the deformed Hamiltonian in (13.33) (omitting any constant terms subleading in L) together with (13.26) to obtain

$$\begin{aligned} \text{Tr}[\hat{\rho}_1 H_2] &= \cosh(2\nu) \text{Tr}[\hat{\rho}_1 H_1] + \frac{2\pi \sinh(2\nu)}{L} \text{Tr} \left[\hat{\rho}_1 \sum_{n=-\infty}^{\infty} a_n \bar{a}_n \right] \\ &\approx \frac{\pi L}{6\beta^2} \cosh(2\nu) + \frac{2\pi \sinh(2\nu)}{L} \text{Tr} [\hat{\rho}_1 a_0 \bar{a}_0]. \end{aligned} \quad (13.203)$$

In the second step we used (13.202) and the fact that the contribution from the trace in the second term only comes from the zero modes. The last term vanishes in the thermodynamic limit. We encountered the following trace in (13.203) while calculating the relative entropy:

$$\text{Tr} \left[e^{-\beta H} \sum_{n=-\infty}^{\infty} a_n \bar{a}_n \right] = \text{Tr} [e^{-\beta H} a_0 \bar{a}_0]. \quad (13.204)$$

The above object can be evaluated in general by taking derivatives with respect to the chemical potentials of the flavoured partition function

$$Z(\tau, \bar{\tau}, \chi, \bar{\chi}) = \text{Tr} \left[q^{L_0 - c/24} \bar{q}^{\bar{L}_0 - c/24} e^{2\pi i \chi a_0} e^{-2\pi i \bar{\chi} \bar{a}_0} \right], \quad (13.205)$$

$$\frac{1}{4\pi^2} \partial_\chi \partial_{\bar{\chi}} Z(\tau, \bar{\tau}, \chi, \bar{\chi})|_{\chi, \bar{\chi}=0} = \text{Tr} \left[q^{L_0 - c/24} \bar{q}^{\bar{L}_0 - c/24} a_0 \bar{a}_0 \right], \quad (13.206)$$

where $q = e^{2\pi i \tau}$ and χ and $\bar{\chi}$ are chemical potentials conjugate to the right and left U(1) currents, respectively. As we are interested in the high-temperature

regime, we need the S-modular transformation of the partition function above. It is well known that the object transforms in a manner similar to a weak Jacobi form [283, Appendix A]:

$$Z(\tau, \bar{\tau}, \chi, \bar{\chi}) = \exp\left(-\frac{i\pi\chi^2}{\tau} + \frac{i\pi\bar{\chi}^2}{\bar{\tau}}\right) Z\left(-\frac{1}{\tau}, -\frac{1}{\bar{\tau}}, \frac{\chi}{\tau}, \frac{\bar{\chi}}{\bar{\tau}}\right), \quad (13.207)$$

where $\tau = i\beta/L$ in our case. The dominant contribution at low temperatures arises from the vacuum. S-modular transforming this result using the above, we get the universal high-temperature behavior

$$Z(\beta/L, \chi, \bar{\chi}) \approx \exp\left(-\frac{i\pi L(\chi^2 + \bar{\chi}^2)}{\beta} + \frac{\pi L}{6\beta}\right) \quad (13.208)$$

for $\beta/L \ll 1$. Corrections beyond this are exponentially suppressed. Now taking derivatives and setting the chemical potentials to zero, as prescribed by the second equation in (13.205), we get $\text{Tr}[e^{-\beta H} a_0 \bar{a}_0] = 0$ in the thermodynamic limit. We thus conclude that the relative entropy takes the form

$$S(\hat{\rho}_1 || \hat{\rho}_2) \approx \frac{\pi L}{3\beta} \sinh^2(\nu) = \frac{\pi L}{3\beta} \frac{(K_1 - K_2)^2}{4K_1 K_2} \quad (13.209)$$

for $L \gg 1$, reproducing the result in (13.200). It obeys the general property of being non-negative and, as expected, gives zero when the Luttinger parameters (compactification radii) are equal. We stress that (13.209) yields a remarkably simple dependence on the Zamolodchikov distance ν and that it is an example of a relation between two different distance measures, namely a quantum information-theoretic distance and a geodesic distance in the space of theories.

Part V

CONCLUSIONS AND OUTLOOK

O U T L O O K

In this thesis we explored different aspects of inhomogeneous and disordered quantum systems, ranging from the topology of disordered Anderson insulators to the dynamics and geometry of periodically driven quantum critical systems in one dimension. In this concluding chapter, we provide a comprehensive overview of the three main parts of the thesis and outline several promising directions for future work.

14.1 CONCLUSIONS ON PART II

First, we explored “beyond tenfold-way” topological phases that belong to the category of delicate multi-gap phases. These phases can be band insulators with $(N-1)$ band gaps, where the number of bands between two successive band gaps is fixed. We obtained a \mathbb{Z} classification for three-dimensional band insulators without any symmetry constraints. Unlike the tenfold-way topological insulators, the N -band Hopf insulator does not host topologically protected gapless modes. Since both the bulk and the boundary are fully gapped, there is no unique way to separate a finite system into bulk and boundary subsystems [102, 105]. Despite this non-uniqueness, we formulated the bulk-boundary correspondence stating that a finite sample of the N -band Hopf insulator consists of the bulk, with total magnetoelectric polarizability of all the bulk bands quantized to an integer value, wrapped in a sheet of Chern insulator with the total Chern number of all the boundary bands equal to minus the same integer value (see Fig. 5.2). The obtained classification and bulk-boundary correspondence is the same as that of the Hopf insulator (the case $N=2$), providing a natural generalization to an arbitrary number of bands.

Second, while the topology of strong TIs poses an obstruction to localization by disorder of all their occupied bulk states, we have found that fully-localized insulators can be topologically non-trivial, too. In particular, we constructed a model for a TLI, a three-dimensional phase with broken time-reversal symmetry, where topology poses an obstruction to localization of its fully-localized bulk states all the way down to the atomic limit. We found that the three-dimensional Anderson insulator, with broken time-reversal symmetry, does not represent a single phase of matter, but rather contains infinitely many phases that are labeled by integers. Here, the Anderson model of localization, in the absence of mobility edge, corresponds to topologically trivial insulator and is labelled by $N_{\text{TLI}} = 0$, whereas topologically non-trivial localized insulators are guaranteed to host states delocalized along the crystal’s insulating boundary that give rise to the quantized Hall conductance $\sigma_{xy}^{\partial} = N_{\text{TLI}} e^2/h$ in Corbino geometry. Crucially, these delocalized boundary states remain topologically protected in the presence of an arbitrarily strong boundary disorder.

There are several extensions of the works presented in Part ii that would be interesting to pursue:

CRITICALITY OF THE TLI PHASE. The topological transition between two inequivalent TLIs is characterized by the appearance of a mobility edge in the bulk, i.e., delocalized states form in the bulk. It is however an open question on

whether such a delocalized regime holds for an extended range of parameters, forming a metallic phase, or whether it is only a phase boundary between two topologically inequivalent fully localized regimes. Writing a non-linear sigma model for the TLI phase would potentially shed light on the nature of the TLI transition as well as providing the associated critical exponent for the divergence of localization length. In particular, the apparent similarity between the $(2+1)D$ AFAI phase (see [284] for its NLSM formulation) and the $(3+0)D$ TLI phase may become manifest by identifying such a field theory.

CLASSIFICATION OF TLI PHASES. The examples of TLIs that we provided, from different constructions, all appeared in three dimensions and in class *A*, for which there is no non-trivial strong TI. One may thus wonder what is the full classification of TLIs, when considering time-reversal, particle-hole and chiral symmetries. In particular, a similar stacking construction than the one presented in Chapter 6 may be applicable to class AII in order to obtain a three-dimensional TLI with time-reversal symmetry. However, proving the bulk-boundary correspondence in this case may be challenging as it is not clear *a priori* what would be the correct \mathbb{Z}_2 invariant in place of the third winding number. Furthermore, it may be relevant to design TLI phases in lower dimensions and in the presence of time-reversal symmetry, in order to open a pathway for an experimental realization in, e.g., metamaterial platforms.

EXTENSION TO INTERACTING SYSTEMS. The TLI phase is protected by Anderson localization, which prevents localization of its bulk and appearance of a mobility edge in the bulk spectrum for large enough values of the disorder in any dimension. Although Anderson localization only holds for non-interacting models, many-body localization (MBL) leads to localization of bulk states in one and two dimensions in the presence of interaction. It would thus be tempting to define a TLI phase protected by MBL. However, the existence of MBL is still debated in $d > 1$, being either a stable phase [285, 286] or only a prethermal phase eventually leading to delocalization after exponentially long times. Therefore, it would be decisive to determine whether an interacting TLI phase may be stabilized by MBL over any experimentally relevant timescales needed to measure its quantized response, i.e., to verify that delocalization of the bulk states takes place sufficiently slowly to observe a quantized charge pumping. It is worth noting that the anomalous Floquet insulating phase, which shares similarities with the TLI phase in the non-interacting setting, can be stabilized by disorder in $d = 2$ thanks to MBL [287].

14.2 CONCLUSIONS ON PART III

In the Part iii of the thesis, we studied the universal properties of driven inhomogeneous critical systems, through exactly solvable models in $(1+1)D$ CFTs. One of our main conclusions is that such driven integrable models display spatially non-trivial heating phases, as opposed to driven generic many-body systems which simply heat up to an infinite temperature state. The main signature of such an “integrable heating phase” is the emergence of Floquet horizons, stroboscopic analogues to black hole horizons that attract all quasiparticles, and share growing quantum entanglement.

The general mathematical picture hiding behind the emergence of such horizons in the heating phase relies on an equivalence between inhomogeneous

Floquet CFTs and dynamical systems on the circle. In this language, the horizons correspond to unstable fixed points of the circle map that encodes the one-cycle dynamics of primary fields under the action of the Floquet drive. This abstract viewpoint applies to arbitrary smooth deformations of the Hamiltonian density, and provides a way to show that the critical exponent between the heating and non-heating phases is always $\frac{1}{2}$.

The phase diagram obtained in the case of periodic drives reduces to a heating diagram in the quasiperiodic driving case, where only a fractal set of measure zero evades heating for infinitely long times. Exceptional points in the phase diagram lead to direct access to the non-heating dynamics under the quasiperiodic drive, for which the system returns to its initial state even after exponentially long times.

The aforementioned features of the driving dynamics turn-out to be independent on the initial state of the Floquet problem, may it be pure or thermal. Furthermore, these features appear in the short-time regime of driven free fermion lattice models, and can still be detected in the presence of small boundary dissipation or dephasing. In particular, the emergent Floquet horizons act as a heating blockade in the case of boundary dissipation, leaving the middle part of the system immune to interaction with the external bath.

In the non-integrable limit of large central charge, the Floquet horizons lead to strongly inhomogeneous scrambling of quantum information, and their Hawking temperature set a time-scale of the Lyapunov exponent of the OTOC. The emergence of quantum chaos thus becomes position dependent.

There are several extensions of the works presented in Part iii that would be interesting to pursue:

NON-HERMITIAN DRIVES. We have studied the dynamics of driven inhomogeneous CFTs with arbitrary real smooth spatial deformations. Nevertheless, one could in principle relax the reality condition on the deformation profile and consider complex deformations of the energy density, leading to a non-vanishing imaginary part in the Hamiltonian. The simplest example of a non-Hermitian spatial deformation is $H = \frac{2\pi}{L}(L_0 + L_1)$, which forms a closed algebra $\{L_0, L_1\}$. For general complex deformations, one could expect rich behaviours of entanglement and energy under the periodic drive, such as fractal scaling of entanglement entropy [128], as the one-cycle Floquet dynamical map may be a chaotic map, such as the logistic map. While such general non-Hermitian deformations may not be analytically tractable in general, one could consider non-Hermitian (or pseudo-Hermitian) $\mathfrak{sl}(2)$ spatial deformations. In the case of Hermitian $\mathfrak{sl}(2)$ deformations, the one-cycle evolution of primary fields under the periodic drive is encoded in Möbius transformations, which can be elliptic, parabolic or hyperbolic depending on driving parameters [see Chapter 7]. However, general Möbius transformations with complex valued parameters also admit the loxodromic class. This class of Möbius transformations, that cannot be triggered with only Hermitian spatial deformations of the CFT, would lead to both oscillations and growth of energy and entanglement. Furthermore, it would be interesting to understand how such non-Hermitian $\mathfrak{sl}(2)$ deformations would affect the structure of the phase diagram. One might expect fully heating (hyperbolic) and fully non-heating (elliptic) phases to be continuously related through loxodromic transformations, instead of going through a phase transition (parabolic point). Moreover, non-Hermitian $\mathfrak{sl}(2)$ deformations could be adapted to the Fibonacci quasiperiodic driving sequence introduced in Chapter 8. In the Hermitian case, such drives almost always lead to heating, with

non-heating lines of measure zero in parameter space. On the other hand, in the non-Hermitian case we anticipate that the non-heating phase can be stabilized, as the Fibonacci trace map invariant (8.23) may take negative values. This would provide a field-theoretic example of a non-Hermitian quasiperiodically driven system that evades heating for *arbitrarily long* times.

RELATION TO MOVING MIRRORS. From a classical viewpoint, the main physical features of inhomogeneous CFTs are captured by quasiparticle motion in a curved spacetime with a spatially dependent local velocity. Alternatively, we may think of such gapless quasiparticles as light rays propagating in a medium with non-trivial refractive index that depends both on space and time, or equivalently light rays propagating in one-dimensional cavity with a moving mirror [169]. The quantum version of the moving mirror has been extensively studied for gapless field theories [288] and led to similar features as Floquet CFTs, such as heating phases with energy density increasing exponentially at a single point, and decreasing exponentially everywhere else, and dynamical Casimir effect with supercooled vacuum far away from the emergent horizons. Moving mirrors are also prototypical theoretical toy models to model Hawking radiation and the page curve of entanglement entropy, and have a known holographic dual in the large central charge limit [289]. From these different perspectives we anticipate the existence of a precise relation between inhomogeneous driven CFTs and moving mirrors, which may shed further light on their holographic dual at large central charge.

MOVING AWAY FROM CRITICALITY. The spatial deformations of the CFT only involve (higher modes of) the stress tensor. It would be interesting to further study the effects of other types of operators in the time evolution of the system. In general, such operators would spoil the conformal symmetry of the problem and thus the system would thermalize. Studying the effect of irrelevant operators in the Floquet time evolution may also be fruitful to understand better the deviation between lattice and CFT calculations in the heating phase, as one needs to include such operators to account for the UV completion at higher energy scales.

HIGHER DIMENSIONS. Throughout Part iii, we have been focusing our attention on $(1+1)$ D CFTs, capitalizing on the infinite dimensional Virasoro algebra to define general deformations of the Hamiltonian density and compute time evolution of primary fields under such deformed Hamiltonians [see Chapter 9]. While this strategy is not directly applicable to higher dimensions, as the Virasoro algebra only emerges in two dimensions, we note that higher dimensional CFTs still admit the global conformal group as symmetry group, whose algebra is spanned by $\{L_0, L_1, L_{-1}\}$. Thus, it may still be possible to encode the time evolution of primary fields for the restricted class of $\mathfrak{sl}(2)$ deformations, and compute one and two-point functions of primary fields in arbitrary dimensions. The existence of the different heating and non-heating phases of the Floquet problem was related to the different topologies of the non-compact $SL(2, \mathbb{C})$ group. In $(d+1)$ D, the conformal group is $SO(d+2, 1)$, which is a non-compact group for any d , thus suggesting the existence of heating and non-heating phases even in higher dimensions. Such phases could be diagnosed from the analysis of, e.g., total energy evolution, for which a higher dimension generalization is clear. This may provide a first pathway

to study exactly solvable inhomogeneous Floquet dynamics in two and three spatial dimensions.

14.3 CONCLUSIONS ON PART IV

In the Part iv of the thesis, we have studied the non-equilibrium dynamics of TLLs under interaction modulations modeled by quenching or periodically driving the Luttinger parameter. These modulations are marginal ($J\bar{J}$) deformations in the low-energy description of TLLs as compactified free bosons, which is the simplest CFT that belongs to a continuous family of CFTs. Two protocols were considered, a quantum quench and a two-step Floquet drive, switching between Hamiltonians H_1 and H_2 with different Luttinger parameters K_1 and K_2 , or equivalently different compactification radii. Using Bogoliubov transformations and an underlying $\mathfrak{su}(1,1)$ -algebraic structure, we derived a number of exact analytical results that depend crucially on the ratio of the Luttinger parameters, which corresponds to the Zamolodchikov distance $\nu = \log \sqrt{K_1/K_2}$ between the theories H_1 and H_2 in the space CFTs.

For the quench, we computed the Loschmidt echo and the time evolution of the energy density for the system initialized in any arbitrary eigenstate of H_1 . We showed that the Loschmidt echo exhibits periodic revivals for all initial states, while if the initial state mixes right- and left-moving excitations, it also has Lee-Yang-Fisher zeros, which are defining features of dynamical quantum phase transitions. For the evolution of the energy-density expectation, we observed periodic discontinuities at times corresponding to the revivals in the Loschmidt echo. Moreover, starting from thermal states, its asymptotic (late-time) expression in the thermodynamic limit was shown to agree with that of the energy density evaluated in a thermal state at an effective temperature β_{eff} that depends on ν .

For the two-step drive, we used a factorization of the Floquet operator into uncoupled discrete-time quantum parametric oscillators to obtain explicit criteria for stability or instability based on the value of the $\mathfrak{su}(1,1)$ Cartan-Killing form for the Floquet Hamiltonian for each individual mode. We showed that this is observable in physical quantities such as the stroboscopic time evolution of the Loschmidt echo for arbitrary eigenstates of H_1 and the particle and energy densities. In the stable phase, these quantities oscillate in time with a period that diverges as one approaches the phase boundary. On the other hand, in the unstable phase, the Loschmidt echo decays and the densities grow exponentially with a rate that vanishes as one approaches the phase boundary. This period and rate were identified as natural order parameters and shown to have critical exponents of 1/2.

Lastly, we used our formalism to non-perturbatively compute the Rényi divergence between thermal states corresponding to the two Hamiltonians H_1 and H_2 , while earlier QFT computations of the Rényi divergence have been perturbative. Taking a certain limit of our result, we obtained the relative entropy, which defines a quantum information-theoretic distance between density matrices, and which in our case has a remarkably simple dependence on ν in the thermodynamic limit. This relation between the relative entropy and the Zamolodchikov distance provides a concrete correspondence between two distance measures: It directly translates the geodesic distance in the moduli space to a quantum information-theoretic distance between thermal density matrices of the corresponding CFTs.

There are several extensions of the work presented in Part iv that would be interesting to pursue:

QUASI-PERIODIC AND RANDOM DRIVES. One direct extension is to consider drives that fully break time-translation invariance, either deterministically or randomly, in the form of quasi-periodic or random drives. The methods we used to compute, e.g., the Loschmidt echo for a periodic drive are readily generalizable to these new drive protocols. One way is to use the generalized $\mathfrak{su}(1, 1)$ rotation relations and properties of products of random $\mathfrak{su}(1, 1)$ matrices and trace-map formulas for, e.g., Fibonacci quasi-periodic drive sequences, cf. [24, 132].

TRAPPED ULTRA-COLD ATOMS. To relate to experiments, it would be interesting to generalize the constant Luttinger parameters $K_{1,2}$ in this chapter to functions $K_{1,2}(x)$ of position x . This arises naturally in cold-atom experiments as a consequence of the trapping potential. The dynamics in such a static environment was recently studied in [259], but the full quench problem or its driven counterpart have yet to be considered. To paint a complete picture, this would optimally also include a quantitative discussion of relevant length scales and effects of physical cutoffs on the number of modes. Another way to connect with experiments is to consider spatially inhomogeneous initial states, e.g., localized excitations on top of the ground state, which is realizable in cold-atom experiments. We expect that the way these excitations propagate under the periodic drive would lead to intricate spatial patterns of energy and particle density in both the stable and unstable phase.

DRIVEN DISSIPATIVE TLLS. The solvability of the marginally driven TLL was greatly facilitated by identifying a closed $\mathfrak{su}(1, 1)$ algebraic structure in the time-dependent Hamiltonian. A similar algebraic structure was identified and used to solve a dissipative harmonic oscillator in [290, 291]. It would be interesting to explore driven dissipative TLLs using methods developed in these works.

MULTI-COMPONENT TLLS AND STRINGS WITH HIGHER-DIMENSIONAL TARGET SPACES. It is natural to consider quenches and periodic drives by marginal deformations in D -component TLLs, which have $U(1)^D$ current algebras generated by J_n^I and \bar{J}_n^I ($n \in \mathbb{Z}$, $I = 1, \dots, D$). These deformations generate the Narain moduli space of the toroidally compactified D -component free boson CFT or D -dimensional bosonic string. The action is [cf. (13.11)]

$$S = \frac{1}{4\pi\alpha'} \int d^2x \left(G_{IJ} \delta^{\alpha\beta} + iB_{IJ} \epsilon^{\alpha\beta} \right) \partial_\alpha X^I \partial_\beta X^J, \quad (14.1)$$

where the space of marginal deformations is parametrized by the symmetric target-space metric G^{IJ} and the anti-symmetric Kalb–Ramond field B^{IJ} . Applications include the low-energy description of a system of multiple copies of XXZ spin chains with the Hamiltonian

$$H = -J \sum_{I,I'=1}^D \sum_{j=1}^N \left(\delta_{I,I'} S_j^{x,I} S_{j+1}^{x,I'} + \delta_{I,I'} S_j^{y,I} S_{j+1}^{y,I'} - \Delta_{I,I'} S_j^{z,I} S_{j+1}^{z,I'} \right), \quad (14.2)$$

where $\Delta_{I,I'}$ is the anisotropy matrix, which is modulated in time. It would be interesting to study how the non-equilibrium dynamics depends on the Zamolodchikov distance in this case.

COMPACTIFIED ORBIFOLD BOSON CFT. The moduli space of $c = 1$ CFTs contains two lines (that meet at a point) [266]. The first corresponds to the compactified free boson CFT and is parametrized by the compactification radius. Here we have studied the physical consequences of dynamically exploring this line. The second corresponds to the \mathbb{Z}_2 orbifold CFT and is parametrized by the radius of the orbifolded circle. Much of the formalism developed in this chapter can be adapted to marginal quenches or drives of this second line. Such protocols could be realized in the Ashkin-Teller quantum spin chain.

WEISS-ZUMINO-WITTEN (WZW) MODELS. A large class of CFTs that admit $J\bar{J}$ deformations is provided by G -WZW models, which have $\dim(\mathfrak{g})$ holomorphic and anti-holomorphic currents, where \mathfrak{g} is the Lie algebra associated with the compact and simply connected Lie group G . A subset of the current-current deformations formed from these are exactly marginal and generate a moduli space of CFTs. More precisely, a JJ -type deformation is exactly marginal if (and only if) both the holomorphic and anti-holomorphic currents belong to a commutative current algebra [264, 292]. How our results generalize to the dynamics of WZW models under time-dependent exactly marginal deformations is an open question.

$T\bar{T}$ DEFORMATIONS. The recently introduced $T\bar{T}$ deformation of CFTs and integrable QFTs [293, 294] provides another arena to explore the dynamics of quenches and drives. This is an irrelevant deformation where the spectrum of the deformed theory is exactly solvable in terms of the undeformed spectrum and degeneracies remain unchanged. A practical starting point to study such dynamics would be to consider a $T\bar{T}$ quench of the free fermion CFT. As the deformation brings about changes in signal propagation velocities, it would be tantalizing to see how individual quantities, such as return probabilities and correlation functions, evolve following the quench. Some work in this direction was carried out in [75].

HOLOGRAPHY. It would be interesting to consider how the dynamics of marginal quenches and drives translate into bulk or gravitational terms through the AdS/CFT correspondence. In the prototypical example of $\text{AdS}_3/\text{CFT}_2$ described by the D1-D5 system, the holographic CFT contains exactly marginal operators [295]¹. The marginal deformations in this case allow an interpolation between stringy and (classical) gravity regimes in AdS_3 . Since we have structures reminiscent of boundary states and conformal interfaces, it is natural to expect that these will have counterparts in the bulk.

¹ Exactly marginal operators do not acquire anomalous dimensions upon deformation, i.e., they are protected by supersymmetry.

Part VI
APPENDIX

In this appendix we give details of the calculations for $N = 2$ and $N = 3$ Hopf pump.

A.1 THE $N = 2$ HOPF PUMP

We compute the winding number for the 2-band model in the adiabatic limit $BT \gg 1$. In this limit, the evolution operator takes the form $U_{k_x k_y t}^F = e^{-2\pi i \hat{n}_{k_x k_y t} \cdot \vec{\sigma}(t-t_0)/T} e^{-iB\sigma_3(t-t_0)}$. This operator takes the form

$$U_{k_x k_y t}^F = \begin{cases} e^{-2\pi i \sigma_2 t / T} e^{-iB\sigma_3 t} \\ -ie^{-2\pi i (\sin(k_y)\sigma_1 + \cos(k_y)\sigma_2)t \frac{1}{4}} \\ \times e^{-iBT\sigma_3 t \frac{1}{4}} \sigma_2 e^{-i\frac{BT}{4}\sigma_3} \\ -e^{-2\pi i (\sin(k_x)\sigma_1 + \cos(k_x)\sigma_2)t \frac{1}{2}} \\ \times e^{-iBT\sigma_3 t \frac{1}{2}} e^{ik_y \sigma_3} \\ e^{-2\pi i (\sin(\delta k)\sigma_1 + \cos(\delta k)\sigma_2)t \frac{3}{4}} \\ \times e^{-iBT\sigma_3 t \frac{3}{4}} \sigma_2 e^{-i(\delta k + \frac{BT}{4})\sigma_3} \end{cases} \quad (\text{a.1})$$

where we introduced the notation $\delta k = k_x - k_y$. We notice that only during the third segment of the drive the unitary $U_{k_x k_y t}^F$ will give a non trivial contribution to the winding number, as it does not depend independently on k_x and k_y for the other segments of the drive. One then finds

$$(U_{k_x k_y t}^F)^\dagger \partial_{k_y} U_{k_x k_y t}^F = i\sigma_3 \quad (\text{a.2})$$

$$\begin{aligned} (U_{k_x k_y t}^F)^\dagger \partial_{k_x} U_{k_x k_y t}^F &= -i \sin^2 \left(\frac{2\pi t}{T} \right) \sigma_3 \\ &\quad - \frac{i}{2} \sin \left(\frac{4\pi t}{T} \right) [\cos(a)\sigma_1 + \sin(a)\sigma_2] \end{aligned} \quad (\text{a.3})$$

$$(U_{k_x k_y t}^F)^\dagger \partial_t U_{k_x k_y t}^F = -i \frac{BT}{T} \sigma_3 - \frac{2\pi}{T} [\cos(a)\sigma_1 - \sin(a)\sigma_2] \quad (\text{a.4})$$

where we introduced the notation $a = k_x - 2k_y + (-1 + \frac{2t}{T})BT$. We conclude that the trace gives $\frac{4\pi}{T} \sin \left(\frac{4\pi t}{T} \right)$, and therefore we obtain $W_3[U_{k_x k_y t}^F] = 1$, for any value of BT as long as the adiabatic limit holds.

A.2 DOUBLING OF THE UNIT CELL

We now consider a redefinition of the unit cell for the adiabatic $N = 2$ Hopf pump of Sec. 5.6. We double the unit cell in the x -direction, hence, there are 4 orbitals per unit cell, as shown on Fig. a.1. The model has 2 bands, both doubly degenerate. Thus the classification discussed in this article cannot apply in this example, as all the bands are not separated by a gap.

We first consider the gauge $|u_{k_x k_y t n}\rangle$, $n = 1, \dots, 4$, that is obtained by Fourier transform of the following four WFs (5.45)-(5.46): $|w_{R_x R_y t 1}\rangle$, $|w_{R_x R_y t 2}\rangle$, $|w_{(R_x+1) R_y t 1}\rangle$, and $|w_{(R_x+1) R_y t 2}\rangle$, see Fig. a.1. The direct calculation of the third winding number defined by such gauge choice gives $W_3[U_{k_x k_y t}] = 1$.

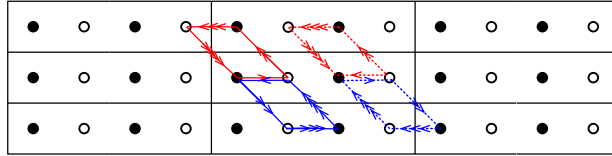


Figure a.1: Redefinition of the unit cell. We consider a unit cell consisting of 4 orbitals.

Next, we introduce a change of basis between the two lower degenerate bands:

$$\begin{cases} |\tilde{u}_{k_x k_y t 1}\rangle = \alpha_{k_x k_y t}|u_{k_x k_y t 1}\rangle + \beta_{k_x k_y t}|u_{k_x k_y t 3}\rangle \\ |\tilde{u}_{k_x k_y t 3}\rangle = \gamma_{k_x k_y t}|u_{k_x k_y t 1}\rangle + \delta_{k_x k_y t}|u_{k_x k_y t 3}\rangle, \end{cases} \quad (\text{a.5})$$

which defines a unitary 2×2 matrix

$$V_{k_x k_y t} = \begin{pmatrix} \alpha_{k_x k_y t} & \beta_{k_x k_y t} \\ \gamma_{k_x k_y t} & \delta_{k_x k_y t} \end{pmatrix}. \quad (\text{a.6})$$

The above gauge defines a new unitary matrix $\tilde{U}_{k_x k_y t}$. We make a choice for $V_{k_x k_y t}$ such that $W_3[V_{k_x k_y t}] = 1$, this can be obtained by taking $V_{k_x k_y t}$ to be the unitary of the 2 sites unit cell example studied previously. Using this definition for the gauge transformation, we obtain $\tilde{U}_{k_x k_y t}$

$$\tilde{U}_{k_x k_y t} = \begin{pmatrix} \cos(t_0)^2 & \sin(t_0) & -\sin(t_0)\cos(t_0) & 0 \\ -\sin(t_0)\cos(t_0) & \cos(t_0) & \sin(t_0)^2 & 0 \\ \cos(t_0)\sin(t_0) & 0 & \cos(t_0)^2 & \sin(t_0) \\ -\sin(t_0)^2 & 0 & -\sin(t_0)\cos(t_0) & \cos(t_0) \end{pmatrix},$$

$$\tilde{U}_{k_x k_y t} = \begin{pmatrix} \sin(t_{\frac{1}{4}})^2 e^{2ik_y} & \cos(t_{\frac{1}{4}}) & \sin(t_{\frac{1}{4}})\cos(t_{\frac{1}{4}})e^{ik_y} & 0 \\ \cos(t_{\frac{1}{4}})\sin(t_{\frac{1}{4}})e^{ik_y} & -\sin(t_{\frac{1}{4}})e^{-ik_y} & \cos(t_{\frac{1}{4}})^2 & 0 \\ -\sin(t_{\frac{1}{4}})\cos(t_{\frac{1}{4}})e^{ik_y} & 0 & \sin(t_{\frac{1}{4}})^2 & \cos(t_{\frac{1}{4}}) \\ -\cos(t_{\frac{1}{4}})^2 & 0 & \cos(t_{\frac{1}{4}})\sin(t_{\frac{1}{4}})e^{-ik_y} & -\sin(t_{\frac{1}{4}})e^{-ik_y} \end{pmatrix},$$

$$\tilde{U}_{k_x k_y t} = \begin{pmatrix} \cos(t_{\frac{1}{2}})^2 e^{2ik_y} & 0 & -\cos(t_{\frac{1}{2}}) \sin(t_{\frac{1}{2}}) e^{i(2k_y - k_x)} & -\sin(t_{\frac{1}{2}}) e^{-i(k_y - k_x)} \\ -\sin(t_{\frac{1}{2}})^2 e^{ik_x} & -\cos(t_{\frac{1}{2}}) e^{-ik_y} & -\sin(t_{\frac{1}{2}}) \cos(t_{\frac{1}{2}}) & 0 \\ \cos(t_{\frac{1}{2}}) \sin(t_{\frac{1}{2}}) e^{ik_x} & -\sin(t_{\frac{1}{2}})^2 e^{-ik_y} & \cos(t_{\frac{1}{2}})^2 & 0 \\ -\sin(t_{\frac{1}{2}}) \cos(t_{\frac{1}{2}}) e^{i(2k_y - k_x)} & 0 & \sin(t_{\frac{1}{2}})^2 e^{2i(k_y - k_x)} & -\cos(t_{\frac{1}{2}}) e^{-ik_y} \end{pmatrix},$$

$$\tilde{U}_{k_x k_y t} = \begin{pmatrix} \sin(t_{\frac{3}{4}})^2 & 0 & \sin(t_{\frac{3}{4}}) \cos(t_{\frac{3}{4}}) e^{i(k_y - k_x)} & -\cos(t_{\frac{3}{4}}) e^{-i(k_y - k_x)} \\ -\cos(t_{\frac{3}{4}})^2 e^{ik_x} & \sin(t_{\frac{3}{4}}) & \cos(t_{\frac{3}{4}}) \sin(t_{\frac{3}{4}}) e^{ik_y} & 0 \\ -\sin(t_{\frac{3}{4}}) \cos(t_{\frac{3}{4}}) e^{i(k_x - k_y)} & -\cos(t_{\frac{3}{4}}) e^{-ik_y} & \sin(t_{\frac{3}{4}})^2 & 0 \\ \cos(t_{\frac{3}{4}}) \sin(t_{\frac{3}{4}}) e^{i(k_y - k_x)} & 0 & \cos(t_{\frac{3}{4}})^2 e^{2i(k_y - k_x)} & \sin(t_{\frac{3}{4}}) \end{pmatrix},$$

for the 4 different segments of the drive, where we introduced the notation $t_n = \frac{2\pi}{T}(t - nT)$. We obtain that only the third and the fourth segments of the drive contribute to the third winding number, both giving an opposite $\frac{1}{2}$ contribution. Therefore $W_3[\tilde{U}_{k_x k_y t}] = 0$, demonstrating that the third winding number is not gauge independent in presence of the band degeneracies.

Furthermore, imposing open boundary conditions in the y -direction, the edge Chern number can be computed using the Wannier cut procedure described in the main text. We consider for concreteness 8 layers in the y -direction, which defines the ribbon supercell of 32 orbitals. We compute the bulk hybrid WFs $|\tilde{w}_{k_x R_y tn}\rangle$ from the Bloch eigenvectors $|\tilde{u}_{k_x k_y tn}\rangle$. Using these bulk hybrid WFs, we obtain the upper edge projector $\mathcal{P}_{k_x t}^{\text{edge}}$ by removing the 16 WFs from the bulk. Explicit computation leads to $\text{Ch}^{\text{edge}} = 0$, since the contribution of the third and fourth time-segments cancel each other.

Lastly, we can define ($N = 4$)-band Hopf pump using the Bloch eigenstates $|\tilde{u}_{k_x k_y tn}\rangle$

$$h_{k_x k_y t} = \sum_{n=1}^4 n |\tilde{u}_{k_x k_y tn}\rangle \langle \tilde{u}_{k_x k_y tn}|, \quad (\text{a.7})$$

such that the 4 bands are now non-degenerate. The abelian part of the third Chern-Simons form can be computed explicitly,

$$\sum_{n=1}^4 P_3^n = -\frac{1}{6}. \quad (\text{a.8})$$

This Hamiltonian (a.7) has $N_{\text{Hopf}} = 0$, since the third winding number of $\tilde{U}_{k_x k_y t}$ vanishes. For this example $N_{\text{Hopf}} \neq \sum_{n=1}^4 P_3^n$ holds, thus, the non-topological orbital magnetization $\sum_{n=1}^4 m_n^{\text{non-top}} = 1/6$ does not vanish.

A.3 THE $N = 3$ HOPF PUMP

For $t \in [0, \frac{T}{6}]$, the states evolve as

$$\begin{cases} |u_{k_x k_y t1}\rangle = \cos(t_0 \delta) |1\rangle - \sin(t_0 \delta) e^{ik_x} |3\rangle, \\ |u_{k_x k_y t2}\rangle = |2\rangle, \\ |u_{k_x k_y t3}\rangle = \cos(t_0 \delta) |3\rangle + \sin(t_0 \delta) e^{-ik_x} |1\rangle, \end{cases} \quad (\text{a.9})$$

where we introduced the notation $t_n = \frac{3\pi}{T}(t - nT)$ and the parameter $\delta \in]0, 1[$ which creates the asymmetry between the trajectories of $|0\rangle$ and $|1\rangle$. For $t \in \left(\frac{T}{6}, \frac{T}{3}\right]$, the states evolve as

$$\begin{cases} |u_{k_x k_y t1}\rangle = \cos(t_{\frac{1}{6}})|u_{k_x k_y \frac{T}{6} 1}\rangle - \sin(t_{\frac{1}{6}})|2\rangle, \\ |u_{k_x k_y t2}\rangle = \sin(t_{\frac{1}{6}})|u_{k_x k_y \frac{T}{6} 1}\rangle + \cos(t_{\frac{1}{6}})|2\rangle, \\ |u_{k_x k_y t3}\rangle = |u_{k_x k_y \frac{T}{6} 3}\rangle. \end{cases} \quad (\text{a.10})$$

For $t \in \left(\frac{T}{3}, \frac{T}{2}\right]$, the states evolve as

$$\begin{cases} |u_{k_x k_y t1}\rangle = -\cos(t_{\frac{1}{3}})|2\rangle - \sin(t_{\frac{1}{3}})e^{-iK}|u_{k_x k_y \frac{T}{6} 1}\rangle, \\ |u_{k_x k_y t2}\rangle = \cos(t_{\frac{1}{3}})|u_{k_x k_y \frac{T}{6} 1}\rangle - \sin(t_{\frac{1}{3}})e^{iK}|2\rangle, \\ |u_{k_x k_y t3}\rangle = |u_{k_x k_y \frac{T}{6} 1}\rangle, \end{cases} \quad (\text{a.11})$$

where the notation $K = k_x + k_y$ has been introduced. For $t \in \left(\frac{T}{2}, \frac{2T}{3}\right]$, the states evolve as

$$\begin{cases} |u_{k_x k_y t1}\rangle = -\cos\left(\delta\left(\frac{\pi}{2} - t_{\frac{1}{2}}\right)\right)e^{-iK}|1\rangle \\ \quad + \sin\left(\delta\left(\frac{\pi}{2} - t_{\frac{1}{2}}\right)\right)e^{-ik_y}|3\rangle, \\ |u_{k_x k_y t2}\rangle = |2\left(\frac{T}{2}\right)\rangle, \\ |u_{k_x k_y t3}\rangle = \sin\left(\delta\left(\frac{\pi}{2} - t_{\frac{1}{2}}\right)\right)e^{-ik_x}|1\rangle \\ \quad + \cos\left(\delta\left(\frac{\pi}{2} - t_{\frac{1}{2}}\right)\right)|3\rangle. \end{cases} \quad (\text{a.12})$$

For $t \in \left(\frac{2T}{3}, \frac{5T}{6}\right]$, the states evolve as

$$\begin{cases} |u_{k_x k_y t1}\rangle = -\cos(t_{\frac{4}{6}})e^{-iK}|1\rangle + \sin(t_{\frac{4}{6}})e^{-ik_y}|2\rangle, \\ |u_{k_x k_y t2}\rangle = -\cos(t_{\frac{4}{6}})e^{iK}|2\rangle - \sin(t_{\frac{4}{6}})e^{ik_y}|1\rangle, \\ |u_{k_x k_y t3}\rangle = |3\rangle. \end{cases} \quad (\text{a.13})$$

For $t \in \left(\frac{5T}{6}, T\right)$, the states evolve as

$$\begin{cases} |u_{k_x k_y t1}\rangle = \cos(t_{\frac{5}{6}})e^{-ik_y}|2\rangle + \sin(t_{\frac{5}{6}})|1\rangle, \\ |u_{k_x k_y t2}\rangle = -\cos(t_{\frac{5}{6}})e^{ik_y}|1\rangle + \sin(t_{\frac{5}{6}})|2\rangle, \\ |u_{k_x k_y t3}\rangle = |3\rangle. \end{cases} \quad (\text{a.14})$$

GEOMETRIC PROPERTIES OF CRITICAL
FLOQUET DRIVES

B.1 PROOF OF PROPERTIES FOR PERIODIC POINTS

In this appendix, we give brief proofs of the properties of our periodic points listed in Sec. 9.2. For simplicity, we prove them for fixed points $x_*^\mp = x_{*1}^\mp$; the properties for periodic points with period $p = 2, 3, \dots$ follow by replacing f_\pm in (9.14) by f_\pm^p in (9.6).

To prove 1, we note that $f_\pm(-L/2) \leq -L/2$ is equivalent to $f_\pm(L/2) \leq L/2$ since $f_\pm \in \widetilde{\text{Diff}}_+(S^1)$, and thus, if the curve $y = f_\pm(x)$ crosses the straight line $y = x$ at a point where $f'_\pm \leq 1$, it must cross this line again at another point where $f'_\pm \geq 1$. Continuity of f_\pm ensures the alternating appearance of the fixed points. 2 is a standard property of stable fixed points; to find the rate, one can use the mean value theorem to conclude that $\lim_{m \rightarrow \infty} |x_{(m+1)t_{\text{cyc}}}^\mp(x) - x_*^\mp| / |x_{mt_{\text{cyc}}}^\mp(x) - x_*^\mp| = f'_\pm(x_*^\mp) < 1$. To prove 3, note that if $x_*^\mp = f_\pm(x_*^\mp)$ then also $f_\mp(y_*^\pm) = y_*^\pm$ by setting $x_*^\mp = f_1^{-1}(f_1(y_*^\pm) \pm v_{1,0}t_1)$ and rearranging. 4 follows using (9.9), (9.14), and $f_j \in \widetilde{\text{Diff}}_+(S^1)$.

B.2 PRACTICAL EQUATIONS FOR FIXED POINTS

For $p = 1$, the formulas in (9.6) and (9.7) can be written in a symmetric way for both \pm -components as follows.

First, define

$$F_j(\xi) = \int_0^\xi d\xi' \frac{1}{w_j(\xi')} \quad (\text{b.1})$$

for $j = 1, 2$. It follows that $F_j(\xi) = (v_j/Lv_{j,0})f_j(\xi L)$.

Second, define ξ_* by $L(v_{1,0}/v_1)\xi_* = f_1(x_*^\mp) \mp v_{1,0}t_1/2$. Using this, any fixed points $x_*^\mp = x_{*1}^\mp$ can be expressed as

$$x_*^\mp = f_1^{-1}(L(v_{1,0}/v_1)\xi_* \pm v_{1,0}t_1/2) = LF_1^{-1}(\xi_* \pm \tau_1/2). \quad (\text{b.2})$$

Third, inserting (b.2) into (9.6) and rearranging implies that x_*^\mp are given by solutions ξ_* to

$$\tau_2 = \int_{\xi_* + \tau_1/2}^{\xi_* - \tau_1/2} d\xi' \frac{w_1(F_1^{-1}(\xi'))}{w_2(F_1^{-1}(\xi'))} \quad (\text{b.3})$$

for given (τ_1, τ_2) .

Fourth, from (9.14) and the above, it follows that (9.7) is equivalent to that tangent points $x_c^\mp = x_{c1}^\mp$ are given by (b.2) with $\xi_* = \xi_c$ that also solves

$$\frac{w_2(F_1^{-1}(\xi_c - \tau_1/2))}{w_1(F_1^{-1}(\xi_c - \tau_1/2))} = \frac{w_2(F_1^{-1}(\xi_c + \tau_1/2))}{w_1(F_1^{-1}(\xi_c + \tau_1/2))}. \quad (\text{b.4})$$

Combining (b.3) and (b.4) gives an equation system for (τ_1, τ_2) for each solution ξ_c .

For the special case when $v_1(x) = v_1$ is constant, (9.6) and (9.7) for $p = 1$ can be written as

$$\tau_2 = \int_{\xi_* + \tau_1/2}^{\xi_* - \tau_1/2} d\xi' \frac{1}{w_2(\xi')} = F_2(\xi_* - \tau_1/2) - F_2(\xi_* + \tau_1/2) \quad (\text{b.5})$$

and

$$w_2(\xi_c - \tau_1/2) = w_2(\xi_c + \tau_1/2), \quad (\text{b.6})$$

respectively.

In general, it follows from the above that any fixed points for the right- and left-moving components (in addition to appearing in pairs of stable and unstable points within a component) come in pairs x_*^\mp given by (b.2) split between the components. This together with (9.14) implies

$$f'_\pm(x_*^\mp) = \frac{v_2(x_*^\mp)}{v_2(x_*^\pm)} \frac{v_1(x_*^\pm)}{v_1(x_*^\mp)}, \quad (\text{b.7})$$

and thus $f'_+(x_*^-)f'_-(x_*^+) = 1$ for each such pair. In other words, if one of these fixed points is stable, then the other is unstable, and vice versa.

The above equations are useful for practical computations, but we emphasize that one must take into account the symmetries for τ_1 and τ_2 when working with them, see Properties 3 and 4 in Sec. 9.2.

B.3 ANALYTICAL RESULTS FOR SPECIAL CASES

In this appendix, we study in greater detail two special cases of our 2-step Floquet drive with H_1 homogeneous and H_2 given first by Ex. 1 and second by Ex. 4 in Table 9.1.

PHASE-TRANSITION LINES FOR EX. 1 IN TABLE 9.1 Consider H_2 given by the deformation of Ex. 1 in Table 9.1, i.e.,

$$w_2(\xi) = 1 + g[2 \cos^2(\pi\xi) - 1], \quad (\text{b.8})$$

which can be seen as a regularization of SSD CFT. From (b.1) and $w_{j,0} = v_{j,0}/v_j$, we obtain $F_2(\xi) = F_{g\text{SSD}}(\xi)$ and $w_{2,0} = w_{g\text{SSD},0}$ with

$$F_{g\text{SSD}}(\xi) = \frac{\arctan(\sqrt{(1-g)/(1+g)} \tan(\pi\xi))}{\pi\sqrt{1-g^2}}, \quad (\text{b.9a})$$

$$w_{g\text{SSD},0} = \sqrt{1-g^2}. \quad (\text{b.9b})$$

It is straightforward to check that

$$F_{g\text{SSD}}(\xi) \xrightarrow{g \rightarrow 1^-} F_{\text{SSD}}(\xi) = \frac{\tan(\pi\xi)}{2\pi}, \quad (\text{b.10a})$$

$$w_{g\text{SSD},0} \xrightarrow{g \rightarrow 1^-} w_{\text{SSD},0} = 0 \quad (\text{b.10b})$$

and

$$F_{\text{SSD}}(\xi) \xrightarrow{g \rightarrow 0^+} \xi, \quad w_{g\text{SSD},0} \xrightarrow{g \rightarrow 0^+} 1. \quad (\text{b.11})$$

The limiting case in (b.10) explains why a regularization of SSD CFT is necessary: For instance, $v_{2,0} = v_2 w_{g\text{SSD},0}$ vanishes as $g \rightarrow 1^-$, meaning that f_2 in (9.9) would not be well defined and thus not be an element of $\widetilde{\text{Diff}}_+(S^1)$, cf. Sec. 9.2.

For $g > 0$, the only nontrivial solutions to (b.6) are $\xi_c = -1/2$ and 0. Inserting this together with (b.9) into (b.5) and making our translation symmetries in (τ_1, τ_2) -space manifest yields

$$\tau_2 = \frac{n}{\sqrt{1-g^2}} + \frac{2 \arctan\left(\sqrt{\frac{1-g}{1+g}} \tan(\pi[m-\tau_1]/2)\right)}{\pi \sqrt{1-g^2}} \quad (\text{b.12})$$

for $m, n \in \mathbb{Z}$. Clearly, it suffices to look at $(\tau_1, \tau_2) \in (0, 1) \times (0, 1/w_{g\text{SSD},0})$, and in this “unit cell” the transition lines are given by

$$\tau_2 = \frac{2 \arctan\left(\sqrt{\frac{1-g}{1+g}} \tan(\pi[1-\tau_1]/2)\right)}{\pi \sqrt{1-g^2}}, \quad (\text{b.13a})$$

$$\tau_2 = \frac{1}{\sqrt{1-g^2}} - \frac{2 \arctan\left(\sqrt{\frac{1-g}{1+g}} \tan(\pi\tau_1/2)\right)}{\pi \sqrt{1-g^2}}. \quad (\text{b.13b})$$

In the limit $g \rightarrow 1^-$, similar to (b.10), it follows from (b.13a) that

$$\tau_2 = \frac{\tan(\pi[1-\tau_1]/2)}{\pi} \quad (\text{b.14})$$

while (b.13b) disappears to infinity [except for $\tau_1 \in \mathbb{Z}$ that give rise to straight vertical lines, see Fig. 9.2(b)]. In the other limiting case, $g \rightarrow 0^+$, similar to (b.11), both (b.13a) and (b.13b) become

$$\tau_2 = 1 - \tau_1, \quad (\text{b.15})$$

i.e., the phase diagram consists of a straight “double” line describing an “empty” transition. The results in (b.13) and (b.14) are plotted in Figs. 9.2(a)–(b) (invoking the symmetries in τ_1 and τ_2).

PHASE DIAGRAMS DUE TO FIXED POINTS AND CUSPS IN THE HEATING RATE FOR EX. 4 IN TABLE 9.1 Consider H_2 given by the deformation of Ex. 4 in Table 9.1, i.e.,

$$w_2(\xi) = \frac{a}{b + \cos(2\pi\xi) + \sin(2\pi k\xi)} \quad (\text{b.16})$$

for $a > 0$, $b > 2$, and $k \in \mathbb{Z}^+$. As we will show, this case has the advantage of analytical tractability at the same time as the parts of the phase diagram due to only fixed points allow for interesting internal structure: There can be cusps in the heating rate and regions with different number of unstable fixed points.

For clarity, we stress that we will consider only fixed-point ($p = 1$) solutions to (9.6) in what follows.

First, we compute the transition lines between regions with different number of unstable fixed points. To do so, we note that (b.6) can be written as

$$\sin(\pi k \tau_1) \cos(2\pi k \xi_c) = \sin(\pi \tau_1) \sin(2\pi \xi_c), \quad (\text{b.17})$$

which has $2k$ solutions. Inserting these into (b.5) gives the transition lines. The obtained heating phases due to only fixed points are shown in Fig. b.1 for $a = 6$, $b = 3$, and different k . One can observe a simple pattern: If k increases by one, the number of leaf-shaped regions at the extremities of the phase diagram increases by one. Such leaves correspond to regions with four unstable fixed points (two for each component). Whenever these leaves intersect, their intersections have 6 unstable fixed points, and higher-order intersections will have more unstable fixed points. In the middle of the overall heating phase, some leaves also appear, but they do not intersect and therefore have four unstable fixed points each.

Second, we analytically show the existence of a cusp in the heating rate for the deformation in (b.16) with $a = 6$, $b = 3$, and $k = 2$. We focus on the large center leaf in Fig. 9.3(a) [equivalently, Fig. b.1(a)] due to fixed points only: The heating rate is then obtained by finding all ξ_* solving (b.5), computing the corresponding x_*^\mp , inserting these into (b.7) to obtain the derivatives, and finally inserting the latter into (9.8). For our particular choice of deformation, finding fixed points is equivalent to solving

$$2 \sin(\pi \tau_1) \cos(2\pi \xi_*) + \sin(2\pi \tau_1) \sin(4\pi \xi_*) = -12\pi \left(\tau_2 + \frac{\tau_1}{2} \right). \quad (\text{b.18})$$

In this case, the periodicities in the τ_1 - and τ_2 -directions are 1 and $1/2$, respectively. Thus, the center of the phase diagram in Fig. b.1(a) is $(\tau_1, \tau_2) = (1/2, 1/4)$, and Fig. 9.3(c) indicates that it corresponds to a cusp in the heating rate. Note that $(\tau_1, \tau_2) = (1/2, 1/4)$ lies in a heating phase with two unstable fixed points $x_{*,1}^-$ and $x_{*,2}^+$, one for each of the \pm -components, and is equivalent to $(1/2, -1/4)$ due to the symmetries illustrated in Fig. 9.2. To interpret the equations correctly, we use $\tau_2 \in [-1/2, 0]$ in practice: Solving (b.18) for $(\tau_1, \tau_2) = (1/2, -1/4)$ yields two solutions $\xi_*^1 = 1/4$ and $\xi_*^2 = -1/4$, and it follows from $x_{*,j}^\mp = L(\xi_*^j \pm 1/4)$ [cf. (b.2)] and (b.7) that $x_{*,1}^- = L/2$ and $x_{*,2}^+ = -L/2$ with $f'_+(x_{*,1}^-) = 2 = f'_-(x_{*,2}^+)$, i.e., both unstable fixed points yield the same contribution to the heating rate, see Fig. b.2.

To prove that $(\tau_1, \tau_2) = (1/2, 1/4)$ corresponds to a cusp in the heating rate, we set $\tau_1 = 1/2$ and study the fixed points as functions of τ_2 . The solutions to (b.18) are now (recall that we use $\tau_2 \in [-1/2, 0]$ in practice):

$$\begin{aligned} \xi_*^1 &= +(1/2\pi) \arccos(-3\pi[1 + 4\tau_2]/2), \\ \xi_*^2 &= -(1/2\pi) \arccos(-3\pi[1 + 4\tau_2]/2). \end{aligned} \quad (\text{b.19})$$

The corresponding $f'_+(x_{*,1}^-)$ and $f'_-(x_{*,2}^+)$ are plotted in Fig. b.2 as functions of τ_2 . Using (b.7), we obtain

$$\begin{aligned} \lim_{\tau_2 \rightarrow -1/4} \partial_{\tau_2} f'_+(x_{*,1}^-) &= -6\pi, \\ \lim_{\tau_2 \rightarrow -1/4} \partial_{\tau_2} f'_-(x_{*,2}^+) &= +6\pi, \end{aligned} \quad (\text{b.20})$$

implying that the maximum of $f'_+(x_{*,1}^-)$ and $f'_-(x_{*,2}^+)$ is not differentiable at $(\tau_1, \tau_2) = (1/2, 1/4)$. This together with (9.8) proves the existence of a cusp in the heating rate, and thus that this is a possibility in general.

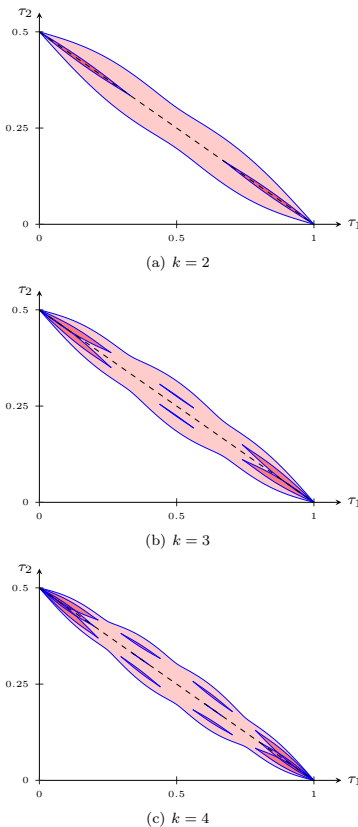


Figure b.1: Phase diagrams showing heating phases due to only fixed points for the special case when H_1 is homogeneous and H_2 is given by Ex. 4 with $a = 6$, $b = 3$, and (a) $k = 2$, (b) $k = 3$, or (c) $k = 4$. In all diagrams, the center leaf-shaped region in light pink contains two unstable fixed points (one for each of the \pm -components), while leaves in dark pink contain four or more (an intersection of two leaves with m unstable fixed points each yields a new leaf with $m + 2$ unstable fixed points). See the caption to Fig. 9.2 for further details.

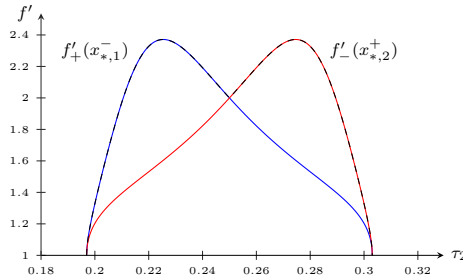


Figure b.2: Plots of $f'_+(x_{*,1}^-)$ (blue curve) and $f'_-(x_{*,2}^+)$ (red curve) obtained using (b.19) as a function of τ_2 for $\tau_1 = 1/2$ fixed. The black dashed curve is the maximum, corresponding to the heating rate through (9.8), and has a cusp at $\tau_2 = 1/4$.

B.4 COMPUTATION OF ENTANGLEMENT ENTROPY

In what follows, we compute the von-Neumann entanglement entropy $S_A(t)$ for a subsystem on the interval $A = [x, y]$ with the rest of the system. This can be defined as

$$S_A(t) = \lim_{m \rightarrow 1} \frac{1}{1-m} \log \left(\text{Tr} [\hat{\rho}_A(t)^m] \right), \quad (\text{b.21})$$

where $\hat{\rho}_A(t) = U_F^n \hat{\rho}_A U_F^{-n}$ for $t = nt_{\text{cyc}}$ and $\hat{\rho}_A$ is the reduced density matrix for the subsystem on A .

The computation of $S_A(t)$ can be done with the help of twist fields $\Phi_m(x; t)$, whose conformal weights are $\Delta_m^\pm = (c/24)(m - 1/m)$ [173]:

$$S_A(t) = \lim_{m \rightarrow 1} \frac{1}{1-m} \log [\langle 0 | \Phi_m(x; t) \Phi_m(y; t) | 0 \rangle], \quad (\text{b.22})$$

see [69] for a review. Using the result in (9.18) and taking the limit yields (9.19).

Before ending this appendix we give two more remarks:

First, for the more general case where the two components in the Hamiltonian have different drives, we note that the entanglement entropy can also decay linearly in time, different from cases (a) and (b) in Sec. 9.3. For example, this can happen in the following case:

(c) Suppose that there are at least two unstable periodic points $x_{*,1}^-$ and $x_{*,2}^-$ with respect to the right-moving component, while the left-moving component remains undriven (or vice versa), and that the interval is chosen as $A = [x_{*,1}^-, x_{*,2}^-]$, see Fig. b.3. In this case,

$$S_+(t) = - \frac{\log [f_+^{p'}(x_{*,1}^-)] + \log [f_+^{p'}(x_{*,2}^-)]}{pt_{\text{cyc}}} t + o(t), \\ S_-(t) = o(t). \quad (\text{b.23})$$

Since $f_+^{p'}(x_{*,1}^-)$ and $f_+^{p'}(x_{*,2}^-) > 1$, the entanglement entropy decays linearly in time. We stress that the system is still heating, i.e., the total energy grows

exponentially even though the entanglement entropy decreases. This generalizes previous results in [125] for Floquet drives in deformed CFTs where the Hamiltonian is a linear combination of the Virasoro generators $\{L_0^\pm, L_m^\pm, L_{-m}^\pm\}$ for some $m \in \mathbb{Z}^+$ to inhomogeneous CFT with general smooth deformations.

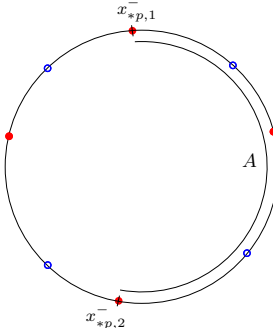


Figure b.3: Illustration of the additional case (c) described in this appendix for the entanglement entropy $S_A(t)$ in the heating phase. See the caption to Fig. 9.6 for further details.

Second, if there is only one unstable fixed point per component (by definition, there cannot be only one periodic point with period $p > 1$, if such exists), the entanglement entropy cannot grow for long times in the case of periodic boundary conditions (which we have here). However, using open boundary conditions, the right- and left-moving components are connected and the entanglement entropy grows linearly in time if A contains one of the two unstable fixed points, as discussed for the special case of $\mathfrak{sl}(2)$ -deformations in [124], where the deformed Hamiltonian is a linear combination of the Virasoro generators $\{L_0^\pm, L_1^\pm, L_{-1}^\pm\}$.

B.5 COMPUTATION OF MUTUAL INFORMATION

Below we compute the mutual information $I_{A;B}(t) = S_A(t) + S_B(t) - S_{A \cup B}(t)$ for two intervals $A = [x_1, x_2]$ and $B = [x_3, x_4]$. We give details only for the right-moving component (without loss of generality, since the two \pm -components commute). Moreover, it follows from Sec. 9.3 that the result is nontrivial if and only if A and B contain at least one unstable periodic point each, denoted $x_{*p,A}^-$ and $x_{*p,B}^- \neq x_{*p,A}^-$, respectively, see Fig. 9.8; we will assume this in what follows.

Computing $S_A(t)$ and $S_B(t)$ can be done using (9.19). To compute $S_{A \cup B}(t)$ requires a 4-point correlation function of twist fields (cf. Appendix b.4) of the form

$$\begin{aligned} & \left(\prod_{j=1}^4 \left[\frac{\partial x_t^-(x_j)}{\partial x} \right]^{\Delta_m^+} \right) \\ & \times \left(\frac{i\pi}{L \sin(\pi[x_t^-(x_1) - x_t^-(x_4)] + i0^+)/L} \right)^{2\Delta_m^+} \\ & \times \left(\frac{i\pi}{L \sin(\pi[x_t^-(x_2) - x_t^-(x_3)] + i0^+)/L} \right)^{2\Delta_m^+} \mathcal{F}(u), \end{aligned} \quad (\text{b.24})$$

where $\mathcal{F}(u)$ is the conformal block, which depends on the operator content of the theory, and

$$\begin{aligned} u = & \frac{\sin(\pi[x_t^-(x_1) - x_t^-(x_4)] + i0^+)/L)}{\sin(\pi[x_t^-(x_1) - x_t^-(x_2)] + i0^+)/L} \\ & \times \frac{\sin(\pi[x_t^-(x_2) - x_t^-(x_3)] + i0^+)/L)}{\sin(\pi[x_t^-(x_4) - x_t^-(x_3)] + i0^+)/L} \end{aligned} \quad (\text{b.25})$$

is the cross ratio. We will use that the conformal block $\mathcal{F}(u)$ does not contribute if u tends to a constant finite value different from 1, see, e.g., Appendix B of [125].

For the two cases (a) and (b) described in Sec. 9.3:

(a) Since $x_t^-(x_2)$ and $x_t^-(x_3)$ flow to $x_{*,p,AB}^-$, while $x_t^-(x_1)$ and $x_t^-(x_4)$ flow to two other different stable periodic points $x_{*,p,1}^-$ and $x_{*,p,4}^-$, it follows that u tends to 0, implying that $\mathcal{F}(u)$ does not contribute for large t and can be neglected in what follows. Due to Property 2 in Sec. 9.2, the contributions to the von-Neumann entanglement entropy $S_{A \cup B}(t)$ from $x_t^-(x_2)$ and $x_t^-(x_3)$ cancel [see the argument for the case (b) in Sec. 9.3], and thus the leading contribution from the right-moving component to $S_{A \cup B}(t)$ is

$$-\frac{c}{12} \log \left[\frac{\partial x_t^-(x_1)}{\partial x} \frac{\partial x_t^-(x_4)}{\partial x} \left(\frac{i\pi}{L \sin(\pi[x_t^-(x_1) - x_t^-(x_4)] + i0^+)/L} \right)^2 \right]. \quad (\text{b.26})$$

The derivative factors above decay exponentially as $x_t^-(x_1)$ and $x_t^-(x_4)$ flow to their respective stable periodic points, which implies that (b.26) goes as

$$-\frac{c}{12} \frac{\log[f_+^{p'}(x_{*,p,1}^-)] + \log[f_+^{p'}(x_{*,p,4}^-)]}{pt_{\text{cyc}}} t + o(t) \quad (\text{b.27})$$

for large t . This and the results for $S_A(t)$ and $S_B(t)$ [cf. (9.20)] imply that the leading contribution to $I_{A;B}(t)$ from the right-moving component is given by (9.22).

(b) We can repeat the argument in (a), recalling that $x_t^-(x_j)$ ($j = 1, 2, 3, 4$) flow to four different stable periodic points. Again, u tends to a constant different from 1, and thus $\mathcal{F}(u)$ does not contribute for large t , as before. The derivative terms in (b.24) will all decay exponentially, while the denominators

stay finite. It follows that the leading contribution to $S_{A \cup B}(t)$ is canceled by the corresponding ones to $S_A(t) + S_B(t)$, meaning that the contribution from the right-moving component to $I_{A;B}(t)$ does not change with time for large t .

To summarize, the intervals A and B have to contain at least one unstable periodic point each and to be separated by a single stable periodic point for $I_{A;B}(t)$ to grow linearly in time for large t .

We solve the recursion relation in (13.135) for the matrix in (13.133). We note that it is enough to solve the recursion for $I_{1,1}^{(n,M)}$ and $I_{1,2}^{(n,M)}$, since they are coupled to each other but decoupled from the rest:

$$\begin{aligned} I_{1,1}^{(n,M)} &= [\cosh^2(\nu) - \sinh^2(\nu)q_2^{2n}] I_{1,1}^{(n,M-1)} \\ &\quad + \frac{1}{2} \sinh(2\nu) (1 - q_2^{2n}) q_2^{2(M-1)n} q_1^{2(M-1)n} I_{1,2}^{(n,M-1)}, \\ I_{1,2}^{(n,M)} &= \frac{1}{2} \sinh(2\nu) (1 - q_2^{-2n}) q_2^{-2(M-1)n} q_1^{-2(M-1)n} I_{1,1}^{(n,M-1)} \\ &\quad + [\cosh^2(\nu) - \sinh^2(\nu)q_2^{-2n}] I_{1,2}^{(n,M-1)}. \end{aligned} \quad (\text{c.1})$$

The seed conditions for the recursion is $I_{1,1}^{(n,0)} = 1$ and $I_{1,2}^{(n,0)} = 0$. The second equation above can be written more symmetrically as

$$\begin{aligned} I_{1,2}^{(n,M)} q_2^{2(M-1)n} q_1^{2(M-1)n} &= \frac{1}{2} \sinh(2\nu) (1 - q_2^{-2n}) I_{1,1}^{(n,M-1)} \\ &\quad + [\cosh^2(\nu) - \sinh^2(\nu)q_2^{-2n}] I_{1,2}^{(n,M-1)} q_2^{2(M-1)n} q_1^{2(M-1)n}. \end{aligned} \quad (\text{c.2})$$

Therefore, multiplying by x^M for an arbitrary $x \in \mathbb{R}$,

$$\begin{aligned} I_{1,1}^{(n,M)} x^M &= [\cosh^2(\nu) - \sinh^2(\nu)q_2^{2n}] I_{1,1}^{(n,M-1)} x^M \\ &\quad + \frac{1}{2} \sinh(2\nu) (1 - q_2^{2n}) I_{1,2}^{(n,M-1)} q_2^{2(M-1)n} q_1^{2(M-1)n} x^M, \\ I_{1,2}^{(n,M)} q_2^{2(M-1)n} q_1^{2(M-1)n} x^M &= \frac{1}{2} \sinh(2\nu) (1 - q_2^{-2n}) I_{1,1}^{(n,M-1)} x^M \\ &\quad + [\cosh^2(\nu) - \sinh^2(\nu)q_2^{-2n}] I_{1,2}^{(n,M-1)} q_2^{2(M-1)n} q_1^{2(M-1)n} x^M. \end{aligned} \quad (\text{c.3})$$

Summing over M from 1 to ∞ , we obtain

$$\begin{aligned} I_{1,1}^{(n)}(x) - 1 &= [\cosh^2(\nu) - \sinh^2(\nu)q_2^{2n}] x I_{1,1}^{(n)}(x) \\ &\quad + \frac{1}{2} \sinh(2\nu) (1 - q_2^{2n}) x I_{1,2}^{(n)}(q_2^{2n} q_1^{2n} x), \\ q_2^{-2n} q_1^{-2n} I_{1,2}^{(n)}(q_2^{2n} q_1^{2n} x) &= \frac{1}{2} \sinh(2\nu) (1 - q_2^{-2n}) x I_{1,1}^{(n)}(x) \\ &\quad + [\cosh^2(\nu) - \sinh^2(\nu)q_2^{-2n}] x I_{1,2}^{(n)}(q_2^{2n} q_1^{2n} x), \end{aligned} \quad (\text{c.4})$$

where we defined the generating functions

$$I_{1,1}^{(n)}(x) = \sum_{M=0}^{\infty} I_{1,1}^{(n,M)} x^M, \quad I_{1,2}^{(n)}(x) = \sum_{M=0}^{\infty} I_{1,2}^{(n,M)} x^M. \quad (\text{c.5})$$

The solutions to the generating functions are

$$I_{1,1}^{(n)}(x) = \frac{2 - 2xq_1^{2n} [\cosh^2(\nu)q_2^{2n} - \sinh^2(\nu)]}{2x^2q_2^{2n}q_1^{2n} - x(1 + q_2^{2n})(1 + q_1^{2n}) - x \cosh(2\nu)(1 - q_2^{2n})(1 - q_1^{2n}) + 2}, \quad (\text{c.6})$$

$$I_{1,2}^{(n)}(q_2^{2n}q_1^{2n}x) = \frac{x \sinh(2\nu)(q_2^{2n} - 1)q_1^{2n}}{2x^2q_2^{2n}q_1^{2n} - x(1 + q_2^{2n})(1 + q_1^{2n}) - x \cosh(2\nu)(1 - q_2^{2n})(1 - q_1^{2n}) + 2}. \quad (\text{c.7})$$

We note that the first expression can be rewritten as

$$\begin{aligned} I_{1,1}^{(n)}(x) &= \frac{1 - \alpha_n q_2^n q_1^n x}{1 - \beta_n q_2^n q_1^n x + (q_2^n q_1^n x)^2} \\ &= \frac{1 - \alpha_n q_2^n q_1^n x}{(q_2^n q_1^n x - [\beta_n - \gamma_n]/2)(q_2^n q_1^n x - [\beta_n + \gamma_n]/2)} \end{aligned} \quad (\text{c.8})$$

with

$$\begin{aligned} \alpha_n &= [\cosh^2(\nu)q_2^n - \sinh^2(\nu)q_2^{-n}] q_1^n, \\ \beta_n &= \frac{(q_1^n + q_1^{-n})(q_2^n + q_2^{-n}) + (q_1^n - q_1^{-n})(q_2^n - q_2^{-n}) \cosh(2\nu)}{2}, \\ \gamma_n &= \sqrt{\beta_n^2 - 4}. \end{aligned} \quad (\text{c.9})$$

Noting that $(\beta_n \pm \gamma_n)/2 = \lambda_n^\pm$ in (13.126) and re-expanding

$$I_{1,1}^{(n)}(x) = \sum_{M=0}^{\infty} I_{1,1}^{(n,M)} x^M \quad (\text{c.10})$$

as a power series in x , we obtain

$$I_{1,1}^{(n,M)} = (q_2^n q_1^n)^M \frac{(\alpha_n - \lambda_n^-)(\lambda_n^-)^M - (\alpha_n - \lambda_n^+)(\lambda_n^+)^M}{\sqrt{\sigma_n - 4}}. \quad (\text{c.11})$$

The result alternatively reads

$$I_{1,1}^{(n,M)} = (q_2^n q_1^n)^M \left| \frac{(1 - \varepsilon_n)(\lambda_n^-)^M + (1 + \varepsilon_n)(\lambda_n^+)^M}{2} \right|^2 \quad (\text{c.12})$$

with

$$\varepsilon_n = -\frac{2[\sin(2\pi n\tau_1)\cos(2\pi n\tau_2) + \cos(2\pi n\tau_1)\sin(2\pi n\tau_2)\cosh(2\nu)]}{\sqrt{4 - \sigma_n^2}} \quad (\text{c.13})$$

using σ_n in (13.125). In conclusion, the Loschmidt echo after M cycles for the ground state is

$$L_\Omega(M[t_1 + t_2]) = \prod_{n>0} L_\Omega^{(n)}(M[t_1 + t_2]), \quad (\text{c.14})$$

$$L_\Omega^{(n)}(M[t_1 + t_2]) = \left| \frac{2}{(1 - \varepsilon_n)(\lambda_n^-)^M + (1 + \varepsilon_n)(\lambda_n^+)^M} \right|^2$$

with λ_n^\pm in (13.126) and ε_n in (c.13).

B I B L I O G R A P H Y

- [1] D. J. Thouless, M. Kohmoto, M. P. Nightingale, and M. den Nijs. “Quantized Hall Conductance in a Two-Dimensional Periodic Potential.” In: *Phys. Rev. Lett.* 49 (6 1982), pp. 405–408.
- [2] A Yu Kitaev. “Unpaired Majorana fermions in quantum wires.” In: *Physics-Uspekhi* 44.10S (2001), pp. 131–136.
- [3] Hua Chen, Wenguang Zhu, Di Xiao, and Zhenyu Zhang. “CO Oxidation Facilitated by Robust Surface States on Au-Covered Topological Insulators.” In: *Phys. Rev. Lett.* 107 (5 2011), p. 056804.
- [4] “Topological origin of equatorial waves.” In: 358 () .
- [5] P. W. Anderson. “Absence of Diffusion in Certain Random Lattices.” In: *Phys. Rev.* 109 (5 1958), pp. 1492–1505.
- [6] Ching-Kai Chiu, Jeffrey C. Y. Teo, Andreas P. Schnyder, and Shinsei Ryu. “Classification of topological quantum matter with symmetries.” In: *Rev. Mod. Phys.* 88 (3 2016), p. 035005.
- [7] Andreas P. Schnyder, Shinsei Ryu, Akira Furusaki, and Andreas W. W. Ludwig. “Classification of Topological Insulators and Superconductors.” In: *AIP Conference Proceedings* 1134 (2009). Ed. by Vladimir Lebedev and Mikhail Feigel'man, pp. 10–21.
- [8] Shinsei Ryu, Andreas P Schnyder, Akira Furusaki, and Andreas W W Ludwig. “Topological insulators and superconductors: tenfold way and dimensional hierarchy.” In: *New Journal of Physics* 12.6 (2010), p. 065010.
- [9] J. T. Chalker and P. D. Coddington. “Percolation, quantum tunnelling and the integer Hall effect.” In: *Journal of Physics C Solid State Physics* 21.14 (May 1988), pp. 2665–2679.
- [10] Masaru Onoda, Yshai Avishai, and Naoto Nagaosa. “Localization in a Quantum Spin Hall System.” In: *Phys. Rev. Lett.* 98 (7 2007), p. 076802.
- [11] Takahiro Morimoto, Akira Furusaki, and Christopher Mudry. “Anderson localization and the topology of classifying spaces.” In: *Phys. Rev. B* 91 (23 2015), p. 235111.
- [12] Mark Srednicki. “The approach to thermal equilibrium in quantized chaotic systems.” In: *Journal of Physics A: Mathematical and General* 32.7 (1999), pp. 1163–1175.
- [13] Dmitry A. Abanin, Ehud Altman, Immanuel Bloch, and Maksym Serbyn. “Colloquium : Many-body localization, thermalization, and entanglement.” In: *Reviews of Modern Physics* 91.2 (2019).
- [14] Sanjay Moudgalya, Nicolas Regnault, and B. Andrei Bernevig. “Entanglement of exact excited states of Affleck-Kennedy-Lieb-Tasaki models: Exact results, many-body scars, and violation of the strong eigenstate thermalization hypothesis.” In: *Phys. Rev. B* 98 (23 2018), p. 235156.

- [15] Daniel K. Mark, Cheng-Ju Lin, and Olexei I. Motrunich. “Unified structure for exact towers of scar states in the Affleck-Kennedy-Lieb-Tasaki and other models.” In: *Phys. Rev. B* 101 (19 2020), p. 195131.
- [16] Michael Schecter and Thomas Iadecola. “Weak Ergodicity Breaking and Quantum Many-Body Scars in Spin-1 XY Magnets.” In: *Phys. Rev. Lett.* 123 (14 2019), p. 147201.
- [17] J. Berges, Sz. Borsányi, and C. Wetterich. “Prethermalization.” In: *Phys. Rev. Lett.* 93 (14 2004), p. 142002.
- [18] M. Gring, M. Kuhnert, T. Langen, T. Kitagawa, B. Rauer, M. Schreitl, I. Mazets, D. Adu Smith, E. Demler, and J. Schmiedmayer. “Relaxation and Prethermalization in an Isolated Quantum System.” In: *Science* 337 (2012), p. 1318.
- [19] M. Olshanii. “Atomic Scattering in the Presence of an External Confinement and a Gas of Impenetrable Bosons.” In: *Phys. Rev. Lett.* 81 (5 1998), pp. 938–941.
- [20] Elliott H. Lieb, Robert Seiringer, and Jakob Yngvason. “One-Dimensional Bosons in Three-Dimensional Traps.” In: *Phys. Rev. Lett.* 91 (15 2003), p. 150401.
- [21] Bastien Lapierre, Titus Neupert, and Luka Trifunovic. “ N -band Hopf insulator.” In: *Phys. Rev. Res.* 3 (3 2021), p. 033045.
- [22] Bastien Lapierre, Titus Neupert, and Luka Trifunovic. “Topologically Localized Insulators.” In: *Phys. Rev. Lett.* 129 (25 2022), p. 256401.
- [23] Bastien Lapierre, Kenny Choo, Clément Tauber, Apoorv Tiwari, Titus Neupert, and Ramasubramanian Chitra. “Emergent black hole dynamics in critical Floquet systems.” In: *Phys. Rev. Research* 2 (2 2020), p. 023085.
- [24] Bastien Lapierre, Kenny Choo, Apoorv Tiwari, Clément Tauber, Titus Neupert, and R. Chitra. “Fine structure of heating in a quasiperiodically driven critical quantum system.” In: *Phys. Rev. Research* 2 (2020), p. 033461.
- [25] Bastien Lapierre and Per Moosavi. “Geometric approach to inhomogeneous Floquet systems.” In: *Phys. Rev. B* 103 (22 2021), p. 224303.
- [26] Kenny Choo, Bastien Lapierre, Clemens Kuhlenkamp, Apoorv Tiwari, Titus Neupert, and Ramasubramanian Chitra. “Thermal and dissipative effects on the heating transition in a driven critical system.” In: *SciPost Phys.* 13 (2022), p. 104.
- [27] Shouvik Datta, Bastien Lapierre, Per Moosavi, and Apoorv Tiwari. *Marginal quenches and drives in Tomonaga-Luttinger liquids*. 2022.
- [28] E. Abrahams, P. W. Anderson, D. C. Licciardello, and T. V. Ramakrishnan. “Scaling Theory of Localization: Absence of Quantum Diffusion in Two Dimensions.” In: *Phys. Rev. Lett.* 42 (10 1979), pp. 673–676.
- [29] Franz Wegner. “The mobility edge problem: Continuous symmetry and a conjecture.” In: *Zeitschrift für Physik B Condensed Matter* 35.3 (Sept. 1979), pp. 207–210.
- [30] K.B. Efetov. “Supersymmetry and theory of disordered metals.” In: *Advances in Physics* 32.1 (1983), pp. 53–127.

- [31] Ferdinand Evers and Alexander D. Mirlin. “Anderson transitions.” In: *Rev. Mod. Phys.* 80 (4 2008), pp. 1355–1417.
- [32] C. M Aegerter, M Störzer, and G Maret. “Experimental determination of critical exponents in Anderson localisation of light.” In: *Eoptiurlphysics Letters (EPL)* 75.4 (2006), pp. 562–568.
- [33] T. Sperling, W. Bührer, C. M. Aegerter, and G. Maret. “Direct determination of the transition to localization of light in three dimensions.” In: *Nature Photonics* 7.1 (2012), 48–52.
- [34] Hefei Hu, A. Strybulevych, J. H. Page, S. E. Skipetrov, and B. A. van Tiggelen. “Localization of ultrasound in a three-dimensional elastic network.” In: *Nature Physics* 4.12 (2008), 945–948.
- [35] J. Fröhlich, F. Martinelli, E. Scoppola, and T. Spencer. “Constructive proof of localization in the Anderson tight binding model.” In: *Communications in Mathematical Physics* 101.1 (Mar. 1985), pp. 21–46.
- [36] Y. Y. Atas, E. Bogomolny, O. Giraud, and G. Roux. “Distribution of the Ratio of Consecutive Level Spacings in Random Matrix Ensembles.” In: *Phys. Rev. Lett.* 110 (8 2013), p. 084101.
- [37] F. D. M. Haldane. “Nonlinear Field Theory of Large-Spin Heisenberg Antiferromagnets: Semiclassically Quantized Solitons of the One-Dimensional Easy-Axis Néel State.” In: *Phys. Rev. Lett.* 50 (15 1983), pp. 1153–1156.
- [38] D. J. Thouless. “Quantization of particle transport.” In: *Phys. Rev. B* 27 (10 1983), pp. 6083–6087.
- [39] J. T. Chalker and P. D. Coddington. “Percolation, quantum tunnelling and the integer Hall effect.” In: *Journal of Physics C Solid State Physics* 21.14 (May 1988), pp. 2665–2679.
- [40] Jian Li, Rui-Lin Chu, J. K. Jain, and Shun-Qing Shen. “Topological Anderson Insulator.” In: *Phys. Rev. Lett.* 102 (13 2009), p. 136806.
- [41] Alexander Altland, Dmitry Bagrets, Lars Fritz, Alex Kamenev, and Hanno Schmiedt. “Quantum Criticality of Quasi-One-Dimensional Topological Anderson Insulators.” In: *Phys. Rev. Lett.* 112 (20 2014), p. 206602.
- [42] Emil Prodan. “Disordered topological insulators: a non-commutative geometry perspective.” In: *Journal of Physics A: Mathematical and Theoretical* 44.11 (2011), p. 113001.
- [43] Hoi Chun Po, Haruki Watanabe, and Ashvin Vishwanath. “Fragile Topology and Wannier Obstructions.” In: *Phys. Rev. Lett.* 121 (12 2018), p. 126402.
- [44] Ricardo Kennedy. “Homotopy Theory of Topological Insulators.” PhD thesis. Universität zu Köln, 2014.
- [45] Barry Bradlyn, L. Elcoro, Jennifer Cano, M. G. Vergniory, Zhijun Wang, C. Felser, M. I. Aroyo, and B. Andrei Bernevig. “Topological quantum chemistry.” In: *Nature* 547 (2017), p. 298.
- [46] Hoi Chun Po, Ashvin Vishwanath, and Haruki Watanabe. “Symmetry-based indicators of band topology in the 230 space groups.” In: *Nature Comm.* 8 (2017), p. 50.

- [47] Wladimir A. Benalcazar, B. Andrei Bernevig, and Taylor L. Hughes. “Quantized Electric Multipole Insulators.” In: *Science* 357 (2017), p. 61.
- [48] Zhi-Da Song, Luis Elcoro, and B. Andrei Bernevig. “Twisted bulk-boundary correspondence of fragile topology.” In: *Science* 367.6479 (2020), pp. 794–797.
- [49] A. Alexandradinata, Aleksandra Nelson, and Alexey A. Soluyanov. “Teleportation of Berry curvature on the surface of a Hopf insulator.” In: *Phys. Rev. B* 103 (4 2021), p. 045107.
- [50] Joel E. Moore, Ying Ran, and Xiao-Gang Wen. “Topological Surface States in Three-Dimensional Magnetic Insulators.” In: *Phys. Rev. Lett.* 101 (18 2008), p. 186805.
- [51] Aleksandra Nelson, Titus Neupert, Tomas Bzdusek, and A. Alexandradinata. “Multicellularity of delicate topological insulators.” In: *arXiv e-prints*, arXiv:2009.01863 (Sept. 2020), arXiv:2009.01863.
- [52] Paraj Titum, Erez Berg, Mark S. Rudner, Gil Refael, and Netanel H. Lindner. “Anomalous Floquet-Anderson Insulator as a Nonadiabatic Quantized Charge Pump.” In: *Phys. Rev. X* 6 (2 2016), p. 021013.
- [53] Paraj Titum, Netanel H. Lindner, Mikael C. Rechtsman, and Gil Refael. “Disorder-Induced Floquet Topological Insulators.” In: *Phys. Rev. Lett.* 114 (5 2015), p. 056801.
- [54] Mark S. Rudner, Netanel H. Lindner, Erez Berg, and Michael Levin. “Anomalous Edge States and the Bulk-Edge Correspondence for Periodically Driven Two-Dimensional Systems.” In: *Phys. Rev. X* 3 (3 2013), p. 031005.
- [55] P. Di Francesco, P. Mathieu, and D. Senechal. *Conformal Field Theory*. Graduate Texts in Contemporary Physics. New York: Springer, 1997.
- [56] Paul H. Ginsparg. “Applied conformal field theory.” In: *Les Houches Summer School in Theoretical Physics: Fields, Strings, Critical Phenomena Les Houches, France, June 28-August 5, 1988*. 1988, pp. 1–168.
- [57] David Simmons-Duffin. *A Semidefinite Program Solver for the Conformal Bootstrap*. 2015.
- [58] William Berdanier, Michael Kolodrubetz, Romain Vasseur, and Joel E. Moore. “Floquet Dynamics of Boundary-Driven Systems at Criticality.” In: *Phys. Rev. Lett.* 118 (26 2017), p. 260602.
- [59] Luca D’Alessio, Yariv Kafri, Anatoli Polkovnikov, and Marcos Rigol. “From quantum chaos and eigenstate thermalization to statistical mechanics and thermodynamics.” In: *Advances in Physics* 65.3 (2016), pp. 239–362.
- [60] Vedika Khemani, Michael Hermele, and Rahul Nandkishore. “Localization from Hilbert space shattering: From theory to physical realizations.” In: *Phys. Rev. B* 101 (17 2020), p. 174204.
- [61] Toshiya Kinoshita, Trevor Wenger, and David S. Weiss. “A quantum Newton’s cradle.” In: *Nature* 440.7086 (Apr. 2006), pp. 900–903.

- [62] Marcos Rigol, Vanja Dunjko, Vladimir Yoptiurlvsky, and Maxim Olshanii. “Relaxation in a Completely Integrable Many-Body Quantum System: An iAb Initio/iStudy of the Dynamics of the Highly Excited States of 1D Lattice Hard-Core Bosons.” In: *Physical Review Letters* 98.5 (2007).
- [63] Lev Vidmar and Marcos Rigol. “Generalized Gibbs ensemble in integrable lattice models.” In: *Journal of Statistical Mechanics: Theory and Experiment* 2016.6 (2016), p. 064007.
- [64] Amy C. Cassidy, Charles W. Clark, and Marcos Rigol. “Generalized Thermalization in an Integrable Lattice System.” In: *Phys. Rev. Lett.* 106 (14 2011), p. 140405.
- [65] Olalla A. Castro-Alvaredo, Benjamin Doyon, and Takato Yoshimura. “Emergent Hydrodynamics in Integrable Quantum Systems Out of Equilibrium.” In: *Phys. Rev. X* 6 (4 2016), p. 041065.
- [66] Bruno Bertini, Mario Collura, Jacopo De Nardis, and Maurizio Fagotti. “Transport in Out-of-Equilibrium XXZ Chains: Exact Profiles of Charges and Currents.” In: *Phys. Rev. Lett.* 117 (20 2016), p. 207201.
- [67] Pasquale Calabrese and John Cardy. “Evolution of entanglement entropy in one-dimensional systems.” In: *J. Stat. Mech.* 2005 (2005), P04010.
- [68] Pasquale Calabrese and John Cardy. “Quantum quenches in extended systems.” In: *J. Stat. Mech.* 2007 (2007), P06008.
- [69] Pasquale Calabrese and John Cardy. “Quantum quenches in 1+1 dimensional conformal field theories.” In: *J. Stat. Mech.* 2016 (2016), p. 064003.
- [70] Marc Cheneau, Peter Barmettler, Dario Poletti, Manuel Endres, Peter Schauß, Takeshi Fukuhara, Christian Gross, Immanuel Bloch, Corinna Kollath, and Stefan Kuhr. “Light-cone-like spreading of correlations in a quantum many-body system.” In: *Nature* 481.7382 (2012), pp. 484–487.
- [71] John Cardy. “Thermalization and revivals after a quantum quench in conformal field theory.” In: *Phys. Rev. Lett.* 112 (2014), p. 220401.
- [72] Pasquale Calabrese and John Cardy. “Entanglement entropy and conformal field theory.” In: *J. Phys.* A42 (2009), p. 504005.
- [73] M. A. Cazalilla. “Effect of Suddenly Turning on Interactions in the Luttinger Model.” In: *Phys. Rev. Lett.* 97 (2006), p. 156403.
- [74] Juho Häppälä, Gábor B. Halász, and Alioscia Hamma. “Universality and robustness of revivals in the transverse field XY model.” In: *Phys. Rev. A* 85 (3 2012), p. 032114.
- [75] John Cardy. “Quantum Quenches to a Critical Point in One Dimension: some further results.” In: (2015).
- [76] Bruno Bertini, Fabian H. L. Essler, Stefan Groha, and Neil J. Robinson. “Prethermalization and Thermalization in Models with Weak Integrability Breaking.” In: *Phys. Rev. Lett.* 115 (18 2015), p. 180601.
- [77] Alexei Kitaev. *A simple model of quantum holography*.
- [78] Daniel A. Roberts, Douglas Stanford, and Leonard Susskind. “Localized shocks.” In: *Journal of High Energy Physics* 2015.3 (2015).

- [79] Jun Li, Ruihua Fan, Hengyan Wang, Bingtian Ye, Bei Zeng, Hui Zhai, Xinhua Peng, and Jiangfeng Du. “Measuring Out-of-Time-Order Correlators on a Nuclear Magnetic Resonance Quantum Simulator.” In: *Phys. Rev. X* 7 (3 2017), p. 031011.
- [80] Ivan Kukuljan, Sašo Grozdanov, and Tomaž Prosen. “Weak quantum chaos.” In: *Physical Review B* 96.6 (2017).
- [81] Jordan S. Cotler, Guy Gur-Ari, Masanori Hanada, Joseph Polchinski, Phil Saad, Stephen H. Shenker, Douglas Stanford, Alexandre Streicher, and Masaki Tezuka. “Black holes and random matrices.” In: *Journal of High Energy Physics* 2017.5 (2017).
- [82] Jonah Kudler-Flam, Laimei Nie, and Shinsei Ryu. “Conformal field theory and the web of quantum chaos diagnostics.” In: *Journal of High Energy Physics* 2020.1 (2020).
- [83] Pavan Hosur, Xiao-Liang Qi, Daniel A. Roberts, and Beni Yoshida. “Chaos in quantum channels.” In: *Journal of High Energy Physics* 2016.2 (2016).
- [84] Amos Chan, Andrea De Luca, and J. T. Chalker. “Spectral Statistics in Spatially Extended Chaotic Quantum Many-Body Systems.” In: *Physical Review Letters* 121.6 (2018).
- [85] Bruno Bertini, Pavel Kos, and Tomaz Prosen. “Exact Spectral Form Factor in a Minimal Model of Many-Body Quantum Chaos.” In: *Phys. Rev. Lett.* 121 (26 2018), p. 264101.
- [86] Jean Ginibre. “Statistical Ensembles of Complex, Quaternion, and Real Matrices.” In: *Journal of Mathematical Physics* 6.3 (Mar. 1965), pp. 440–449.
- [87] Saumya Shivam, Andrea De Luca, David A. Huse, and Amos Chan. *Many-body quantum chaos and emergence of Ginibre ensemble*. 2022.
- [88] Chunxiao Liu, Farzan Vafa, and Cenke Xu. “Symmetry-protected topological Hopf insulator and its generalizations.” In: *Phys. Rev. B* 95 (16 2017), p. 161116.
- [89] Rahul Roy and Fenner Harper. “Periodic table for Floquet topological insulators.” In: *Phys. Rev. B* 96 (15 2017), p. 155118.
- [90] Junyeong Ahn, Dongwook Kim, Youngkuk Kim, and Bohm-Jung Yang. “Band Topology and Linking Structure of Nodal Line Semimetals with Z_2 Monopole Charges.” In: *Phys. Rev. Lett.* 121 (10 2018), p. 106403.
- [91] QuanSheng Wu, Alexey A. Soluyanov, and Tomas Bzdusek. “Non-Abelian band topology in noninteracting metals.” In: *Science* 365.6459 (2019), pp. 1273–1277.
- [92] Apoorv Tiwari and Tomas Bzdusek. “Non-Abelian topology of nodal-line rings in \mathcal{PT} -symmetric systems.” In: *Phys. Rev. B* 101 (19 2020), p. 195130.
- [93] Andrew M. Essin, Ari M. Turner, Joel E. Moore, and David Vanderbilt. “Orbital magnetoelectric coupling in band insulators.” In: *Phys. Rev. B* 81 (20 2010), p. 205104.
- [94] L. Pontryagin. “A classification of mappings of the three-dimensional complex into the two-dimensional sphere.” In: *Rec. Math.* 9 (51 1941), p. 331.

- [95] Ari M. Turner, Yi Zhang, Roger S. K. Mong, and Ashvin Vishwanath. “Quantized response and topology of magnetic insulators with inversion symmetry.” In: *Phys. Rev. B* 85 (2012), p. 165120.
- [96] Luka Trifunovic and Piet W. Brouwer. “Bott periodicity for the topological classification of gapped states of matter with reflection symmetry.” In: *Phys. Rev. B* 96 (19 2017), p. 195109.
- [97] A. Hatcher. *Vector Bundles and K-Theory*. 2003.
- [98] F. Nur Ünal, André Eckardt, and Robert-Jan Slager. “Hopf characterization of two-dimensional Floquet topological insulators.” In: *Phys. Rev. Research* 1 (2 2019), p. 022003.
- [99] Adrien Bouhon, Tomas Bzdusek, and Robert-Jan Slager. “Geometric approach to fragile topology beyond symmetry indicators.” In: *Phys. Rev. B* 102 (11 2020), p. 115135.
- [100] Adrien Bouhon, QuanSheng Wu, Robert-Jan Slager, Hongming Weng, Oleg V. Yazyev, and Tomas Bzdusek. “Non-Abelian reciprocal braiding of Weyl points and its manifestation in ZrTe.” In: *Nature Physics* 16.11 (2020), pp. 1137–1143.
- [101] Xiao-Liang Qi and Shou-Cheng Zhang. “Spin-Charge Separation in the Quantum Spin Hall State.” In: *Phys. Rev. Lett.* 101 (2008), p. 086802.
- [102] Luka Trifunovic. “Bulk-and-edge to corner correspondence.” In: *Phys. Rev. Research* 2 (4 2020), p. 043012.
- [103] Thomas Olsen, Maryam Taherinejad, David Vanderbilt, and Ivo Souza. “Surface theorem for the Chern-Simons axion coupling.” In: *Phys. Rev. B* 95 (7 2017), p. 075137.
- [104] Penghao Zhu, Taylor L. Hughes, and A. Alexandradinata. “Quantized surface magnetism and higher-order topology: Application to the Hopf insulator.” In: *Phys. Rev. B* 103 (1 2021), p. 014417.
- [105] Shang Ren, Ivo Souza, and David Vanderbilt. “Quadrupole moments, edge polarizations, and corner charges in the Wannier representation.” In: *Phys. Rev. B* 103 (3 2021), p. 035147.
- [106] P Streda. “Theory of quantised Hall conductivity in two dimensions.” In: *Journal of Physics C: Solid State Physics* 15.22 (1982), pp. L717–L721.
- [107] Luka Trifunovic, Seishiro Ono, and Haruki Watanabe. “Geometric orbital magnetization in adiabatic processes.” In: *Phys. Rev. B* 100 (5 2019), p. 054408.
- [108] T. Thonhauser, Davide Ceresoli, David Vanderbilt, and R. Resta. “Orbital Magnetization in Periodic Insulators.” In: *Phys. Rev. Lett.* 95 (13 2005), p. 137205.
- [109] Michael Victor Berry. “Quantal phase factors accompanying adiabatic changes.” In: *Proceedings of the Royal Society of London. A. Mathematical and Physical Sciences* 392.1802 (1984), pp. 45–57.
- [110] T. Thonhauser and David Vanderbilt. “Insulator/Chern-insulator transition in the Haldane model.” In: *Physical Review B* 74.23 (2006).
- [111] W. P. Su, J. R. Schrieffer, and A. J. Heeger. “Solitons in Polyacetylene.” In: *Phys. Rev. Lett.* 42 (25 1979), pp. 1698–1701.

- [112] David M. Long, Philip J. D. Crowley, and Anushya Chandran. “Nonadiabatic Topological Energy Pumps with Quasiperiodic Driving.” In: *Phys. Rev. Lett.* 126 (10 2021), p. 106805.
- [113] Juntao Song and Emil Prodan. “AIII and BDI topological systems at strong disorder.” In: *Phys. Rev. B* 89 (22 2014), p. 224203.
- [114] Vadim Oganesyan and David A. Huse. “Localization of interacting fermions at high temperature.” In: *Phys. Rev. B* 75 (15 2007), p. 155111.
- [115] J. Šuntajs, T. Prosen, and L. Vidmar. “Spectral properties of three-dimensional Anderson model.” In: *Annals of Physics* (2021), p. 168469.
- [116] Arijit Kundu, Mark Rudner, Erez Berg, and Netanel H. Lindner. “Quantized large-bias current in the anomalous Floquet-Anderson insulator.” In: *Phys. Rev. B* 101 (4 2020), p. 041403.
- [117] Max Geier, Luka Trifunovic, Max Hoskam, and Piet W. Brouwer. “Second-order topological insulators and superconductors with an order-two crystalline symmetry.” In: *Phys. Rev. B* 97 (20 2018), p. 205135.
- [118] S A Sato, P Tang, M A Sentef, U De Giovannini, H Hübener, and A Rubio. “Light-induced anomalous Hall effect in massless Dirac fermion systems and topological insulators with dissipation.” In: *New Journal of Physics* 21.9 (2019), p. 093005.
- [119] Akira Furusaki. “Anderson Localization due to a Random Magnetic Field in Two Dimensions.” In: *Phys. Rev. Lett.* 82 (3 1999), pp. 604–607.
- [120] Jérôme Dubail, Jean-Marie Stéphan, Jacopo Viti, and Pasquale Calabrese. “Conformal field theory for inhomogeneous one-dimensional quantum systems: the example of non-interacting Fermi gases.” In: *SciPost Phys.* 2 (2017), p. 002.
- [121] Jerome Dubail, Jean-Marie Stéphan, and Pasquale Calabrese. “Emergence of curved light-cones in a class of inhomogeneous Luttinger liquids.” In: *SciPost Physics* 3, 019 (2017), p. 019.
- [122] Mohammadamin Tajik et al. *Experimental Observation of Curved Light-Cones in a Quantum Field Simulator.* 2022.
- [123] Xueda Wen and Jie-Qiang Wu. “Floquet conformal field theory.” In: (2018).
- [124] Xueda Wen and Jie-Qiang Wu. “Quantum dynamics in sine-square deformed conformal field theory: Quench from uniform to non-uniform conformal field theory.” In: *Phys. Rev.* B97.18 (2018), p. 184309.
- [125] Ruihua Fan, Yingfei Gu, Ashvin Vishwanath, and Xueda Wen. “Emergent Spatial Structure and Entanglement Localization in Floquet Conformal Field Theory.” In: *Phys. Rev. X* 10 (3 2020), p. 031036.
- [126] Malthe Andersen, Frederik Nørkjær, and Nikolaj Thomas Zinner. “Real-time correlation function of Floquet conformal fields.” In: *Phys. Rev. D* 103 (5 2021), p. 056005.
- [127] Diptarka Das, Roopayan Ghosh, and Krishnendu Sengupta. “Conformal Floquet dynamics with a continuous drive protocol.” In: *Journal of High Energy Physics* 2021.5 (2021).

- [128] Dmitry S. Ageev, Andrey A. Bagrov, and Askar A. Iliasov. “Deterministic chaos and fractal entropy scaling in Floquet conformal field theories.” In: *Phys. Rev. B* 103 (10 2021), p. L100302.
- [129] Ruihua Fan, Yingfei Gu, Ashvin Vishwanath, and Xueda Wen. “Floquet conformal field theories with generally deformed Hamiltonians.” In: *SciPost Physics* 10.2 (2021).
- [130] Bo Han and Xueda Wen. “Classification of SL2 deformed Floquet conformal field theories.” In: *Physical Review B* 102.20 (2020).
- [131] Xueda Wen, Ruihua Fan, Ashvin Vishwanath, and Yingfei Gu. “Periodically, quasiperiodically, and randomly driven conformal field theories.” In: *Phys. Rev. Research* 3 (2 2021), p. 023044.
- [132] Xueda Wen, Yingfei Gu, Ashvin Vishwanath, and Ruihua Fan. “Periodically, Quasi-periodically, and Randomly Driven Conformal Field Theories (II): Furstenberg’s Theorem and Exceptions to Heating Phases.” In: *SciPost Phys.* 13 (2022), p. 082.
- [133] Hosho Katsura. “Sine-square deformation of solvable spin chains and conformal field theories.” In: *Journal of Physics A: Mathematical and Theoretical* 45.11 (2012), p. 115003.
- [134] Kouichi Okunishi. “Sine-square deformation and Möbius quantization of 2D conformal field theory.” In: *Progress of Theoretical and Experimental Physics* 2016.6 (June 2016).
- [135] Nobuyuki Ishibashi and Tsukasa Tada. “Infinite circumference limit of conformal field theory.” In: *Journal of Physics A: Mathematical and Theoretical* 48.31 (2015), p. 315402.
- [136] Nobuyuki Ishibashi and Tsukasa Tada. “Dipolar quantization and the infinite circumference limit of two-dimensional conformal field theories.” In: *Int. J. Mod. Phys.* A31.32 (2016), p. 1650170.
- [137] Xueda Wen, Shinsei Ryu, and Andreas W. W. Ludwig. “Evolution operators in conformal field theories and conformal mappings: Entanglement Hamiltonian, the sine-square deformation, and others.” In: *Physical Review B* 93.23 (2016).
- [138] Ian MacCormack, Aike Liu, Masahiro Nozaki, and Shinsei Ryu. “Holographic duals of inhomogeneous systems: the rainbow chain and the sine-square deformation model.” In: *Journal of Physics A: Mathematical and Theoretical* 52.50 (2019), p. 505401.
- [139] Paola Ruggiero, Yannis Brun, and Jérôme Dubail. “Conformal field theory on top of a breathing one-dimensional gas of hard core bosons.” In: *SciPost Phys.* 6 (4 2019), p. 51.
- [140] R.B. Mann, A. Shiekh, and L. Tarasov. “Classical and quantum properties of two-dimensional black holes.” In: *Nuclear Physics B* 341.1 (1990), pp. 134 –154.
- [141] J. D. Brown, Marc Henneaux, and Claudio Teitelboim. “Black holes in two spacetime dimensions.” In: *Phys. Rev. D* 33 (2 1986), pp. 319–323.
- [142] R. B. Mann, S. M. Morsink, A. E. Sikkema, and T. G. Steele. “Semiclassical gravity in 1+1 dimensions.” In: *Phys. Rev. D* 43 (12 1991), pp. 3948–3957.

- [143] John Cardy and Erik Tonni. “Entanglement hamiltonians in two-dimensional conformal field theory.” In: *J. Stat. Mech.* 1612.12 (2016), p. 123103.
- [144] Somnath Maity, Utso Bhattacharya, Amit Dutta, and Diptiman Sen. “Fibonacci steady states in a driven integrable quantum system.” In: *Phys. Rev. B* 99 (2 2019), p. 020306.
- [145] Philipp T. Dumitrescu, Romain Vasseur, and Andrew C. Potter. “Logarithmically Slow Relaxation in Quasiperiodically Driven Random Spin Chains.” In: *Phys. Rev. Lett.* 120 (7 2018), p. 070602.
- [146] Dominic V. Else, Wen Wei Ho, and Philipp T. Dumitrescu. “Long-Lived Interacting Phases of Matter Protected by Multiple Time-Translation Symmetries in Quasiperiodically Driven Systems.” In: *Physical Review X* 10.2 (2020).
- [147] Krzysztof Giergiel, and Krzysztof Sacha. “Discrete time quasicrystals.” In: *Phys. Rev. B* 99 (22 2019), p. 220303.
- [148] Hongzheng Zhao, Florian Mintert, and Johannes Knolle. “Floquet time spirals and stable discrete-time quasicrystals in quasiperiodically driven quantum many-body systems.” In: *Physical Review B* 100.13 (22 2019), p. 220303.
- [149] Dov Levine and Paul Joseph Steinhardt. “Quasicrystals: A New Class of Ordered Structures.” In: *Phys. Rev. Lett.* 53 (26 1984), pp. 2477–2480.
- [150] J. Bellissard, B. Iochum, E. Scoppola, and D. Testard. “Spectral properties of one-dimensional quasi-crystals.” In: *Comm. Math. Phys.* 125.3 (22 1989), pp. 527–543.
- [151] Stephen Strogatz. *Nonlinear Dynamics And Chaos: With Applications To Physics, Biology, Chemistry, And Engineering (Studies in Nonlinearity)*. Vol. 99. Westview Press, 2001, p. 220303.
- [152] Marcelo Viana. *Lectures on Lyapunov Exponents*. Vol. 99. Cambridge Studies in Advanced Mathematics. Cambridge University Press, 2014, p. 220303.
- [153] Mahito Kohmoto, Bill Sutherland, and Chao Tang. “Critical wave functions and a Cantor-set spectrum of a one-dimensional quasicrystal model.” In: *Phys. Rev. B* 35 (3 1987), pp. 1020–1033.
- [154] Leo P. Kadanoff and Chao Tang. “Escape from strange repellers.” In: *Proceedings of the National Academy of Sciences* 81.4 (22 1984), pp. 1276–1279.
- [155] Mahito Kohmoto, Leo P. Kadanoff, and Chao Tang. “Localization Problem in One Dimension: Mapping and Escape.” In: *Phys. Rev. Lett.* 50 (23 1983), pp. 1870–1872.
- [156] Enrique Maciá. “Thermal conductivity of one-dimensional Fibonacci quasicrystals.” In: *Phys. Rev. B* 61 (10 2000), pp. 6645–6653.
- [157] András Sütő. “The spectrum of a quasiperiodic Schrödinger operator.” In: *Communications in Mathematical Physics* 111.3 (22 Sept. 1987), pp. 409–415.
- [158] William Yessen. *Newhouse phenomena in the Fibonacci trace map*. 2015.
- [159] David Damanik, Anton Gorodetski, and William Yessen. “The Fibonacci Hamiltonian.” In: *Inventiones mathematicae* 206.3 (22 2016), 629–692.

- [160] M. Baake, U. Grimm, and D. Joseph. “Trace maps, invariants, and some of their applications.” In: *International Journal of Modern Physics B* 07.06n07 (22 1993), 1527–1550.
- [161] Andras Suto. “Singular continuous spectrum on a cantor set of zero Lebesgue measure for the Fibonacci Hamiltonian.” In: *J. Stat. Phys.* 56 (22 Aug. 1989), pp. 525–531.
- [162] David Damanik and Anton Gorodetski. “Spectral and Quantum Dynamical Properties of the Weakly Coupled Fibonacci Hamiltonian.” In: *Communications in Mathematical Physics* 305 (22 Jan. 2010), p. 220303.
- [163] Krzysztof Gawedzki, Edwin Langmann, and Per Moosavi. “Finite-Time Universality in Nonequilibrium CFT.” In: *Journal of Statistical Physics* 172.2 (22 2018), 353–378.
- [164] Edwin Langmann and Per Moosavi. “Diffusive Heat Waves in Random Conformal Field Theory.” In: *Phys. Rev. Lett.* 122 (2 2019), p. 020201.
- [165] P. Moosavi. “Inhomogeneous Conformal Field Theory Out of Equilibrium.” In: *Ann. Henri Poincaré* 99 (22 2021), p. 220303.
- [166] Yanting Cheng and Zhe-Yu Shi. “Many-body dynamics with time-dependent interaction.” In: *Phys. Rev. A* 104 (2 2021), p. 023307.
- [167] Changyuan Lyu, Chenwei Lv, and Qi Zhou. “Geometrizing Quantum Dynamics of a Bose-Einstein Condensate.” In: *Phys. Rev. Lett.* 125 (25 2020), p. 253401.
- [168] Pengfei Zhang and Yingfei Gu. “Periodically and quasi-periodically driven dynamics of Bose-Einstein condensates.” In: *SciPost Phys.* 9 (22 2020), p. 079.
- [169] Ivar Martin. “Floquet dynamics of classical and quantum cavity fields.” In: *Annals of Physics* 405 (22 2019), pp. 101–129.
- [170] Welington de Melo and Sebastian van Strien. *One-Dimensional Dynamics*. Vol. 99. Springer, Berlin Heidelberg, 1993, p. 220303.
- [171] K. Gawędzki, E. Langmann, and P. Moosavi. “Finite-time universality in nonequilibrium CFT.” In: *J. Stat. Phys.* 172 (22 2018), p. 353.
- [172] Edwin Langmann, Joel L. Lebowitz, Vieri Mastropietro, and Per Moosavi. “Time evolution of the Luttinger model with nonuniform temperature profile.” In: *Phys. Rev. B* 95 (23 2017), p. 235142.
- [173] J. L. Cardy, O. A. Castro-Alvaredo, and B. Doyon. “Form Factors of Branch-Point Twist Fields in Quantum Integrable Models and Entanglement Entropy.” In: *Journal of Statistical Physics* 130.1 (22 2007), pp. 129–168.
- [174] Marlon Rodney, H. Francis Song, Sung-Sik Lee, Karyn Le Hur, and Erik S. Sørensen. “Scaling of entanglement entropy across Lifshitz transitions.” In: *Phys. Rev. B* 87 (11 2013), p. 115132.
- [175] Heinz-Peter Breuer and Francesco Petruccione. *The Theory of Open Quantum Systems*. Vol. 99. Oxford: Oxford University Press, 2007, p. 220303.
- [176] Peter Haenggi. *Driven quantum systems*. Vol. 99. American Physical Society, Oct. 2018, p. 220303.

- [177] Marin Bukov, Luca D'Alessio, and Anatoli Polkovnikov. "Universal high-frequency behavior of periodically driven systems: from dynamical stabilization to Floquet engineering." In: *Advances in Physics* 64.2 (22 2015), pp. 139–226.
- [178] Takashi Oka and Sota Kitamura. "Floquet Engineering of Quantum Materials." In: *Annual Review of Condensed Matter Physics* 10.1 (22 2019), pp. 387–408.
- [179] E. M. Kessler, G. Giedke, A. Imamoglu, S. F. Yelin, M. D. Lukin, and J. I. Cirac. "Dissipative phase transition in a central spin system." In: *Phys. Rev. A* 86 (1 2012), p. 012116.
- [180] Farokh Mivehvar, Francesco Piazza, Tobias Donner, and Helmut Ritsch. "Cavity QED with quantum gases: new paradigms in many-body physics." In: *Advances in Physics* 70.1 (22 2021), pp. 1–153.
- [181] Christian Gross and Immanuel Bloch. "Quantum simulations with ultracold atoms in optical lattices." In: *Science* 357.6355 (22 2017), pp. 995–1001.
- [182] Adam Smith, M. S. Kim, Frank Pollmann, and Johannes Knolle. "Simulating quantum many-body dynamics on a current digital quantum computer." In: *npj Quantum Information* 5.1 (22 2019), p. 220303.
- [183] M. B. Plenio, S. F. Huelga, A. Beige, and P. L. Knight. "Cavity-loss-induced generation of entangled atoms." In: *Physical Review A* 59.3 (22 1999), pp. 2468–2475.
- [184] Daniel Braun. "Creation of Entanglement by Interaction with a Common Heat Bath." In: *Phys. Rev. Lett.* 89 (27 2002), p. 277901.
- [185] S. Schneider and G. J. Milburn. "Entanglement in the steady state of a collective-angular-momentum (Dicke) model." In: *Phys. Rev. A* 65 (4 2002), p. 042107.
- [186] M. S. Kim, Jinhyoung Lee, D. Ahn, and P. L. Knight. "Entanglement induced by a single-mode heat environment." In: *Phys. Rev. A* 65 (4 2002), p. 040101.
- [187] F. Benatti, F. Carollo, and R. Floreanini. "Dissipative entanglement of quantum spin fluctuations." In: *Journal of Mathematical Physics* 57.6 (22 2016), p. 062208.
- [188] F. Benatti and R. Floreanini. "Entangling oscillators through environment noise." In: *Journal of Physics A: Mathematical and General* 39.11 (22 2006), pp. 2689–2699.
- [189] B. Kraus, H. P. Büchler, S. Diehl, A. Kantian, A. Micheli, and P. Zoller. "Preparation of entangled states by quantum Markov processes." In: *Phys. Rev. A* 78 (4 2008), p. 042307.
- [190] S. Diehl, A. Micheli, A. Kantian, B. Kraus, H. P. Büchler, and P. Zoller. "Quantum states and phases in driven open quantum systems with cold atoms." In: *Nature Physics* 4.11 (22 2008), 878–883.
- [191] Loredana M. Vasiloiu, Federico Carollo, and Juan P. Garrahan. "Enhancing correlation times for edge spins through dissipation." In: *Phys. Rev. B* 98 (9 2018), p. 094308.

- [192] Loredana M. Vasiloiu, Apoorv Tiwari, and Jens H. Bardarson. *Dephasing enhanced strong Majorana zero modes in 2D and 3D higher-order topological superconductors*. 2022.
- [193] Bastien Lapierre, Kenny Choo, Clément Tauber, Apoorv Tiwari, Titus Neupert, and Ramasubramanian Chitra. “Emergent black hole dynamics in critical Floquet systems.” In: *Phys. Rev. Res.* 2 (2 2020), p. 023085.
- [194] Ingo Peschel and Viktor Eisler. “Reduced density matrices and entanglement entropy in free lattice models.” In: *Journal of Physics A: Mathematical and Theoretical* 42.50 (22 2009), p. 504003.
- [195] Crispin Gardiner and Peter Zoller. *Quantum Noise*. Vol. 99. Springer, 2004, p. 220303. ISBN: 3540223010.
- [196] Angel Rivas and Susana F. Huelga. *Open Quantum Systems*. Vol. 99. Springer Berlin Heidelberg, 2012, p. 220303. ISBN: 9783642233548.
- [197] G. Lindblad. “On the generators of quantum dynamical semigroups.” In: *Comm. Math. Phys.* 48.2 (22 1976), pp. 119–130.
- [198] Vittorio Gorini, Andrzej Kossakowski, and E. C. G. Sudarshan. “Completely positive dynamical semigroups of N-level systems.” In: *J. Math. Phys.* 17.5 (22 1976), pp. 821–825.
- [199] Daniel Manzano. “A short introduction to the Lindblad master equation.” In: *AIP Adv.* 10.2 (22 2020), p. 025106.
- [200] Tomaž Prosen. “Third quantization: a general method to solve master equations for quadratic open Fermi systems.” In: *New Journal of Physics* 10.4 (22 2008), p. 043026.
- [201] Paolo Molignini, Evert van Nieuwenburg, and R. Chitra. “Sensing Floquet-Majorana fermions via heat transfer.” In: *Phys. Rev. B* 96 (12 2017), p. 125144.
- [202] Maximilian Behr, Peter Benner, and Jan Heiland. *Solution Formulas for Differential Sylvester and Lyapunov Equations*. 2018.
- [203] Xiangyu Cao, Antoine Tilloy, and Andrea De Luca. “Entanglement in a fermion chain under continuous monitoring.” In: *SciPost Phys.* 7 (2 2019), p. 24.
- [204] Daniel Crow and Robert Jooynt. “Classical simulation of quantum dephasing and depolarizing noise.” In: *Phys. Rev. A* 89 (4 2014), p. 042123.
- [205] O. Alberton, M. Buchhold, and S. Diehl. “Entanglement Transition in a Monitored Free-Fermion Chain: From Extended Criticality to Area Law.” In: *Phys. Rev. Lett.* 126 (17 2021), p. 170602.
- [206] Michael Buchhold and Sebastian Diehl. “Nonequilibrium universality in the heating dynamics of interacting Luttinger liquids.” In: *Phys. Rev. A* 92 (1 2015), p. 013603.
- [207] J J Mendoza-Arenas, S Al-Assam, S R Clark, and D Jaksch. “Heat transport in the XXZ spin chain: from ballistic to diffusive regimes and dephasing enhancement.” In: *Journal of Statistical Mechanics: Theory and Experiment* 2013.07 (22 2013), P07007.
- [208] Daniel A. Roberts and Douglas Stanford. “Two-dimensional conformal field theory and the butterfly effect.” In: *Phys. Rev. Lett.* 115.13 (22 2015), p. 131603.

- [209] Stephen H. Shenker and Douglas Stanford. “Black holes and the butterfly effect.” In: *Journal of High Energy Physics* 2014.3 (22 2014), p. 220303.
- [210] Juan Maldacena, Stephen H. Shenker, and Douglas Stanford. “A bound on chaos.” In: *Journal of High Energy Physics* 2016.8 (22 2016), p. 220303.
- [211] A. Liam Fitzpatrick, Jared Kaplan, and Matthew T. Walters. “Universality of long-distance AdS physics from the CFT bootstrap.” In: *Journal of High Energy Physics* 2014.8 (22 2014), p. 220303.
- [212] Kanato Goto, Masahiro Nozaki, Kotaro Tamaoka, Mao Tian Tan, and Shinsei Ryu. *Non-Equilibrating a Black Hole with Inhomogeneous Quantum Quench*. 2021.
- [213] Suchetan Das, Bobby Ezhuthachan, Arnab Kundu, Somnath Porey, Baishali Roy, and K. Sengupta. “Out-of-Time-Order correlators in driven conformal field theories.” In: *Journal of High Energy Physics* 2022.8 (22 2022), p. 220303.
- [214] Blagoje Oblak. “Berry phases on Virasoro orbits.” In: *Journal of High Energy Physics* 2017.10 (22 2017), p. 220303.
- [215] Masashi Ban. “Decomposition formulas for $\text{su}(1, 1)$ and $\text{su}(2)$ Lie algebras and their applications in quantum optics.” In: *Journal of the Optical Society of America B Optical Physics* 10.8 (22 Aug. 1993), pp. 1347–1359.
- [216] Ashley Milsted and Guifré Vidal. “Extraction of conformal data in critical quantum spin chains using the Koo-Saleur formula.” In: *Phys. Rev. B* 96 (24 2017), p. 245105.
- [217] Yijian Zou, Ashley Milsted, and Guifré Vidal. “Conformal Fields and Operator Product Expansion in Critical Quantum Spin Chains.” In: *Phys. Rev. Lett.* 124 (4 2020), p. 040604.
- [218] Ruoshui Wang, Yijian Zou, and Guifré Vidal. “Emergence of Kac-Moody symmetry in critical quantum spin chains.” In: *Phys. Rev. B* 106 (11 2022), p. 115111.
- [219] A. Iucci and M. A. Cazalilla. “Quantum quench dynamics of the Luttinger model.” In: *Phys. Rev. A* 80 (22 2009), p. 063619.
- [220] C. Karrasch, J. Rentrop, D. Schuricht, and V. Meden. “Luttinger-liquid universality in the time evolution after an interaction quench.” In: *Phys. Rev. Lett.* 109 (22 2012), p. 126406.
- [221] J. Rentrop, D. Schuricht, and V. Meden. “Quench dynamics of the Tomonaga-Luttinger model with momentum-dependent interaction.” In: *New J. Phys.* 14 (22 2012), p. 075001.
- [222] Balázs Dóra, Frank Pollmann, József Fortágh, and Gergely Zaránd. “Loschmidt Echo and the Many-Body Orthogonality Catastrophe in a Qubit-Coupled Luttinger Liquid.” In: *Phys. Rev. Lett.* 111 (4 2013), p. 046402.
- [223] Stéphane Ngo Dinh, Dmitry A. Bagrets, and Alexander D. Mirlin. “Interaction quench in nonequilibrium Luttinger liquids.” In: *Phys. Rev. B* 88 (22 2013), p. 245405.
- [224] Ádám Bácsi and Balázs Dóra. “Quantum quench in the Luttinger model with finite temperature initial state.” In: *Phys. Rev. B* 88 (22 2013), p. 155115.

- [225] Rashi Sachdeva, Tanay Nag, Amit Agarwal, and Amit Dutta. “Finite-time interaction quench in a Luttinger liquid.” In: *Phys. Rev. B* 90 (22 2014), p. 045421.
- [226] J.-S. Bernier, R. Citro, C. Kollath, and E. Orignac. “Correlation dynamics during a slow interaction quench in a one-dimensional Bose gas.” In: *Phys. Rev. Lett.* 112 (22 2014), p. 065301.
- [227] Balázs Dóra and Frank Pollmann. “Absence of Orthogonality Catastrophe after a Spatially Inhomogeneous Interaction Quench in Luttinger Liquids.” In: *Phys. Rev. Lett.* 115 (22 2015), p. 096403.
- [228] Michael Buchhold, Markus Heyl, and Sebastian Diehl. “Prethermalization and thermalization of a quenched interacting Luttinger liquid.” In: *Phys. Rev. A* 94 (22 2016), p. 013601.
- [229] E. Langmann, J. L. Lebowitz, V. Mastropietro, and P. Moosavi. “Steady states and universal conductance in a quenched Luttinger model.” In: *Commun. Math. Phys.* 349 (22 2017), p. 551.
- [230] Paola Ruggiero, Pasquale Calabrese, Thierry Giamarchi, and Laura Foini. “Electrostatic solution of massless quenches in Luttinger liquids.” In: *SciPost Phys.* 13 (22 2022), p. 111.
- [231] P. Moosavi. *Exact Dirac-Bogoliubov-de Gennes dynamics for inhomogeneous quantum liquids*. arXiv:2208.14467 [cond-mat.stat-mech]. 2022.
- [232] Vladimir Gritsev, Eugene Demler, Mikhail Lukin, and Anatoli Polkovnikov. “Spectroscopy of Collective Excitations in Interacting Low-Dimensional Many-Body Systems Using Quench Dynamics.” In: *Phys. Rev. Lett.* 99 (22 2007), p. 200404.
- [233] Jarrett Lancaster and Aditi Mitra. “Quantum quenches in an XXZ spin chain from a spatially inhomogeneous initial state.” In: *Phys. Rev. E* 81 (22 2010), p. 061134.
- [234] Frank Pollmann, Masudul Haque, and Balázs Dóra. “Linear quantum quench in the Heisenberg XXZ chain: Time-dependent Luttinger-model description of a lattice system.” In: *Phys. Rev. B* 87 (22 2013), 041109(R).
- [235] Mario Collura, Pasquale Calabrese, and Fabian H. L. Essler. “Quantum quench within the gapless phase of the spin – $\frac{1}{2}$ Heisenberg XXZ spin chain.” In: *Phys. Rev. B* 92 (22 2015), p. 125131.
- [236] Jean-Marie Stéphan. “Return probability after a quench from a domain wall initial state in the spin-1/2 XXZ chain.” In: *J. Stat. Mech.* 2017 (22 2017), p. 103108.
- [237] Marcus Kollar and Martin Eckstein. “Relaxation of a one-dimensional Mott insulator after an interaction quench.” In: *Phys. Rev. A* 78 (22 2008), p. 013626.
- [238] Dominik Muth and Michael Fleischhauer. “Dynamics of Pair Correlations in the Attractive Lieb-Liniger Gas.” In: *Phys. Rev. Lett.* 105 (22 2010), p. 150403.
- [239] Dominik Muth, Bernd Schmidt, and Michael Fleischhauer. “Fermionization dynamics of a strongly interacting one-dimensional Bose gas after an interaction quench.” In: *New J. Phys.* 12 (22 2010), p. 083065.

- [240] Jorn Mossel and Jean-Sébastien Caux. “Exact time evolution of space- and time-dependent correlation functions after an interaction quench in the one-dimensional Bose gas.” In: *New J. Phys.* 14 (22 2012), p. 075006.
- [241] Deepak Iyer, Huijie Guan, and Natan Andrei. “Exact formalism for the quench dynamics of integrable models.” In: *Phys. Rev. A* 87 (22 2013), p. 053628.
- [242] Pasquale Calabrese and Pierre Le Doussal. “Interaction quench in a Lieb-Liniger model and the KPZ equation with flat initial conditions.” In: *J. Stat. Mech.* 2014 (22 2014), P05004.
- [243] Jacopo De Nardis, Bram Wouters, Michael Brockmann, and Jean-Sébastien Caux. “Solution for an interaction quench in the Lieb-Liniger Bose gas.” In: *Phys. Rev. A* 89 (22 2014), p. 033601.
- [244] A. B. Zamolodchikov. “Irreversibility of the Flux of the Renormalization Group in a 2D Field Theory.” In: *JETP Lett.* 43 (22 1986), p. 730.
- [245] Markus Heyl. “Dynamical quantum phase transitions: A review.” In: *Rep. Prog. Phys.* 81 (22 2018), p. 054001.
- [246] Dénes Petz. “Quasi-entropies for finite quantum systems.” In: *Rep. Math. Phys.* 23 (22 1986), p. 57.
- [247] V. Vedral. “The role of relative entropy in quantum information theory.” In: *Rev. Mod. Phys.* 74 (22 2002), p. 197.
- [248] S. Tomonaga. “Remarks on Bloch’s method of sound waves applied to many-fermion problems.” In: *Prog. Theor. Phys.* 5 (22 1950), p. 544.
- [249] J. M. Luttinger. “An exactly soluble model of a many-fermion system.” In: *J. Math. Phys.* 4 (22 1963), p. 1154.
- [250] D. C. Mattis and E. H. Lieb. “Exact solution of a many-fermion system and its associated boson field.” In: *J. Math. Phys.* 6 (22 1965), p. 304.
- [251] T. Giamarchi. *Quantum Physics in One Dimension*. Vol. 99. International Series of Monographs on Physics. Oxford: Oxford University Press, 2003, p. 220303.
- [252] H. J. Schulz, G. Cuniberti, and P. Pieri. “Fermi liquids and Luttinger liquids.” In: *Phys. Rev. B* 99 (22 1998), p. 220303.
- [253] Edwin Langmann and Per Moosavi. “Construction by bosonization of a fermion-phonon model.” In: *J. Math. Phys.* 56 (22 2015), p. 091902.
- [254] H. P. Büchler, G. Blatter, and W. Zwerger. “Commensurate-Incommensurate Transition of Cold Atoms in an Optical Lattice.” In: *Phys. Rev. Lett.* 90 (22 2003), p. 130401.
- [255] M. A. Cazalilla. “Bosonizing one-dimensional cold atomic gases.” In: *J. Phys. B: At. Mol. Opt. Phys.* 37 (22 2004), S1.
- [256] D. S. Petrov, D. M. Gangardt, and G. V. Shlyapnikov. “Low-dimensional trapped gases.” In: *J. Phys. IV France* 116 (22 2004), p. 5.
- [257] M. A. Cazalilla, R. Citro, T. Giamarchi, E. Orignac, and M. Rigol. “One dimensional bosons: From condensed matter systems to ultracold gases.” In: *Rev. Mod. Phys.* 83 (22 2011), p. 1405.

- [258] F. D. M. Haldane. “Effective Harmonic-Fluid Approach to Low-Energy Properties of One-Dimensional Quantum Fluids.” In: *Phys. Rev. Lett.* 47 (25 1981), p. 1840.
- [259] Marek Gluza, Per Moosavi, and Spyros Sotiriadis. “Breaking of Huygens-Fresnel principle in inhomogeneous Tomonaga-Luttinger liquids.” In: *J. Phys. A: Math. Theor.* 55 (22 2022), p. 054002.
- [260] Vladimir Gritsev, Anatoli Polkovnikov, and Eugene Demler. “Linear response theory for a pair of coupled one-dimensional condensates of interacting atoms.” In: *Phys. Rev. B* 75 (22 2007), p. 174511.
- [261] Izabella Lovas, Roberta Citro, Eugene Demler, Thierry Giamarchi, Michael Knap, and Edmond Orignac. “Many-body parametric resonances in the driven sine-Gordon model.” In: *Phys. Rev. B* 106 (22 2022), p. 075426.
- [262] Moshe Goldstein, Michel H. Devoret, Manuel Houzet, and Leonid I. Glazman. “Inelastic Microwave Photon Scattering off a Quantum Impurity in a Josephson-Junction Array.” In: *Phys. Rev. Lett.* 110 (22 2013), p. 017002.
- [263] Ananda Roy, Dirk Schuricht, Johannes Hauschild, Frank Pollmann, and Hubert Saleur. “The quantum sine-Gordon model with quantum circuits.” In: *Nucl. Phys. B* 968 (22 2021), p. 115445.
- [264] Stefan Forste and Daniel Roggenkamp. “Current current deformations of conformal field theories, and WZW models.” In: *J. High Energy Phys.* 05 (22 2003), p. 071.
- [265] J. Polchinski. *String theory. Vol. 1: An introduction to the bosonic string.* Vol. 99. Cambridge Monographs on Mathematical Physics. Cambridge: Cambridge University Press, 1998, p. 220303.
- [266] Paul H. Ginsparg. “Curiosities at $c = 1$.” In: *Nucl. Phys. B* 295 (22 1988), p. 153.
- [267] Askold Perelomov. *Generalized Coherent States and Their Applications.* Vol. 99. Theoretical and Mathematical Physics. Berlin, Heidelberg: Springer, 1986, p. 220303.
- [268] Marlan O. Scully and M. Suhail Zubairy. *Quantum Optics.* Vol. 99. Cambridge: Cambridge University Press, 1997, p. 220303.
- [269] D. Dominici, S.J. Johnston, and K. Jordaan. “Real zeros of ${}_2F_1$ hypergeometric polynomials.” In: *J. Comput. Appl. Math.* 247 (22 2013), p. 152.
- [270] Thomás Fogarty, Ayaka Usui, Thomas Busch, Alessandro Silva, and John Goold. “Dynamical phase transitions and temporal orthogonality in one-dimensional hard-core bosons: From the continuum to the lattice.” In: *New J. Phys.* 19 (22 2017), p. 113018.
- [271] Paola Ruggiero, Laura Foini, and Thierry Giamarchi. “Large-scale thermalization, prethermalization, and impact of temperature in the quench dynamics of two unequal Luttinger liquids.” In: *Phys. Rev. Research* 3 (22 2021), p. 013048.
- [272] A. M. Perelomov and V. S. Popov. “Group-theoretical aspects of the variable frequency oscillator problem.” In: *Theor. Math. Phys.* 1 (22 1969), p. 275.

- [273] Vladimir Gritsev and Anatoli Polkovnikov. “Integrable Floquet dynamics.” In: *SciPost Phys.* 2 (22 2017), p. 021.
- [274] Serena Fazzini, Piotr Chudzinski, Christoph Dauer, Imke Schneider, and Sebastian Eggert. “Nonequilibrium Floquet Steady States of Time-Periodic Driven Luttinger Liquids.” In: *Phys. Rev. Lett.* 126 (22 2021), p. 243401.
- [275] M. Bukov and M. Heyl. “Parametric instability in periodically driven Luttinger liquids.” In: *Phys. Rev. B* 86 (22 2012), p. 054304.
- [276] David D. Blanco, Horacio Casini, Ling-Yan Hung, and Robert C. Myers. “Relative entropy and holography.” In: *J. High Energy Phys.* 2013 (22 2013), p. 060.
- [277] Daniel L. Jafferis, Aitor Lewkowycz, Juan Maldacena, and S. Josephine Suh. “Relative entropy equals bulk relative entropy.” In: *J. High Energy Phys.* 2016 (22 2016), p. 004.
- [278] Nima Lashkari. “Relative entropies in conformal field theory.” In: *Phys. Rev. Lett.* 113 (22 2014), p. 051602.
- [279] Nima Lashkari. “Modular Hamiltonian for excited states in conformal field theory.” In: *Phys. Rev. Lett.* 117 (22 2016), p. 041601.
- [280] Paola Ruggiero and Pasquale Calabrese. “Relative entanglement entropies in 1+1-dimensional conformal field theories.” In: *J. High Energy Phys.* 2017 (22 2017), p. 039.
- [281] Alice Bernamonti, Federico Galli, Robert C. Myers, and Jonathan Oppenheim. “Holographic second laws of black hole thermodynamics.” In: *J. High Energy Phys.* 2018 (22 2018), p. 111.
- [282] Barsha G. Chowdhury, Shouvik Datta, and Justin R. David. “Rényi divergences from Euclidean quenches.” In: *J. High Energy Phys.* 2020 (22 2020), p. 094.
- [283] Per Kraus and Finn Larsen. “Partition functions and elliptic genera from supergravity.” In: *J. High Energy Phys.* 2007 (22 2007), p. 002.
- [284] Kun Woo Kim, Dmitry Bagrets, Tobias Micklitz, and Alexander Altland. “Quantum Hall criticality in Floquet topological insulators.” In: *Phys. Rev. B* 101 (16 2020), p. 165401.
- [285] Eli Chertkov, Benjamin Villalonga, and Bryan K. Clark. “Numerical Evidence for Many-Body Localization in Two and Three Dimensions.” In: *Phys. Rev. Lett.* 126 (18 2021), p. 180602.
- [286] Thorsten B. Wahl, Arijeet Pal, and Steven H. Simon. “Signatures of the many-body localized regime in two dimensions.” In: *Nature Physics* 15.2 (22 2018), pp. 164–169.
- [287] Frederik Nathan, Dmitry Abanin, Erez Berg, Netanel H. Lindner, and Mark S. Rudner. “Anomalous Floquet insulators.” In: *Physical Review B* 99.19 (22 2019), p. 220303.
- [288] Carl K. Cole and William C. Schieve. “Radiation modes of a cavity with a moving boundary.” In: *Phys. Rev. A* 52 (6 1995), pp. 4405–4415.
- [289] Ibrahim Akal, Yuya Kusuki, Noboptiurl Shiba, Tadashi Takayanagi, and Zixia Wei. “Entanglement Entropy in a Holographic Moving Mirror and the Page Curve.” In: *Phys. Rev. Lett.* 126 (6 2021), p. 061604.

- [290] Stefano Scopa, Gabriel T. Landi, and Dragi Karevski. “Lindblad-Floquet description of finite-time quantum heat engines.” In: *Phys. Rev. A* 97 (22 2018), p. 062121.
- [291] Stefano Scopa, Gabriel T. Landi, Adam Hammoumi, and Dragi Karevski. “Exact solution of time-dependent Lindblad equations with closed algebras.” In: *Phys. Rev. A* 99 (22 2019), p. 022105.
- [292] S. Chaudhuri and J. A. Schwartz. “A criterion for integrably marginal operators.” In: *Phys. Lett. B* 219 (22 1989), p. 291.
- [293] F. A. Smirnov and A. B. Zamolodchikov. “On space of integrable quantum field theories.” In: *Nucl. Phys. B* 915 (22 2017), p. 363.
- [294] Andrea Cavaglià, Stefano Negro, István M. Szécsényi, and Roberto Tateo. “ $T\bar{T}$ -deformed 2D quantum field theories.” In: *J. High Energy Phys.* 2016 (22 2016), p. 112.
- [295] Justin R. David, Gautam Mandal, and Spenta R. Wadia. “Microscopic formulation of black holes in string theory.” In: *Phys. Rept.* 369 (22 2002), p. 549.